FACULTY OF ENGINEERING AND APPLIED SCIENCE
DEPARTMENT OF ELECTRONICS AND COMPUTER SCIENCE

VIBRATION POWERED GENERATORS FOR SELF-POWERED MICROSYSTEMS

by

Peter Glynne-Jones

A thesis submitted for the degree of
Doctor of Philosophy

University of Southampton
June 2001

UNIVERSITY OF SOUTHAMPTON

ABSTRACT

FACULTY OF ENGINEERING AND APPLIED SCIENCE

DEPARTMENT OF ELECTRONICS AND COMPUTER SCIENCE

Doctor of Philosophy

VIBRATION POWERED GENERATORS FOR SELF-POWERED MICROSYSTEMS

by Peter Glynne-Jones

Methods are examined for deriving energy from vibrations naturally present around sensor systems. Devices of this type are described in the literature as self-powered. This term is defined as describing systems that operate by harnessing ambient energy present within their environment. Traditionally, remote devices have used batteries to supply their energy, which offer only a limited life span to a system. The recent rapid advances in integrated circuit technology have not been matched by similar advances in battery technology, thus, power requirements place important limits on the capability of modern remote microsystems. Self-power offers a potential solution to power requirements, and when combined with some form of wireless communications, can produce truly wireless autonomous systems.

A generator based on the thick-film piezoelectric material, PZT, is produced. The resulting device is tested, and methods are devised to measure the material properties of its constituent layers. Power output is low at only 3μW. Modelling shows that the low power output is due to the low electromagnetic coupling of thick-film PZT. The modelling includes the development of a new model of a resistively shunted piezoelectric element undergoing pure bending. Numerical optimisation is used to predict the power output from piezoelectric generators of arbitrary dimensions and excitation conditions.

Experiments have been devised to assess the long-term stability of thick film PZT materials. A technique for measuring the ageing rate of the d_{31} and K_{33} coefficients of a PZT thick-film sample is presented. The d_{31} coefficient is found to age at −4.4% per time decade, and K_{33}, at −1.34% per time decade (PZT-5H).

An electrical equivalent circuit model of a generator based on electromagnetic induction has been described, and verified by producing a prototype generator. The prototype could produce 4.9mW in a volume of $4cm^3$ at a resonant frequency of 99Hz. A typical configuration is modelled, and numerical methods used to find optimum generator dimensions, and predict power output for various excitations. The model is used to compare this type of generator to piezoelectric generators, and hence evaluate the two technologies. Graphs are produced to permit estimates of how much power could be produced by either generator type under arbitrary excitation conditions. It is concluded that neither generator type is superior under all excitation conditions, but that severe manufacturing difficulties with piezoelectric generators mean that they are unlikely to be commonly used in future applications.

The following points have been identified as the key contributions to knowledge made by this thesis: A thick-film piezoelectric generator has been presented for the first time, and its performance assessed. A simple way of calculating the power that can be produced by a piezoelectric generator has been presented, including a new model of a resistively shunted piezoelectric element undergoing bending. An investigation to measure the previously unquantified long-term stability of thick-film PZT has been described. Idealised generator models have been used to make predictions of how much power can be generated from both piezoelectric and magnet-coil generators for a range of harmonic excitation frequencies and amplitudes. This data has been collected in a graph that permits future designers to simply calculate the most suitable technology for a given application, and to obtain an estimate of how much power can be produced.

To Mum and Dad.

Acknowledgements

I would like to thank Dr. Neil White, my supervisor, for his support and friendship throughout my studies. The trust and freedom to explore in my own way was really appreciated.

Special thanks to Steve Beeby and Neil Grabham for the many times they have given their time and support, and to Thomas Papakostas, and Seyed Almodarresi for making the lab a friendly place to work.

Thanks also to Danny Patrick and Ken Frampton, for their great patience as my many designs unfolded in their workshop.

This PhD would not have been possible without the many friends who I am lucky enough to have shared the past three years. In particular, a deep bow to Henry and Jenny for lunch and much more.

"In the beginner's mind there are many possibilities, in the expert's there are few"

Shunryu Suzuki

Contents

List of Figures

List of Tables

List of Symbols

General Symbols

η^{T}	diagonal matrix of clamped susceptibility
$\varepsilon_3^{S_1}$	permittivity in the 3 direction, of a material clamped in the 1 direction
ζ	damping factor / damping ratio
ω	circular frequency
Λ	a non dimensional function
Δ	deflection
δ	logarithmic decrement
η	loss factor
ρ	non-dimensional frequency, density, radius of curvature
ρ_{bound}	area bound charge density
ρ_{free}	area free charge density
ρ_{volume}	volume charge density inside dielectric
χ	inverse of radius of curvature
α	ratio of the layer thickness to the distance from the neutral axis to the centre of the layer, base excitation amplitude
β	ratio of gap to core width
ε	permittivity
ε_0	permittivity of free space
ζ_E	electrical damping factor
ζ_L	unwanted / lossy damping factor
ω_n	natural circular frequency
ε^T	matrix of un-clamped permittivity
ψ	relates to the amount of magnetic energy stored per core volume
Ψ	the value of ψ_{max}
$(YI)_b$	real bending stiffness
$(YI)_{complex}$	complex bending stiffness
A	area, amplitude, maximum beam deflection
b	width
B	constant based on layer thickness, magnetic flux density

c	viscous damping coefficient, the distance of the outer surface of a beam from its neutral axis
c_{ij}	elements of stiffness matrix
C	capacitance
C^S	clamped capacitance
D	vector of electrical displacements, average core density
d	piezoelectric constant matrix
d	height of piezoelectric layer
$d_{33,eff}$	effective d_{33}
d_{ij}	element of piezoelectric constant matrix
E	vector of electrical field
$E_{den,a}$	energy density in actuation
$E_{den,g}$	energy density in generation
E_m	peak value of elastic energy
F	force
f	frequency
F_1, F_2	frequencies
F	force
f_n	natural frequency
g	gap width
h	height
H	height
I	second moment of area, current
k	spring constant
K	frequency amplitude density, constant based on degree of electromechanical coupling, ageing constant
k_{ij}	electromechanical coupling coefficient, constants
K_{ij}	constants, dielectric constant
l	length
L	length, inductance
m	mass
M	moment
N	number of cycles, number of coil windings
P	electrical power, pressure
P	vector of electric polarisation
P_E	electrical power

$P_{E,RES}$	electrical power at resonance
Q	charge
R	resistance
R'	normalised load resistance
R_{SU}	shunting resistance
S	vector of material engineering strains
s	stiffness matrix
s	Laplace complex frequency variable
s_{ij}	element of stiffness matrix
T	vector of material stresses, stress, depth
T^r	stress at beam surface
t	thickness
Tc	coefficient of thermal expansion
T_{max}	maximum rated stress
U	Maximum strain energy
V	voltage
v	velocity
W	width
W_n	amplitude of nth cycle
W_d	electrical energy produced per cycle
x	displacement of coil
y	position variable
Y	modulus of elasticity
y(t)	base excitation
Y_0	amplitude of base excitation
y_b	distance from neutral surface to bottom of PZT layer
y_m	distance to the centre of the piezoelectric layer from the neutral surface.
Y_{SU}	shunting admittance
y_t	distance from neutral surface to top of PZT layer
z(t)	beam displacement relative to enclosure
Z_{max}	maximum possible beam amplitude
Z^{ME}	complex mechanical impedance

Mathematical Symbols

$( )^D$	open circuit boundary conditions

$( )^E$	short circuit boundary conditions
$( )^S$	clamped boundary conditions
$( )_t$	matrix transpose
$( )^T$	un-clamped boundary conditions
bold	Laplace transform of variable, Matrix / vector
j	$\sqrt{-1}$
ln()	natural logarithm
log()	decadic logarithm

Glossary of Terms

Bulk PZT	PZT that has been formed by pressing the sintered powder into the desired shape before firing.
Thick-film printing	A process of depositing viscous pastes in patterns by pushing them through a mesh screen that has selected areas masked off.
MEMS	Micro Electro Mechanical Systems
IC	Integrated Circuit
Self-powered	Describes a device that derives power from ambient energy surrounding the system.
Piezo-generator	A generator that converts energy from vibrations to electrical energy using a piezoelectric material (see chapter 4)
PZT	Lead Zirconate Titanate
SEM	Scanning Electron Microscope
TCE	Thermal Coefficient of Expansion (ppm K^{-1})
Magnet-coil generator	A generator that converts energy from vibrations to electrical energy using electromagnetic induction (see chapter 7)
Cermet	used to describe a ceramic / metal thick-film paste or film

CHAPTER 1

Introduction

This thesis examines power sources for devices that are often described in the literature as 'self-powered'. In particular, there is a focus on methods for deriving energy from vibrations naturally present around sensor systems.

The term self-powered is confusing, and brings to mind perpetual-motion type systems that somehow defy the first law of thermodynamics. To avoid ambiguity, self-powered systems are defined here as those that operate by harnessing ambient energy present within their environment. Power sources of this type are also described as micro power supplies, and self-sufficient power supplies in the literature. Possible sources of ambient energy include vibration, solar energy, and temperature difference. They are comparable, if at a smaller scale, to sources of alternative energy such as wind, wave, and geothermal power.

Self-powered systems have several potential advantages over more conventional alternatives. As Micro Electro Mechanical Systems (MEMS) become cheaper and more widespread, the cost of connecting sensors to both power supplies and communications links will become a more dominant factor. For a high unit-cost system such as a hard drive head this is not an issue, but there is a trend towards distributed sensor systems utilising several orders of magnitude more sensors than currently used. Such systems have the advantage of higher reliability, and the ability to compensate for the peculiarities of any single sensor through data fusion. The drawback is the need to connect and power all the devices. Appropriate power supplies are also difficult to engineer in systems that are physically some distance from normal power sources, or in inaccessible places. Examples include systems on buildings, aircraft structures, and inside of large machinery.

Traditionally, remote devices have used batteries to supply their energy, which offer only a limited life span to a system. The recent rapid advances in integrated circuit technology have not been matched by similar advances in battery technology. Thus, power requirements place important limits on the capability of modern remote microsystems. Self-power offers a potential

solution to power requirements, and when combined with some form of wireless communications, can produce truly wireless autonomous systems.

As the literature review chapter will reveal, self-power is not a new area of study; the first self-winding watch was built by Abraham-Louis Perrelet in 1770 [1]. Interest in self-power is currently growing rapidly with several sessions dedicated to the subject in recent international conferences [2]. Technologies vary in the level of research undertaken to date. Solar power is a particularly mature and well characterised technology, while vibration powered devices by comparison have attracted little interest. No existing studies survey different techniques for extracting power from vibrations, or permit a comparison of techniques. Neither have simple models or graphs been produced to enable designers to predict how much power might be produced from a given vibration source by a practical generator. This thesis fills these gaps, and sets out to form a sound basis for future vibration-powered applications.

1.1 Thesis Outline

Chapter 2 reviews existing power sources for self-powered systems, and describes some of the many applications that have been explored. It concludes with a description of some other current research projects in this area.

Chapter 3 introduces possible transduction technologies that may be used in vibration powered generators, including piezoelectric and electrostrictive materials, and electromagnetic induction. A simple first order model of a generic resonant vibration generator is presented and some of its implications explored. The question of how much power a generator needs to produce to be considered 'useful' is addressed.

Chapter 4 describes the development of a thick-film PZT generator. It includes fabrication details and discussion of technical problems. The resulting device is tested, and methods are devised to measure the material properties of its constituent layers.

Chapter 5 develops a method for modelling the response of piezoelectric generators. It includes the development of a new model of a resistively shunted piezoelectric element undergoing pure bending. The model is supported by experimental results. The model is used in conjunction with numerical methods to find optimum generator dimensions, and predict power output for a range of excitations that might be found in practice.

Chapter 6 investigates the long-term stability of thick film PZT materials. In particular, experimental techniques are developed to measure the ageing rate of the d_{31} and K_{33} coefficients.

Chapter 7 explores generators based on electromagnetic induction. Typical design configurations are examined. An electrical equivalent circuit model is described, and verified by producing a prototype generator. A demonstrator mounted on a car engine block is shown to produce a useful amount of power. A typical configuration is modelled, and numerical methods used to find optimum generator dimensions, and predict power output for various excitations. The model is used to compare this type of generator to piezoelectric generators, and hence evaluate the two technologies.

Chapter 8 presents conclusions, drawing out the main points established by the thesis and discusses possible directions for further work.

CHAPTER 2

Self-Powered Systems, A Review

The first small-scale self-powered device was the self-winding watch, built by Abraham-Louis Perrelet in 1770 [1]. It is only recently, however, that other self-powered devices have become feasible thanks to the revolution in integrated circuit design. Interest in self-power is currently growing rapidly with several sessions dedicated to the subject in recent international conferences [2]. To date, no review of this subject has been published (although this chapter has now been published, see appendix A). This chapter draws together a range of work that focuses on alternative sources of energy suitable for small portable or embeddable systems, and examines some integrated systems.

2.1 Sources of Power

2.1.1 Vibration (Inertial Generators)

When a device is subject to vibration, an inertial mass can be used to create movement between parts of a generator. This movement can then be converted to electrical energy using either electromagnetic induction, a piezoelectric material, or an electrostrictive material. A possible design for an electromagnetic generator is illustrated in figure 1.

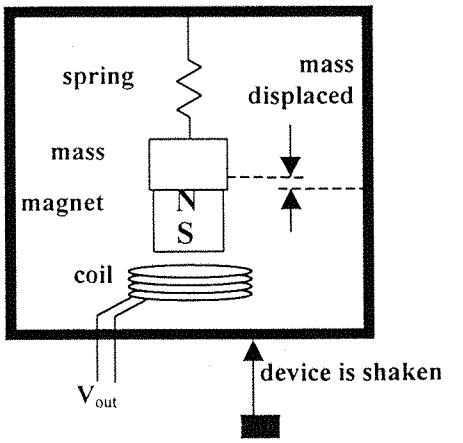

Figure 1: An electromangnetic vibration-powered generator

Williams and Yates [3] make predictions for this type of generator by applying a standard damped spring mass model (as described in section 3.2) to this type of device. Using this model they predict how much power could be generated in a given volume for a number of different excitation amplitudes, and excitation frequencies. The predictions are based on a fixed damping factor, and are thus not optimum values; also, no account is taken of whether a practical generator could be produced to meet the model parameters chosen.

In another paper [4], Williams *et al* consider how much power could be generated from the vibrations induced in road bridges by passing traffic to enable the remote detection of bridge condition. The results showed that relatively large devices of volume 1000cm^3 and 1kg mass would be required to produce power in the range 50-500μW. Scaling the figures to the dimensions typically found in microsystems, only nW would be produced for these types of vibrations.

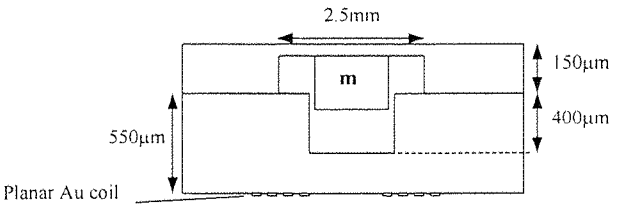

Figure 2: Generator to produce power from vibrations (after Shearwood [5])

Shearwood and Yates [5] continue the work of Williams, and fabricate the generator shown in figure 2. It consists of a magnet mass, connected to a flexible polyimide membrane. A planar coil mounted underneath the lower substrate generates power as the magnet oscillates up and down. The device is micro-machined in Silicon using etching techniques, and the magnet is glued to the membrane. The generator was initially designed as a micro-loudspeaker, so it was not optimised as a generator. This resulted in low power output at practical vibration levels, caused by over-extension of the spring membrane. Even at low vibration levels, the device obtains damping ratios of only 0.002, significantly less than the 0.1 assumed by Williams in his analysis. Operating under a vacuum t o remove significant air damping, the maximum energy the device could produce was 20μW.

Li *et al* [6] present a micromachined generator that comprises a permanent magnet mounted on a laser-micromachined spring structure next to a PCB coil. Their device, occupying around 1cm^3, generates 10μW power at 2V DC with an input excitation frequency of 64Hz and amplitude of 100μm.

A macro-sized device (500mg mass) of a similar design is constructed by Amirtharajah and Chandrakasan [7]. The device is designed to work from vibrations induced by human walking, and is predicted to produce 400μW of power. A sophisticated low-power signal-processing system is connected to the generator, and shown to perform 11000 cycles of operation from a single impulse excitation.

Umeda *et al* [8] consider a different approach. Rather than having a resonant system, they examine the power that is generated when a steel ball strikes a piezoelectric membrane. They report a maximum conversion efficiency of 35% (the ratio of initial kinetic energy to stored electrical energy after many bounces). The idea is illustrated in figure 3. It has been reported [9] that a demonstrator was produced that supplied enough energy to power a digital watch unit when shaken up and down by hand.

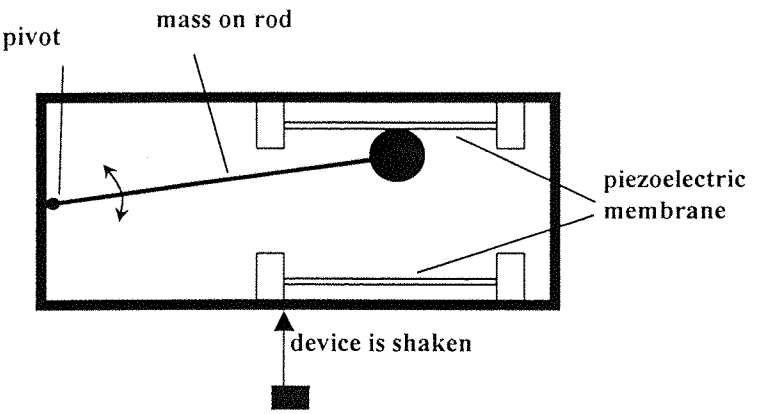

Figure 3: A non-linear piezoelectric vibration powered generator (after Umeda *et al* [8]).

A well-known example of a self-powered system is the Seiko Kinetics™ wristwatch [10]. The design is illustrated in figure 4. The generator works by connecting a weight with an eccentric centre of rotation to a speed increasing gear train. As the wrist is moved, the centre of mass of the weight is raised relative to the axle. Gravity causes the weight to rotate until the centre of mass again lies at its lowest position. The gear train supplies rotation to a dynamo at an increased rate of rotation. No figures have been found for the amount of energy that this system produces, but rough calculations, based on a weight of 2 grams falling through 1 cm once a second, show that up to 200μW might be available. The watch is sold commercially, and works well.

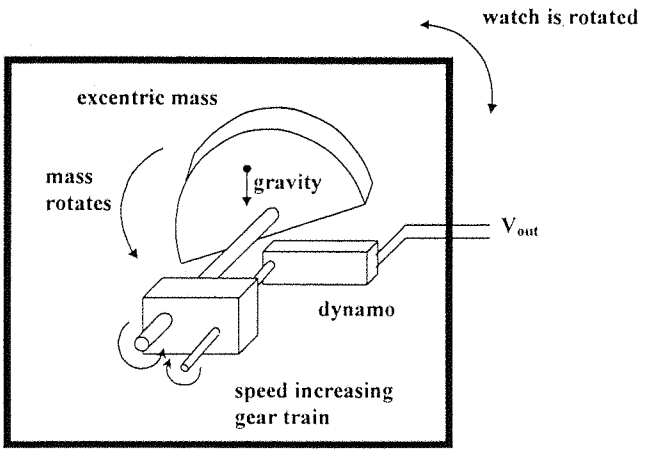

Figure 4: Principle of operation of the Seiko Kinetics™ watch (after Hayakawa [10]).

2.1.2 Non-inertial mechanical sources

Koeneman *et al* [11] develop the concept of a self-powered active bearing. A magnet is attached to the central hub of a bearing. An armature coil on the rim is used to generate power as it passes through the magnetic field, which is then used to actuate small deflections in the bearing surface via a polysilicon heater. A combination of micromachining for the silicon parts and hand construction of the coil and battery components is suggested. It is shown that if only one percent of the energy flowing through a shaft were accessible to a device then there would be ample power for many applications, however, the question of how much energy the generator mechanism could practically expect to extract is not addressed.

Konak *et al*, [12], use a piezoelectric element attached to a vibrating beam to power an active vibration damper. Such devices are of considerable interest to the aerospace industry in damping aircraft shells. The paper does not supply details about the amount of power generated. The same piezoelectric element is used for both power generation and actuation for vibration suppression. At resonance, the system was found to offer better vibration suppression than a resistively shunted passive device. It was noted, however, that away from resonance the device was not supplied with enough power, and became less effective than passive shunting.

There are many applications for sensor systems, and other devices that are mounted on or in the human body. These include portable (even wearable) computing, communications, medical and biological monitoring, and active prostheses. Starner [13] examines the energy used and discarded by the human body to evaluate how much energy might feasibly be extracted. Table 1

compares the energy stored in some typical power sources, and compares it to the power provided by a typical human daily diet.

Table 1: Comparisons of common energy sources after Starner [13]

Energy Source	Energy (J)
AA alkaline battery	10^4
Camcorder battery	10^5
One litre petrol	10^7
Average daily human food intake (2500kcal)	1.05×10^7

Starner argues that if even a small proportion of the energy that drives a human being could be tapped, then conventional batteries could be eliminated. Starner examines several techniques for deriving energy from everyday human activity including:

(a) The motion of air through the mouth of a subject is considered, including adverse physiological effects on the user. Starner predicts that 0.40W could be recovered, but points out that this is a rather unpractical source of power. Alternatively, the motion of the chest walls during breathing can be harnessed to generate power. Starner suggests a band around the chest attached to a flywheel and ratchet, and calculates that this arrangement could generate 0.42W.

(b) Blood flow. The flow of blood through the aorta is shown to do work at a rate of 0.93W against blood pressure. A small proportion of this could be harnessed to power implanted devices without significantly loading the heart.

(c) Typing motions. The fingers are shown to do work of 1.3mJ per keystroke on a keyboard. An average typist of 40 words per minute is predicted to generate around 6.9mW. Starner notes that this is not enough to power a portable computer, but that it may be enough to produce a wireless and battery free keyboard that derives its communications power from keystrokes.

(d) Walking. Starner places a maximum bound on the amount of power that might be generated from a device placed in a shoe, by considering the body weight of a 68kg subject falling through a distance of 5cm at a rate of 2 steps per second. This would result in 67W of power being available, but it is pointed out that extracting this amount of power would seriously interfere with a normal gait pattern. Starner considers how a piezoelectric laminate might be inserted into the sole of the shoe, and concludes that 5W could be generated in this manner. This estimate assumes that the entire body weight of the user can be applied to the tip of the laminate in such a manner as to cause bending. The author feels that this would have serious

effect on the gait of the user, and is thus an overestimate of the power that might be produced. Starner also considers a rotary electromagnetic generator mounted in the heel of a shoe. A typical running shoe is shown to only return 50 percent of the energy stored in the heel material, so a generator that extracted a similar amount of power would not interfere with the gait. Starner thus concludes that taking into account the efficiency of a generator, 8.4Wcould be generated. This estimate, however, is based on the assumption above that the body falls 5cm with each step; this may be true of the feet, but the centre of mass of the body rises less than a centimetre with each step. Thus, the author feels that 8.4W is an overestimate.

(e) Body heat: Discussed below.

Other workers have considered shoe-based generators. Chen holds a patent [14] for a simple heel mounted generator that uses a speed increasing gear train to transfer the motion of a pivot plate in the heel to a dynamo. Another patent [15] describes an elaborate design for a rotary generator mounted inside a ski-boot. Kymissis *et al* [16] construct 3 different prototypes:

(a) A PVDF (poly-vinylidine-fluoride, a piezoelectric plastic, see section 3.1.1.2) stave was specially constructed to conform to the foot-shape, and bending distribution of a standard shoe sole. The laminate consisted of 16 sheets of 28μm thick electroded PVDF surrounding a 2mm plastic core. As the stave is deformed by the walking action, sheets are placed under compression and tension according to their position, and generate useful electrical energy. At a foot strike frequency of 1Hz, the device was found to generate an average of 1mW when loaded with a 250kΩ load. Maximum voltages were around 20 Volts. The insert was reported to be barely noticeable under the foot, and have no effect on the gait.

(b) To generate energy from the heel strike phase of the gait, a pre-curved PZT / steel unimorph was mounted on a plate under the heel. As the heel descends, the unimorph is flattened against the plate resulting in a charge displacement across its electrodes. At a foot strike frequency of 1Hz, the device was found to generate an average of 1.8mW when loaded with a 250kΩ load. Maximum voltages were around 60 Volts. Again, the insert was reported to be barely noticeable under the foot, and have no effect on the gait.

(c) A simple rotary generator was mounted on the outside of a shoe. A small generator driven torch that is cranked by a lever was adapted, and connected to a hinged heel plate. The device generated an average of 0.23W at a foot strike frequency of 1Hz. The device was reported to be awkward, and to interfere with the gait.

Kymissis *et al* also describe how the PVDF stave and PZT unimorph were combined with a rectifier and a simple voltage converter to power a self-powered RF tag system. The shoes transmitted a signal whenever enough energy had been accumulated, and were seen to transmit an ID every 3-6 steps that could be received anywhere in a 60 foot room by their receiver. The paper

is a proof of concept paper, and its authors predict that significant improvements in generated power are possible.

Hausler and Stein [17] propose generating power from the motions that occur between the ribs during breathing. They construct a device that consists of a roll of PVDF material that is attached at each end to different ribs. As breathing occurs the tube is stretched and generates power. The device was surgically implanted in a mongrel dog. Spontaneous breathing resulted in an average power of only a few microwatts. The author questions whether it is ethical to perform such an experiment, when the poor results could easily be predicted by theory, and no significant improvements in surgical technique are derived. They predict that if the coupling factor of the PVDF film were increased by materials research to 0.3 (a rather optimistic increase of around 300%) then the device could produce up to 1mW.

The well publicised windup radio invented by Trevor Baylis [18] is a familiar self powered device. The design was motivated by a desire to provide battery free radio reception to disseminate advice on the prevention of AIDS in Africa. Users wind a spring using a crank-handle; the energy from the spring is fed via a speed increasing gear chain to a dynamo. The radio is reported to run for 30 minutes from a full wind that takes 30 seconds to perform.

A novel power system for active bullets has been described by Segal and Bransky [19]. The generator consists of a piezoelectric disc connected to an inertial mass mounted inside a bullet. As the bullet is fired the acceleration causes the mass to compress the disc and displace charge between the PZT's electrodes; this charge is fed onto a capacitor by a rectifier. A bullet fired with an acceleration of $4.9 \times 10^5 ms^{-2}$, and muzzle velocity of $1.4 kms^{-1}$ (typical of a powder charge) caused 0.19J to be stored on the capacitor.

2.1.3 Optical Energy sources

2.1.3.1 Solar and Incident Light

Solar cells are a mature and well characterised technology. Solar self-powered devices such as calculators and watches are commonplace. Lee *et al* [20] develop a thin film solar cell specifically designed to produce the open circuit voltages required to supply MEMS electrostatic actuators. The array consists of 100 single solar cells connected in series, occupying a total area of only $1 cm^3$. By connecting the array to a micro-mirror, a microsystem is produced that responds to modulation of the applied light.

Calculations by van der Woerd *et al* [21] show that under incandescent lighting situations, an area of $1cm^2$ will generate around 60μW of power. A prototype solar power directional hearing aid was integrated into a pair of spectacles. With solar cells, as the light intensity varies the solar cell voltage also fluctuates. This problem was overcome by producing a power converter integrated circuit.

2.1.3.2 Fibre Optic supplies

Systems operate on electrical power generated from light will be examined here, rather than the more familiar distributed, all optical sensors

Ross [22] delivers optical power to a remote system with an optical fibre. The light is converted to electrical power by a photocell, and voltage converters are used to produce a useful voltage. With a GaAs photocell an overall efficiency (both optical to electrical and voltage conversion) of around 14% is predicted. Typically, 4mW is injected into the fibre by the laser, but, at a price, up to 1W can be applied. This results in typically 0.5mW of power being available for sensing. Information in this case is transmitted back via a separate fibre, although other studies [23] have discussed using the same fibre for both power, and duplex information transmission. See also Gross [24].

Connecting systems by optical fibre has several advantages over more conventional wired systems:

(a) Owing to the wide bandwidth of optical fibres, a large number of devices can be connected to the same fibre, reducing large amounts of wiring.
(b) Optical fibres neither send nor receive electromagnetic energy, so they are free from EMI.
(c) The low powers involved means that the system is ideal for applications where low power is a safety requirement. See Kuntz and Mores [23], for a discussion of this topic. (Al-Mohandi *et al* [25] found that energy stored in the inductors of certain power converters can compromise this safety though, by causing a spark hazard)
(d) Electrical isolation enables operation in areas of high electromagnetic fields

The disadvantages of this technology over the other power sources discussed here, is that the system is still not truly wireless, however, the power generated from the light is of an order of magnitude higher than solar power, and thus forms an important source of power.

2.1.4 Thermoelectric and Nuclear Power Sources

Temperature differences can be exploited to generate power. Unless the temperature difference is large, the low efficiency of this type of conversion means that very little power can be extracted.

Starner [13], calculates the amount of energy that could be extracted from the skin temperature of a human being. The temperature difference between the skin and the surrounding atmosphere drives a flow of heat energy that could be captured. Using a simple model, Starner predicts that 2.4-4.8W of electrical power could be obtained if the entire body surface were covered. Noting the restrictive nature of a full body suit, it is predicted that a neck covering device should have access to a maximum of 0.20-0.32W.

Thermoelectric power has found applications in cardiac pacemakers. Renner *et al* [26] describe a pacemaker that uses a radioactive plutonium source to generate heat. A thermocouple array is used to convert this into useful electrical energy. The device could supply up to 180μW power. "The nuclear pacemaker program was discontinued some 20 years ago, hindered by bureaucratic obstacles, and superseded by the lithium battery" [27]

More recently, Stordeur and Stark [28] have developed a thermoelectric generator targeted specifically at microsystems. Based on thermocouples, the device uses modern materials systems to improve efficiency. The device combines 2250 thermocouples in an area of $67mm^2$, and can produce 20μW at a temperature difference of 20K. The device offers relatively high output voltages of $100mVK^{-1}$.

2.1.5 Radio Power and Magnetic Coupling

Radio waves have been used to supply power, and communicate with smart cards and Radio Frequency Identity Tags (RFID) for several years. The commercially available Texas Instruments TIRIS system [29] has been available since 1991. The design is described by Kaiser and Steinhagen [30]. A ferrite coil picks up energy from an interrogating reader module. The energy is stored and managed, allowing the transponder to return a unique identity code. Data is returned by modulating the impedance of the coil, and thus varying the back-scattered RF energy. Ranges of around 2m are achieved, depending on the size of the antenna and allowable field strength. Another commercial system produced by IBM is described by Friedman *et al* [31]. Typical applications for RFID tags include vehicle identification, animal tagging, and smart inventory systems. Warwick [32] became the first human to receive an RFID implant in 1998. His intelligent building project connects the implant to a computer system that operates doors, lights, and other computers.

To produce low-cost smart card solutions, integrated coils have been developed [33]. A reader also contains a coil, which couples magnetically with the smart card, allowing the transmission of

power, and data. The small dimensions of these devices, however, limit the transmission distance to an order of millimetres.

These technologies present a feasible means of powering a microsystem. They have the advantage of combining both power, and communications. The limitation is the necessity to periodically bring the reader / power unit within transmission range of the device. The amount of power available is relatively large (very application specific, but in the region of 1mW) compared to other sources of energy discussed here, so with modern battery technology energy could be stored within the device between readings, to allow autonomous functions to be carried out.

Matsuki *et al* [34] address the need for power for implanted devices by developing an implantable transformer. The device, designed with artificial hearts in mind, couples power from an external coil into a woven coil design that is implanted under the skin. A trial transformer (70 x 30 x $1mm^3$) was able to supply 6W of power without significant temperature rise.

2.1.6 Battery Energy

A Battery is not a renewable power source, and it is the purpose of this work to eliminate the need for a primary battery, so that the operational lifetime of a system is not limited by the amount of energy it can store. It is, however, worth considering how much energy a battery can contain, since for some systems of fixed life, a battery will provide an ideal solution.

The lithium battery has a high energy density, and a long shelf life. A commercial example [35] shows that a battery of 7.20 cm^3 can hold 1,300 mAh of energy, a density of 0.65 x 10^6 J/L. If this battery were operated at 100μW (similar to the amount of power that a solar cell might produce), it would last for around 18 months.

2.2 Power Management

Self-powered systems often rely on ambient power taken from the environment. Since this power is not placed there with the system in mind, the power is not always going to be present in a continuous and uniform way. This is especially true of vibrational, solar, and radio powered devices. To smooth out this variation in supply some form of energy storage is required.

A particular type of system will arise when power is never present at a high enough level to directly power the system. In this case the system must use a strategy of storing up energy until enough has accumulated to perform the task required, then going back to 'sleep' again. The feasibility of this approach will be determined by the application. There must be enough energy present so that energy gathers faster than it leaks away. If the scheduling of tasks is not easily

predictable, then the device might need to store enough energy to perform the task more than once. We must also consider what to do if not enough energy is ready when a task needs to be performed.

Table 2: Energy density of storage mediums (after Koeneman *et al* [11])

Storage Method	Energy Density (J/L)	Parameters
Nuclear Fission	1.5e12	U235
Combustible Reactants	3.5e7	Petrol
Electrochemical cell	2.1e6	Li – aV2O5
Heat Capacity	8.4e5	Water, ΔT=20K
Latent Heat	1.0e5	Refrigerant, 11
Fuel Cell	6.5e3	H2 – O2, 1atm
Elastic Strain Energy	6.4e3	Spring steel
Kinetic (translational)	3.3e3	Lead, v=24m/s
Magnetic Field	9.0e2	B=1.5T
Electric Field	4.0e2	E=3e8V/m
Pressure Differential	7.0e1	1 atm, Vo/Vf=2
Kinetic (rotational)	2.0e0	Pb ,3600rpm, d=4.5mm
Gravitational Potential	5.0e-1	Lead, h=4.5mm

Table 2 (taken from Koeneman *et al* [11]) is a table comparing the amount of energy that can be stored in different storage mediums. Apart from nuclear devices, and the hard to handle combustible reactants, batteries offer one of the best forms of energy storage. Bates *et al* [36] develop a micro-battery especially well suited to microsystems. It is a thin film rechargeable battery, based on a Lithium system. It can be fabricated as thin as 5μm, and has an energy density of 2.1×10^6 J/L. It is ideal for use as a small, integrated reservoir.

Further power management is needed for bootstrap circuits, to handle start-up after a system has been completely drained of power. The system must also watch out for surges in input voltage, and guard against over-charging any storage medium. To minimise power consumption of digital electronics, the system can aggressively scale the supply voltage, until the voltage is just sufficient to maintain the required throughput. Since power dissipation is a function of the square of the supply voltage, this produces a large decrease in power consumption. This technique is

used by Amirtharajah and Chandrakasan [7], along with a number of other state-of-the-art low power techniques.

2.3 Systems design

The concept of a self-powered sensor would not have seemed practical some 30 years ago. White and Brignell [37] anecdotally report the derision expressed by industrialists when the concept of combining computer systems with individual sensor elements was expressed in the 1980s. The cause of this response is that "at that time a microprocessor cost considerably more than a basic sensor and it did not make sense to dedicate the former to the latter". The well-documented revolution in speed, size, cost and power consumption of microprocessor units means that this practice is now common place.

In the literature, this new generation of devices is variously labelled as intelligent or smart systems. The advantages of these devices are that they offer increased reliability and accuracy, can pre-process data, and can perform measurements that simply would not have been possible before. Recent devices have combined the intelligent sensor concept with small, efficient communications, facilitating remote wireless sensor systems. For background on the field of intelligent sensors the reader is directed towards Brignell and White [37].

Below are some recent projects whose aims include pushing back the frontiers of power consumption for wireless sensor systems. These, currently battery powered, devices are the types of system that are likely to benefit from self-power technologies.

(a) **Smart Dust**

This well-established project is the work of a group based at Berkeley. The group aims to incorporate sensing, communications, and computing hardware, and a power supply in a volume no more than a few cubic millimetres [38]. They label the resulting intelligent sensors "Smart Dust", anticipating that perhaps these sensors may one day permeate our environment in much the same manner as dust. The project focuses upon free-space optical communications, by both active laser transmission, and a novel corner-cube retroreflector (CCR) design. The principle is illustrated in figure 5. A CCR will reflect any incident ray of light back to its source (provided the source lies within a certain solid angle). The device can be used to communicate information by modulating the stream of reflected light. This is achieved by fractionally displacing one of the mirrors, which removes the retroreflective property. The CCR's have been successfully fabricated in gold coated polysilicon, and Chu *et al* [39] have demonstrated data transmission at 1 kilobit per second over a range of 150 meters, using a 5-milliwatt illuminating laser.

The group has recently produced a device that occupies 1000mm^3 (this was non-functional due to faults in the CMOS design) and plans to construct one occupying only 20mm^3 in the near future.

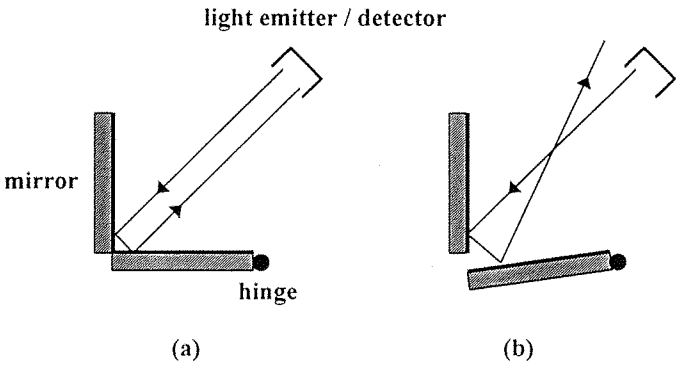

Figure 5: Communications using a 2-D CCR mirror (after Chu *et al* [39])

(b) **Wireless Integrated Network Sensors (WINS)**

This project at UCLA is very similar in spirit to the Smart Dust project. Its main difference is that WINS has chosen to concentrate on RF communications over short distances, and that some techniques for low power sensing have been examined. The group has created new micro-power CMOS RF circuits operating in the 400-900MHz region. Their papers focus on efficient VCO and mixer designs, producing designs which are claimed to give the lowest power dissipation reported at the time [40].

A complete sensor, and communications design is described by Bult *et al* [41]. A micromachined accelerometer, and loop antenna is combined with the requisite CMOS circuitry using a compact flip-chip bonding technique. Each section of the system is described, but it is not clear whether the group produced a functional device. Two different communications systems are described: the first is described as consuming an average of only 90μW, operating at a low data rate (10kbsps), short range (10-30m), and low duty cycle (this is unspecified, and makes these figures hard to interpret); the second reports a receiver consumption of 90μW at a data rate of 100kbps (this from a 1mW transmitter power, 10m range and 1cm^2 single loop antenna area).

(c) **Ultra Low Power Wireless Sensor Project**

This program, based at MIT, proposes "developing a prototype wireless image sensor system capable of transmitting a wide dynamic range of data rates (1bit/s - 1Mbit/s) over a wide range of average transmission output power levels (10μW - 10mW)"[42]. They also propose an initial

prototype that consumes approximately 50mW. To date, no results have been published from this program.

2.4 Summary

There is no single technological answer to self-power; each potential application must be evaluated to determine where power might be derived. Applying such solutions will require careful tailoring to the specific application, as devices will often need to scavenge for power at the edges of feasibility.

The future is bright for self-power. There is wide interest in this field that ranges from mature solutions such as solar cells to vibration generators that have still to be fully evaluated. As the power requirements for integrated circuits continue to fall, more and more applications will become feasible candidates for self-power.

CHAPTER 3

Background Material

3.1 Transduction Technologies

Existing work has examined both piezoelectric, and magnet-coil based techniques for extracting power from vibrations. These are examined here, along with electrostrictive polymers, as potential transduction mechanisms for an inertial generator.

3.1.1 Piezoelectric Materials

Piezoelectricity is the ability of certain crystalline materials to develop an electric charge proportional to a mechanical stress (termed the direct piezoelectric effect), and conversely to produce a geometric strain proportional to an applied voltage (the indirect effect). The direct effect was first discovered by J. and P. Curie in 1880 [43]. Early piezoelectric materials were crystalline substances such as quartz and Rochelle salt. These materials rely on the presence of a spontaneous electric moment or dipole in the crystal structure. Ceramics are isotropic polycrystalline substances, and require a process called polarisation (see below) before they exhibit piezoelectric behaviour.

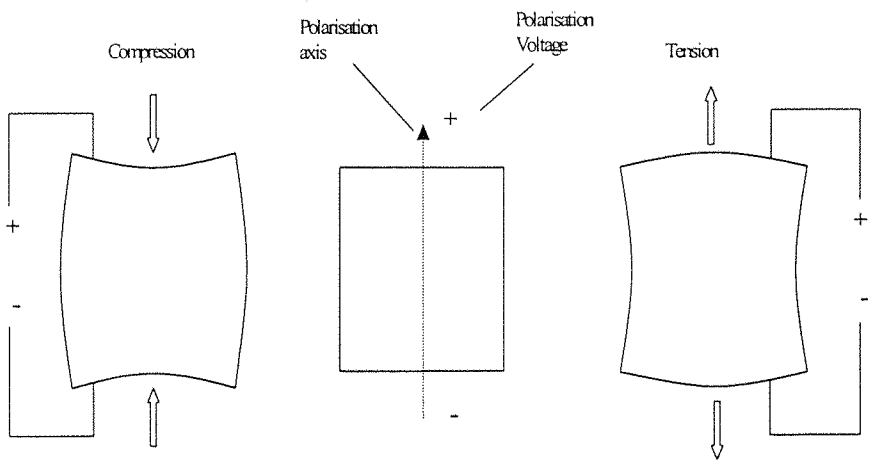

Figure 6: The Polarity of Piezoelectric Voltages from Applied Forces (after Matroc [44])

3.1.1.1 Piezoelectric Notation

A general expression coupling both mechanical and electrical parameters can be written [45] as

$$\begin{bmatrix} \mathbf{D} \\ \mathbf{S} \end{bmatrix} = \begin{bmatrix} \varepsilon^{T} & \mathbf{d} \\ \mathbf{d}_t & \mathbf{s}^{E} \end{bmatrix} \begin{bmatrix} \mathbf{E} \\ \mathbf{T} \end{bmatrix} \qquad \textbf{Equation 3.1}$$

where $\boldsymbol{D}$ is a vector of electrical displacements (charge/area), $\boldsymbol{E}$ is the vector of electrical field in the material (volts/metre), $\boldsymbol{S}$ is the vector of material engineering strains, and $\boldsymbol{T}$ is the vector of material stresses (force/area). The subscript, $(\,)_t$, denotes the conventional matrix transpose.

$$\mathbf{D} = \begin{bmatrix} D_1 \\ D_2 \\ D_3 \end{bmatrix}, \quad \mathbf{E} = \begin{bmatrix} E_1 \\ E_2 \\ E_3 \end{bmatrix}, \quad \mathbf{S} = \begin{bmatrix} S_{11} \\ S_{22} \\ S_{33} \\ 2S_{23} \\ 2S_{13} \\ 2S_{12} \end{bmatrix}, \quad \mathbf{T} = \begin{bmatrix} T_{11} \\ T_{22} \\ T_{33} \\ T_{23} \\ T_{13} \\ T_{12} \end{bmatrix}$$

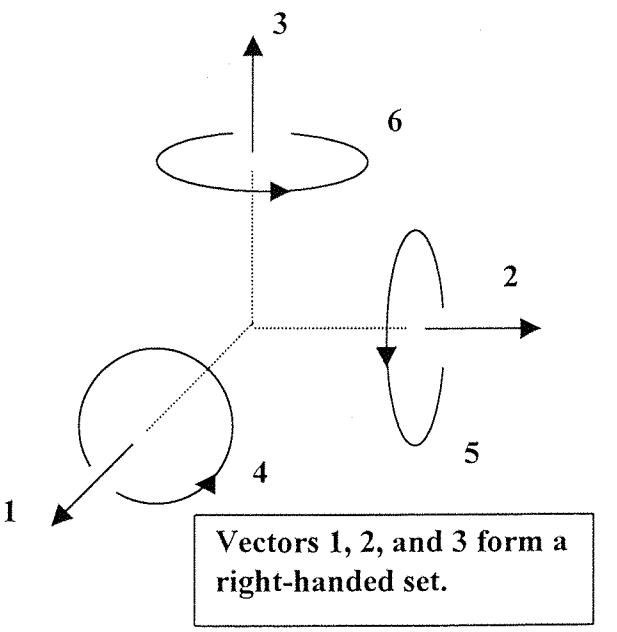

Figure 7: Notation of Axes.

In polarised ceramics, the "3" direction is the axis of polarisation, and "1" and "2" refer to arbitrarily chosen orthogonal axis, as shown figure 7. In the following definitions, the

superscripts $(\ )^E$ and $(\ )^D$ refer to boundary conditions of constant field (e.g. short circuit) and constant electrical displacement (e.g. open circuit) respectively. The superscript $(\ )^T$, signifies that the values are measured at constant stress. The matrix that relates the two electrical variables, electrical field and electrical displacement, is composed of the dielectric constants for the materials. The matrix is written

$$\varepsilon^T = \begin{bmatrix} \varepsilon_1^T & 0 & 0 \\ 0 & \varepsilon_2^T & 0 \\ 0 & 0 & \varepsilon_3^T \end{bmatrix}$$

The stress and strain are related through the compliance matrix, which is written

$$\mathbf{s}^E = \begin{bmatrix} s_{11}^E & s_{12}^E & s_{13}^E & 0 & 0 & 0 \\ s_{12}^E & s_{11}^E & s_{13}^E & 0 & 0 & 0 \\ s_{13}^E & s_{13}^E & s_{33}^E & 0 & 0 & 0 \\ 0 & 0 & 0 & s_{55}^E & 0 & 0 \\ 0 & 0 & 0 & 0 & s_{55}^E & 0 \\ 0 & 0 & 0 & 0 & 0 & s_{66}^E \end{bmatrix}$$

Due to symmetry, the material properties are identical in the "1" and "2" directions.

The matrix of piezoelectric constants, relates both the electrical displacements to the stress, and also has the same coefficients (a result of the thermodynamic reversibility of piezoelectric processes) as the matrix relating strain to electrical field.

$$\mathbf{d} = \begin{bmatrix} 0 & 0 & 0 & 0 & d_{15} & 0 \\ 0 & 0 & 0 & d_{15} & 0 & 0 \\ d_{31} & d_{31} & d_{33} & 0 & 0 & 0 \end{bmatrix}$$

The subscripts of the members of this matrix, are ordered with the first term signifying the electrical axis, and the second the mechanical. Thus d_{31} refers to the strain developed in the "1" direction in response to a field in the "3" direction. The formula described above is one of several different commonly used ways of representing the piezoelectric relations; for a more detailed discussion of this area, refer to the IEEE Standard on Piezoelectricity [46]. Note that the above matrices show the non-zero terms for polarised piezoelectric materials, other types of material may have other non-zero terms.

The electromechanical coupling factor, k, is a useful measure of the strength of the piezoelectric effect for a material, and is an important parameter when power generation is required. It measures the proportion of input electrical energy converted to mechanical energy when a field is applied (or vice versa when a material is stressed). The relationship is expressed in terms of k^2:

$$k^2 = \frac{\text{electrical energy converted to mechanical energy}}{\text{input electrical energy}}$$

or

$$k^2 = \frac{\text{mechanical energy converted to electrical energy}}{\text{input mechanical energy}}$$

Since this conversion is always incomplete, k is always less than one.

3.1.1.2 Piezoelectric Materials

The earliest piezoelectric materials were crystalline materials, that exhibited a natural polarisation. To use such materials, single crystals must be cut into the required shape, and can only be cut along certain crystallographic directions, thus limiting the possible shapes. In contrast, piezoelectric ceramics can be fabricated into a wide range of sizes and shapes, so they are more suitable for generator designs.

The material barium titanate ($BaTiO_3$) is a piezoelectric ceramic. Figure 8 shows the structure of a crystal from this material. Above the material's Curie point of 120°C, the crystal has a symmetrical cubic structure figure 8a). In this form, there are no piezoelectric effects. Below this temperature, an asymmetrical tetragonal structure exists, and the crystal becomes piezoelectric. The piezoelectric effects are the result of relative displacements of the ions, rotation of dipoles, and redistribution of electrons within the unit cell in response to mechanical and electrical stimuli.

Ceramics are polycrystalline materials. A ceramic formed from a piezoelectric material will, after firing, be composed of small grains (crystallites), each containing domains in which the electric dipoles are aligned. At this stage, the domains are randomly orientated, so the net electric dipole is zero, and the ceramic does not exhibit piezoelectric properties. To produce a piezoelectric material, the domains must be aligned in a process know as polarisation. For this to be possible, the ceramic must be a ferroelectric material. Ferroelectricity is defined as "reversibility in a polar crystal of the direction of the electric dipole by means of an applied electric field"[43]. Figure 9

shows the alignment that occurs as the material is polarised. During polarisation, unit cell dipoles oriented almost parallel to the applied field tend 'grow' at the expense of other less favourably orientated domains. Domains can also change their crystallographic axis, 'flipping over', through various angles determined by the crystal structure. The remnant polarisation is never complete, but in PZT ceramics can reach 80-90% (depending on the polarisation conditions, and precise material composition).

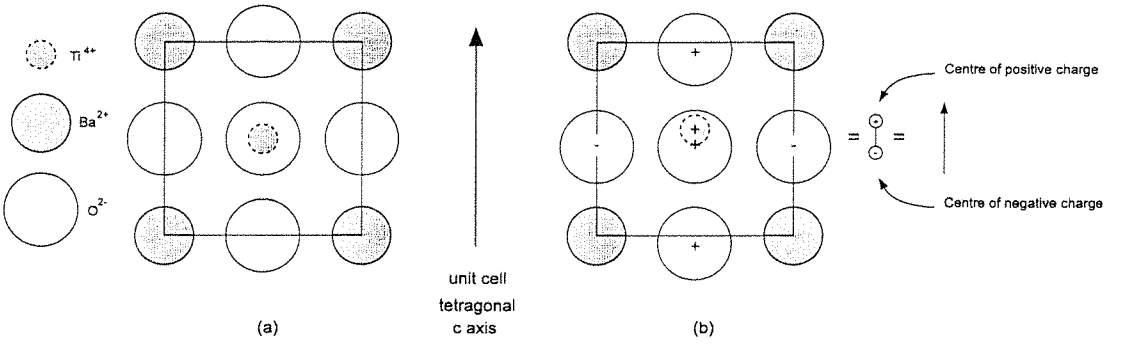

Figure 8: Cubic and Tetragonal forms of $BaTiO_3$ (after Shackleford [47])

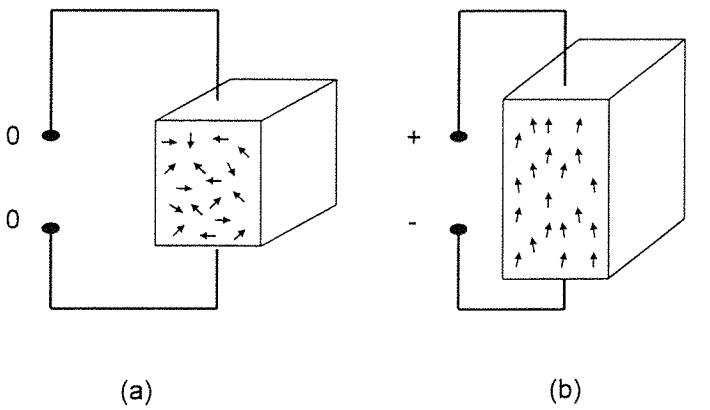

Figure 9: Alignment of dipoles in (a) unpolarised ceramic and (b) polarised ceramic (after Matroc [44])

In practice the piezoelectric ceramic is generally heated as the field is applied, to reduce the energy required for domain processes.

The piezoelectric properties of lead zirconate titanate (PZT) were discovered in the 1950's [43]. PZT with various additives has since become the dominant piezoelectric ceramic, as a result of its high activity and stability. Various types of PZT are produced, tailored for different applications.

The materials can be roughly divided into two groups: hard, and soft materials. Hard materials such as PZT 4 or PZT 8 (UK notation) are suitable for power applications, possessing low mechanical and dielectric losses. Soft materials such as PZT 5H offer better sensitivity, at the cost of more losses, and a lower coercive field (the field required to depolarise the material). Other specialist materials are also available for requirements such as high stability. Table 3 compares these materials. In this thesis PZT 5H was used for initial work as it was readily available. The results of modelling, however, suggest that harder materials are better for power generation.

Polyvinylidene fluoride (PVDF) is another important piezoelectric material. PVDF is a fluorocarbon polymer, commonly used as an inert lining or pipe-work material. Since its discovery as a piezoelectric material by Kawai in 1969 [48], it has been the subject of much research, and is available commercially as a pre-polarised film. Like ceramic materials, PVDF requires polarisation, which means that it can be manufactured in a wide variety of shapes. It is less active than common ceramic materials, but its low cost, lower stiffness, and easy manufacturability makes it ideal for many applications. Table 3 lists some key properties.

Table 3: Comparing Piezoelectric Materials

Material	d_{33} (pCN^{-1})	s_{33}^E ($x10^{-12}m^2N^{-1}$)	k_{33}
PZT 8 [44]	-225	74	0.64
PZT 5H [44]	-593	48	0.75
PVDF [48]	-18	400	0.10

3.1.2 Electrostrictive Polymers

The term electrostriction in its general sense covers 'any interaction between an electric field and the deformation of a dielectric in the field'[49], and hence includes the piezoelectric effect. However, it is common practice to reserve the term to refer to phenomena where the deformation is independent of the direction of the field, and proportional to the square of the field [49]. This phenomenon is generally caused by a combination of Maxwell stresses, and a dependence of the dielectric constant upon the strain. In electrostrictive polymers described here, the former is the dominant mechanism. The effect is generally small, and can be ignored unless field strengths exceed $20kVcm^{-1}$.

Kornbluh *et al* [50] describe an electrostrictive polymer system. Thin sheets of an elastomeric polymer are sandwiched between compliant electrodes (Figure 10a). When a voltage is applied to the electrodes, the electrostatic forces between the free charges on the electrodes, squeezes the sheet thinner, and cause it to extend sideways (Figure 10b). Sheets are typically in the region of 10-100μm thick, and have a breakdown field of typically 50-200MVm^{-1}. Typical polymers include silicone and polyurethane.

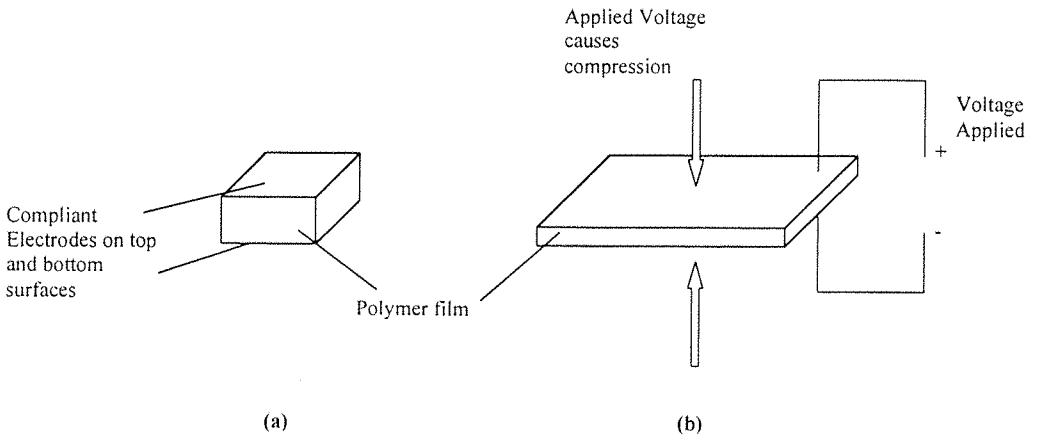

Figure 10: Principle of Operation of an Electrostrictive Polymer Actuator (after Kornbluh *et al* [50])

Electrostrictive polymers can also be used to generate power. The transducer is held under tension, so that it is mechanically in the state shown in figure 10b. A voltage is then applied to the electrodes, and the source then removed, charging the capacitor formed by the two electrodes. As the tension is released, the polymer will move towards its initial shape, further separating the charges on the electrodes. This causes an increase in the electrode voltage which can be exploited to do work. Similarly, the process can be reversed if the polymer is to be compressed. The requirement for a large external voltage to be applied before an electrostrictive generator can produce power, will add complexity, and volume to any generator system formed from this technology.

The transducers described by Kornbluh *et al* typically have a low mechanical stiffness, and are capable of producing high strains (typically up to 30%). They have an energy density similar to piezoelectric materials, and have been likened to artificial muscles. An important difference between piezoelectric ceramics, and electrostrictive polymers is the relatively high level of material damping that the polymers exhibit. The electrostrictive polymers typically have

hysteretic losses of 20% at 200Hz, which means that a high Q-factor resonator could not be built from this material.

Although electrostrictive polymers may be useful for generator applications where the material is actively deformed, they are not considered to be useful for inertial generators of the type described in this thesis. They could be modelled in a similar manner to the piezoelectric generators described in Chapter 5, however, they have an even lower electromagnetic coupling factor than piezoceramics and will thus not generate significant power (see section 5.8 for discussion of this relationship). For this reason, and also their high level material damping described above, electrostrictive polymers will not be considered further in the remainder of this thesis.

3.1.3 Electromagnetic Induction

Electromagnetic induction is another method of converting mechanical energy to electrical energy. The principles are well known, and the pertinent equations will be described here as an aid to memory. For a wire of length, L, carrying a current, I, that runs through a perpendicular magnetic field of flux density, B, the perpendicular force on that wire, F, is given by

$$\mathbf{F} = I \cdot \mathbf{B} \times \mathbf{L} \qquad \textbf{Equation 3.2}$$

Similarly the voltage, V, induced across the wire is given by

$$V = \mathbf{B} \times \mathbf{L} \cdot v \qquad \textbf{Equation 3.3}$$

where v is the velocity of the wire. Generators based on electromagnetic induction are explored further in chapter 7.

3.2 Principles of Resonant Vibration Generators

In this section, generators will be modelled as first order resonant systems. This generalisation will lay a framework that will enable generators of different technologies to be compared in section 7.6.

3.2.1 First Order Modelling of Generator Structures

It is possible to represent the resonant generators described in this thesis using a simple first order model as shown in figure 11. The seismic mass, m, combines the effect of the actual mass in the system with any effective mass added by reactive load circuits. The spring, stiffness k, combines

the actual physical spring of the system with any effective spring added by the electrical load. Excitation, *y(t)* is applied to the generator housing, which results in differential movement between the mass and the housing, *z(t)*. The energy in the system is removed by both unwanted sources of loss (such as gas damping), and taken away as useful electrical power. These two types of damping are represented by viscous damping coefficients c_L and c_E respectively. The damping, in reality, may not be viscous; Magnet-coil arrangements with a resistive load are essentially viscous, while piezoelectric and electrostatic methods of extracting power with resistive loading are closer to a rate independent hysteretic damping model. Unwanted damping, such as support damping, may also be of this type. If the model is described at a particular operating frequency, however, the effective viscous damping factors can be calculated as described by Thompson [51], who discusses this type of model in detail (see also Nashif *et al* [52]).

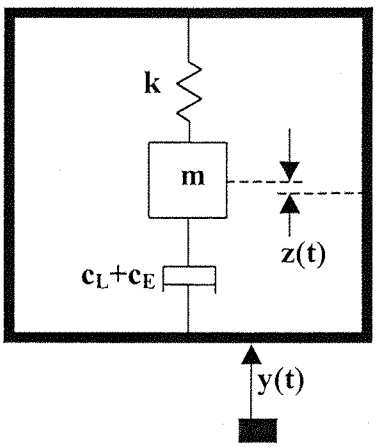

Figure 11: Model of a Single Degree of Freedom Damped Spring-Mass System

It should be noted that predictions, and analysis based solely on this model will be simplistic, as it takes no account of the constraints that will be present when this type of generator is implemented in a particular transduction technology (e.g. piezoelectric, or electromagnetic). It will be seen in sections 5.7 and 7.4 that the limitations of materials, and the competition for space between the various generator elements leads to a complicated interdependence of parameters that is hard to capture in simple equations of the type that are described below.

For the case where the unwanted damping factor is arbitrarily small, the useful electrical power produced from such a device can be shown [3] to be

Equation 3.4

$$P_E\big|_{\zeta_L=0} = \frac{m\zeta_E Y_0^2 \left(\frac{\omega}{\omega_n}\right)^3 \omega^3}{\left[1-\left(\frac{\omega}{\omega_n}\right)^2\right]^2 + \left[2\zeta_E \frac{\omega}{\omega_n}\right]^2}$$

where Y_0 is the displacement amplitude of excitation, and the undamped natural frequency,

$$\omega_n = \sqrt{\frac{k}{m}}$$

and the viscous damping factor, or damping ratio is given by

$$\zeta = \frac{c}{2m\sqrt{\frac{k}{m}}}$$

Equation 3.4 is not exact, and ignores the (usually) small differences between the undamped natural, damped natural, and resonant frequencies (see Nashif *et al* [52], pp.123).

The useful electrical power generated at resonance, including the effect of unwanted damping can be shown [3] to be

Equation 3.5

$$P_{E,RES} = \frac{\zeta_E}{4(\zeta_E+\zeta_L)^2} m Y_0^2 \omega_n^3$$

Figure 12 plots P_E with no unwanted damping from equation 3.4 against frequency for a range of damping factors. It can be seen that reducing the damping factor causes an increase in the amount of power available at resonance. Decreasing the damping factor will increase the amplitude of *z(t)* at resonance. The maximum value that *z(t)* can take is limited by the geometry of the device, so the damping factor must be large enough to prevent *z(t)* reaching this value. Decreasing the damping factor also results in more energy being dissipated in the sources of unwanted damping. In the case where *z(t)* is not bounded, the optimum value of ζ_E, that balances increased resonant amplitude against unwanted losses, can be shown to be: $\zeta_E = \zeta_L$. The sharp increase seen in generated power as excitation frequency increases should not be taken to mean that a device should be operated at as high a frequency as possible; in practical examples the displacement amplitude would fall as frequency is increased. This is allowed for in the following section by modelling an excitation as having a constant power spectral density.

Reducing damping increases the frequency selectivity of the device, so in an environment where the excitation frequency is not stable a higher damping factor may yield better average power output (see section 3.2.2). Figure 12 is plotted for the case where the damping factor is independent of frequency. This is not the case for hysteretic damping mechanisms such as piezoelectric transduction, where the equivalent viscous damping factor decreases with increasing frequency. The observations made above, however, are still valid for hysteretic damping.

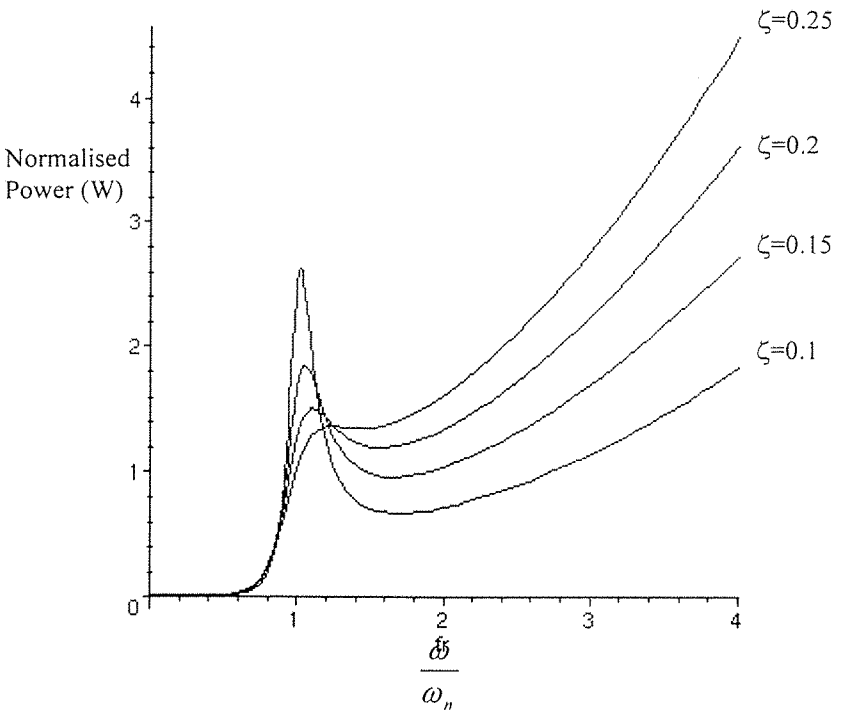

Figure 12: Power From a Generator of Unit Mass, Unit Amplitude Excitation, Unit Natural Frequency

It is of interest to note from equation 3.5 that the electrical power produced at resonance is a function of the cube of the resonant frequency. This indicates that inertial generators will perform better in applications that provide vibrations at higher frequencies. The mass term in equation 3.5 indicates that designs should include as much mass as space will allow, although a trade off will occur between space for mass and space for the transduction mechanism.

The maximum electrical power than can be generated from a generator whose amplitude of beam oscillation is limited to Z_{max} is found [3] to be

$$P_{\max} = \zeta_E m \omega_n^3 Z_{\max}^2 \qquad \textbf{Equation 3.6}$$

It is assumed for this equation that the amount of excitation of the device is sufficient to achieve this maximum amplitude, overcoming any unwanted damping.

3.2.2 Placement of Resonant Frequency and Choice of Damping Factor

The resonant frequency of a system can be modified at the design stage by adjusting the spring constant, or the mass. When the excitation to the system is at a single sinusoidal frequency, most power is generated when the resonant frequency of the beam coincides with the excitation frequency (This is evident from figure 13 discussed below, taking the limiting case of an arbitrarily narrow excitation band).

In the case where the excitation frequency tends to vary with time, a higher damping factor may be used to reduce the frequency selectivity of the device (widening the resonant peak). The exact combination of parameters will depend on the distribution of excitation frequencies. A statistical analysis would be required to find the optimum design for a given application. Another option is to use a generator that has an actively tuneable resonant frequency, a possible area for further research.

Many potential applications can supply broadband excitation. For instance a simple model of crankcase of a car has been shown by Priede [53] to have "at least some 20 natural frequencies of the crankcase walls ... in a very narrow frequency range of one-third octave". The optimum choice of resonant frequency and damping factor will depend on the nature of the application, but the calculations below give an indication of the best strategy.

Wide band excitation can be modelled as a uniform distribution of frequencies with a constant spectral power density, K, over the frequency range F_1 to F_2. The total power that can be generated from such an excitation can be calculated by integrating the power spectral density (with no unwanted damping) derived from P_E in equation 3.4 over the frequencies F_1 to F_2. The symbolic integration package Maple® was used to perform the integration to produce figure 13. The graph is plotted for broadband excitation between 300 and 500Hz, and shows how the average power output varies with device resonant frequency and damping factor. The resulting expression for power is of the form

$$P = \frac{K}{m} f(F_1, F_2, \omega_n, \zeta_E)$$ **Equation 3.7**

Thus, the actual values chosen for K and m do not affect the shape of the graph, which is plotted for unit K and unit m. The graph shows that maximum power output is achieved by reducing the damping factor. This decrease can continue until unwanted damping becomes significant, or the amplitude of beam oscillation grows too large. The graph also shows that the natural frequency of the device should lie in the same frequency band as the excitation, and that at lower damping factors the natural frequency is best placed near the high frequency end of the band. Other ranges of excitation frequency (wider and narrower bands) have also been examined, and show the same trends.

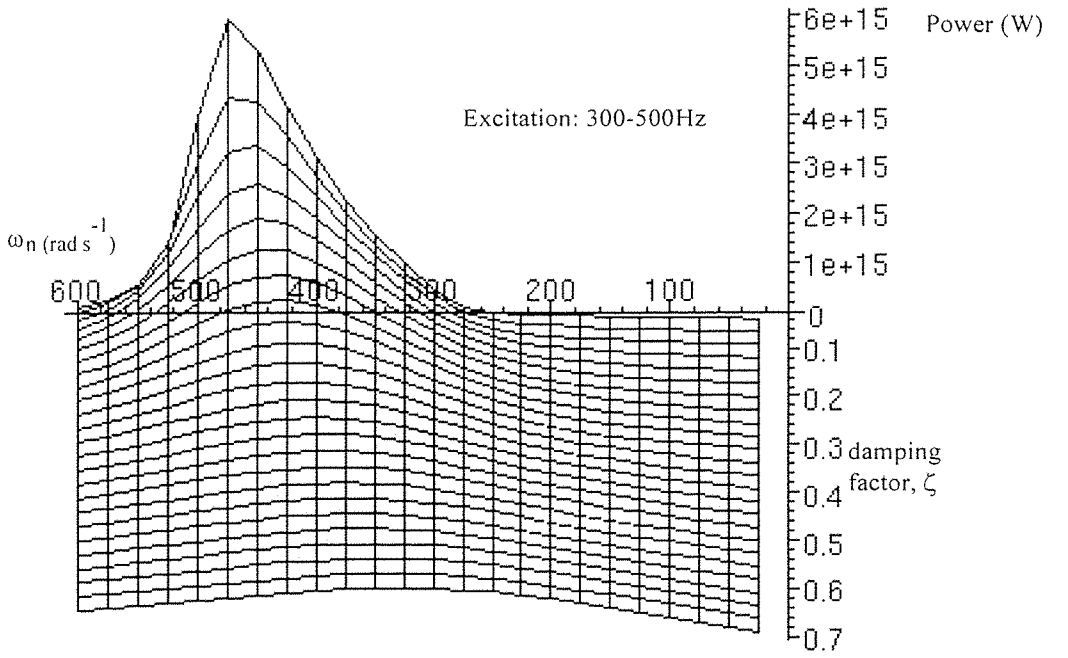

Figure 13: The Effect of Damping Factor and Natural Frequency on the Power Generated from Broadband Excitation.

Another possible design strategy in a broadband excitation environment is to have more than one generator, with each generator tuned to a different resonant frequency. The success of this strategy will depend on the constraints imposed by the application, including the frequency distribution, and geometrical constraints. Analysis of both this configuration and just a single generator would be required to determine which is the best strategy for a given application.

3.2.3 Coupling Energy Into Transduction mechanisms

Once energy has been taken from the vibrations exciting the generator, and captured by the resonant system, it must be converted into an electrical form.

To generate power from a piezoelectric (or electrostrictive) material, the material must be deformed. This deformation causes charge to be displaced across the material, which gives rise to a potential difference which can be exploited to do work. The piezoelectric material will contribute to both the stiffness, and the loss factor of the system. Piezoelectric materials are generally too stiff to be connected mechanically in series with the mass, which must be connected to a lower mechanical impedance to resonate at typical vibration frequencies. Instead, the piezoelectric material can form part of a beam. One method is to attach the piezoelectric material to the root of a beam. This arrangement is not ideal, as the elastic energy is shared between the stiffness of the beam and the piezoelectric material. In a situation where the proportion of elastic energy that can be converted to electrical energy is limited (especially the case with thick-film and polymer piezoelectrics) this is important as it reduces the power generating capacity. Alternatively, the beam can be formed from only piezoelectric material (this is harder to manufacture). It is important to note that a symmetrical piezoelectric beam formed from a single piece of PZT, with no substrate, will have its neutral axis at its centre and thus develop no charge between its top and bottom electrodes, since the charge produced by the tension at one surface will cancel that caused by compression at the other.

Electromagnetic induction can also be used to extract the energy from the resonant system, either in the form of a magnet mounted on the oscillating beam moving through a fixed coil, or vice versa. In this case, the design of the magnet and coil does not directly influence the stiffness of the resonator.

3.3 Power requirements of Vibration-Powered Systems

Portions of this thesis deal with the question of whether vibration-powered generators can produce enough power to be useful. Before this can be answered we must first establish how much power can be considered to be 'useful'.

A vibration-powered system will typically have three distinct power consuming functions: sensing, data processing, and communications.

Sensing: Typical applications could use any of a wide range of different sensors, so the power required will be highly application specific. For example a device periodically checking the condition of a structure with a resistive strain gauge could achieve an average power consumption of below a microwatt if only a low duty cycle were required. In contrast a device sending back live video information will require up to 10mW [42]. Little work has been found on existing ultra-low power sensors, however, given the large range of different sensor types and technologies there is likely to be ample scope for future research.

Data processing: Digital electronics is still undergoing the expansion predicted by Moore's law. Along with the improvements in speed and density that this facilitates, the miniaturisation and trend towards lower supply voltages reduces the amount of power required. Discussing medium throughput DSP circuits that in 1998 consumed around 1mW to 0.01mW, Amirtharajah and Chandrakasan [7] predict that "projecting current power scaling trends into the future (based on deep voltage scaling, and other power management techniques), we expect the power consumption to be reduced to tens of μW to hundreds of nW". Vittoz [54] states that current watch circuits containing several tens of thousands of transistors are routinely produced with a power consumption of below 0.5μW.

Communications: The power required to actively transmit data using a radio signal depends on factors such as the data rate, the operating frequency, the range, and the aerial sizes. Given sufficiently large receiving aerials (for instance those used to receive power from deep space probes) even very faint signals can be decoded. Bult *et al* [41] work on a state of the art low power communications system, and report two devices: the first is described as consuming an average of only 90μW, operating at a low data rate (10kbsps), short range (10-30m), and low duty cycle (this is unspecified, and renders these figures almost meaningless); the second reports a receiver consumption of 90μW at a data rate of 100kbps (this from a 1mW transmitter power, 10m range and $1cm^2$ single loop antenna area). An MIT project proposal states that chips have been produced that demonstrate a "transmitter capable of 1.25Mb/s at 1.8GHz using only 22mW"[42]. Radio is not the only way to communicate, the 'smart dust' system using passive retro-reflective mirrors (described in section 2.3) offers a passive communications technique. The near-field coupling used in RFID tags (described in section 2.1.5) is another possibility, although this technology can also supply power, so a vibration powered system is unlikely to be required in applications that are amenable to this approach.

Comparing the sub-systems, it can be seen that in many applications communications will demand the most power. Given the low energy cost of processing, it will often be more efficient to process data to reduce its bulk before transmission. An example of this technique is a condition based monitoring system; a sensor could spend most of its time processing input data to evaluate the health of a structure, then communicate at a higher power once a day at a low data rate to signal the state of the structure.

The MIT 'Ultra Low Power Wireless Sensor Project' [42] is working on producing a ' prototype image sensor system ... capable of wirelessly transmitting a wide range of data rates (1 bit/sec - 1 megabit/sec) over a wide range of average transmission output power levels (10 microwatts - 10

milliwatts)'. The group holds expertise in ultra-low power circuits, so these figures should represent an achievable goal. For the evaluation of devices discussed in the remainder of the thesis, any power above 50μW will be considered potentially useful.

CHAPTER 4

Development of a Thick-Film PZT Generator

Thick-film techniques (see below) allow piezoelectric materials to be accurately, and repeatably deposited on substrates. Thicknesses in excess of 100μm can be routinely deposited. Alternative deposition techniques (sol gel [55], sputtered [56] or metal-organic chemical vapour deposition (MOCVD) [57]) cannot, at present, deposit material in such film thicknesses.

In this section processes required to produce a thick-film generator are developed, and a prototype generator is produced. The design is not optimised, but chosen to provide reliable experimental data. Mechanical and electrical properties of the thick-film PZT layer (which have not previously been measured) are examined. The prototype is tested and assessed for power generating capacity.

4.1 Introduction to Thick-Film Processes

Thick-film devices typically consist of successively printed layers of materials of varying electrical and mechanical properties. An key factor distinguishing thick-film technologies from others is the manner in which the films are deposited. This is screen-printing, similar to that used in the traditional silk screen-printing of T-shirts, mugs, etc. Printing is only part of the process, and the other stages are described below.

Thick-film technology was introduced around thirty years ago as a means of producing hybrid circuits [58] (thick-film tracks and resistors combined on a substrate with silicon die). More recently thick-film techniques have been used to produce a wide range of sensors. Thick-film processes can be automated with relative ease, and together with the additive nature of the techniques, this means that low cost devices may be produced with little waste. Thick-film devices are also generally compact and robust as a result of the solid state nature of the layers. Despite the high precision that can be achieved with micro-machined silicon devices, thick-film technologies still have wide applications. The cost of capital equipment is considerably lower than that required for semiconductor manufacture, and short production runs can be undertaken relatively cheaply.

4.1.1 Paste Composition

A thick-film paste or ink is generally composed of four main types of ingredient; active material, permanent binder, temporary binder, and solvent and thinner. The active material gives the film it intended function. Examples include metals, piezoelectric materials, resistive materials, and electrochemical sensing materials. The permanent binder remains in the final fired film; it promotes adhesion between the active material and the substrate, and also modifies the mechanical properties of the film. The temporary binder holds the other ingredients together during the drying and firing processes, and together with the solvent modifies the rheological properties of the paste to facilitate printing (see below). The temporary binder is typically an organic polymer or compound, and the solvent a mixture of organic solvents. Temporary binders and solvents are removed by evaporation and oxidation during the drying and firing stages.

The type of binder used will dictate the processing requirements of the film. A paste with a polymer binder, for instance, needs to be fired at a relatively low temperature (typically 100-200°C) to cause the polymerisation of the polymer. In contrast, a glass based paste must be fired at a much higher temperature (typically 500-900°C) to cause the glass to melt and flow.

4.1.2 Deposition

The pattern of paste that is deposited on the substrate is determined by the screen or stencil. The screen consists of a mesh mounted within a frame. Most of the mesh is sealed with an emulsion (stencil), except for the areas to be printed, which are open. The stencil is formed by applying the photosensitive emulsion to the entire mesh; the emulsion is flush with the top of the mesh, but extends below the bottom of the mesh. This extra thickness (typically 10 to 25 microns [65]) forms a gasket-like seal with the substrate, and also increases the thickness of the wet printed film. To form the apertures in the stencil through which paste passes during printing, a photo-positive mask is placed over the emulsion and UV light is used to harden the exposed areas of the stencil. The undeveloped areas are washed away leaving the apertures.

The printing process is shown in figure 14. The screen is mounted at a defined height (the gap) above the substrate. To produce the print a rubber squeegee is drawn across the surface of the screen, dragging a quantity of the paste in front of it. As the squeegee passes, the stencil is pushed into contact with the substrate. The paste is formulated to be thixotropic in nature. This means that when the paste is placed under shear (pushed along and into the mesh) its viscosity decreases, so that it flows more easily into the stencil. After the paste has flowed into the stencil, the squeegee moves on, and the screen returns (the 'snap off') to its original height, leaving a layer of paste on the substrate. Undisturbed, the paste returns to a higher viscosity, preventing it from flowing out into unwanted areas. The thickness of the deposited layer is determined largely

by the emulsion thickness, but the squeegee traverse speed, squeegee down pressure, screen gap, and paste properties also have an effect on this thickness.

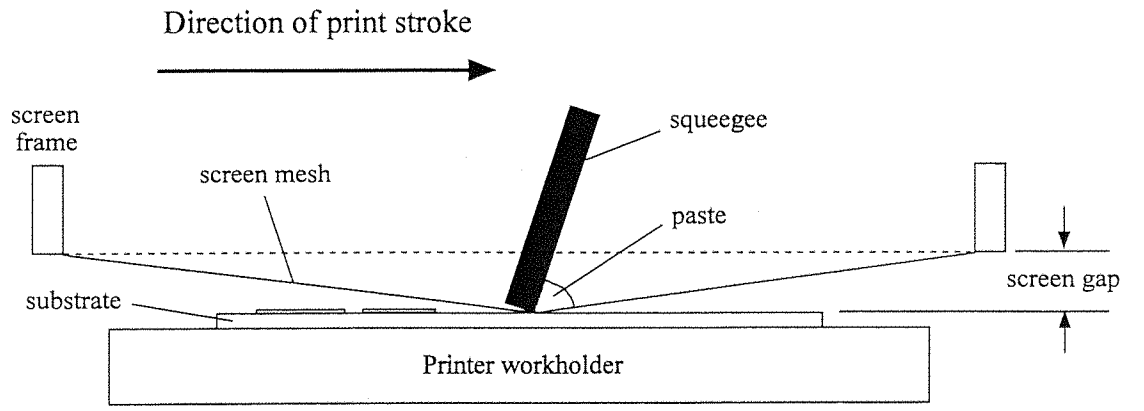

Figure 14: The thick-film printing process

4.1.3 Drying and firing

Following the printing, the wet print is left to settle for typically 10-15 minutes. This allows irregularities in the surface of the print (caused by the impression of the mesh in the print surface) to smooth out as the print flows a little. After the settling time, the print is dried. For cermet (ceramic / metal) type pastes, this typically consists of using infra-red heating to hold the paste at 150-175°C for 10-15 minutes [65]. This process causes most of the solvent to evaporate, which typically reduces the thickness of the wet print by up to 50%.

The firing profile depends upon the type of permanent binder used. Low temperature polymer based pastes are generally cured using either an oven or by exposing the paste to UV-light. Higher temperature (typically glass based) pastes are often fired in a multi-zone belt furnace. A typical furnace will consist of a metal belt which carries the substrate through a number of different temperature zones, which are arranged to give the required temperature profile. In the initial stages of the firing process, any remaining solvent is evaporated or oxidised, along with the temporary binder. This leaves behind a porous structure composed of the active material, and the permanent binder, separated by gas filled voids left by the temporary binder. As the permanent binder melts, it wets the surface of the active material. Particles are then drawn together by surface tension, leaving a denser, thinner film [65]. Trapped gas will not fully escape and some porosity will remain. After firing, the resulting layer of sintered paste is referred to as a film.

Following firing, the printing process can be repeated to create multi-layered devices.

4.2 Development of Materials, and Processes for Printing Thick-Film PZT on Steel Beams

A set of experiments were performed, with the intention of finding a reliable method of producing piezoelectric elements printed on steel beams.

4.2.1 Choice of Substrate

316 stainless steel was chosen for the substrate (Goodfellow FE240261: Hardened AISI 316 steel). Mechanically, steel offers a good stiffness, and a low material damping factor. 316 steel has a low carbon content (less than 0.08%[59]). This is important since during the PZT firing cycle, the substrate is heated to around 950°C. A steel with a higher carbon content would tend to oxidise at this temperature.

316 steel is an austenitic steel, which means that the steel can only be hardened by cold working. This is a drawback, since as the steel is heated during the PZT, and two electrode firing stages, any hardening produced through initial cold-work will be lost. In the designs discussed in this project, however, the tensile strength of the steel is not an issue, as the maximum beam deflection is governed by the strength of the PZT layers.

4.2.2 Thermal Mismatch and Substrate Warping

The first problem encountered during thick-film printing was that the thermal expansion mismatch between the thick-film materials, and the steel caused warping during the firing phase.

The steel has a coefficient of thermal expansion, Tc=16-18μ-strain K^{-1}, large compared to typical 6μ-strain K^{-1} of PZT-5H (The temperature coefficients of both materials, especially the PZT, are actually highly temperature dependent). During the cooling phase of the film firing (whether electrode, insulator or PZT film) the film binds to the substrate, and as cooling continues, the double layer bends in the manner of a bimorph.

Exact measurements were not performed, but the degree of mismatch is such that a single-sided 50μm thick layer of PZT on a 100μm thick 316 steel sheet results in a bent substrate with a bending radius of around 3cm. This degree of bending prevents any further thick-film processing of the substrate. To counteract this problem, all subsequent substrates were printed with a symmetrical pattern on the front and back sides. The two patterns must be carefully aligned, as a mismatch of 0.5mm was found to be large enough to cause sufficient bending of a 100μm thick substrate to prohibit further processing. A further difficulty is that the screen printing process does not always result in an even film thickness across the substrate. This can be caused by an

uneven squeegee, or a slight angle between the screen and the substrate, which will produce a variation in snap-off speed. The variation in thickness will not be repeated symmetrically on the opposite face of the substrate, which will again cause warping.

These problems place a lower bound on the thickness of substrates that can be used. Using manual alignment marks (the only method possible with the screen printer used), It was not found possible to work reliably with substrates less than 100μm thick. Even with arbitrarily good alignment, the thickness variation will limit the substrate thickness.

As a result of the thermal mismatch the thick-film layers in a double sided structure will be under compression, even when there are no external loads. This has advantages for the device as a whole, as it means that when the beam is flexed, the brittle PZT layer (a ceramic) will not be placed under tension until a certain deflection is passed. Since the breaking strain of a ceramic is greater under compression than it is under tension, it means that more strain can be stored in the piezoelectric element, resulting in a higher capacity to generate power.

4.2.3 Substrate Preparation

To ensure good adhesion between the substrate and the subsequent layers, the following method was adopted to roughen, and degrease the surface:

(1) The surface was sanded with a grade P1000 emery paper.

(2) The substrate was immersed, and washed in acetone.

Following this procedure, gloves must be worn when handling the substrate to avoid contamination with finger grease.

4.2.4 Chemical Interaction Between PZT layers and Steel substrate

Initially, silver electrodes were printed directly onto the prepared steel, followed by the PZT paste. After firing, the PZT became a discoloured yellow, and the steel in areas adjacent to the PZT had reacted in some manner, causing it to darken. The effect is similar in appearance to that observed by Beeby *et al* [60]. Beeby's experiments involved printing the same thick-film paste onto Silicon. The effect is thought to be caused by the volatile Lead Oxide in the PZT reacting with the substrate.

4.2.5 Dielectric Layer

To eliminate the problem of chemical interaction between the steel and the PZT, a dielectric material was chosen to separate the layers. The paste used was the IP222L paste produced by Heraeus Silica and Metals Ltd. The paste is an 850°C firing glaze for Cr-Steels.

The Heraeus data sheet [61] recommends printing 3 separate layers to achieve a printed thickness of 50μm for reliable electrical insulation. It was found that this many layers produced a substrate that was too mechanically stiff to be useful, and experimentation showed that a single layer of around 20μm was sufficient to prevent damaging interaction between the steel and the PZT.

The data sheet also recommends a peak firing temperature of 860°C for 8-12 minutes. At this temperature, the film was found to not adhere properly to the steel. The Heraeus data sheet for steel pre-treatment [62] advises etching the steel in a 60°C nitric acid bath to improve adhesion, however, this did not solve the problem. A profile with a peak firing temperature of 890°C for 10 minutes was chosen instead, which resulted in good adhesion of the film, even without a nitric acid etch.

4.2.6 Electrodes

To make electrical connection with the PZT, top and bottom electrodes must be printed. The original intention was to use the steel as the bottom electrode to reduce complexity, however, the dielectric layer blocks this connection.

The bottom electrode must be made using a cermet film, so that it can withstand subsequent firing of the PZT layers. A wide range of conducting pastes exists. Gold and Platinum were rejected as too expensive – at least for development work. Initially the 9635C Silver Palladium paste [63] produced by Electro-Science Laboratories Inc. was tested. This is a standard conductor for volume hybrid production. Printing proceeded well; however, after the PZT layer was fired areas of PZT over the electrode became discoloured, indicating that silver was leaching from the film into the PZT. This leaching reduces the piezoelectric activity of the PZT. To remove the problem, a low migration silver paste, 9633B [64], was chosen.

Initially top electrodes were also fabricated with a cermet paste, however, the cermet films are mechanically stiff, and a top electrode substantially reduces the proportion of elastic strain stored in the PZT when the beam is flexed. A silver loaded polymer paste (ESL 1107) was chosen for the top electrode. Since the polymer is cured at only 180°C, silver leaching is not an immediate problem. In older samples produced by other researchers, however, I have observed significant poisoning of the PZT through slow silver leaching. Thus, in devices produced for commercial use it would be better to replace the silver with a more inert conductor such as gold.

4.2.7 Piezoelectric Layers

Commercial piezoelectric pastes are not currently available. The pastes used in this project are based on a PZT5H powder of particle size 6μm supplied by Morgan Matroc Ceramics. The

composition of the paste used here has been developed and studied already [60,65]. The stability of the material over time is examined in chapter 6.

4.2.7.1 Thick-Film PZT Paste Composition

The paste is mixed by hand. 76 percent (by weight) of the dry PZT powder is mixed with 4 percent of a lead borosilicate glass (Corning 7575). These are then mixed with 20 percent ESL type 400 vehicle. The paste is mixed with a spatula, then transferred to a Pascal Engineering Triple Roll Mill, where the paste is milled for 5 minutes to ensure even mixing. The paste is then transferred to a pot, where it is stored ready for printing. The amount of vehicle can be varied to achieve a good consistency for reliable screen-printing; this should not have a significant effect on the properties of the resulting film, as the vehicle burns off during the drying phase.

The purpose of the lead borosilicate glass is to promote liquid phase sintering. Bulk PZT is sintered by holding the ceramic at temperatures of around 1200°C. Solid-state sintering occurs as solid material is transferred to areas of contact between particles. The resulting structure consists of tightly bound crystallites, with only a small amount of remaining porosity [66]. The thick-film process used here precludes the use of such elevated temperatures for so long. During liquid phase sintering the glass melts and penetrates between the PZT grains. The grains of PZT are drawn together by surface tension [65]. The resulting structure will be denser than the dried paste, but still has a significant amount of porosity. This increased porosity is the reason for the reduced piezoelectric activity of the thick-film PZT compared to bulk material.

4.2.7.2 Processing the film

Standard thick-film processing techniques normally produce layers around 8-15μm thick. In this case a significant thickness of PZT is required to produce power, and to avoid any pin-hole defects that would prevent polarisation at high field strengths. To produce a 70μm thick final layer, a wet thickness of around 140μm is required, assuming a shrinkage of 50% during the drying and firing cycles. Using a thick emulsion layer on the screen, and a thick mesh would produce such a layer, but the surface of the resultant print would not be even due to the coarse mesh.

Another associated problem is 'river bed' cracking, which occurs when a thick print is fired. As the print is fired, the top surface of the deposit dries first, forming a crust. Shrinkage of the deposit as a whole then occurs as it dries. The top layer however is unable to shrink and cracks through stress [65]. This cracking reduces the piezoelectric activity of the material when it is placed under tension, and increases the risk of short circuits occurring when the top electrode is

printed over the PZT. This problem was encountered during initial tests, figure 15 shows a typical set of cracks.

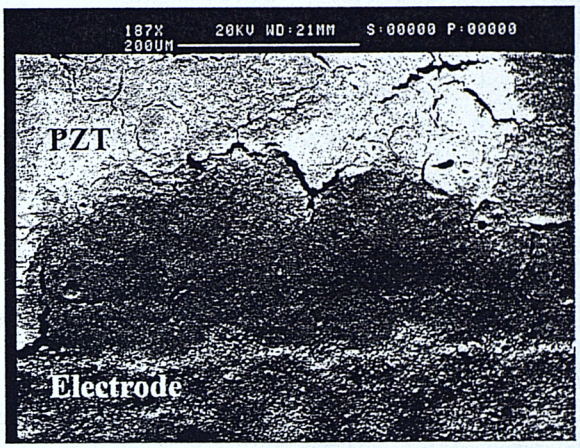

Figure 15: SEM image of PZT layer with 'river-bed cracking'

To produce a reliable thick layer it is necessary to print several layers on top of each other, firing once every 50-70μm to prevent 'river bed cracking'. The exact sequence of printing, drying and firing used is described in section 4.3.3. By forming the PZT in several layers it is possible to use a finer mesh, which results in a better resolution, and a more uniform top surface. However the extra firing cycles required may increase the possibility of lead loss from the PZT, and hence lower performance.

The paste is fired at a peak temperature of 890°C dwelling at the peak for around 8-10minutes. Total firing time is one hour. Current work is being undertaken to determine the effect of longer firing cycles and lower firing temperatures.

4.2.7.3 Polarisation

To render the PZT piezoelectric, it must be polarised (see section 3.1.1.2). Polarisation of devices was performed in a box oven. Samples are heated to 150°C then left for 10 minutes to become thermally stable. A field of $3.5MVm^{-1}$ is then applied via the electrodes. The field is maintained for 60 minutes in total, 30 minutes at temperature, followed by another 30 as the sample is allowed to cool down. The d_{33} value obtained by polarisation is a logarithmic function of time. The procedure outlined above should result in a d_{33} value of some 60% of the final value that would be obtained in 24 hours [65]. Higher fields can be applied to the devices, Dargie reports maximum field strengths of around $4.5MVm^{-1}$. Variations in sample thicknesses, especially localised thin areas, mean that the actual field being applied can be hard to measure if the polarising field is applied using the devices own electrodes. Thus the lower field described above

is used to reduce failure rates. Since heating one side of the substrate results in heating of the other side, it is necessary to polarise both sides simultaneously. For commercial devices longer polarisation times would be advantageous, but are unnecessary for the type of feasibility study undertaken here, since we do not require the maximum power output.

4.3 Fabrication of a Test Device

A test device was produced that was designed to help evaluate the methods described above and to facilitate the modelling described in the next chapter.

4.3.1 Design Criteria

The device was designed to be easy to model. A tapered beam of the design shown in figure 16 was chosen. The shape of a tapered beam means that for a given deflection caused by a force at the beam point, there will be an equal stress at all points in the PZT at a given distance from the neutral axis (ignoring, for now, the non-negligible edge effects). This simplifies the modelling discussed below. The other option was to use a beam of constant width, and use a short piece of PZT near the beam root. This design was rejected, as the first design will produce more power due to its larger PZT area.

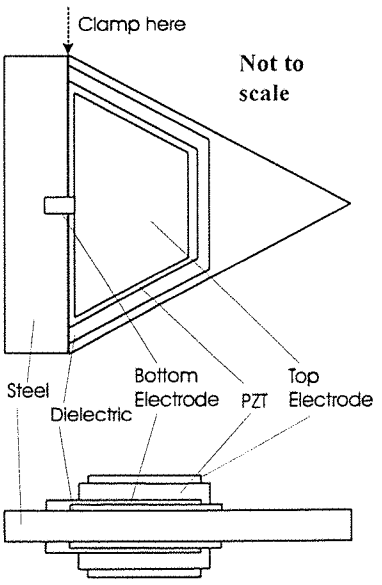

Figure 16: Design of test device

Table 4: Test device dimensions

Device dimension	value (mm)
Beam length from clamp at root	23
Beam width at root	23
PZT width at root	20
PZT width at tip	10
PZT length	10
PZT thickness	0.07
Electrode width at root	18.5
Electrode width at tip	9.5
Electrode length	9
Bottom electrode thickness	0.015
Top electrode thickness	0.015
Distance from beam root to electrode	0.5
Dielectric width at root	22
Dielectric width at tip	11
Dielectric length	11
Dielectric thickness	0.020
Steel thickness	0.100

At the root of the beam, the PZT element stops short of the clamping area. This results in a more reliable clamping of the beam root, improving experimental repeatability; however, it does reduce the amount of strain energy stored in the layer, and would not be recommended in a generator design.

The screens were chosen to be symmetrical, so that the same screen could be used for the front and back patterns. A small border of uncovered steel is provided around the edge of the PZT to allow easy guillotining of the printed substrates.

4.3.2 Choice of Screens

The screens for printing the various layers are listed in table 5, below.

Table 5: Screen Parameters

Layer	Mesh size (pitch per inch)	Emulsion thickness (μm)	Screen material
Dielectric	180	23	Steel
Bottom electrode	230	13	Polyester
PZT	200	23	Polyester
Top electrode	230	18	Polyester

The dielectric, and PZT screens were of a coarser mesh size, to give a thicker layer, whereas the electrodes need to be as thin as possible, and have a better print resolution. The dielectric and PZT screens also had a thicker emulsion to give a thicker layer. The top electrode screen was used to print polymer pastes, so a slightly thicker emulsion was chosen. A steel screen was used for the dielectric layer, as it produces a clearer print, and ages better. The more flexible polyester screens are required for subsequent layers as they permit printing even when the substrate is slightly warped.

4.3.3 Processing Information

Processing was performed in the University of Southampton clean-rooms in a class 1000 atmosphere to prevent dust contamination. A DEK-1750 screen printer was used for all printing.

The following procedure was used to manufacture the devices (see section 4.1 for a discussion of each stage):

1) Sheets of steel (Goodfellows FE240261: 100μm thick, hardened AISI 316 steel) are cut into 50mm squares using a guillotine.
2) Both sides are roughened with P1000 emery paper.
3) The squares are soaked in acetone for 10 minutes, then wiped with clean-room tissues to degrease them. Dry nitrogen is blown across the substrates to dry them.
4) **Dielectric layer**: Heraeus IP222L dielectric paste is printed using the dielectric screen (Print speed slow (a setting on the DEK-1750 printer), print pressure = 2.2N, print gap = 0.6mm). Each side is dried at 200°C for 15 minutes after printing; the reverse face is printed after the front face has been dried. Both sides are then fired simultaneously in a BTU Belt furnace (model QA41-6-54) using a temperature profile known as Dupont60 (A peak temperature of 890°C for 10 minutes, total firing time 60 minutes). To prevent the devices sticking to the furnace belt, they are supported at each side by ceramic strips.

5) **Bottom electrode**: ESL 9633B Silver Palladium paste is printed using the bottom electrode screen. (Print speed slow, print pressure = 2.2N, print gap = 1.2mm). Each side is dried and fired in the same way as the dielectric layer.
6) **PZT layer**: The paste is made up as described in section 4.2.7. On each side, the following sequence is followed: Double print, dry, double print, dry, fire, double print, dry, double print, dry, fire. Print speed slow, print pressure = 2.2N, print gap = 1.1mm (Double printing involves printing, then printing again over the wet layer, to ensure full coverage. This is necessary when the paste fails to print evenly on the first pass – a problem with the current formulation of PZT paste).
7) **Top electrode**: ESL 1107 silver loaded polymer paste is printed using the top electrode screen (Print speed slow, print pressure = 2.2N, print gap = 1.2mm). The paste is cured at 200°C for 60 minutes after printing. Double wet printing is required to ensure coverage (this could be due to the age of the paste used).
8) A guillotine is used to separate each device from its neighbours on the substrate.
9) Wires are soldered to the electrodes.
10) The device is polarised as described in section 4.2.7.3.

4.4 Testing Material Properties

To produce meaningful models of the piezoelectric beam generators, it is necessary to have information on the electrical and mechanical properties of the various materials. Thick-film technology is typically used for hybrid electronics applications, so while thermal and electrical properties are readily available, mechanical properties must be measured. The electrical properties of the PZT film are dependent on the exact processing parameters, so these too must be measured.

4.4.1 Measuring Device Dimensions

The thickness of the various layers was measured using a Tencor Alphastep Profiler (model 10-0040). The uneven nature of the substrate (caused by thermal-mismatch warping and variations in print thickness) reduces the measurement accuracy to around ±3μm. Vernier callipers were used to measure the dimensions of each device

4.4.2 Dielectric Constants

The mathematical models used below require only the permittivity in the polarisation direction. To calculate the permittivity, a Wayne Kerr Automatic LCR meter 4250 was used to measure the capacitance between the electrodes of a sample. The permittivity was derived from the equation for a parallel plate capacitor.

The thickness was measured as described above, however, even though a migration resistant film was used for the bottom electrode some migration may have still occurred. This would lower the effective thickness of the PZT and hence give an artificially high value for the permittivity. Since the piezoelectric constants themselves are subject to wide variation (see section 4.4.4), this effect has been ignored.

4.4.3 Young's Modulus

The Young's modulus of each layer was measured by determining the bending stiffness of thin uniform composite beams (i.e. rectangular beams, rather than the tapered beams of other sections). The bending stiffness is deduced by displacing the beam root vertically, while holding the beam tip still. The force at the beam tip is measured and hence, the beam stiffness can be determined

Figure 17 shows the apparatus used: The beam under test is held by an aluminium clamp, which is attached in place of the microscope barrel on a Chesterman Engineer's microscope. The microscope base is placed on its side, thus by adjusting the microscope slider the beam can be moved vertically. The displacement is read off on a vernier scale, accurate to ±0.01mm. A screw is placed upside down on the centre of a Precisa 1600C weighing scales. The tip of the beam rests on the point of the screw, allowing the force applied to the tip of the beam to be determined to ±0.01 grams.

The elastic deflection of the clamp assembly, and deflection of the weigh-pan of the scales for a given force was measured by resting the aluminium clamp on the screw point. This was found to be $0.6kg(mm)^{-1}$. Subsequent measurements were normalised by removing the effect of this stiffness from the stiffness obtained experimentally. Since typical beams measured here have a stiffness of $0.01kg(mm)^{-1}$ this is not a large effect.

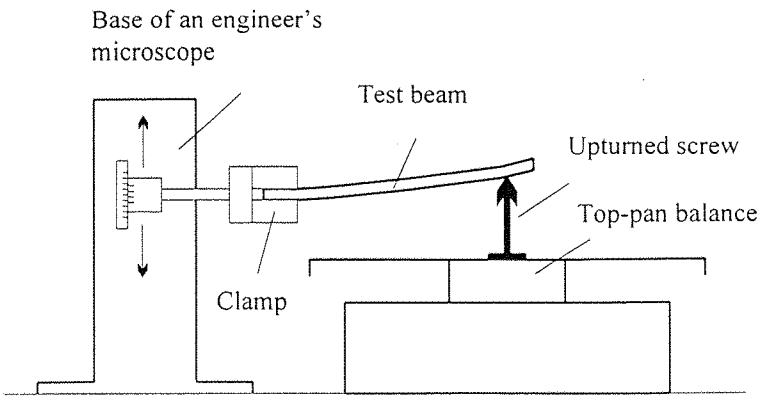

Figure 17: Beam stiffness apparatus

The Young's modulus, Y, can be determined by using Bernoulli-Euler beam theory. The deflection, Δ, of a beam is given by:

Equation 4.1

$$\Delta = \frac{FL^3}{3\sum YI}$$

The summation represents the summation of the product of Y and I for each layer of a composite beam, where F is the force at the beam tip, L is the length of the beam, and I is the second moment of area of the layer about a line through the neutral axis of the beam.

Initially a simple steel only beam was tested to determine the Young's modulus of the steel. A composite beam with a layer of dielectric on steel was then tested, and the Young's modulus of the dielectric determined using the result from the steel experiment to eliminate the effect of the steel. The Young's modulus of PZT was determined in a similar way with a composite steel-dielectric-PZT beam. The experimental data is repeatable and consistent. The layers being tested, however, are thin and uneven, so there is considerable error in measuring their thickness. Results are listed below in table 6.

This method of measuring the Young's modulus of the beam is also limited in accuracy by the lack of lateral freedom provided by the upturned screw point. At larger deflections this will cause tension in the test beam; a component of this tension will add to the force measured by the top-pan balance. To minimise this effect, deflections of less than 2% of the beam length were used. The resulting force-displacement graphs were examined, and did not reveal any of the non-linearities that would indicate that this effect was a problem. To further verify the results, finite element analysis of a beam was performed to predict the resonant frequency. The resonant

frequency was measured experimentally (see section 4.5.2), and found to lie within the bounds of experimental error.

Table 6: Young's Modulus of device materials

Material	Young's Modulus (GPa)	Error (±GPa)
316 Steel (fired)	162	10
IP222 dielectric	74	5
PZT	18	5

4.4.4 Measuring the d_{33} Coefficient of Thick-Film PZT

Background material about piezoelectric coefficients can be found in section 3.1.1.

There are 3 fundamental methods for measuring the d_{33} coefficient:

1) The direct effect: A known force is applied to the PZT, and the resulting charge measured. The force that is applied can either be determined in advance, or deduced by placing a piezoelectric standard mechanically in series with the sample. To maintain the constant displacement boundary condition, the electrodes are usually short circuited into a charge amplifier.
2) The indirect effect: A known voltage is applied to the PZT, and the resulting displacement measured. To maintain the constant stress boundary condition, the top surface are usually unclamped.
3) Resonant techniques: The resonant frequency of a suitably excited piece of PZT is measured. A piezoelectric analysis that includes secondary piezoelectric effects is required to calculate the relevant d coefficients.

For crystals and bulk samples, Mason and Jaffe [67] suggest that resonant techniques are by far the most accurate. In thick-film samples, however, the presence of the substrate means that the mechanical resonant frequency of the sample is largely determined by geometry and the mechanical properties of the materials. Due to the generally low nature of this resonant frequency, the electromechanical coupling coefficients have little influence on its frequency. Thus this method is unsuitable for thick-film samples.

The direct and indirect methods are essentially quasi-static techniques, in that they are performed well away from the resonant frequency of the material. The shape of the test specimen is

important, as the various piezoelectric constants are closely interrelated. An ideal shape will allow easy measurement of the desired parameter, without needing to remove the effect of the other unwanted parameters.

The value of the d_{33} coefficient is a function of the preparation process, and individual samples are subjected to fluctuations even within a given batch. It is stated by Jaffe [68] that d_{33} can vary by up to 10% even in ceramics of known composition and high density. Thus, statistical methods are required to determine the average value of a constant for a particular composition.

4.4.4.1 Prior Work

Many authors have published work on thick-film piezoelectric materials, but with the exception of Dargie, described below, there has been little published data on the exact methods used to measure thick-film piezoelectric constants.

Dargie [65] begins by developing apparatus to make an indirect measurement of d_{33}. The sample was clamped to a base, and a voltage in the range 30-180V was applied. Both a capacitive displacement probe and a fibre-optic reflectance sensor were used to measure the displacement of the top electrode. The two measurement techniques yielded similar values, however, the results did not truly reflect the d_{33} of the sample, as it was discovered that the lateral expansion of the PZT (caused by the d_{31} coefficient) caused the substrate to flex, as shown in figure 18. Even with careful clamping, this phenomenon continued to effect the results. Consequently, the indirect method was abandoned.

Dargie also describes an indirect method used by Professors Morten and Prudenziati at the University of Modena Italy. The method is similar to Dargie's, and he concludes that a similar bowing problem will effect the results from this method.

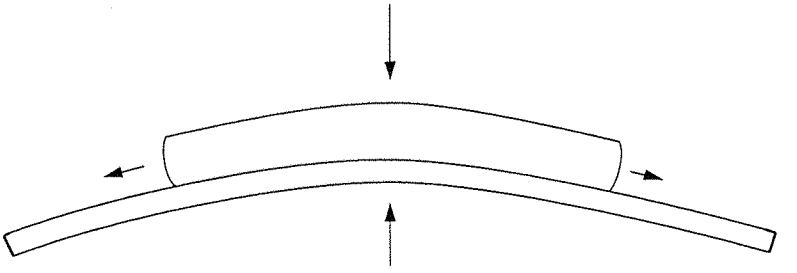

Figure 18: Device bending due to negative strain in thick film PZT layer

Dargie had more success with direct techniques. Initially, samples were placed on a flat steel surface, and a force, generated by hanging a weight on a lever, applied through a 4mm pin. A charge amplifier was used to measure the resulting charge. Small bending moments applied to the sample by the base were found to obscure the results, so the steel base was replaced by a 4mm pin as shown in figure 19 (extracted from his thesis [65]). This method, however, was found to be sensitive to the point of application, and the short term previous stress profile of the sample.

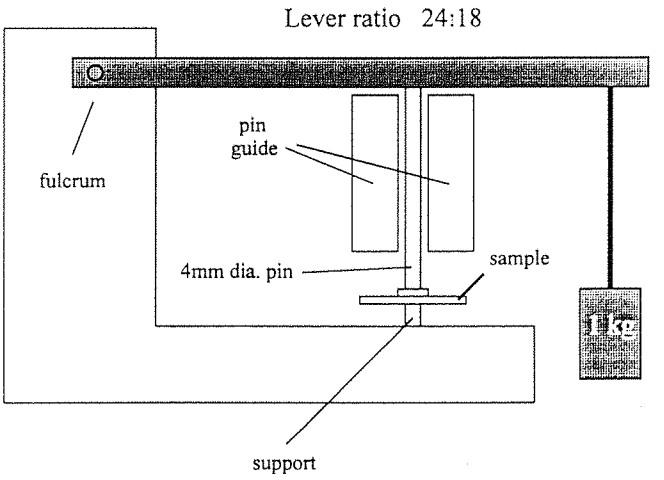

Figure 19: Initial direct d_{33} measurement rig (after Dargie [65])

Dargie's final method is shown in figure 20 (extracted from his thesis [65]). A shaker applies an alternating force to the sample. Contact is made to each side of the sample by a ball bearing to minimise damage, and reduce sample bending. A load cell, connected mechanically in series with the sample, measures the force that is applied. Typically, an alternating force of one Newton was superimposed on a standing force of 3 to 4 Newtons.

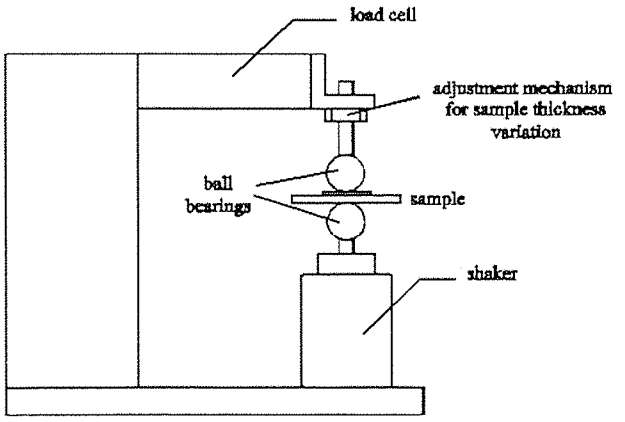

Figure 20: Alternating load d_{33} measurement rig (after Dargie [65])

Commercial d_{33} meters are available. The Piezo-d meter produced by Sensor Technology Limited, and the Pennebaker 8000 supplied by the American Piezo Ceramics Company, both use an alternating force method. Dargie evaluated the Pennebaker 8000, and found it gave repeatable results and was easy to use.

The major drawback with the alternating force systems described above is that they fail to damp flexural vibrations of the sample. As the alternating force system applies its force, the vibrations will excite longitudinal bending modes of the substrate. This bending will cause a response determined by the d_{31} coefficient of the substrate. Dargie found that the results obtained by alternating force methods were consistent [65], but higher than those measured by other methods [69]. On thicker, smaller substrates this is less of a problem.

4.4.4.2 Design of a Direct Measurement System

A system was designed to measure the d_{33} coefficient using the direct method. The apparatus is shown in figure 21. A knife-edge pivot supports a beam with a weight at one end. A point of diameter 3mm directly beneath the weight applies a force to the sample under test. The point is raised and lowered by a motor driven cam at the opposite end of the beam. The sample is supported from beneath by a similar point, and a pair of piano wire beams. The points touching the sample are electrically isolated from the rest of the system by a plastic thread and washer. This is to reduce electromagnetic interference, and charge leakage onto the sample. The sample mounting is placed on a Precisa 1600C top-pan balance to record the force applied to the sample. All the experiments described here were performed with a force of 3.8 Newtons. Assuming an even stress distribution, this produces a stress of 0.54 MPa. It has been found [70] that bulk PZT is linear up to at least 1.5MPa, so the experiments conducted here should be well within the region of linear operation.

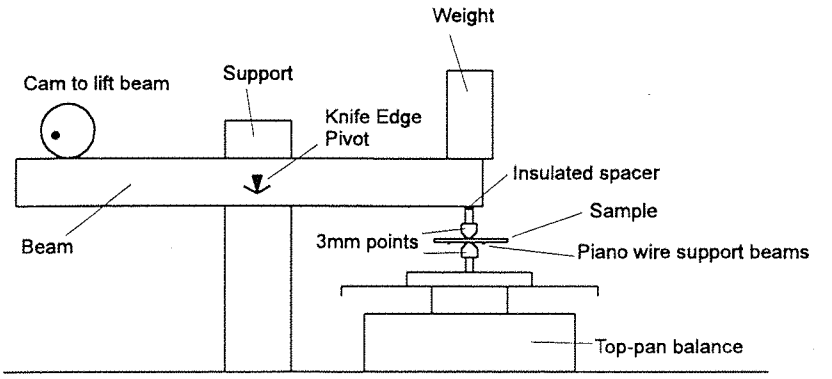

Figure 21: Final d_{33} testing rig

It was found that the friction in the mechanism supporting the weight was an important factor. Friction causes any small vibration in the surrounding environment (e.g. people walking past the test bench), to be coupled directly into the sample. This can have a significant effect on the observed response. By using a longer beam, leverage factors down any small torques applied by the knife edge pivot.

Like Dargie, the initial design of sample holder consisted of a flat surface, and a clamp. When this was tested, it was found that bending moments within the sample (caused by an uneven base, or warped substrate) could contribute to the charge produced. By applying forces to the substrate next to the piezoelectric area, it was found that the bending could produce a signal at least as large as the one caused by the d_{33} coefficient. Experiments were performed with samples firmly glued to a block of aluminium with super glue. This reduced the bending significantly, but it was still large enough to interfere with samples having d_{33} coefficients of an order of $50pCN^{-1}$. Gluing the samples is also a destructive test, which is not satisfactory.

The final design uses a set of springy piano wire beams (diameter 0.5mm, length 10cm) to support the sample between the steel point below the sample, and the point on the force unit. This arrangement allows the sample to rotate as necessary when the force is applied, so that all forces are tangential to the sample. Experiments showed that this reduces the charge caused by bending to around 2pC on ceramic substrates around 5cm long.

The output from the PZT's electrodes was fed directly into a Kistler 5001 Charge Amplifier. The output from the charge amplifier was measured using an Hewlett Packard HP35660A Dynamic Signal Analyser. To make a reading, the sample is placed between the points, and the piano wire beams adjusted to support the sample at the right height. The top-pan balance is examined to

record the force being applied to the sample, then the cam is used to raise the beam. The Signal Analyser is paused to allow the amount of charge displaced to be recorded.

The surrounding material which constrains the PZT where the force is applied, must also be considered. The measurement rig applies a force to only a small fraction of the total electrode area of the sample. This means that the material surrounding the clamped area will constrain any lateral expansion of the PZT layer, and cause a corresponding change in the observed response. The effective d_{33} is calculated by Nemirovsky *et al* [71] as

$$d_{33,eff} = d_{33} - 2 d_{31} (c_{13}^{E} / c_{33}^{E}) \qquad \textbf{Equation 4.2}$$

Where c_{13}^{E} and c_{33}^{E} are terms of the stiffness matrix for the PZT under boundary conditions of constant field. Using typical material constants for bulk PZT [44], we obtain

$$d_{33,eff} = d_{33} + 1.4 \times d_{31} \qquad \textbf{Equation 4.3}$$

The main source of error in this experiment arises from the mains hum picked up by the circuit, which limits accuracy to around $\pm 3 pCN^{-1}$. This was present even after screening connecting wires, and earthing major conductors. Since these results were not required for the remainder of this work, significant effort was not applied to reducing this error.

Bending moments are also still present, and limit the substrate thickness to being thicker than around 200μm. The limit on thickness means that it is not possible to directly measure the d_{33} of the test devices described in section 4.3. To determine the d_{33} produced by this process, the same steps were performed on a 1mm thick substrate. This resulted in a effective d_{33} coefficient of around $-120 pCN^{-1}$. Taking the results for d_{31} described below, and using equation 4.3, this yields a value of $-135 pCN^{-1}$ for d_{33}.

4.4.5 Measuring the d_{31} Coefficient of Thick-Film PZT

The d_{31} coefficient can be measured using the same basic techniques described above for d_{33} (direct, indirect, and resonant techniques). The thin nature of the thick-film materials being measured, however, means that it is difficult to directly apply or measure forces and displacements in directions perpendicular to the thickness. Like the d_{33} coefficient, there is little available information in the literature, on experimental methods of measuring d_{31}.

The d_{31} coefficient is measured using the direct effect. Beams of the design described in section 4.3 are clamped in the shaker rig described in section 4.5.1 (all of the apparatus referred to below is described in this section) . The beams are shaken, and the drive to the shaker adjusted until the beam amplitude (measured using the vernier screw gauge) reaches a predetermined level. The charge amplifier is used in conjunction with the signal analyser to determine the charge displaced at the point of maximum displacement for the beam. Figure 22 shows a graph of charge displaced against excitation amplitude for a sample polarised in the manner described in section 4.2.7.3, at a temperature of 22°C. A least squares method is used to estimate the slope of the graph. A finite element analysis is performed as described in section 5.5 to calculate the average longitudinal stress in the layer. This data is combined with the surface area of the layer, to calculate the d_{31} coefficient.

$$d_{31} = \frac{\text{Charge}}{\text{Area} \cdot \text{Stress}}$$

The d_{31} values for a set of four samples were measured and found to yield an average value of $15 pCN^{-1}$. As discussed above, the d_{31} coefficient will vary considerably even within a given batch, as a result of variations in cooling rates, and film thicknesses.

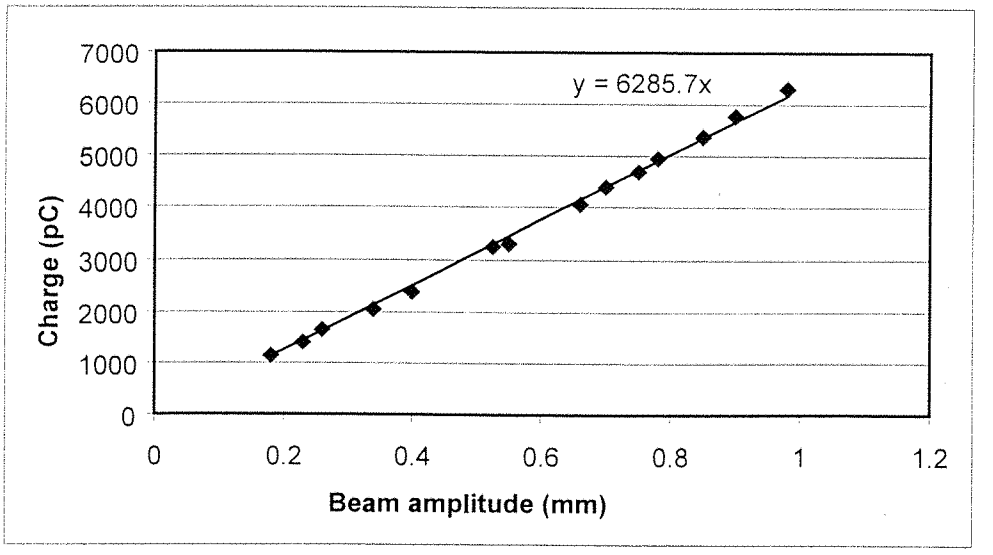

Figure 22: Graph of Charge Displaced Against Amplitude, to Find d_{31}

4.5 Response of Prototype Tapered Beams

4.5.1 Experimental Apparatus

The results described in this section have been obtained using the apparatus shown in figure 23.

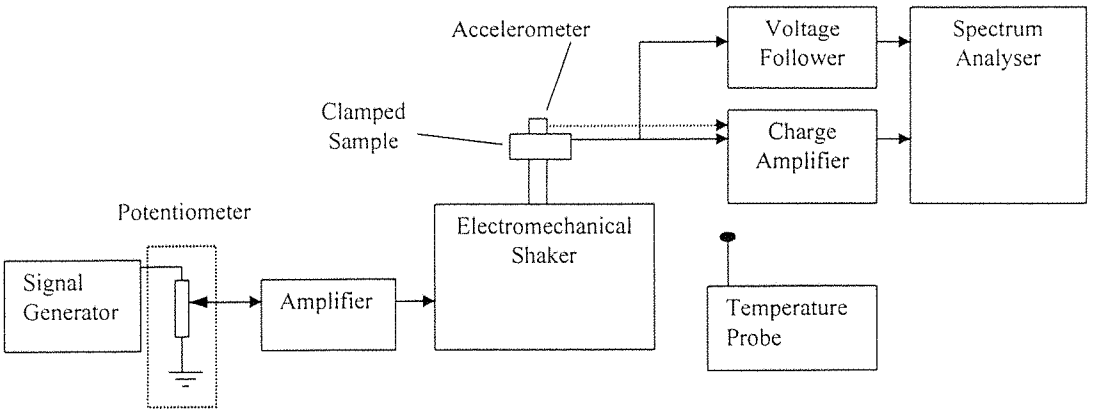

Figure 23: Experimental Set-up

A Goodman V.50 Mk.1 (Model 390) Vibration Generator (shaker) is used to supply mechanical vibrations to the samples under test. Auxiliary suspension is fitted to the shaker, which improves the lateral constraint of the central spindle, and reduces the load on the shaker suspension. The loads mounted during the course of these experiments are below the 2lb limit suggested by the manufacturer [72]. The shaker can supply vibrations in the range 5Hz-4kHz (limited by the current consumption of the coil, and its first resonant frequency respectively). The shaker is driven by a Ling PA50VA valve amplifier. The amplifier is driven from the frequency source incorporated into a Hewlett Packard HP35660A Dynamic Signal Analyser. The output from the signal analyser is reduced by feeding it through a 20 turn, wire-wound 1kΩ potentiometer. This allows fine adjustments to be made to the output of the signal analyser.

The samples are clamped, and mounted on the shaker using the specially designed clamp shown in figure 25. Figure 24 shows a photograph of a prototype beam in the clamp. The clamp is mounted on the shaker spindle thread, and held by a lock-nut. An accelerometer is mounted axially above the spindle on a short thread (Bruel & Kjaer Accelerometer Type 4369). The accelerometer provides data on the amplitude of vibrations applied to the samples, which can not be determined solely from the electrical drive to the shaker, since the shaker has a non-linear response. The accelerometer has a first resonance at 36kHz, which is well above frequencies of interest in the experiments described here. The clamp consists of an aluminium plate at each end of the aluminium base, held in place by a pair of bolts through each plate. The end surfaces are

machined with the plates in position to ensure that the end surfaces of the plates and the base lie in the same plane. The twin plates allow two samples to be clamped at once, which is useful for holding a reference sample. To clamp a sample, shims of the same thickness as the sample are held under the rear edge of the plate to ensure that the plate is parallel to the base.

A vernier screw gauge is mounted on a plate that is attached by threaded steel rods to the shaker. The screw gauge has a resolution of 0.01mm, and allows the tip amplitude of a vibrating beam to be measured. Figure 26 shows the shaker, suspension, clamp block, accelerometer, screw gauge, and a typical sample as they are mounted together. The accuracy of measurements obtained this way is limited by the size of the point at the tip of the gauge, since as the amplitude of the beam changes, the point of contact with the screw gauge will also change.

A mass can be attached to the tip of a sample using the method illustrated in figure 27. A short thread holds a pair of nuts that are tightened on either side of the sample to hold the mass in place. Washers separate the sample from the nuts, and have a flattened edge, which provides a more even stress distribution in the area of the sample next to the mass.

Connecting wires can be attached to the sample using either solder, or a conductive epoxy. Soldering was found to be reliable, and produced a conveniently small bond for attaching wires to the cermet bottom electrodes of the samples described in section 4.3. The clamp described above has channels cut in the top plates (as shown in figure 25) to allow the connecting wire from the bottom electrode to pass under the plate. A hole drilled down to the channel from the top of the plate makes room for the soldered joint. The contact resistance of these soldered joints is negligible. For the polymer top electrode, soldering was found to be unreliable. The elevated temperatures required for soldering also partially depolarise the sample, and there is a risk that the solder or flux will penetrate into to piezoelectric layer and cause changes to the piezoelectric response of the sample. A silver loaded epoxy (Circuit Works, CW2400) was found to be suitable. A typical joint has a contact resistance of less than 0.1Ω. A lacquered 0.2mm diameter copper wire was chosen for the electrical connections. It is important to chose a thin wire for connecting to the top electrode, as the wire can interact mechanically with the sample. The wire is attached to the base with double sided tape so that movement of wires distal to the sample will not have a mechanical effect on the sample. This wire is soldered to thicker single core wire, which is in turn held by crocodile clips attached to BNC cables. The BNC cables reduce interference from mains hum in the experiments. The effect of mains hum is also reduced by conducting experiments at frequencies that are not multiples of 50Hz, adjusting the resonant frequency of beams by changing the clamping position where necessary.

To measure the charge displaced by the piezoelectric materials, and the charge signal from the accelerometer, a Kistler Charge Amplifier (model 5001) is used. The charge amplifier was calibrated by applying a reference voltage to the built-in calibration capacitor. The charge amplifier has three built-in discharge resistors. A larger discharge resistor gives better frequency performance, at the expense of higher DC drift. The experiments performed here are at a sufficiently high frequency that the smallest discharge resistor ($10^9\Omega$, labelled 'short' on the amplifier) can be used, to minimise DC drift.

To measure the open circuit voltage produced by the piezoelectric samples, and to measure the voltage developed across load resistors, a voltage follower was constructed. Measuring these voltages directly is difficult with a conventional oscilloscope, as the impedance of the oscilloscope will discharge the piezoelectric layer. The voltage follower was implemented using a TLC251 JFET-input op-amp, which has very low input bias and offset currents (typically 0.1pA, and 0.6pA respectively). Since the voltage follower is used in experiments where frequency analysis is used to isolate the required signal from other components, issues such as supply voltage ripple rejection, and voltage offsets do not have significant impact on the accuracy of the experiments.

The outputs from the voltage follower and the charge amplifier, are both monitored by a Hewlett Packard HP35660A Dynamic Signal Analyser.

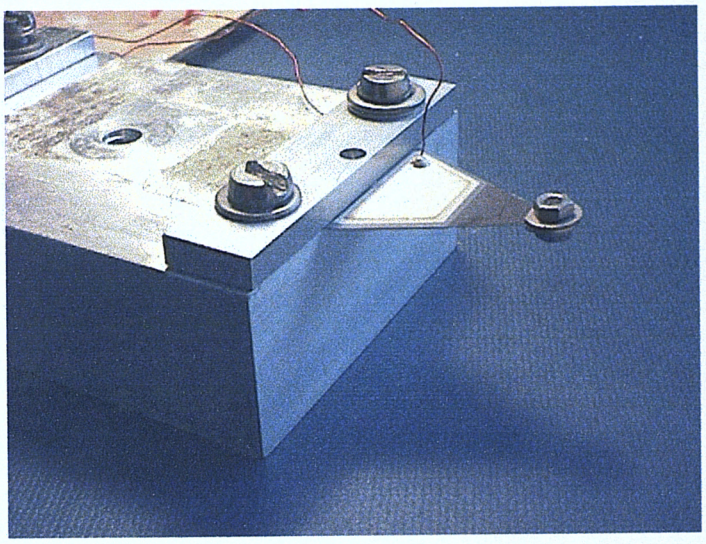

Figure 24: Photograph of prototype beam in clamp

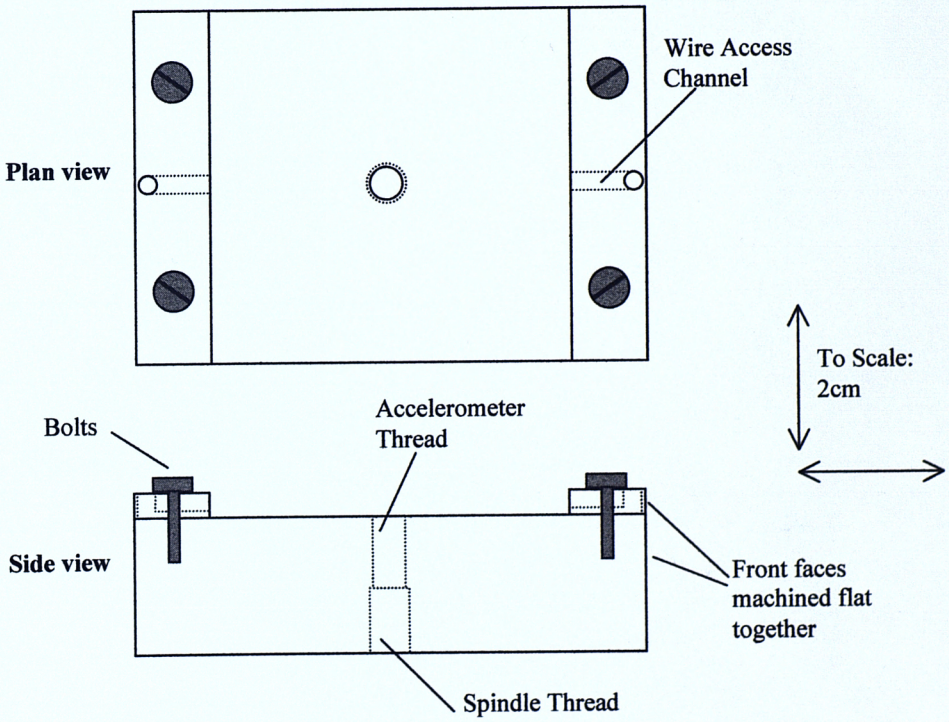

Figure 25: Sample Clamp Block

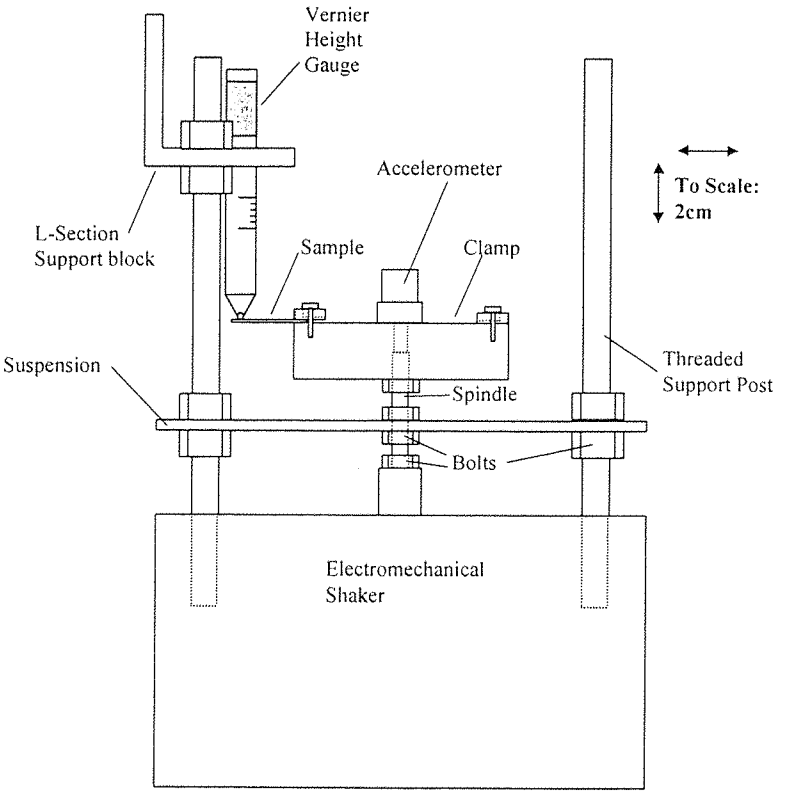

Figure 26: Shaker, Clamp, and Vernier Gauge Arrangement

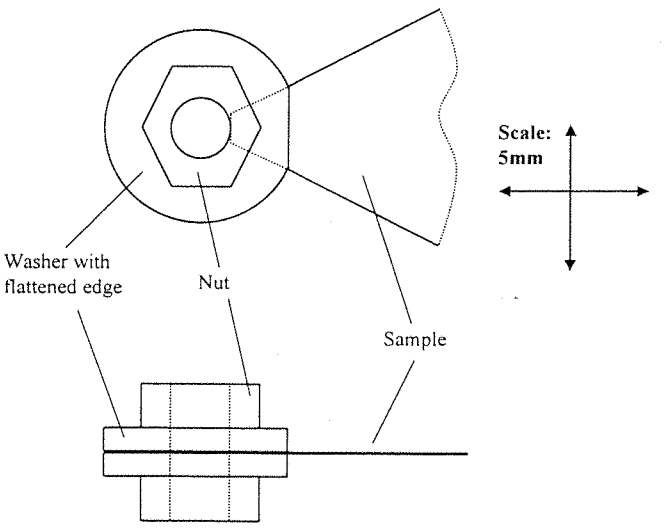

Figure 27: Mounting a Mass on Samples, Detail.

4.5.2 Device Performance

The results in this section characterise the response of a tapered PZT on steel device of the type described in section 4.3.

The device is polarised as described in section 4.2.7.3, then left for one week to stabilise the piezoelectric constants. Wires and a tip mass were attached to the device as described above, and the device secured in the clamp.

The resonant frequency of the device was determined by using the signal analyser to supply a periodic chirp (a sine-wave scan across the frequencies 73-85.5Hz in a total time of 2s) to the shaker. The charge produced by the PZT was fed through the charge amplifier, and into the signal analyser. The analyser took 512 samples at a sampling frequency of 256 samples per second. A Fourier transform was performed to produce the trace shown in figure 28, where the beam amplitude at resonance was measured as 0.8mm. The graph shows the resonant nature of a beam's response, with a resonant frequency of 80.2Hz..

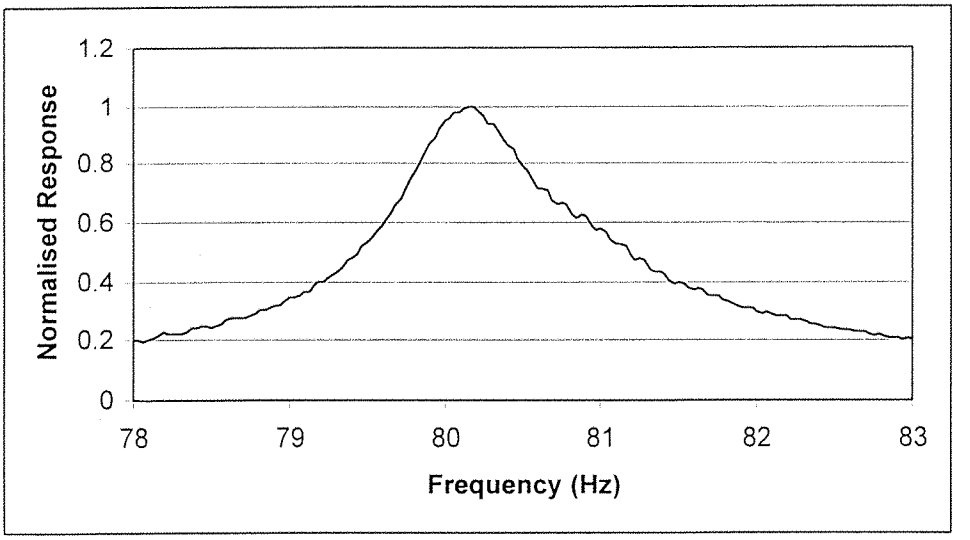

Figure 28: Graph of a Typical Resonant Response of a Sample.

Load resistors were connected between the terminals of the device, and the voltage developed across the resistors monitored using the signal analyser. Figure 29 is a graph showing how the power dissipated by the load resistor varies with both the load resistance, and the amplitude of the beam. The graphs show an increase in power output with increasing beam amplitude. They show that there is an optimum load resistance (333kΩ) for extracting power from the device, and that this resistance is independent of the beam amplitude over the range shown here.

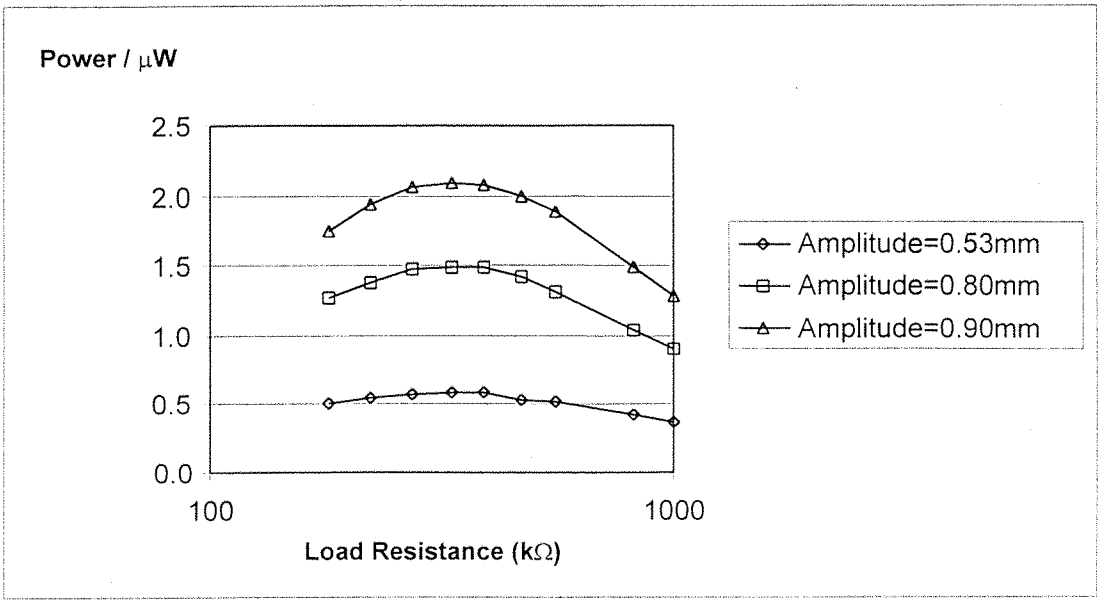

Figure 29: Beam Power Versus Load Resistance for different Beam Amplitudes.

Figure 30 plots the voltage across an optimum load resistor of 333kΩ against beam amplitude. The graph is linear with a zero intercept. This shows that the PZT is operating within its range of linear operation. If the graph were extended to higher beam amplitudes then the graph would be affected by both the non-linear relation between deflection and stress of a cantilever beam, and by the non-linear nature of the piezoelectric materials at higher stress levels. The graph has not been plotted in this range, as the experimental apparatus does not provide an accurate measure of beam deflection at these higher amplitudes.

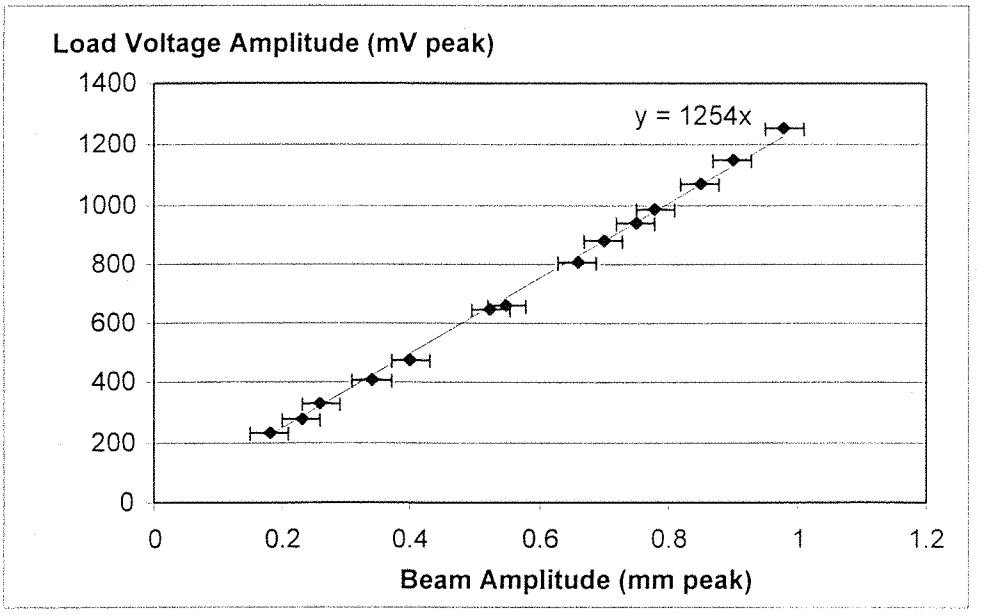

Figure 30: Load Voltage Versus Beam Amplitude for an Optimally Shunted Beam.

The quality factor, Q, was measured by examining the width of the resonant peak. The relation

$$\zeta = \frac{\omega_2 - \omega_1}{2\omega_n}$$ **Equation 4.4**

is used where ω_2 and ω_1 are the frequencies where the response falls by 3dB from its peak value. A series of four measurements at a beam amplitude of 0.55mm revealed a Q-factor of 111.5 ±10%.

4.6 Summary

Techniques have been developed for depositing a functional thick-film layer of PZT on thin stainless-steel substrates. Chemical interaction between the two materials is prevented with an intermediate layer of a glassy dielectric, and thermal mismatch is compensated for using symmetrical structures.

Mechanical and electrical properties of the thick-film PZT layer have been measured. The practical measurement of piezoelectric thick-films on substrates is not straightforward. Although previous work has quoted piezoelectric properties, there has been little published data on the experimental methods used to measure piezoelectric constants of these materials. Thus methods have been developed for measuring the d_{31} and d_{33} coefficients of thick-film piezoceramics. The Young's modulus of thick-film PZT has also been measured. The following results are obtained:

Table 7: Summary of PZT material properties

Property	Value	Error (%)
d_{31}	15pC/N	30
d_{33}	135pC/N	20
Young's Modulus	18GPa	10

A prototype piezoelectric generator has been produced, and tested. A maximum of 3μW was produced at an amplitude of 1.9mm. Since the maximum stress permitted in the PZT before depolarisation or mechanical damage occurs is unknown, the maximum power output for long-term operation cannot be stated. At the amplitude of 1.9mm no immediate damage was observed, but experiments were discontinued to preserve the generator. See chapter 6 for more discussion on stress related changes in PZT layers. The results show that the amount of power that is supplied to the load is influenced by the type of loading applied. The power produced by the

prototype generators is not large enough to be practically useful (as discussed above in section 3.3). The cause of this low power output will be investigated in the following Chapter.

CHAPTER 5

Modelling Piezoelectric Generators

This chapter focuses on techniques for modelling the electrical and mechanical responses of a piezoelectric beam generator of the type described in the previous chapter (referred to in this section as a piezo-generator). Mathematical modelling of layered generators is performed, including a new model for the mechanical impedance of a resistively shunted piezoelectric beam. The modelling is used to provide predictions to compare with the experimental data from the prototype. Confident that the modelling provides realistic estimates of generator performance, the model is used to assess how much power could possibly be extracted from a generator of arbitrary dimensions and excitation.

Figure 31 is an energy flow diagram, showing how energy is taken from the external environment and converted into a useful electrical form, including energy losses. The energy undergoes a series of conversions, from the initial kinetic energy of the beam through elastic energy of the beam, electrical energy in the piezoelectric material and load circuit, and is finally stored in a chemical form in a battery. An important point to note is that the amount of energy generated by the system is determined by both the amount of energy lost at each stage (related to the efficiency), and by the proportion of energy that is converted from one stage to the next. The efficiency of such a generator system is generally not important, as the energy taken from the excitation medium is generally only a tiny proportion of that available, so it doesn't matter if some of it is wasted. We are interested in maximising the output power, even if that means a lowered efficiency.

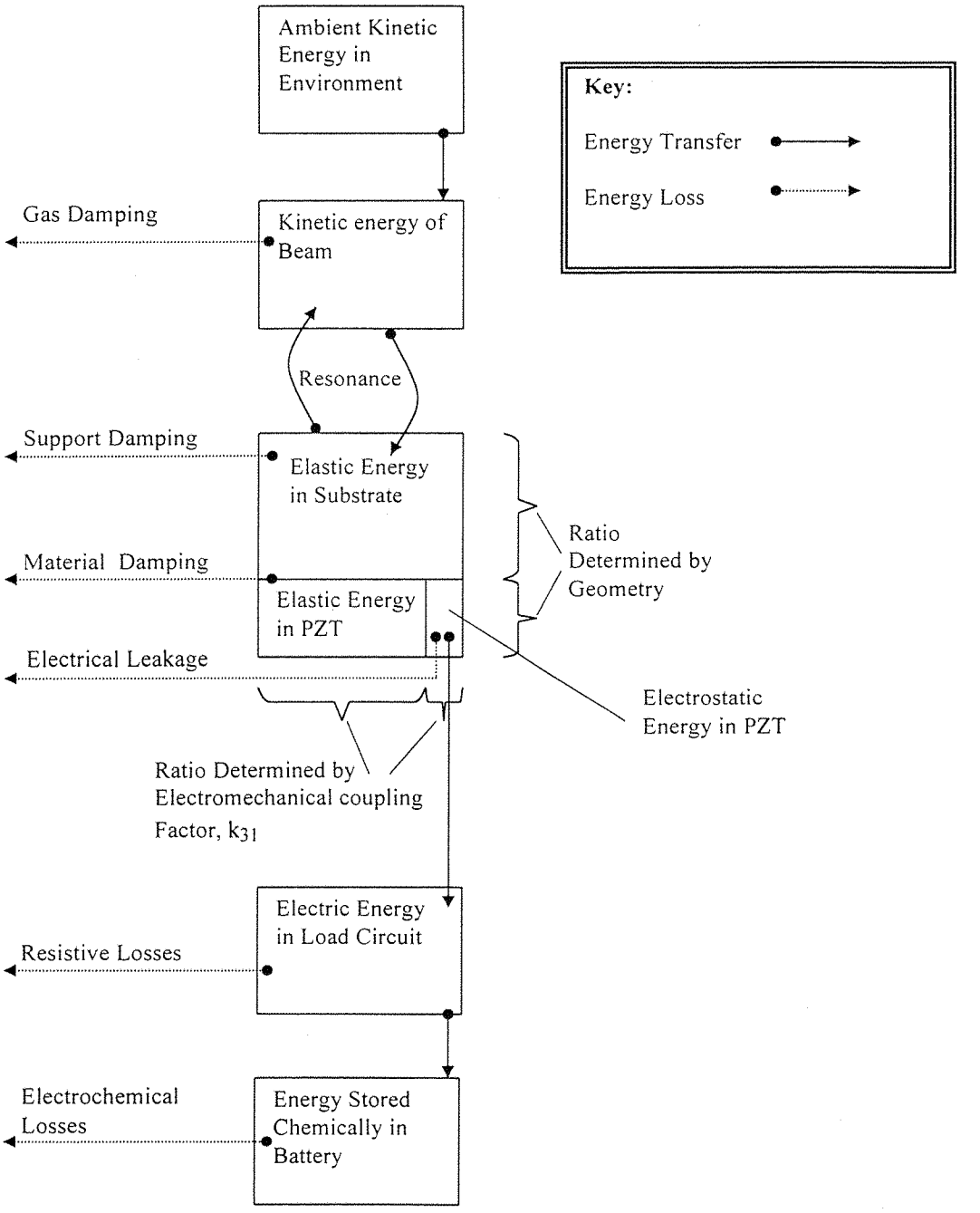

Figure 31: Energy Flow Diagram for a Resonant PZT Generator

5.1 Approaches to Modelling

It would be useful to be able to model a piezo-generator using closed form equations, based on solving the differential equations of motion and current flow derived from the electromechanical system. When this approach is attempted, however, the equations quickly become too large to reveal simple insights into the design. Analytic solutions have produced results for comparable,

but simpler systems [73], but the piezo-generators are more complex, due to the following features:

(a) The strain induced by flexure of the sample varies through the thickness of the piezoelectric material, and must be modelled accordingly. (See section 5.3).

(b) The electrical load interacts dynamically with the capacitive piezoelectric layer, creating a set of electrical poles and zeroes that couple with the mechanical system.

(c) The shapes of the piezoelectric layer and the substrate produces complicated mode shapes, and boundary conditions.

(d) Air and support damping both have an important effect on the system, and must be taken into account.

(e) Non-rectangular beams exhibit significant edge effects.

Finite Element Analysis (FEA) would solve many of the difficulties mentioned above. The FEA package ANSYS® was examined to find a means of directly predicting the response, and power produced by a generator. The package does provide the capability for limited piezoelectric field coupling (Elements SOLID5, PLANE13, etc), however, it does not allow the simultaneous mechanical and electrical load conditions that would be required to model resistively shunted piezoelectric elements. This is a restriction common to all current FEA packages (discussed in a review by Soderkvist [74]).

The material parameters of the thick-film materials (e.g. d_{31}, Young's modulus) can vary considerably. Jaffe *et al* [43] state that typical piezoelectric parameters can vary by up to 10 percent within a single batch. Experience confirms this statement, and shows that mechanical parameters are subject to similar variation. This variation limits the degree of accuracy with which the models presented here can be verified to a few percent.

5.2 Decoupling the Electrical and Mechanical Responses of a Shunted Piezoelectric Element

The methods adopted below decouple the electrical and mechanical domains, allowing the problem to be solved in smaller, more tractable pieces.

A model of a generally shunted piezoelectric material is developed by Hagood and von Flotow [45]. The model is expressed in the Laplacian domain, and is based on a block-shaped piezoelectric element shunted by a passive electrical load, and with arbitrary driving currents. Hagood shows that in the steady state the element can be represented mechanically as having a frequency dependent complex stiffness, whose value depends on the electrical load conditions.

That is, that at a given frequency and with a given electrical load across the layer, the energy dissipated into the load is a proportion of the maximum strain energy stored within the material. The paper assumes that the electrical field within the piezoelectric material is uniform; i.e. that external forces on the faces of the element are constant across each face. The model is a quasi-static one, as the mechanical vibrations are assumed to be at a low frequency compared to the frequencies of electromechanical resonance of the piezoelectric material.

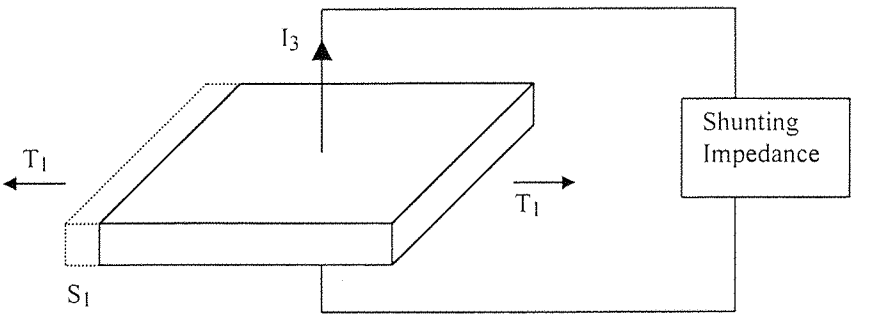

Figure 32: A Piezoelectric Element Shunted in the Polarisation Axis, Stressed Along "1" Axis

Taking the special case of a resistive load connected to electrodes in the direction of the polarisation (3-axis), with stress perpendicular to this (1-axis), as shown in figure 32, Hagood shows that for stress applied uniformly to the surface as shown, that the complex mechanical impedance of the slab along the 1-axis, Z_{11}^{ME}, is given by:

$$Z_{11}^{ME}(s) = Y(\omega)[1 + i\eta(\omega)] \qquad \textbf{Equation 5.1}$$

where $Y(\omega)$ is the shunted stiffness, and $\eta(\omega)$ is the electrical loss factor of the shunted piezoelectric material. These are given by:

$$Y(\omega) = Y^{D}[1 - \frac{k_{31}^{\ 2}}{(1+\rho^{2})}] \qquad \textbf{Equation 5.2}$$

and

$$\eta(\omega) = \frac{\rho k_{31}^{\ 2}}{(1 - k_{31}^{\ 2}) + \rho^2}$$

Equation 5.3

where Y^D is the open circuit stiffness of the material, and ρ is the non-dimensional frequency,

$$\rho = RC^S\omega$$

where R is the shunting resistance, C^S is the clamped capacitance of the piezoelectric material, and ω is the circular frequency.

The materials exhibit a maximum loss factor of

$$\eta_{\max} = \frac{k_{31}^{\ 2}}{2\sqrt{1 - k_{31}^{\ 2}}}$$

Equation 5.4

at a non-dimensional frequency of

$$\rho = \sqrt{1 - k_{31}^{\ 2}} \overset{\text{small } k_{31}}{\approx} 1$$

Equation 5.5.

To model a piezoelectric layer on a beam, the bending of the layer must be incorporated into the model. Using the Bernoulli-Euler model of beam bending, the bending can be modelled as causing longitudinal strain in the layer. If we assume the layer is thin compared to the beam, then we can assume that the strain is uniform throughout its cross section, and hence use Hagood's model described above. In practise, the strain is proportional to the distance from the neutral axis and will thus vary through the thickness causing a non-uniform electric field. For generator applications, the piezoelectric layers will often be of either thicker or of similar thickness to the supporting beam. The following section addresses this issue to determine the effect of this non-uniform strain.

5.3 Model of a Generally Shunted Piezoelectric Beam

5.3.1 Introduction

In this section, a model is developed for the complex bending stiffness of a resistively shunted piezoelectric beam of rectangular cross-section, of the type shown in figure 33. The polarisation axis is perpendicular to the neutral axis of the beam as it undergoes transverse oscillations. The piezoelectric beam is shunted by a load impedance via electrodes on the faces of the beam normal to the polarisation axis.

The piezoelectric layer is assumed to be bonded to another material, and to form part of a symmetrical structure as shown in figure 34. The symmetry implies that the neutral axis of the composite beam will remain at the centre of the structure regardless of the actual stiffness of the piezoelectric layer. The beam width, b, is assumed to be small.

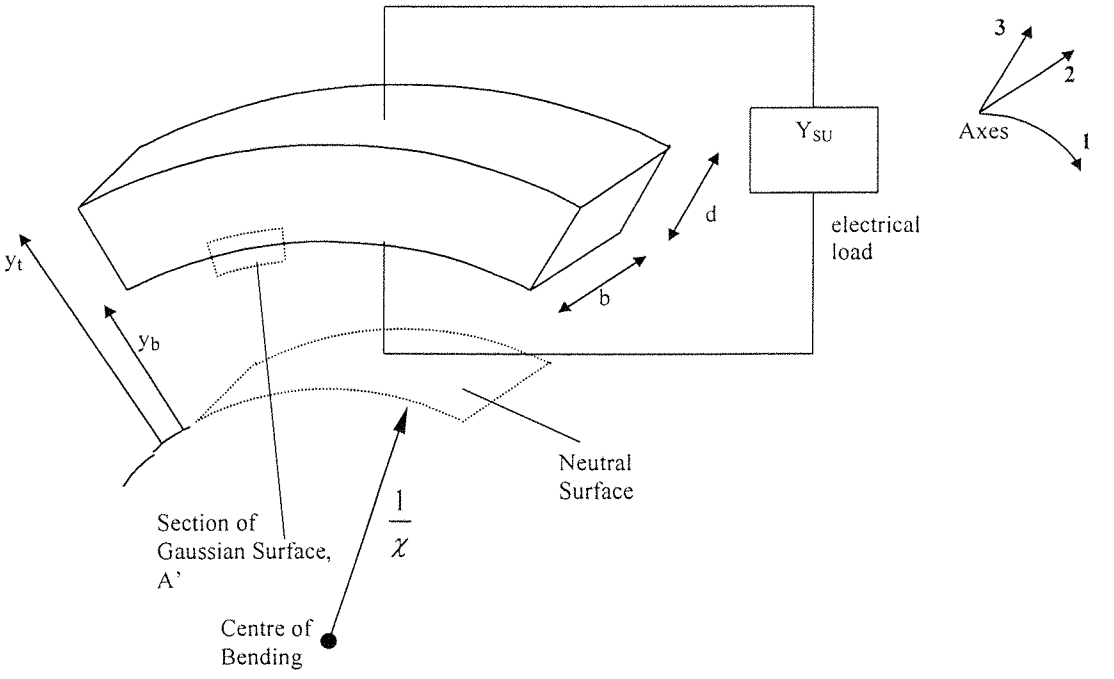

Figure 33: Diagram of Beam Undergoing Pure Bending.

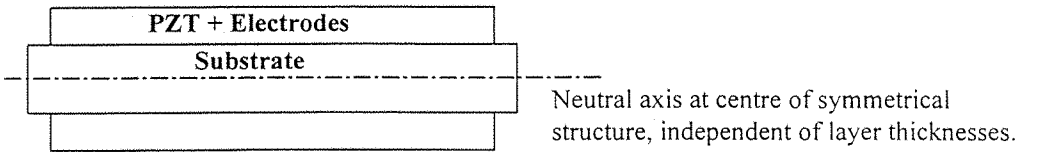

Figure 34: A Symmetrical Sandwich Structure.

5.3.2 Procedure

Starting with the basic equations of linear piezoelectricity, a piezoelectric beam undergoing pure bending is examined. Generalised expressions for the electrode voltage, and bending moment in terms of the radius of curvature and driving current are derived. These equations are similar in form to the basic piezoelectric equations, with the stress and strain terms replaced by bending moments and radius of curvature respectively, and the electric field and dielectric polarisation replaced by voltage and driving current.

This similarity is exploited, to produce a complex bending stiffness model of a resistively shunted piezoelectric beam, in a manner similar to that used by Hagood and von Flotow [45] for blocks of piezoelectric material undergoing plane stress.

5.3.3 Electrode Voltage

The constitutive equations for a unit of piezoelectric material can be formulated as:

$$\begin{bmatrix} \mathbf{P} \\ \mathbf{S} \end{bmatrix} = \begin{bmatrix} \eta^{T} & \mathbf{d} \\ \mathbf{d} & \mathbf{s}^{E} \end{bmatrix} \begin{bmatrix} \mathbf{E} \\ \mathbf{T} \end{bmatrix} \qquad \textbf{Equation 5.6}$$

where $\boldsymbol{E}$ is the vector of electrical field in the material (volts/metre), $\boldsymbol{S}$ is the vector of material engineering strains, $\boldsymbol{T}$ is the vector of material stresses (force/area), and $\boldsymbol{P}$ is the vector of electric polarisation (Coulombs/square metre). η^{T} is the diagonal matrix of clamped susceptibility, and d is a matrix of piezoelectric constants, as described in section 3.1.1.1.

Susceptibility is related to the dielectric constants [75] by:

$$\eta^T = \varepsilon_0 \cdot (\varepsilon_r^T - 1)$$ **Equation 5.7**

Assuming that the beam is unconstrained laterally (a thin beam), then

$T_2 = T_3 = 0$.

By symmetry,

$E_1 = E_2 = 0$.

Expanding equation 5.6 for the P_3 and S_1 components:

$$P_3 = \eta_3 E_3 + d_{31} T_1$$ **Equation 5.8**

$$S_1 = d_{31} E_3 + s_{11}^E T_1$$ **Equation 5.9**

Assuming Bernoulli-Euler bending, we can write [76]:

$$S_1 = \chi y = \frac{1}{\rho} y$$ **Equation 5.10**

where y is the perpendicular distance to the neutral axis (since the neutral axis runs along the 1,2 plane, this is the distance in the 3 direction), and $\rho = \frac{1}{\chi}$ is the radius of curvature of the neutral axis of the beam.

Substituting equation 5.10 into equation 5.9 we have

$$\chi y = d_{31} E_3 + s_{11}^E T_1$$ **Equation 5.11**

expressing this in terms of T_1, and substituting into equation 5.8:

$$P_3 = \eta_3 E_3 + \frac{d_{31}}{s_{11}^E} \cdot (\chi y - d_{31} E_3)$$ **Equation 5.12**

Applying Gauss' law to the surface A' in figure 33 (a box whose sides have unit area, with a top surface at a distance y from the centre of bending):

$$\varepsilon_0 E_3 = \rho_{free} + \rho_{bound} + \int_{y_b}^{y} \rho_{volume} dy$$ **Equation 5.13**

where y_t and y_b are the distances from the neutral surface to the top and bottom of PZT layer respectively, ρ_{free} is the area free charge density on the electrode, ρ_{bound} is the area bound charge density (the result of the dielectric polarisation) on the electrode, and is given by:

$$\rho_{bound} = -P_3(y_b),$$ **Equation 5.14**

ρ_{volume} is the volume charge density inside the dielectric, which is given [75] as:

$$\rho_{volume} = -\frac{dP_3}{dy}$$ **Equation 5.15**

Thus equation 5.13 can be written:

$$\varepsilon_0 E_3 = \rho_{free} - P_3(y)$$ **Equation 5.16**

Substituting equation 5.12 into equation 5.16, and using equation 5.7 to remove reference to η^T, we have

$$E_3 \cdot \left(\varepsilon_3{}^T - \frac{d_{31}^2}{s_{11}^E} \right) = \rho_{free} - \frac{d_{31}}{s_{11}^E} \chi y$$ **Equation 5.17**

Introducing the electromechanical coupling coefficient, given by Hagood and von Flotow [45] as

$$k_{31} = \frac{d_{31}}{\sqrt{s_{11}^E \cdot \varepsilon_3^T}}$$

and substituting this into equation 5.17 we have:

$$E_3 \cdot \varepsilon_3{}^T \cdot \left(1 - k_{31}^2\right) = \rho_{free} - \frac{d_{31}}{s_{11}^E} \chi y$$ **Equation 5.18**

Now the voltage at the top electrode with respect to the bottom electrode is given by:

$$V_{tb} = \int_{y_b}^{y_t} -E_3 dy$$ **Equation 5.19**

In evaluating this integral, the increase in the distance between the top and bottom electrodes, caused by the strain S_3 will be ignored (this assumption is also made by Hagood and von Flotow [45] in their equation 7a). This second order effect should not cause significant error, as the piezoelectric strain is of an order of less than 0.1%, which would be the extent of the error in the effective field.

Evaluating equation 5.19, and substituting the relation [45]:

$$\varepsilon_3^{S_1} = \varepsilon_3^T\left(1-k_{31}^2\right)$$

where $\varepsilon_3^{S_1}$ is the permittivity in the 3 direction, of a piezoelectric block clamped in the 1 direction, we have:

$$V_{th} = \frac{d_{31}\cdot d\cdot y_m}{s_{11}^E\cdot\varepsilon_3^{S_1}}\chi - \frac{d}{\varepsilon_3^{S_1}}\cdot\rho_{free} \qquad \textbf{Equation 5.20}$$

where $d = y_t - y_b$, the height of the piezoelectric layer, and $y_m = \frac{y_t + y_b}{2}$, the distance to the centre of the piezoelectric layer from the neutral surface.

5.3.4 Bending Moments

Defining M_2 as the moment required at the right-hand side of the beam to maintain the curvature, then

$$M_2 = b\int_{y_b}^{y_t} yT_1 dy \qquad \textbf{Equation 5.21}$$

where b is the width of the piezoelectric layer

Now, substituting equation 5.18 into equation 5.11 to eliminate E_3, we have:

$$T_1 = \frac{\chi y}{s_{11}^E}\left(1+\frac{d_{31}^2}{s_{11}^E\varepsilon_3{}^T\cdot\left(1-k_{31}^2\right)}\right) - \frac{d_{31}}{s_{11}^E\varepsilon_3{}^T\cdot\left(1-k_{31}^2\right)}\cdot\rho_{free} \qquad \textbf{Equation 5.22}$$

Substituting this into equation 5.21, and solving, we have:

$$M_2 = \frac{I_2}{s_{11}^E\left(1-k_{31}^2\right)}\chi - \frac{d_{31}\cdot b\cdot d\cdot y_m}{s_{11}^E\varepsilon_3^{S_1}}\cdot\rho_{free} \qquad \textbf{Equation 5.23}$$

where $I_2 = b\int_{y_b}^{y_t} y^2 dy$, the 2nd moment of area of the piezoelectric layer about the neutral axis.

5.3.5 Introducing an Electrical Load and Drive Current

Equation 5.20 can be combined with equation 5.23 to form the matrix equation:

$$\begin{bmatrix} V_{tb} \\ M_2 \end{bmatrix} = \begin{bmatrix} k_{11} & k_{12} \\ k_{21} & k_{22} \end{bmatrix} \begin{bmatrix} \rho_{free} \\ \chi \end{bmatrix}$$ **Equation 5.24**

where the coefficients k_{ij} are taken from equation 5.20 and equation 5.23.

Inverting the matrix, this can also be written:

$$\begin{bmatrix} \rho_{free} \\ \chi \end{bmatrix} = \begin{bmatrix} K_{11} & K_{12} \\ K_{21} & K_{22} \end{bmatrix} \begin{bmatrix} V_{tb} \\ M_2 \end{bmatrix}$$ **Equation 5.25**

where $[\mathbf{K}] = [\mathbf{k}]^{-1}$. If the piezoelectric layer is shunted, and a driving current I_i is applied as shown in figure 35, we can apply Kirchoff's current law to the top electrode node:

$$I_{SU} = A\frac{d\rho_{free}}{dt} + I_i$$ **Equation 5.26**

where I_{SU} is the current flowing from the top to the bottom electrode through the shunting admittance, Y_{SU}, and A is the area of the top electrode.

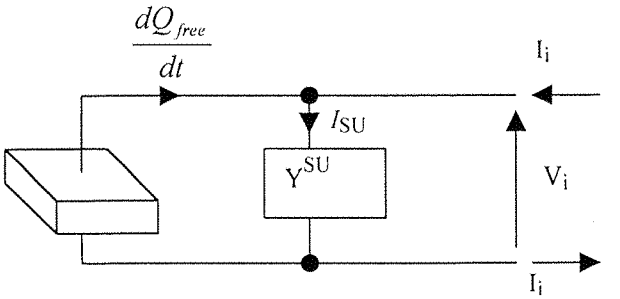

Figure 35: Current Flow for a Shunted PZT Element.

Applying $I_{SU}=YV_{SU}$, and entering the frequency domain (bold variables represent the Laplace transform):

$$\mathbf{I}_i = -sA\rho_{free} + Y_{SU}\mathbf{V}_{tb}$$ **Equation 5.27**

where s is the Laplace frequency variable. Substituting the top partition of equation 5.25 into equation 5.27, we have

$$\mathbf{I}_i = (-sAK_{11} + Y_{SU})\mathbf{V}_{tb} - sAK_{12}\mathbf{M}_2 \qquad \textbf{Equation 5.28}$$

Combining this with the bottom partition of equation 5.25, we can write

$$\begin{bmatrix} \mathbf{I}_i \\ \chi \end{bmatrix} = \begin{bmatrix} -sAK_{11} + Y_{SU} & -sAK_{12} \\ K_{21} & K_{22} \end{bmatrix} \begin{bmatrix} \mathbf{V}_{tb} \\ \mathbf{M}_2 \end{bmatrix} \qquad \textbf{Equation 5.29}$$

This is a governing equation for a shunted piezoelectric beam, with arbitrary shunting impedance, driving current, and mechanical boundary conditions.

5.3.6 Resistive Shunting

Taking the top partition of equation 5.29, and setting the driving current to zero:

$$\mathbf{V}_{tb} = \frac{-sAK_{12}}{sAK_{11} - Y_{SU}}\mathbf{M}_2 \qquad \textbf{Equation 5.30}$$

Taking the bottom partition of equation 5.29 and substituting equation 5.30 to eliminate V_{tb}:

$$\chi = \left[K_{22} - K_{21}\frac{sAK_{12}}{sAK_{11} - Y_{SU}} \right]\mathbf{M}_2 \qquad \textbf{Equation 5.31}$$

This gives the mechanical response of a resistively shunted piezoelectric layer. All electrical terms have been eliminated. It is analogous to the Bernoulli-Euler law of elementary bending [76]:

$$\chi = \frac{1}{\rho} = \frac{1}{YI}M \qquad \textbf{Equation 5.32}$$

where Y is the young's modulus of the beam. In our case, the bending stiffness has been modified by the piezoelectric coupling, and the resistive shunt, has introduced a complex component to the stiffness.

Equation 5.31 can be written as

$$\chi = \frac{1}{(YI)_{complex}}\mathbf{M}_2$$ **Equation 5.33**

where

$$(YI)_{complex} = \frac{1}{K_{22} - K_{21}\dfrac{sAK_{12}}{sAK_{11} - Y_{SU}}}$$ **Equation 5.34**

Expressing $(YI)_{complex}$ as:

$$(YI)_{complex} = (YI)_b\left(1 + j\eta_b\right)$$

then inverting the matrix k, and substituting the resulting values for K into equation 5.34, we have:

$$(YI)_b = \frac{I_2}{\left(1 - k_{31}{}^2\right)s^E} - \frac{Y_{SU}{}^2 \cdot d^3 \cdot y_m{}^2 \cdot b \cdot k_{31}{}^2}{\left(Y_{SU}{}^2 \cdot d^2 + \omega^2 \cdot A^2 \cdot \varepsilon_3^{S_1}{}^2\right)s^E}$$ **Equation 5.35**

$$\eta_b = \frac{\omega \cdot A \cdot \varepsilon_3^{S_1} \cdot Y_{SU} \cdot d^2 \cdot y_m{}^2 \cdot b \cdot k_{31}{}^2 \cdot \left(1 - k_{31}{}^2\right)}{I_2\left(Y_{SU}{}^2 \cdot d^2 + \omega^2 \cdot A^2 \cdot (\varepsilon_3^{S_1})^2\right) - Y_{SU}{}^2 \cdot d^3 \cdot y_m{}^2 \cdot b \cdot k_{31}{}^2 \cdot \left(1 - k_{31}{}^2\right)}$$ **Equation 5.36**

Where ω is the circular frequency. Introducing the load resistance,

$$R_{SU} = \frac{1}{Y_{SU}}$$

and the capacitance of the piezoelectric layer clamped in the 1 direction,

$$C^{S_1} = \frac{\varepsilon_3^{S_1} A}{d}$$

and the ratio of the layer thickness to the distance from the neutral axis to the centre of the layer,

$$\alpha = \frac{d}{y_m}$$

and expanding I_2 as

$$I_2 = b \cdot d\left({y_m}^2 + \frac{1}{12} d^2 \right)$$

we can write:

$$\eta_h = \frac{\omega \cdot C^{S_1} \cdot R \cdot {k_{31}}^2 \cdot \left(1 - {k_{31}}^2\right)}{\left(1 + \frac{\alpha^2}{12}\right)\left(1 + \omega^2 \cdot C^{S_1 2} \cdot R^2\right) - {k_{31}}^2 \cdot \left(1 - {k_{31}}^2\right)}$$

Equation 5.37

This takes a maximum value of

$$\eta_{\max} = \sqrt{\frac{K^2}{4B(B-K)}}$$

Equation 5.38

where

$$B = 1 + \frac{\alpha^2}{12} \quad \text{and} \quad K = {k_{31}}^2 \cdot \left(1 - {k_{31}}^2\right)$$

This maximum occurs at a frequency of,

$$\omega \cdot C^{S_1} \cdot R = \sqrt{\frac{B-K}{B}}$$

Equation 5.39

5.3.7 Implications of the Beam Model

Figure 36 shows a graph of the ratio $\frac{\eta_{\max}}{\eta_{\max}|_{\alpha=0}}$ for several values of k_{31}. The condition α=0 corresponds to a piezoelectric layer that is thin in comparison to the substrate it is mounted on. (And is thus analogous to the model developed by Hagood, discussed in section 5.2). The figure shows that Hagood's assumption of uniform stress is accurate to 5 percent for values of α of up to around 0.8. The decline in loss factor with α is relatively independent of the electromechanical coupling coefficient. The graph is plotted for values of α between zero, and two. This range covers piezoelectric layers of negligible thickness, and extends up to layers whose neutral axis is the bottom surface of the material (e.g. a beam composed of two piezoelectric layers, sandwiching a thin electrode)

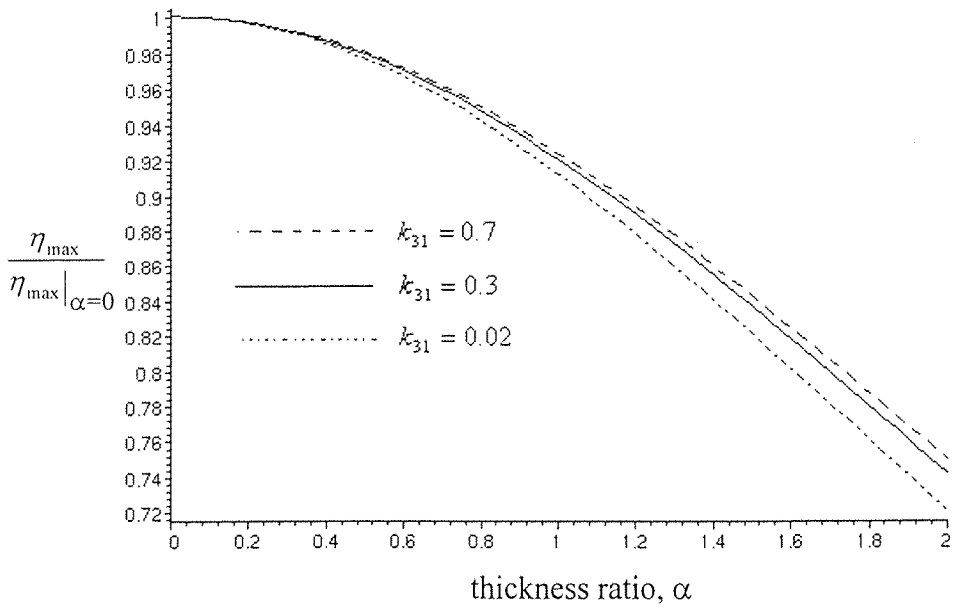

Figure 36: Graph of Normalised Damping Ratio versus Layer Thickness Ratio, and K-factor

To compare the model derived here with Hagood's, we implement Hagood's assumption of uniform stress by setting α=0. Using the relation (Hagood's equation 29)

$$C^{S_1} = C^T\left(1 - k_{31}^2\right)$$

and substituting this into equation 5.37 we have

$$\eta_h = \frac{\omega \cdot C^{S_1} \cdot R \cdot k_{31}^{\ 2}}{\frac{1-k_{31}^{\ 2}\cdot\left(1-k_{31}^{\ 2}\right)}{k_{31}^{\ 2}\cdot\left(1-k_{31}^{\ 2}\right)} + \omega^2 \cdot C^{T_1\,2} \cdot R^2}$$

Equation 5.40

This is similar to the result derived by Hagood, although his model gives the result for a different set of boundary conditions.

The prototype generator developed in chapter 4 has a value for α of 0.583. This model predicts that this will result in a damping ratio that is 3 percent lower than that predicted by Hagood's theory. This value will be used in the following analyses.

5.4 Harmonic Response of a Piezoelectric Generator

By representing the piezoelectric layer mechanically as having a complex stiffness, as described above, conventional mechanical models can be used to predict the mechanical response of a composite piezoelectric-steel beam, of the type described in section 4.3. Once this response has been determined, damping theory can be used to determine the electrical power produced.

For rectangular beams, Bernoulli-Euler approximations can be used in conjunction with Rayleigh-Ritz methods to predict the amplitude of vibration, and resulting stresses in a piezo-generator. The beams described in section 4.3, however, are of a tapered nature, and show significant edge effects. The shape causes a concentration of stress near the centre of the beam, away from the lateral edges (See figure 40, Section 5.5). Further edge effects are introduced by the thickness of the piezo-electric layer, which is not clamped at its root. Including these effects in this model is not straightforward, and the resulting mode shapes will not yield solutions that are easy to grasp intuitively (a motivation for using this method).

Comparing the results obtained by this method to the Finite Element Analysis described below, for the test device described, this method is found to give a natural frequency that is around 6% higher than the FEA result. Thus, finite element analysis is judged to give more reliable results.

A third option is described by Hagood *et al* [77]. In this model, the dynamic piezoelectric coupling between a structure and an electrical network is predicted. The governing equations are derived, and discretised with assumed elastic and electrical field shapes in a Rayleigh-Ritz formulation. This model is well suited to the problem of piezoelectric generators described here, however, the simpler models described above offer sufficient accuracy, and are simpler as they reflect the quasi-static nature of the piezoelectric coupling in the generators.

5.4.1 Finite Element Analysis (FEA)

To determine the mechanical response of a piezo-generator to being shaken, and the proportion of the strain energy stored within the piezoelectric layer, the finite element package ANSYS(R) was used. Finite element analysis has an advantage over analytical methods based on Bernoulli-Euler approximations (see above), as it takes account of edge effects, and the shear lag caused by thin layers such as the electrodes, and the dielectric insulator.

Modelling piezo-generators is complicated by the small thickness of the individual layers in comparison to the overall lateral dimensions of the devices. For an accurate analysis, the elements used in a model must not typically be more than around 20 times longer than they are thick [78]. This means that many elements are required when simulating thin layers, which causes long computation times for the models. To reduce the number of elements, a composite element type SOLID46 is used which represents a number of laminated layers in a single element. This element type is used to model the combination of the substrate and dielectric layers on either side of the substrate. A planar mesh was also initially considered to reduce the computation time, however this does not allow for the edge effects described in section 5.5.

Figure 37 shows the mesh of finite elements employed for calculating the amplitude of vibration of the beam, and the amount of strain energy stored within the piezoelectric layer. The program listing used to generate the mesh, is listed in appendix B. The symmetry of the model about its central axis was exploited, so that only half of the structure was modelled, reducing computation time. Three different types of material are defined for the beam: substrate only, substrate covered with a dielectric film, and piezoelectric material. The top electrode is not modelled, as it is assumed that the compliant polymer material has a small effect on the stiffer ceramic layers that it is printed upon. The effect of the bottom electrode is included by increasing the thickness of the piezoelectric layer by the thickness of the bottom electrode. Since the bottom electrode is of similar stiffness to the piezoelectric layer, this will not affect the overall stiffness of the beam, however, it will overestimate the energy available from the piezoelectric layer. For the cases considered here, where the bottom electrode is thin in comparison to the piezoelectric layer, this should not introduce significant errors. The substrate nodes are constrained in all directions at the root of the beam to model the beam clamping. The nodes along central axis are constrained in the Y-direction to model the missing half of the mesh. The mass is modelled by stiff but light elements, connected to a short line of dense elements placed at the centre of mass of the mass. It should be noted that this ignores any rotational inertia of the mass, however, when the model is compared to experimental results the model is seen to be sufficiently accurate.

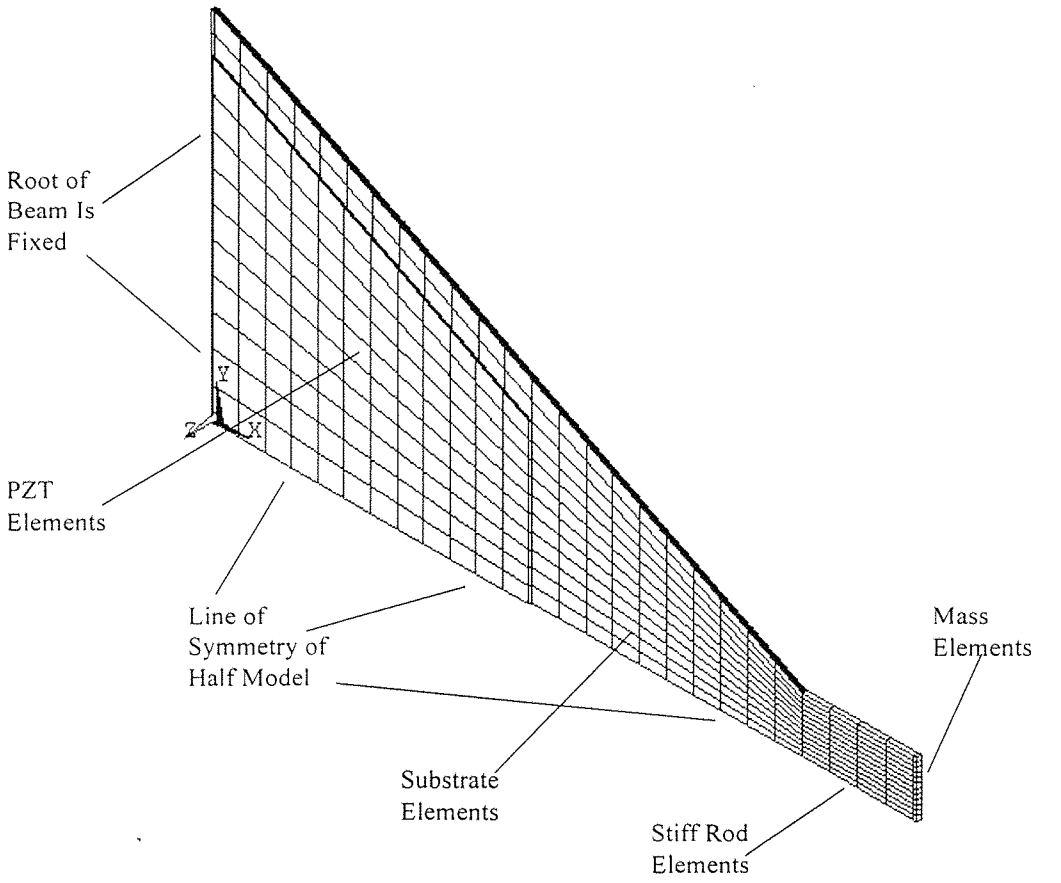

Figure 37: Finite Element Mesh Model of Tapered Generator.

Material parameters for the thick-film layers and some of those for steel were set using results from the experiments described in section 4.4. The stiffness, and damping of the piezoelectric layer are calculated from the complex stiffness model presented in section 5.2. Appendix B contains a full list of the parameters used to produce the results shown in section 5.5.

To determine the natural frequency of the beam, a modal analysis is performed using the commands listed in appendix B. Since the stiffness of the piezoelectric element is determined by the frequency at which it operates, it may be necessary to iteratively repeat this process, changing the stiffness according to equation 5.3. In most cases this is not necessary however, as an initial estimate of the frequency will provide a sufficiently accurate value for the complex stiffness of the layer. The natural frequency of the real structure is simple to measure. By comparing the real natural frequency to the predicted value, the finite element model can be verified, and the accuracy of the mechanical parameters fed into the model can also be assessed. To ensure that the element sizes are small enough, smaller elements are applied and the results checked to ensure that no change occurs. Once the natural frequency has been found, the amplitude of beam

vibration can be determined using an harmonic analysis. The analysis is performed using the commands listed in appendix B.

To find the energy produced at a particular amplitude of vibration, it is necessary to determine the amount of strain energy stored in the structure when the beam is at the point in is vibration cycle of maximum deflection. This is done using a static analysis. The beam tip is held at a deflection, equivalent to the vibration amplitude, and the energy stored within the different layers is calculated. This makes the approximation that the mode shape of the vibration at the resonant frequency is identical to this static shape. This is reasonable since we are only working around the natural frequency of the beam and most of the mass is concentrated at the tip of the beam. This approximation has been tested by comparing the two shapes; the maximum error in the displacement of any node is found to be only 0.3% of the tip deflection. The analysis is set up, and the results derived as detailed in appendix B.

5.4.2 The Electrical Energy Available to a Resistive Load

Damping theory can be applied to find how much of the strain energy stored within the piezoelectric layer is released as electrical energy. Treating the shunted piezoelectric material as a material with a complex stiffness, as described in section 5.2, the electrical power dissipated in the load, P, is given [52] by:

$$P = 2\pi f \, \eta(f) U_m \qquad \textbf{Equation 5.41}$$

where $\eta(f)$ is the frequency dependant loss factor of the shunted piezoelectric material, and U_m the peak strain energy stored within the piezoelectric material, and f, the frequency of vibration.

The energy dissipated electrically is a combination of the energy dissipated in both the shunting resistance, and the series resistance of the electrodes. However, the series resistance of the electrodes is of an order of a few ohms, much smaller than the tens or hundreds of kilo-ohms of the shunting resistance, and can be ignored here.

5.5 Analysis of a Piezoelectric Generator Beam

Figure 38 shows the sequence of calculations used to find the energy available from a piezo-generator.

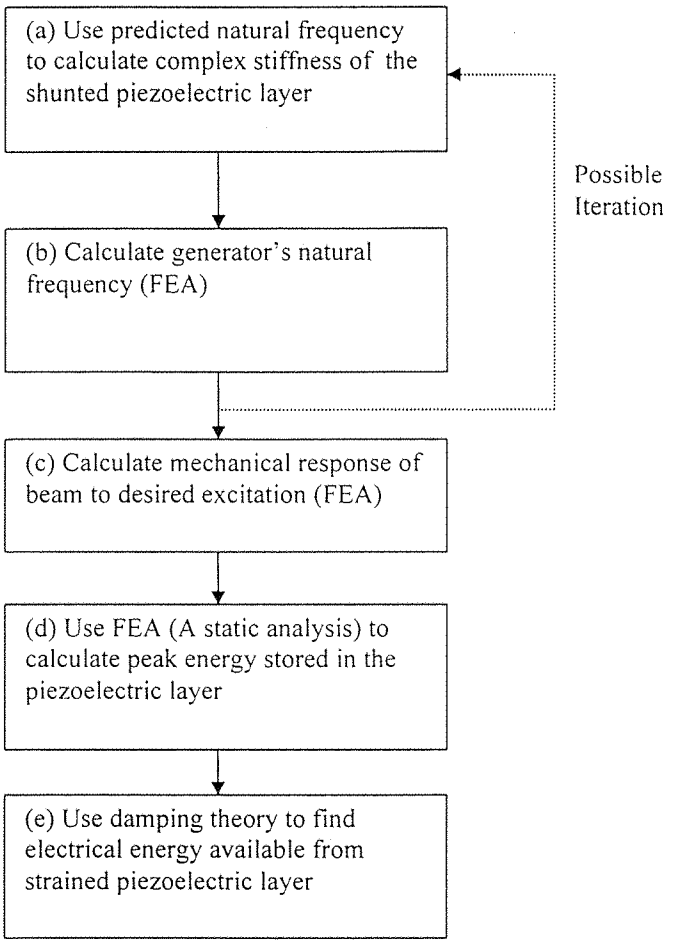

Figure 38: Sequence of Calculations for Calculating the Power from a Piezo-Generator

The calculations are applied below to the generator described in section 4.3, each stage identified by the letter used in the flow chart. Appendix B contains programs suitable for use with ANSYS$^{(R)}$,for the steps requiring finite element analysis.

(a) To calculate the mechanical properties of the shunted piezoelectric layer, the natural frequency, measured experimentally, is substituted into equation 5.35 and equation 5.37. Assuming f_n=95Hz and k_{31} = 0.029, and E_{PZT} = 15GPa, then for an optimally resistively shunted element of PZT, the stiffness, E_{PZT} = 15GPa (The low electromechanical coupling of thick-film PZT means that the stiffness of the shunted material is within 0.1% of the un-shunted material), and the electrical loss factor, η_E= 4.0x10^{-4}.

(b) To calculate the natural frequency of the beam (required for an harmonic analysis), a modal analysis is performed. The mechanical parameters shown in the program, are taken from the experiments discussed in section 4.4. For the parameters used here, the results shown in table 8 are produced.

Table 8: Bending modes of Test Beam

Longitudinal Bending mode	Frequency (Hz)
1	94.6
2	1048
3	3277

The predicted natural frequency is within 1% of the value measured experimentally (95.5Hz). This supports the values entered as mechanical parameters, and is close to the value used in part (a), so there no need to re-iterate this step with a new complex stiffness for the PZT. It is also interesting to note that the first torsional bending mode occurs at 5.7kHz, so it should not significantly influence calculations for devices operating around the frequency of the first bending mode. It should be noted that the natural frequency is very sensitive to geometrical parameters, and that even small errors in measuring parameters such as beam length can cause larger errors in natural frequency. (For example, reducing the length of the beam described here by 0.5mm causes the natural frequency to change to 98.1Hz).

(c) To produce values to compare with the experiments described in section 4.5, this step (calculating the response of the beam to a given excitation) is not needed, as the experiments measured the deflection of the tip of the beam.

(d) A static analysis is performed, applying a deflection of 0.8mm at the beam tip. Figure 39 shows a longitudinal stress plot of the bent beam. The graph is plotted along a cross section that passes through the row of PZT elements that are both above the central axis of the beam, and in the outer layer of PZT elements (i.e. the graph shows the stress along the surface of the PZT layer, at the centre of the beam). The graph shows a reasonably constant level of stress; this shows that the design objective of maintaining a reasonably even level of stress along the length of the beam (achieved by use of the tapered shape, see section 4.3.1) has been met. Figure 40 shows a longitudinal stress plot along the surface of the PZT layer at the beam root, running from the centre of the beam to a lateral edge. The variation in stress across the beam is not ideal, and is a result of the tapering. The design is still superior to a rectangular beam for producing an even stress distribution, since the stresses in a rectangular beam would reach zero at the beam tip. The energy stored in both the PZT layers at this deflection is returned by ANSYS as E_{PZT}=13.4μJ, compared to 40μJ stored in the rest of the structure.

(e) To calculate the power dissipated into the load resistor, equation 5.41 is applied. The power available in the optimally damped layer is calculated as P_{load}=1.47μW. This is within 2% of the value obtained experimentally. Given the inaccuracies in the mechanical and electrical parameters used in the modelling (see section 4.4) this is a reasonable prediction.

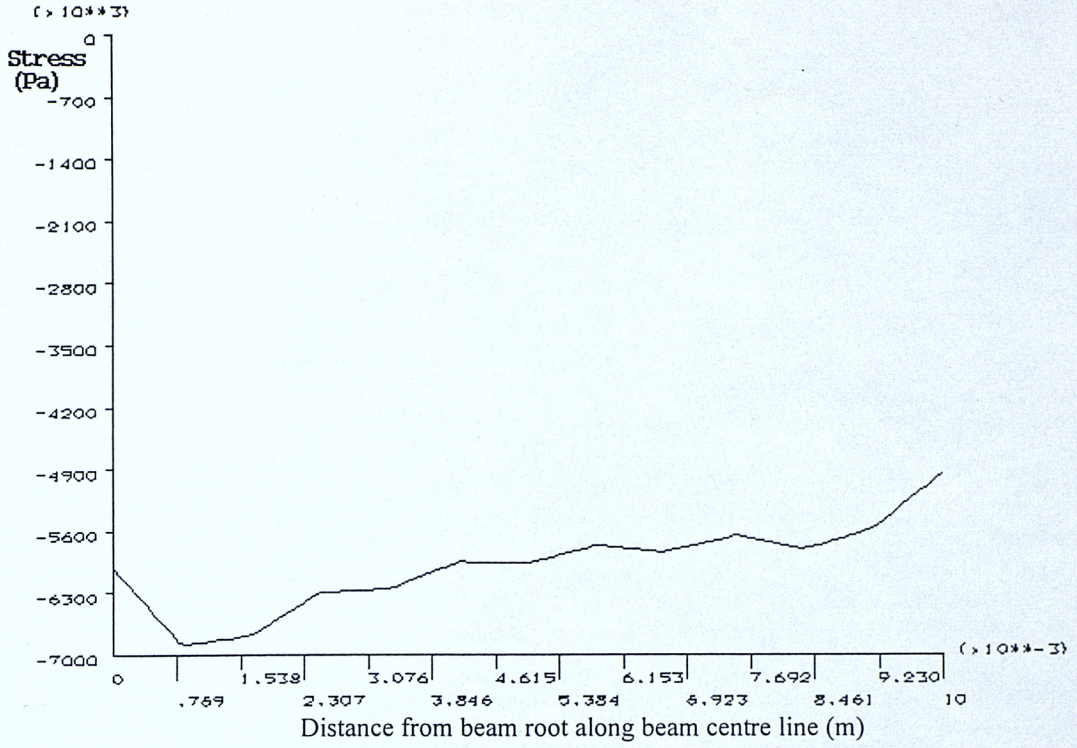

Figure 39: Longitudinal Stress Across the Surface of the PZT Layer, Along Beam Axis (Deflection = 0.8mm).

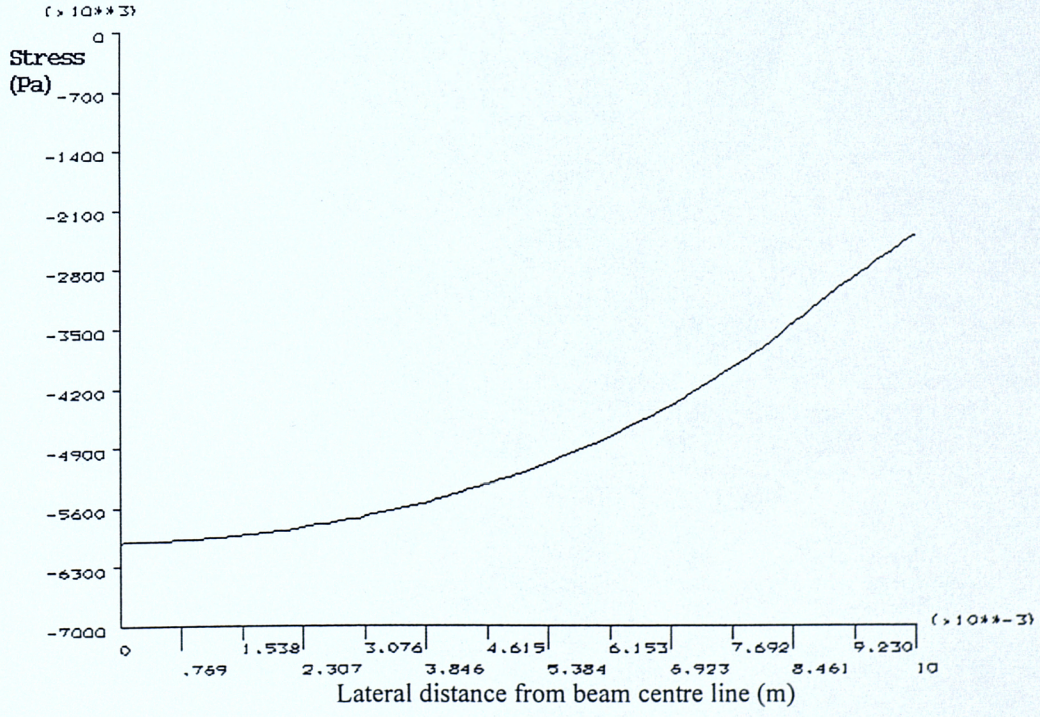

Figure 40: Longitudinal Stress Across the Surface of the PZT Layer, Along Beam Root (Deflection = 0.8mm).

The process described above is repeated for a range of deflections and load resistances to provide the results shown in figure 41, which compares the modelling process to the experimental results described in section 4.5. To find the effect of errors in the modelling parameters on the final result, the parameters were individually varied to determine their influence on the result. Summing these, the errors discussed in section 4.4 give rise to around 10 percent error in the predicted power output. The measurement errors in the experimental data are less significant (of order 3%) and have been omitted from the graph for clarity. The modelling assumes a linear system; The experiments show this to be a reasonable assumption, as demonstrated in figure 42, a graph of load voltage against beam amplitude under conditions of optimal damping. The graph is linear to a first approximation, but does grow steeper at higher deflections (possibly caused by non-linear piezo-electric effects or the non-linear nature of strain with large deflections of a cantilever). The effect of this non-linearity is seen in figure 41, where as the amplitude increases the predictions tend to underestimate the power developed in the load resistor.

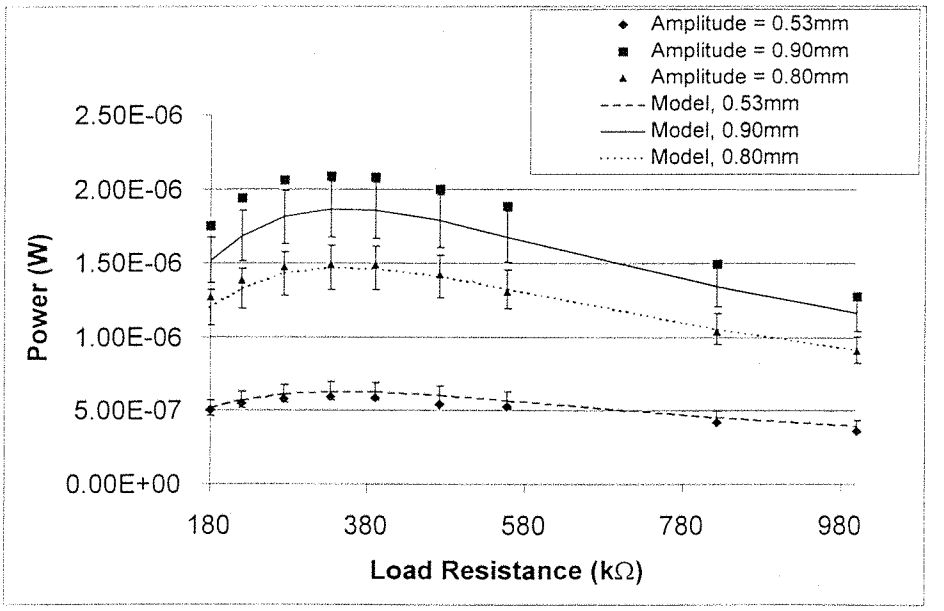

Figure 41: Experimental and Predicted Values for Generator Power Output (error bars show potential error in model).

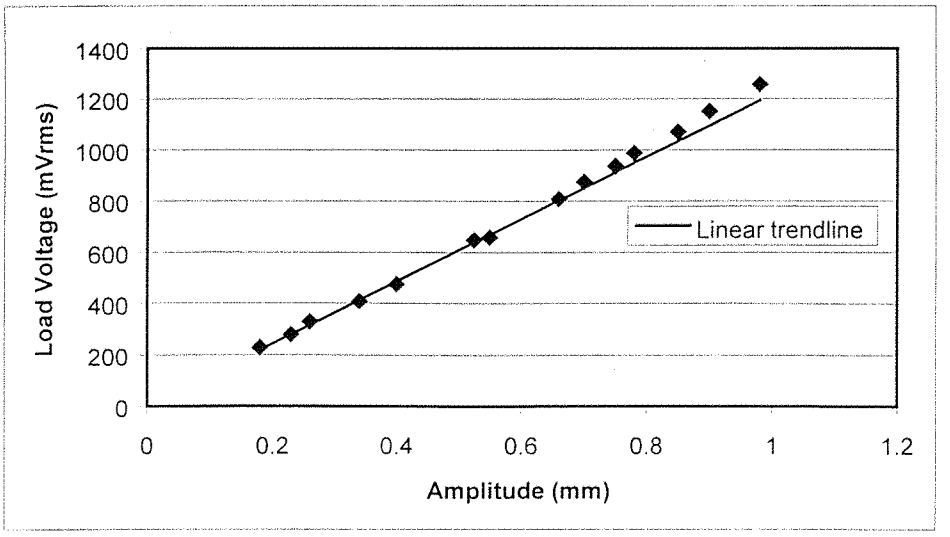

Figure 42: The Relationship Between Beam Amplitude, and Load Voltage.

5.6 Design Considerations for Piezoelectric Generators

Some of the implications of the modelling work described above on the design of thick-film piezoelectric generators can now be explored.

It can be seen from figure 31 that the geometry of the device determines what proportion of the elastic energy stored within the beam is held in the piezoelectric material. Only the energy held in the piezoelectric material can be converted into an electrical form. For the prototype beam generator, this proportion is determined by the relative thicknesses of the substrate and piezoelectric layers. The ratio of energy stored in the piezoelectric layer to total energy in the beam is shown in appendix C to be

$$\frac{E_{piezo}}{E_{total}} \approx 1 - \left(\frac{y_b}{y_t}\right)^3$$ **Equation 5.42**

where y_t and y_b are the distances from the neutral surface to the top and bottom of PZT layer respectively. The derivation assumes that the Young's modulus of the piezoelectric material and the substrate are the same (see appendix B for exact values). Thus by making the substrate thinner, more of the energy is stored in the piezoelectric material.

It has been shown in section 5.3 that the damping that can be applied by a piezoelectric layer decreases as the layer thickness becomes a significant proportion of the total beam thickness. To maintain a higher level of damping in beams with a thick PZT layer, a laminated structure could

be adopted. By interleaving electrodes into the structure, the thickness of each layer will be small in comparison to the total thickness. The optimum number of layers in such a laminated structure will depend on the technology used to produce them, since the electrodes will use up space that could be occupied by piezoelectric material. (In thick-film technology, electrode layers can be as thin as 10μm.)

The shape of the beam also has an effect on the electromechanical coupling. The prototype devices are tapered, to produce a longitudinal stress that doesn't vary along the length of the beam. If a beam of a rectangular shape (rectangular in plan view) were constructed with a single top electrode, then the stress would be greater at the root of the beam than at the tip. This uneven stress distribution would have a similar effect to the case described in section 5.3, where an uneven stress distribution exists through the thickness of the material; the resulting electromechanical damping would be lower than that expected if the same amount of strain energy were distributed evenly through a similar piece of material.

5.7 Theoretical Limits for inertial generators

Any real generator application will have a complex set of constraints governing its design, including required output characteristics, geometrical constraints, material properties, manufacturing considerations, cost and the excitation environment. To predict the maximum amount of power that can be produced under any particular set of constraints would involve a detailed analysis specific to that application, and may not even be possible. By making certain simplifications and assumptions, however, it is possible to place bounds on the amount of power that can be produced.

A piezoelectric generator of the form shown in figure 43 will now be considered. The figure shows a mass (mass, m; height h), and spring beam (length, l; thickness, t) mounted within an enclosure (box) of fixed dimensions (length, L; height, H; width, W). For simplicity, the clearance, g, required at the end of the box to prevent the corners of the mass touching the end wall will be assumed to be small enough to be ignored in the following analyses. As a further approximation, it will also be assumed that the centre of mass of the mass will move by a distance $0.5(H-h)$ when the mass is displaced to its maximum extent (while in reality, the corner of the mass will strike the enclosure before this displacement is reached). This design is not an optimal one; The mass could be shaped to take up more space, without reducing the available beam deflection. Predictions made with the design of figure 43, however, will yield insights that are easier to grasp, and will provide reasonable approximations to the performance of a more optimal generator.

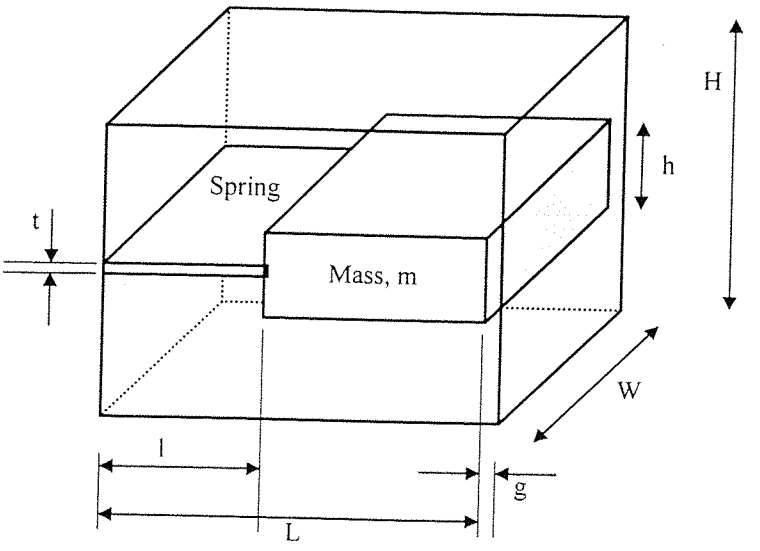

Figure 43: Simplified Inertial Generator.

For a given beam length, and mass size, the spring constant, k, is determined by the required resonant frequency of the system, and is given by

$$k = m\omega_n^{\,2}$$ **Equation 5.43**

where m is the mass of the mass, and ω_n the circular natural frequency (the mass of the beam is ignored). The mass can be calculated as

$$m = \rho(L-l)hW$$ **Equation 5.44**

where ρ is the density of the mass material. The strain energy, U, stored in the beam at maximum deflection, A, is given by

$$U = \frac{1}{2}kA^2$$ **Equation 5.45**

The useful electrical power that can be extracted by from the system can be calculated from equation 5.41.

$$P = \omega_n \eta_E U = \frac{1}{2}\omega_n^{\,3}\eta_E \rho \cdot W(L-l)h \cdot A^2$$ **Equation 5.46**

where η_E is the loss factor (also called the structural damping factor) associated with energy being extracted from the system in some manner. For piezoelectric materials, this can be obtained from equation 5.3. For low levels of damping, the amplitude, A, is approximately given by

$$A = \frac{\alpha}{\eta_E + \eta_L}$$ **Equation 5.47**

where η_L is the loss factor due to unwanted damping, and α is the amplitude of base excitation.

Using the relation

$$k = \frac{3YI}{l^3}$$ **Equation 5.48**

where Y is the Young's modulus of the beam, and I, the second moment of area of the beam, is given by

$$I = \frac{1}{12} W t^3$$ **Equation 5.49**

We can substitute this into equation 5.43 to write the thickness of the beam as

$$t = \sqrt[3]{\frac{4\omega^2 \rho h l^3 (L-l)}{Y}}$$ **Equation 5.50**

The stress in the beam must not exceed the maximum rated stress, T_{max}, for the material. The stress in the outer fibres at the root of the beam, T_{root}, is given by

$$T_{root} = \frac{M \cdot c}{I} = \frac{k \cdot A \cdot l \cdot t}{2I} = \frac{3Y \cdot t}{2l^2} A$$ **Equation 5.51**

where M is the bending moment at the root of the beam, and c the distance of the outer surface of the beam from the neutral axis. Thus, to prevent beam damage

$$\frac{3Yt}{2l^2} A < T_{\max}$$ **Equation 5.52**

The effect of the bending radius upon the effective loss factor caused by non-uniform stress distributions, as discussed in section 5.3, will be ignored here, as it is assumed that a laminated structure with many electrodes could be produced if this effect caused significant departures from

ideal behaviour. The degree of damping applied by a piezoelectric material can be controlled by varying the electrical load attached to the material, up to a maximum value as described in section 5.2.

Using the above equations, we are in a position to find the optimum internal dimensions for a generator of arbitrary size and base excitation. The problem is to find the optimum values for l, h, and η_E, for a fixed set of input parameters (W, H, L, ρ, T_{max}, Y, ω, η_L, α). Figure 44 illustrates how difficult this is to perform analytically, by showing a cross-section through part of a typical problem space. It shows how the maximum energy stored in the beam, U, varies with the length of the beam, and the height of the mass for a particular set of parameters (H=1cm, L=1cm, ρ=8000kgm^{-3}, f_n=100Hz, Y=75GPa, T_{max}=40MPa, base excitation sufficient to cause beam to fill all available space). The points where the stress in the beam exceeds the maximum rated stress for the material have been omitted, and plotted white. The figure shows that for this particular configuration U is at a maximum when the length of the beam, l, is 8.0mm and the height of the mass, h, is 6.1mm (at which point the stress in the root of the beam is at its maximum rated value).

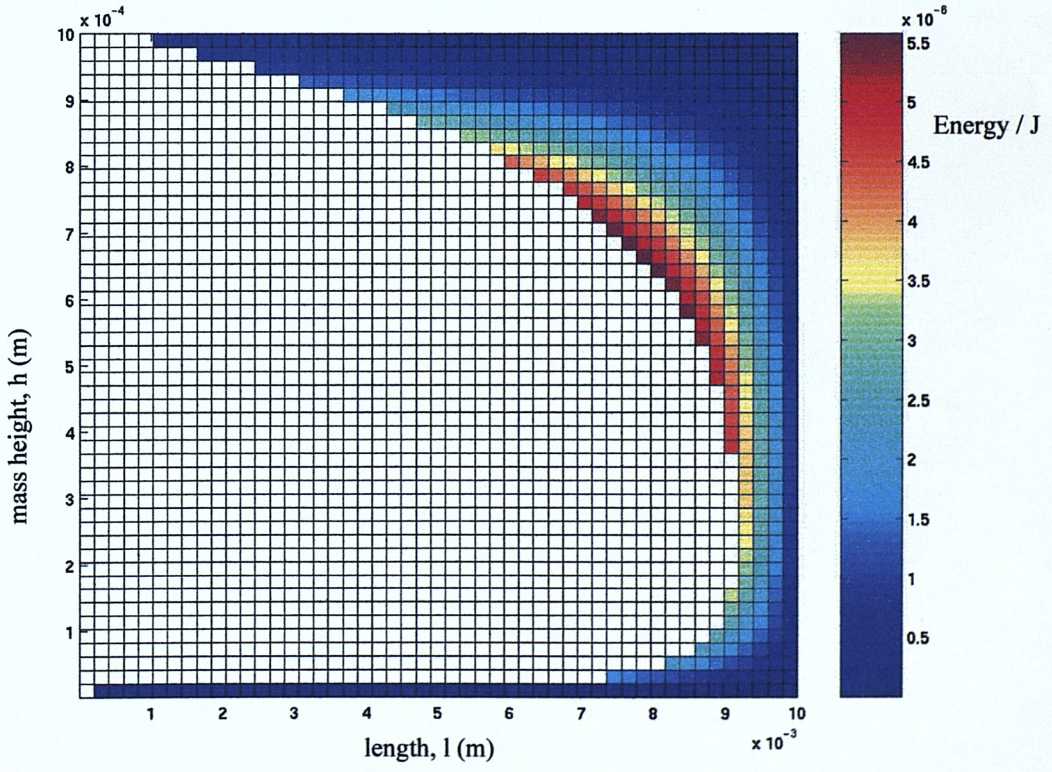

Figure 44: Strain energy of a generator beam versus internal dimensions.

Adding in the extra dimension of a lower base excitation (with the associated problem of optimising η_E), it becomes necessary to resort to a numerical approach to locate the maximum power. The Matlab® environment has been used to numerically find the maximum using the *fmins()* function which performs a non-linear unconstrained search for the maximum. The code for this program is listed in appendix D. Note the code has been written in such a way that if the beam amplitude exceeds the available space then extra unwanted damping is applied to constrain it to this volume. Energy is wasted in this manner, but in such cases the optimisation will move the search towards higher electrical damping (although if the technology can only apply a finite amount of damping then for applications with high base excitation the optimum generator may include extra unwanted damping).

An upper bound for the amount of power that can be generated from a resonant inertial generator of any type can be formed by ignoring the strain energy constraint described by equation 5.52, and setting the spring length to zero. In this ideal generator, the spring is arbitrarily small, and the transduction mechanism (which could be of any type) used to extract the energy from the system takes no space. The code to perform this search is also listed in appendix D.

An initial exploration of the parameter space shows the trend observed in figure 45. The plot shows how the maximum energy density, U_{den}, of a generator with arbitrarily large excitation varies with the length, L, and half height, H, of the enclosing box. (i.e. U_{den}, is the maximum value of U, found at optimum beam length, l, and mass height, h, divided by the volume of the generator). The energy density is independent of the width of the enclosing box. The plot is calculated for a resonant frequency of 100Hz, and material properties of PZT-8 [44] (Y_{PZT}=75Gpa; T_{max}=40MPa, half rated value at 25°C). The graph shows that the energy density increases with increasing enclosure length, and that there is an optimum enclosure height, that tends to increase with enclosure length. The existence of this optimum value is a result of the balance between the quadratic energy-displacement relationship of the spring, and the finite rated stress of the piezoelectric material. This trend has also been confirmed at other typical resonant frequencies, and with other material parameters. It follows from this observation, that for a given generator volume, with a height larger than the optimum value for energy density, the amount of power that can be generated can be increased by splitting the volume into several generators of more optimum height, as shown in figure 46b.

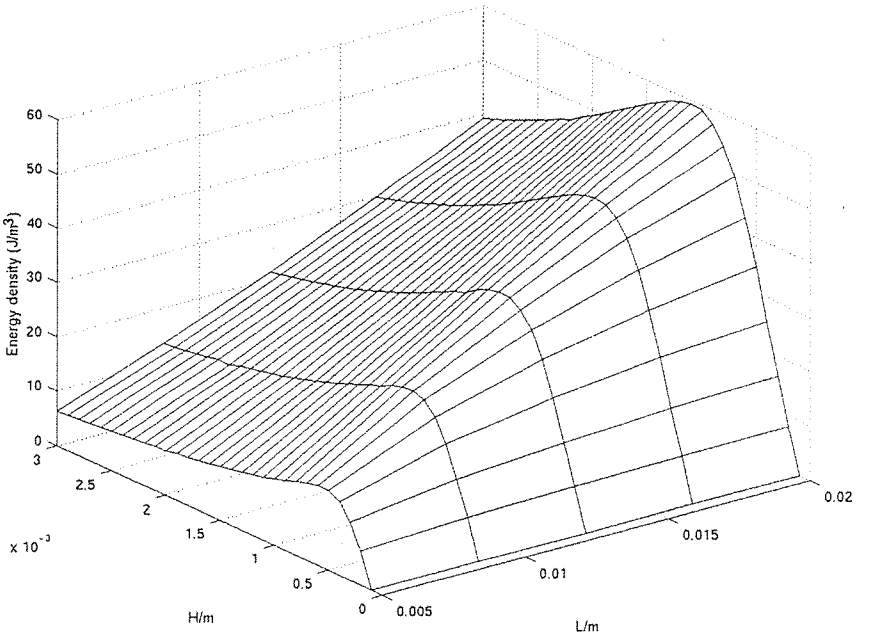

Figure 45: Energy Density for Generator of Optimal Dimensions Versus Enclosure Size.

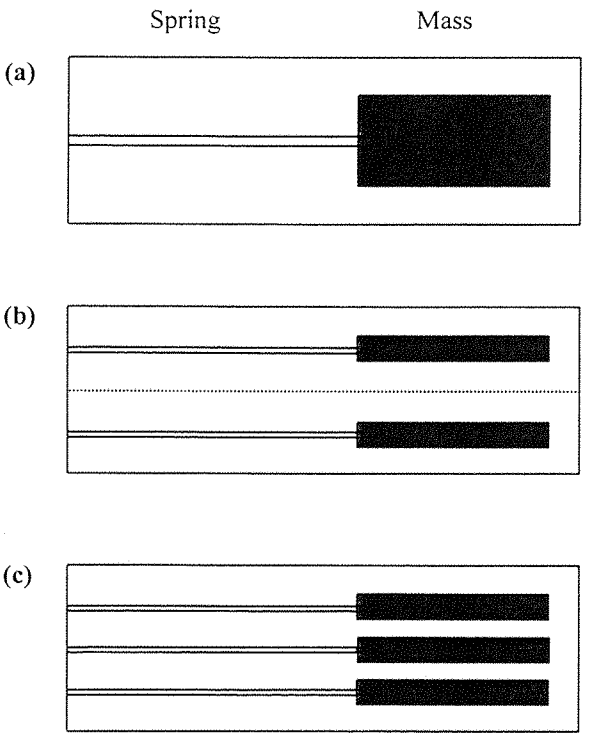

Figure 46: Splitting a Generator into Partitions to Increase Energy Density.

To take account of this multi-beam possibility the code listed in appendix B optimises for power density, then returns the power that would be produced by a multi-beam generator by multiplying this power density by the available volume. In practice, the beams could be moved closer together as shown in figure 46c, taking advantage of that fact that all the beams will move together (although some clearance would still be necessary, to allow for the rotation of the masses as the beam deflects). Laminated piezoelectric elements may be required to maintain ideal behaviour due to the varying stress through the beam thickness (see section 5.3). The multi-beam configuration described here would require thinner laminations than a design with only a single beam, and the technology used to produce the laminations will limit the lamination thickness.

The above methods have been applied to the example applications listed in table 9, to produce the results listed in table 11. Table 10 lists the material parameters used in the analysis.

Table 9: Example application excitations

Application	Frequency, f. (Hz)	Excitation amplitude, α. (μm)	Spectral Excitation Energy, $f^2\alpha$. (Hz^2m)	Source of Data, Comments
Car floor	10	401	0.0401	Griffin [79], pp.494 fig 12.7(6)
Truck floor	10	817	0.0817	Griffin [79], pp.497 fig 12.10
Caulking hammer handle	1000	2.15	2.15	Griffin [79], pp.689 fig 18.3
Motor cycle handlebars	300	35.8	3.22	Griffin [79], pp.698 fig 18.12
Loaded Pinion	250	0.631	0.0394	Chen [80]. Vibration caused by meshing forces (18 teeth; radius 27mm; mesh frequency 250Hz; 235W delivered by pinion (100N force on primary of 65 teeth); device placed at 25mm from centre)
Bearing cap in heavy machinery	100	3.58	0.0358	Jackson [81] pp. 44 fig 8-2. Typical vibration caused by minor faults in the bearing.
Note: These sources are modelled as a sinusoidal excitation at the highest frequency in the excitation spectra.				

Table 10: Piezoelectric model parameters

Parameter	**Value**
Q-factor of unloaded beam	100
PZT Max stress, T_{max}	40 MPa (half max rated value)
Young's Modulus of PZT, Y.	75 GPa
Density of mass material, ρ	8000
Maximum material damping, η_{max}, that can be applied by: Bulk PZT-8 Thick-film PZT-5H	 0.049 $4x10^{-4}$

Table 11: Predicted power output for a range of practical applications

Application (see Table 9)	Total generator height, H (mm)	Bulk PZT-8 (η_{max}=0.049) Power (μW) [2d.p.]	Thick-film PZT-5H (η_{max}=4E-4) Power (μW) [2d.p.]	Ratio of powers: bulk to thick-film [1d.p.]
Car floor	2.5	0.26	0.00	122.5
	5	4.56	0.04	122.5
	10	67.11	0.55	122.5
Truck floor	2.5	0.26	0.00	122.5
	5	4.56	0.04	122.5
	10	67.11	0.55	122.5
Caulking hammer	2.5	1 684.91	8.39	200.7
	5	17 757.07	107.13	165.7
	10	181 434.96	5 806.74	31.2
Motorbike handlebars	2.5	135.80	1.07	126.7
	5	1 745.55	14.25	122.5
	10	22 328.77	182.27	122.5
Loaded pinion	2.5	6.74	0.69	9.7
	5	60.45	6.87	8.8
	10	517.92	62.36	8.3
Bearing cap in machinery	2.5	7.59	0.17	44.4
	5	75.49	3.68	20.5
	10	724.31	50.60	14.3

Note: The maximum damping that can be applied (η_{max}) has been calculated from equation 5.4.

For each application type, the power that can be produced is calculated for three sizes of generator. The sizes are: 2.5x5x5mm, 5x10x10mm, 10x20x20mm (height x width x depth). For each of these sizes, power is calculated for both bulk and thick-film piezoelectric materials. The level of unwanted damping is assumed to be η_L=0.01, which corresponds to a Quality factor of 100 for the unloaded beam. This figure is close to the value measured for the prototype beam,

and to permit comparison, is the same as that used for predictions for magnet-coil generators in section 7.4.

The table shows a wide variation in the amount of power that can be generated from the various applications. A column shows the ratio between the power that could be produced from a generator using bulk PZT-8, and one using the thick-film PZT-5H material discussed in the previous chapter. It can be seen that the bulk PZT offers much higher power output, and that the thick-film PZT produces a useful amount of power in only a few cases that have a high excitation energy. The table only contains data for piezoceramic materials, PVDF has been omitted as it will produce even less energy than the thick-film PZT (due to its low activity).

The same program has been used to produce the graph shown in figure 47a. The graph shows data for a generator of fixed size (5mm high x 10mm x 10mm) using the material PZT-8. The power for a device of optimum internal dimensions is plotted for a range of excitation amplitudes and frequencies. To permit simpler comparison between frequencies, the x-axis shows the spectral energy of the excitation (the product of the frequency squared and the excitation amplitude). Figure 48 shows the value of the parameters that correspond to each point on the graph. An interesting feature of these graphs is that they show a sudden transition between a multi-beam configuration (ratio of cell height to total height < 1.0) to a single beam (cell height equals total height). It can be seen that a multi-beam configuration becomes optimum at higher frequencies, and lower excitations, and that the optimum cell height is almost independent of excitation. As the excitation is increased the height of the mass decreases, and the length of the beam increases until a critical point is reached when a single beam becomes the better design. The small maxima seen in the power graph are thought to be artefacts of the optimisation process around this transition, although they are not large enough to detract from the utility of these results as 'ball-park' estimates (the assumptions used in the derivation above mean that these results are for an ideal generator; in practice non-ideal elements will reduce the actual power produced).

Figure 47(a) can be compared to (b) which shows the theoretical limit for the maximum power that could be produced from a resonant generator of any type, as discussed above. It can be seen that at higher frequencies and lower excitation, the piezoelectric generators approach this maximum. A reason that causes the piezoelectric generators to fail to reach this upper bound in other cases can be seen from figure 48(c). The piezoelectric material is operating by applying as much damping as is possible. To approach the maximum more damping is required, which could only be achieved by finding a material with a higher electromechanical coupling factor, k (see section 5.2).

The data described here will be compared to results for magnet-coil generators in section 7.4, to form a comparison of the two technologies.

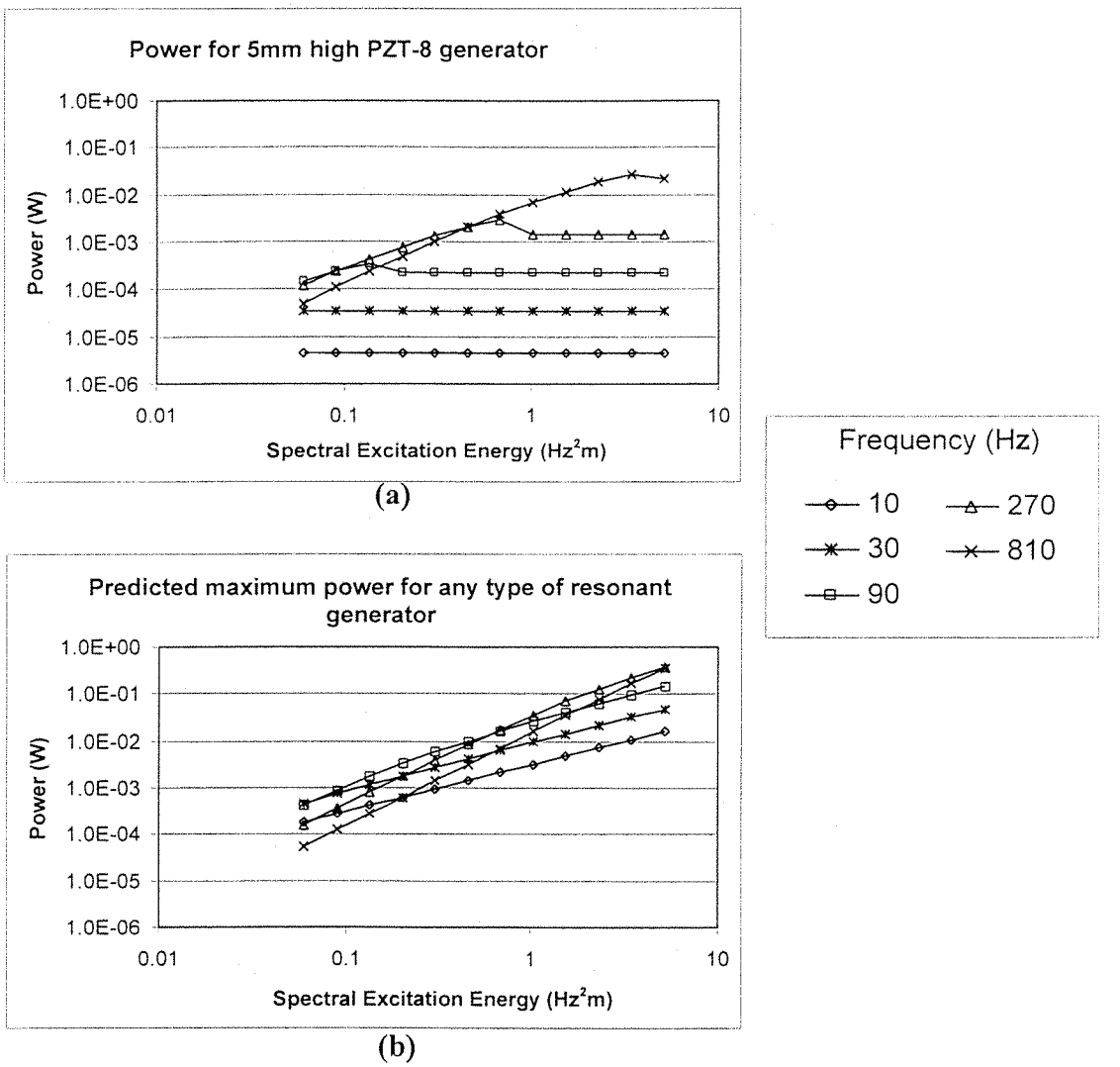

Figure 47: Predicted generator power

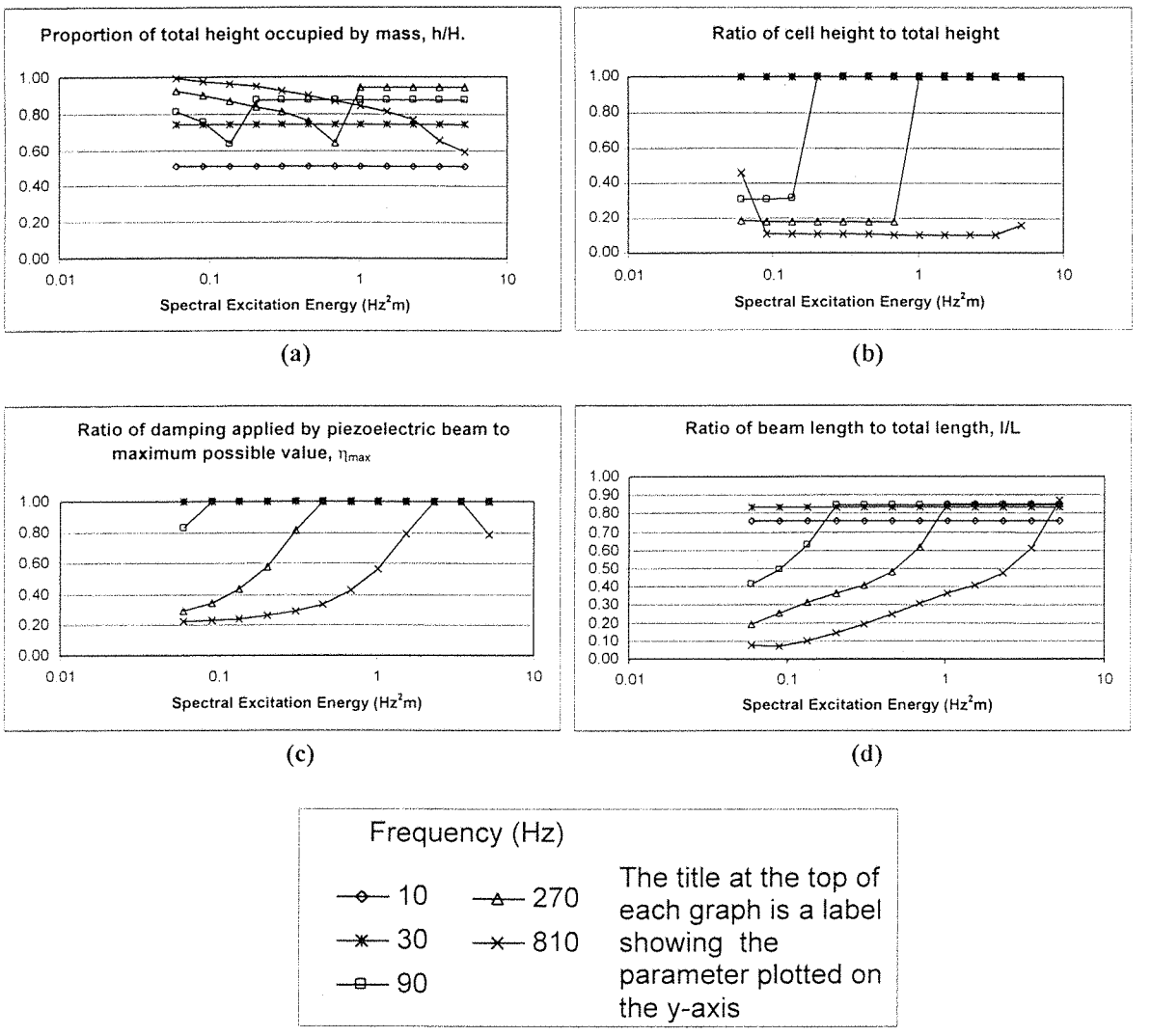

Figure 48: Parameters that lead to optimum PZT generators

5.8 Summary

A method has been described for modelling the power that can be produced from piezoelectric inertial generators. Analytical methods have been shown to be too complex to produce useful results. The method presented uses a combination of FEA and a complex stiffness model of a resistively shunted piezoelectric element. This complex stiffness model enables the mechanical and electrical domains to be de-coupled, permitting a more straightforward analysis.

Comparing the model to experimental results, accurate predictions are seen at low beam amplitude, with slight under prediction at higher amplitudes due to non-linear effects.

The power output from the prototype generators reaches a maximum of only a few microwatts. This power output is too low to be of practical use (see section 3.3). The model (see equation 5.4) reveals that this low power is due to the low electromagnetic coupling produced by thick-film piezoceramics when they are operated in a 3-1 coupling mode. If bulk PZT were used in place of the thick-film material, the model predicts a 100 fold increase in generated power. Thus, research (e.g. Glynne-Jones *et al* [82] and Kosec *et al* [83]) to improve thick-film piezoelectric materials has the potential to significantly improve the performance of the prototype.

The model has been applied to a simplified generator structure to make predictions of how much power a piezoelectric generator of an arbitrary size might produce under ideal conditions. These calculations have been applied to a range of example applications, and reveal that the generated power varies widely from application to application, and that bulk PZT offers superior performance. The same examples will be used in chapter 7 to enable a comparison between piezoelectric and magnet-coil generators.

CHAPTER 6

Ageing Characteristics of Thick-Film PZT

6.1 Introduction

It has long been known that piezoelectric ceramics suffer a long term ageing process after polarisation [84]. When these materials are used in sensors, actuators, and generators there is a concern that this ageing will decrease the efficiency, sensitivity or accuracy of the devices. It is thus important to characterise the ageing process so that designs can be made which allow for degradation over the lifetime of a device.

Owing to the difficulties in measuring the coupling coefficients of thick-film piezoelectric ceramics, which stem from the presence of an underlying substrate, there are no reports in the literature of any attempts to measure the ageing of these thick-film properties. Making a preliminary study of this effect was thus deemed important for piezoelectric generators. This section does not attempt to explore the ageing process in detail, but to provide some confidence in the long-term stability of thick-film PZT.

Methods for studying two types of ageing process are presented. The first measures the decrease in magnitude of the d_{31} coefficient (which relates stress applied perpendicular to the polarisation direction to charge displaced along the polar axis) and the dielectric constant, K_{33}, with time after polarisation. Finally, a method to examine the effect of cyclical stress on the d_{31} coefficient is explored.

6.2 Background

From the time that a sample of bulk PZT is cooled after polarisation, it can be noted that the ageing cycles described in table 12 begins.

Jaffe *et al* [43] state that for any of these properties the effect can be expressed for practical time intervals as $K=K_0 - m\ log(t)$ where K is the value of the constant, K_0 its value at $t=1$, and t the time elapsed since cooling. Jaffe also notes that by mathematical necessity the ageing rate must

eventually diminish (this has been observed after several years of elapsed time), thus the time law is not precisely semi-logarithmic.

Table 12: Ageing processes (after Jaffe *et al* [43])

piezoelectric coupling factors	Diminish
dielectric constant	
dielectric loss	
mechanical Q	Increase
elastic stiffness	
frequency constants	

Ageing cycles also begin after any subsequent thermal changes, application of strong mechanical stresses, or strong electrical signals; thus when performing experiments these types of disturbance must be avoided, otherwise they will cause smaller ageing cycles that will be superimposed on the cycle of interest [84].

Significant work has been performed to explore the accuracy of this model, and the mechanisms that cause it for both bulk ceramics [84,85] and for thin film deposited ceramics [86]. The mechanisms proposed generally reflect some form of domain rearrangement [43]. One proposed mechanism [84] is that the loss of activity is due to a decrease in the remnant polarisation of the ceramic that occurs to relieve elastic and electrical stresses that are created during the polarisation process. A major cause of these stresses is the fact that the unit cell of the PZT material is longer along its polar axis than any of the other allowable directions for the polar axis

The ageing effect in PZT ceramics is sensitive to the precise composition of the material, for instance the 'hard' high power material PZT8 has a d33 ageing rate of –6.3% per time decade, while PZT7A has been tailored for low ageing and is quoted at less than 0.05% per time decade [44]. Values of a few percent per decade are typical for bulk materials. Thus to determine experimentally the ageing rate, the measurement method must be sensitive to small changes over relatively long periods of time. Measurement techniques are discussed in section 4.4.4, where the difficulties of measuring the piezoelectric coefficients of thick-film materials are described. Commercially available d_{33} meters tend to be limited to an accuracy of around ±2% for the types

of sample described here, thus the challenge is to find a measurement technique that is both accurate and stable over a period of days.

6.3 Compensation of Charge Amplifier Response

During experimentation, it was found necessary to measure two quantities of charge simultaneously. To do this two charge amplifiers were used. These, however, were not sufficiently stable with temperature and over the long duration of the experiment. To eliminate any long-term drift the following procedure was devised.

Assume that the two charge amplifiers have unknown amplification factors K and L respectively (unknown due to poor calibration or long-term drift). We wish to determine the ratio, R, between the amplitudes of the charge signals being produced by two samples.

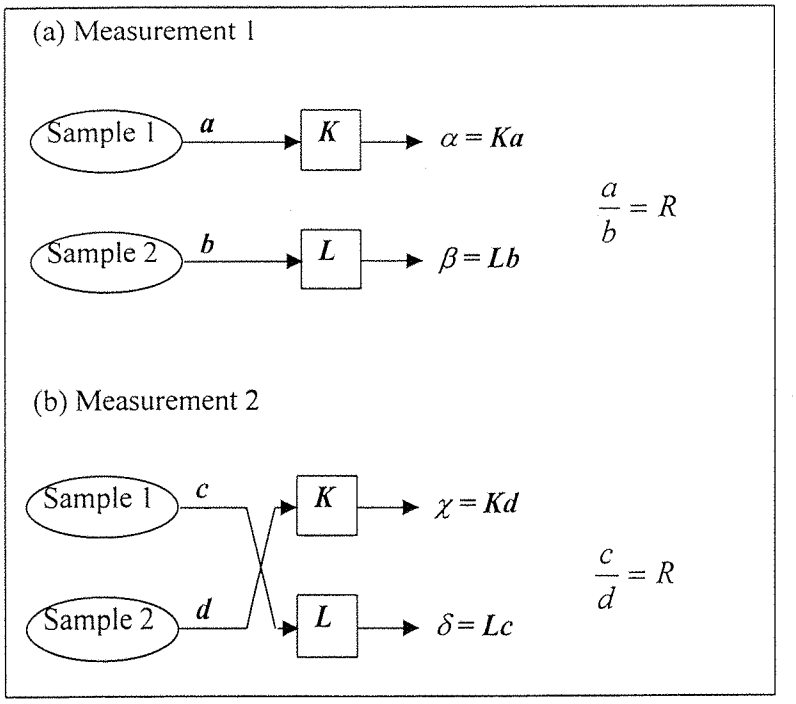

Figure 49: Compensation of charge amplifiers

The charge amplifiers are connected to the samples and a reading is taken. If the two samples yield charges a and b respectively, then the outputs from the charge amplifiers are given by $\alpha=Ka$ and $\beta=Lb$. The wires are now reversed, as illustrated in figure 49, and another reading is taken. Since the reading is taken after the first one, the charge signals will have changed, but their ratio, R, will remain constant. If we denote these second signals as c and d respectively, then the outputs from the charge amplifiers are now given by $\chi=Kc$ and $\delta=Ld$.

It can be shown that the ratio between the input signals, R, can be determined by the following equation that is in terms of the measured outputs from the charge amplifiers, and is independent of K and L.

$$R = \sqrt{\frac{\alpha\delta}{\beta\chi}}$$ **Equation 6.1**

6.4 Temporal ageing after polling

The experiments described here use the composite steel / dielectric / PZT beams described in chapter 4. When these beams are mounted in a clamp and shaken the resulting signal at the electrodes is a function of the d_{31} coefficient of the PZT. Thus, by examining this signal after polarisation, the ageing of the d_{31} coefficient can be observed. The ageing of the dielectric constant, K_{33}, of the PZT layer can also be measured through the capacitance of the sample.

6.4.1 Experimental procedure

The composite beams were produced as described in section 4.3, including attaching a mass to the tips of the beams, and wires to the electrodes. A device is polarised as described in section 4.2.7.3 using a temperature of 150°C for a period of 35 minutes. Immediately following polarisation the beam is clamped at one end of the clamp of the shaker rig described in section 4.5.1.

Preliminary experiments showed that both the base excitation supplied by the shaker and the response of a clamped sample to shaking varied with environmental temperature; this variation obscured the ageing present in the sample (see figure 51). To compensate for this effect, a reference sample was used. The reference sample was mounted at the opposite end of the clamp to the main sample. This reference sample was prepared in an identical manner to the main sample, except that it was polarised one month before the experiment. If the system is assumed to be linear, then if the base acceleration is increased, the ratio between the signals from the reference sample and the main sample should remain unchanged. Similarly, the reference sample should compensate for any linear temperature dependence of the d_{31} coefficient with temperature. By polarising the reference sample one month before the experiment, it should not age more than a further -0.12% over the course of a 2-day experiment (given the rate of ageing found experimentally).

The shaker was driven by the amplifier and frequency source described above. The frequency of excitation was set at 60Hz, around two thirds of the 90Hz natural frequencies of the sample and reference beams. Preliminary experiments had been performed operating at the resonant frequency of the sample; it was found, however, that as temperature variations occurred the

natural frequencies of the beams would change causing large variations in the beams' amplitudes. It was also found that at resonance the positions of the connecting wires had large effects on the beams' amplitudes, leading to unreliable results (at resonance the amplitude is controlled by the amount of damping present; the connecting wires cause a significant part of this damping). Operating at 60Hz is a compromise between using higher frequencies with the associated damping problems, and lower frequencies which would produce a smaller signal to noise ratio.

The main sample was placed in the clamp immediately after it was polarised. The amplitude of the acceleration applied by the shaker was set to $28ms^{-2}$ (measured using the accelerometer), which produced a strong signal without being large enough to cause mechanical change in the test apparatus. The amplitude of the beam at this excitation was measured as 0.3mm. Using the finite element model described in section 5.4.1, it was found that this results in a maximum longitudinal stress in the PZT layer of 2.7 MPa. This is in the linear range described for bulk PZT5A [44], which is given a maximum rated static compressive stress perpendicular to the polar axis of 13.8MPa. It is thus reasonable to assume that the device is operating in its linear range, and that the shaking should not contribute any stress-induced ageing cycles.

To measure the charge displaced by the two beams a pair of Kistler Charge Amplifiers (model 5001) were used. The charge amplifiers were set to a sensitivity of 1000pC/V with a feedback resistance of $10^9\Omega$. The signal analyser monitored the output from the charge amplifiers, and was used with a flat-top (sinusoidal) windowing function, which gave better amplitude accuracy than the other available functions. The signal analyser was set to a sampling rate of 256Hz, with a total number of 512 samples. The analyser performed Fourier transforms to show the average signal amplitude over the sampling period.

Once the sample was polarised and clamped, and the shaker activated, then a set of measurements were taken periodically. To take a set of measurements, first the charge signals were measured with the main sample connected to charge amplifier 'A', and the reference connected to charge amplifier 'B'. A reading was taken simultaneously of both quantities. (The signal analyser has two input channels that are logged concurrently. Both can be paused simultaneously to allow this measurement). The connecting leads were then switched so that the main sample was connected to charge amplifier 'B', and the reference connected to charge amplifier 'A'; readings of the charge signals were again taken simultaneously. Equation 6.1 was then used to determine the ratio of sample response to reference response. The experiments described here continued for up to 2 days, with the interval between readings increasing to provide suitable data to plot a semi-logarithmic graph of the results.

The ageing of the dielectric constant of the PZT layer was examined as follows: a sample was polarised as described above, then the capacitance of the sample was measured periodically using a Wayne-Kerr Automatic LCR Meter (model 4250). To compensate for any linear dependence on environmental conditions, the response of the sample was compared to a reference sample that had been pre-aged for one month before the experiment, as described above. Whenever the sample capacitance was measured, the reference sample was tested shortly afterwards, so that the two measurements related to nearly the same instant in time.

6.4.2 Results and Discussion

Figure 50 shows how the ratio of sample response to reference response (for the d_{31} experiment) varied with time after polarisation. The data is normalised (linearly scaled) so that the initial value of the ratio has a value of one. The figure includes a linear best-fit line, found using a least squares method. The graph exhibits a linear semi-logarithmic relationship that corresponds well to the type of ageing found with bulk samples. Figure 51 shows a typical response of a sample without compensation by a reference beam; a reference beam is clearly useful in compensating for environmental and excitational variations.

Three other samples were also tested; the results are listed for each side of each sample in table 13. The average ageing rate of the layers was -4.40% per time decade, with a standard deviation of 0.41%. The variation observed between samples is not unexpected; it is stated by the IRE standard for the measurement of piezoelectric crystals [68] that parameters can vary by up to 20%, even in ceramics of known composition and high density. The thick-film printing process is also very sensitive to processing conditions, and individual samples are subjected to fluctuations even within a given batch. The rate of ageing is similar to that described by Morgan Electroceramics [44] for the d_{33} coefficient of PZT-5H, reported at –3.9% per decade.

The results of this experiment indicate that thick-film PZT materials can be used in future designs with the confidence that they will not age significantly faster than traditional bulk materials (under conditions of low stress, and low electrode voltage).

Figure 52 shows how the ratio of sample capacitance to reference capacitance varied with time after polarisation. The data is normalised (linearly scaled) so that the initial value of the ratio has a value of one. The figure includes a linear best-fit line, found using a least squares method. The figure again exhibits a clear linear semi-logarithmic relationship that corresponds well to the type of ageing found with bulk samples. The results for 4 samples are presented in table 14. The mean ageing rate is found to be –1.34% per time decade. This is higher than the value of –0.6% reported by Morgan Electroceramics for bulk PZT-5H [44].

Table 13: d_{31} ageing rates of samples

	d_{31} Ageing rate (% decay/ time decade)	
	Side one	**Side two**
Sample1	4.72	4.93
Sample 2	4.69	4.59
Sample 3	4.26	4.35
Sample 4	3.94	3.73

Table 14: K_{33} ageing rates of samples

	Dielectric Constant, K_{33}, Ageing rate (% decay/ time decade)
Sample A	1.11%
Sample B	1.33%
Sample C	1.37%
Sample D	1.54%
Mean Value	1.34%

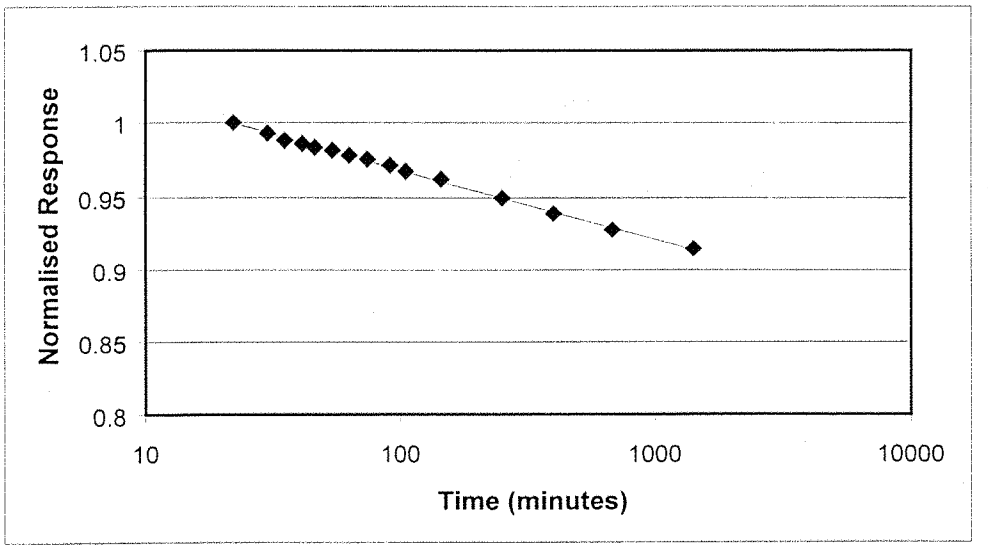

Figure 50: Graph of normalised d31 versus time after polarisation

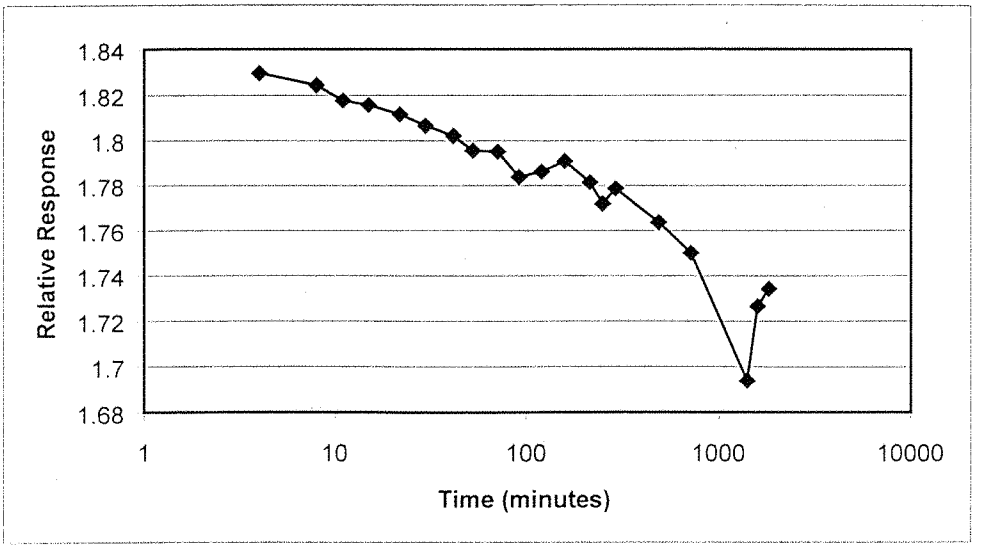

Figure 51: Graph of d_{31} response versus time without compensation

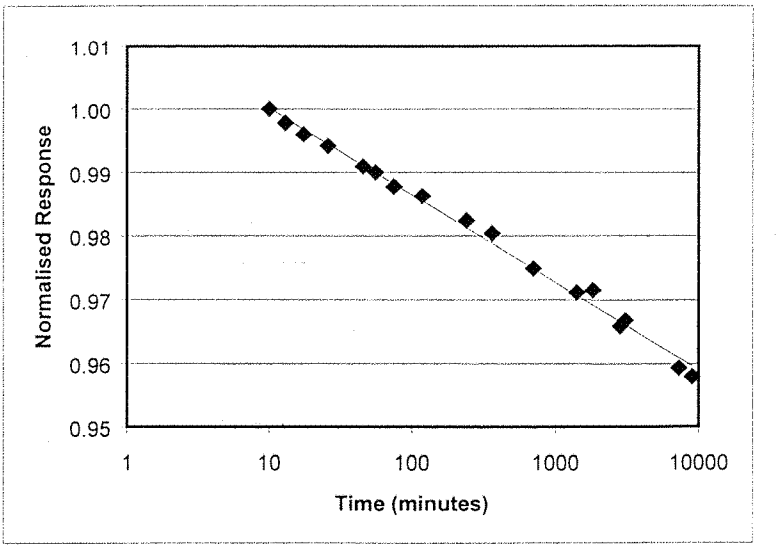

Figure 52: Graph of normalised k_{33} versus time after polarisation.

6.5 Ageing caused by cyclic stress

The experiments described in this section attempt to examine the rate of ageing induced by cyclical stress on thick-film samples. The response of a sample that is caused to oscillate at large amplitudes is examined over a large number of cycles. The response is compared to a reference sample with less mass, that oscillates at a smaller amplitude, and hence less stress. The method is found to give unreliable results at the high amplitudes required to cause classical semi-logarithmic

ageing of the sample; lower amplitudes are, however, found to cause a small linear ageing effect that is presented as interesting and potentially important.

6.5.1 Method

Sample and reference composite beams were prepared and equipped with wires as described in the previous experiment. Both beams were polarised, then left for 60 days so that the amount of natural ageing over the course of the experiment would be negligible (over the course of an 8 day experiment the d_{31} of these samples will decrease by only a further 0.2%, assuming an ageing rate of –4% per decade).

The two beams were mounted in the shaker rig as before. In this experiment, a tip mass was placed on the sample beam, but not the reference beam. This means that when the clamp was shaken, the sample oscillates with a much higher amplitude than the reference beam. The sample beam was thus being shaken at an amplitude that may cause it to age due to the cyclic stresses induced in it. The reference beam should not age in this manner, and should allow for compensation of any variation in the excitation amplitude and linear temperature-related coefficient changes.

For the reasons described in the previous experiment, the shaker was operated at 55Hz. Samples were tested at two different excitation amplitudes. Table 15 lists the beam amplitudes, and the associated base excitation, and the maximum stress in the PZT at these amplitudes predicted using the FEA model. The longitudinal stresses predicted in the PZT layer would place the samples in the linear region of operation were they formed from bulk material (PZT-5A has a maximum rated compressive stress perpendicular to the polar axis of 13.8MPa)

Larger beam amplitudes were investigated, but it was found that at such amplitudes there were large variations in the results that obscured any meaningful trends. These variations could be due to the large amount of base excitation required to achieve these beam amplitudes in a sub-resonant beam causing mechanical changes in the clamping arrangement, or perhaps that the strength of the thick-film layer in tension or compression is exceeded.

The charge signals from the two samples were fed into the pair of charge amplifiers. These were set to sensitivities of 1000pC/V and 50pC/V for the sample and reference beams respectively. The output from the charge amplifiers was monitored by the signal analyser described above. As before, a flat-top windowing function was used. The signal analyser was set to a sampling rate of 128Hz, with a total number of 512 samples.

The shaker was activated, then at intervals a set of measurements were taken. Sets of simultaneous measurements were taken as described above for the temporal ageing experiment, and the ratio of sample response to reference response was again determined using equation 6.1. Experiments were conducted for up to 9 days in duration.

Table 15: Beam amplitudes for ageing experiment.

Beam Amplitude (mm)	Magnitude of Base acceleration (ms^{-2})	Maximum Longitudinal Stress in the PZT Layer (MPa)
0.51	48	4.8
0.85	79	8.1

6.5.2 Results and Discussion

Figure 53 shows how the ratio of sample to reference response varied with shaking time for a beam shaken at an amplitude of 0.51mm. In this graph, there is an initial period (around 3 hours) of increase in the normalised response of the sample, followed by a steady linear decrease. The reason for this increase is unclear; a possible reason is stress-induced stiffening of the steel substrate.

The rates of ageing (after the initial increase period) of the samples are listed in table 16. It is interesting to note that the rate of ageing is the same for both of the beam amplitudes examined here. The total amount of ageing observed over the course of this experiments is less than one percent. This is much smaller than the 10% total ageing (in a similar time span) observed over the course of the post-polarisation experiments described above. Note that previous work [65] to measure the piezoelectric coefficients of thick-film PZT has achieved accuracies of only a few percent *for each reading*, and that the experiments describe here offer an order of magnitude increase in experimental accuracy.

The ageing in the samples' responses has several possible sources: a decrease in the activity of the PZT layer, damage to the PZT layer, or a stress-induced stiffening of the steel substrate. The stresses in the PZT are at a low level compared to the level where the onset of non-linear response is seen in bulk PZT. The region of non-linear response is closely associated with the range of stresses that will induce ageing cycles in a sample [84]. That the ageing is linear with respect to time also indicates that the observed results are not a result of classical domain rearrangement

ageing of the PZT [84]. We thus tentatively deduce that the ageing is due to work hardening of the steel or cyclical fatigue of the PZT.

Since the experimental set-up has proved unsuitable for generating larger stresses within the PZT layer, further insight into classical stress induced ageing of the screen-printed PZT would require a different approach.

Table 16: Stress induced ageing of samples.

Sample	Ageing rate (%/minute)	Ageing rate (%/million cycles)
Amplitude = 0.85mm	-7.45E-05	-0.023
Amplitude = 0.51mm, side 1	-7.51E-05	-0.023
Amplitude = 0.51mm, side 2	-7.45E-05	-0.023

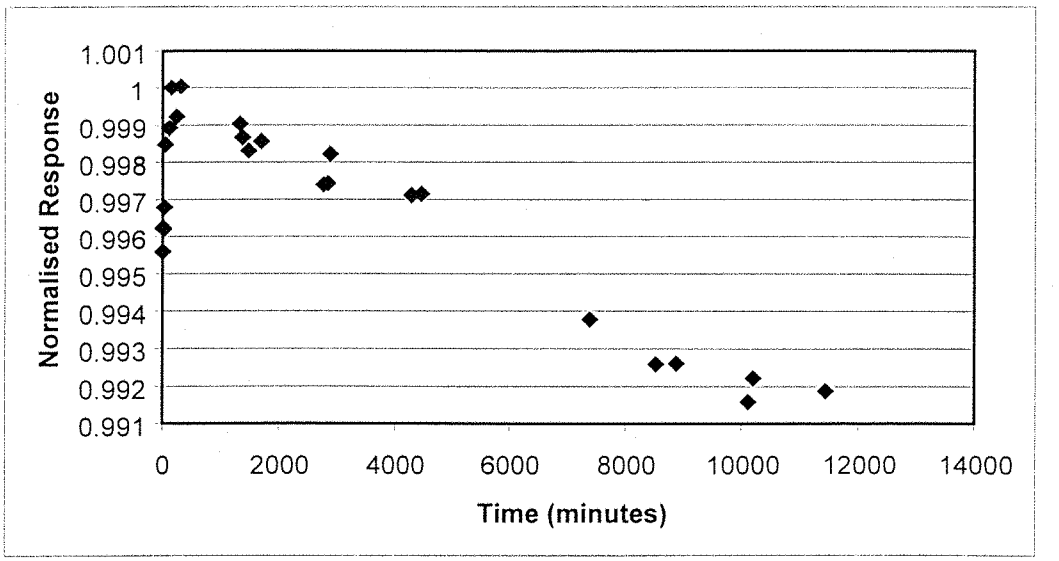

Figure 53: Ageing of response of a sample with amplitude 0.51mm

6.6 Summary

A technique for measuring the ageing rate of the d_{31} coefficient of a PZT thick-film sample has been presented. The method is found to be reliable, and be sufficiently accurate for observing the decaying response. The accuracy obtained is of an order of magnitude higher than that reported previously. The d_{31} coefficient is found to age at –4.4% per time decade (for PZT-5H). A method is presented for measuring the ageing of the dielectric constant, K_{33}, and found to show an ageing

rate of −1.34% per time decade. Future studies into the effect of polarisation conditions and other processing parameters on the rate of ageing are recommended.

A technique for exploring the ageing induced by cyclical stress has also been described. The method has been found to be unreliable at the higher stresses required to induce classical ageing, however, at lower amplitudes, a small linear ageing effect has been found that warrants further study.

CHAPTER 7

Generators based on Electromagnetic Induction

Electromagnetic induction was discovered in 1831 by Faraday, and has been used to generate power ever since. Some basic equations relating magnetic and electrical quantities are described for reference in section 3.1.3. Previous interest in this method of producing an inertial generator has produced several working prototypes that are summarised table 17.

Table 17: Electromagnetic inertial generators to date

Name	**Volume (mm^3)**	**Freq. (Hz)**	**Measured Power (μW)**
Shearwood and Yates [5]	4.9	4400	0.3 (20 in vacuum)
Amirtharajah and Chandrakasan [7]	unknown	94	unknown, 400 predicted
Li *et al* [6]	~3000	104	5
Seiko kinetic watch [10]	unknown	N/A	estimated 200

These prototypes have been published along with some simple models, but to date there have been no studies that attempt to predict where the theoretical limits for these generators lie, and how much power might be produced in typical applications in a given volume. This section aims to provide such an analysis, and discuss some of the issues controlling the design of a generator. Prototypes are also produced that improve on existing designs by increasing the degree of electromagnetic coupling.

Generators based on electromagnetic induction will be referred to as a magnet-coil generator in the remainder of this section.

7.1 Possible Design Configurations

A typical magnet-coil generator will consist of a spring-mass combination attached to a magnet or coil in such a manner that when the system resonates, a coil cuts through the flux formed by a magnetic core. The beam can either be connected to the magnetic core, with the coil fixed relative to the enclosure, or vice versa. Attaching the magnetic core to the beam has the advantage of using the dense core as part of the mass so that less volume is required for extra mass to produce the required resonant frequency. A drawback of this configuration is that there will be attraction between the magnet and the surrounding enclosure (if it is formed from a ferromagnetic material), which may cause problems for a design.

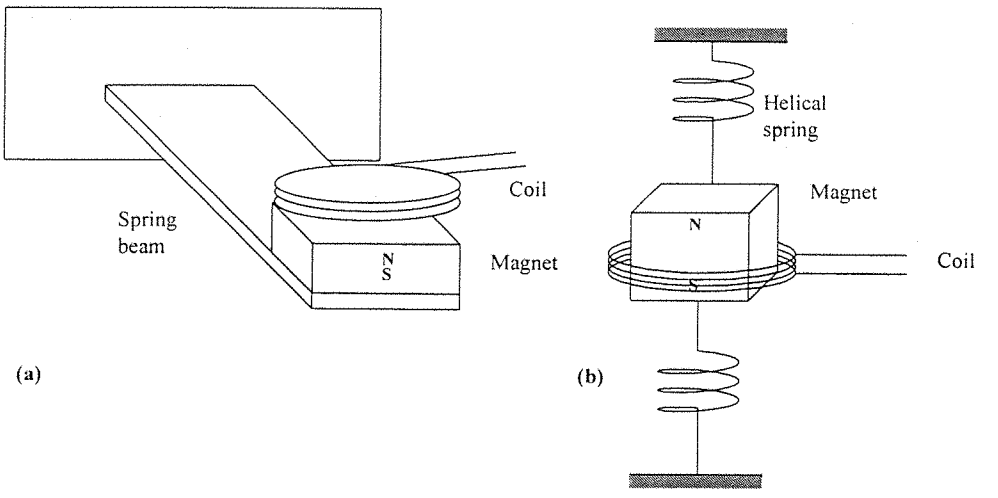

Figure 54: Typical generator configurations

Figure 54 shows designs based on a planar spring beam (a), and a helical spring (b). The advantage of the planar spring is that it posses stiffness in the lateral direction, and hence the locus of movement of the beam tip is more precisely defined in the presence of vibrations, and static gravitational loading in the lateral direction. This means that the magnet and coil can be brought closer together to improve the electromechanical coupling, since there is less risk of collision between the two parts. The helical spring offers a more compact design, which may be useful when designing devices of low resonant frequency that would otherwise require too much volume to produce a suitable spring. The second spring in design (b) improves the lateral

constraint of the mass, but is not as effective as the planar spring. A guide rail of some form would improve this problem, but would significantly reduce the Q-factor of the resonator.

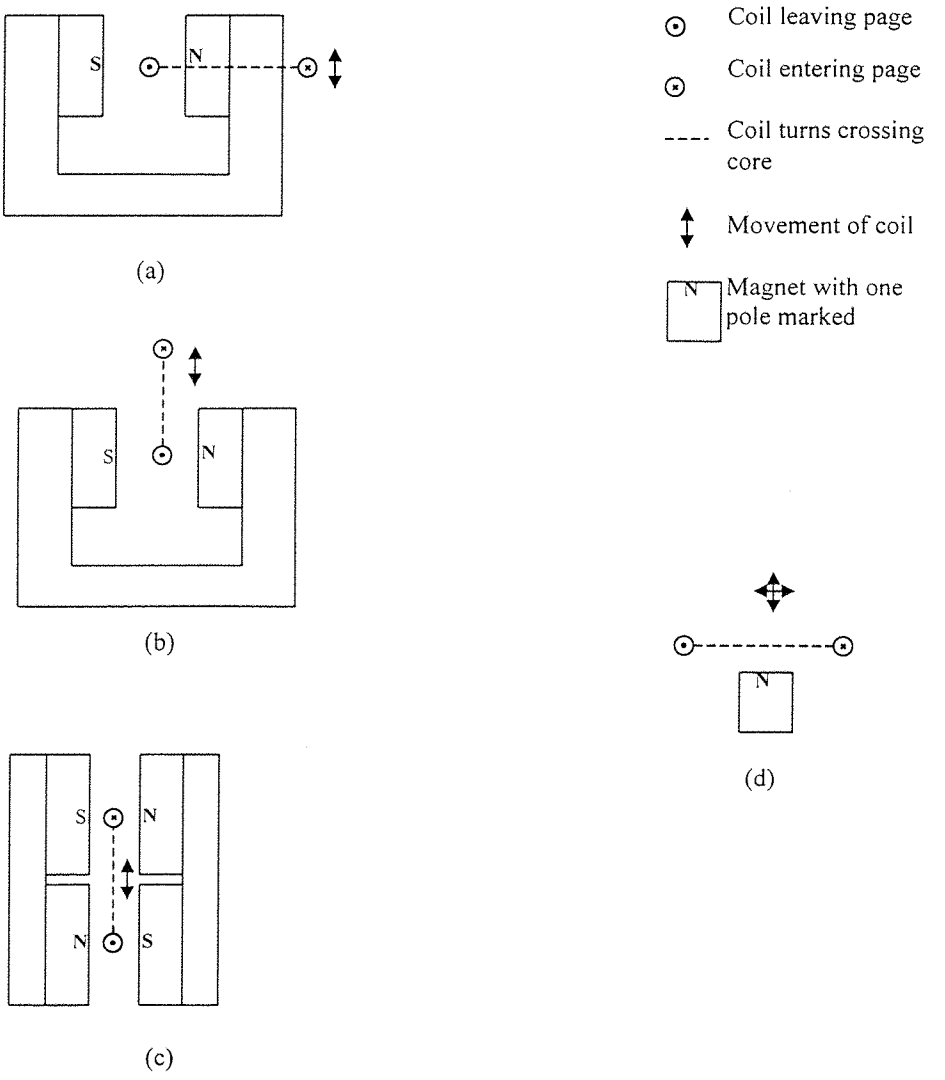

Figure 55: Magnetic circuit configurations

The magnetic circuit comprising the magnetic core, and the coil that resides in the magnetic field created by the core can be arranged in many ways. Figure 55 shows some of the alternatives for the overall layout. (a) and (b) show coils that are aligned so that relative motion between the coil and core causes the amount of flux encircled by the core to change. Electromagnetically there is little difference between (a) and (b), and the coil position can be chosen to make the best use of available space. Design (c) creates a magnetic field through a greater proportion of the length of each winding. Comparing it to a design of type (b) with the same total air-gap and twice the

number of coils to achieve the degree of electromagnetic coupling, it can be seen that the total length of coil is twice that required for design (c) (assuming that the height of the coil, h, is not significant). Thus, design (c) has the potential to reduce the resistive losses in the coil windings by shortening the coil. However, this comparison is not wholly accurate as the clearance required at the side of the coil is ignored, and the coil height will often be significant. Design (d) is of the type used by Chan [87]. The advantage of this design is its ease of manufacture, especially during MEMS processes, however, the degree of electromagnetic coupling achieved with this layout will be much smaller than the other layouts described here (especially for small coil amplitudes). To achieve suitable output voltages with this configuration, Chan had to use a torsional vibration mode. In some higher source amplitude applications this may not be a problem, as the best design is not always the one that provides the highest degree of coupling (see section 7.4.5).

To improve the degree of coupling, it is important to choose a type of magnet that will produce a strong flux density. Rare earth magnets are ideal for this application, and offer up to 5 times the magnetic energy density of conventional Alnico magnets. "Neodymium Iron Boron magnets have the most powerful magnetic properties per cubic cm known at this time [2001]"[88], and can operate at up to 120°C. If higher temperature operation is required, the less powerful Samarium Cobalt can be used, with a working temperature of up to 250°C.

The coil is characterised by the proportion of the coil that passes through the magnetic field, the number of turns in the coil, and its series resistance. Second-order effects such as coil inductance can often be ignored due to the low frequency of many applications. Two types of coil have been used in the past: wound coils, and printed coils (as used by Chan [87]). A printed coil can be formed by screen printing layers of conductive materials and insulators onto a substrate in much the same manner as PCBs are produced. (Printed coils are sometimes known as planar coils – although here, both coils will tend to be essentially planar in nature as a consequence of the advantage of having a thin air-gap.) A printed coil can be made very thin (printed layers will typically be 10μm thick), which makes it particularly attractive for small scale devices (see section 7.5.2). A printed coil may also be easier to manufacture as it only involves standard thick-film printing processes, as opposed to a wound coil, which becomes more difficult to manufacture as the scale decreases. The disadvantage of a printed coil is that the small thickness of each layer will result in a high series resistance for the coil. If windings of a larger thickness than are traditionally available from thick-film technology (e.g. >50μm) are required, it is anticipated that a wound coil will be more economic to manufacture. Printed coils have the added advantage of already being connected to a substrate, which may add rigidity to the coil, and hence decrease the clearance required between the coil and the magnetic core.

7.2 Equivalent circuit model of a generator

The generator configuration shown in figure 56 will now be examined. The figure shows a generator with the magnetic core mounted on the mass, and a fixed coil, however, the results derived below are valid for the converse case. The combined mass of the weight, and the mass of the magnetic core is denoted by m. This is connected to the housing by a spring of stiffness k, and a viscous damping element with viscous damping coefficient c_L, which represents any air, material and support damping present in the design. A magnetic flux, whose flux density perpendicular to the coil is given by B is present in the air gap that the coil resides in. Each of the N windings of the coil passes through a length l of this field. Excitation, $y(t)$ is applied to the generator housing, which results in differential movement between the mass and the housing, $z(t)$. Figure 57 shows a free body diagram of the mass relative to the generator housing. Choosing this inertial reference, it is shown by Thompson [51] that the base excitation can be represented as a force on the mass, F_{ACEL}:

$$F_{ACEL} = -m\ddot{y}$$

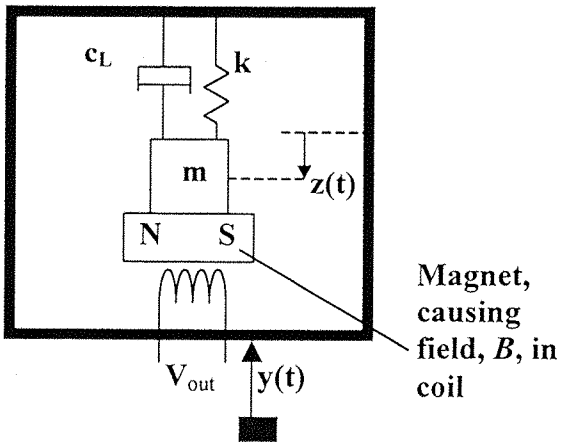

Figure 56: Schematic diagram of a magnet-coil generator

The system can be represented by the equivalent circuits shown in figure 58(a,b). Table 18 justifies circuit (a) by listing, and comparing the equations governing the variables against those of the physical model. It can be seen that if the substitutions shown in table 19 are made then the two models are equivalent. Circuit (b) transforms (a), removing the ideal transformer by scaling the components and driving current to the left of the transformer. The model is validated below in section 7.3.2.2. It should be noted that the inductance of the coil has been omitted, since for the

generators described in this text the frequencies of interest are low enough to make its effect negligible.

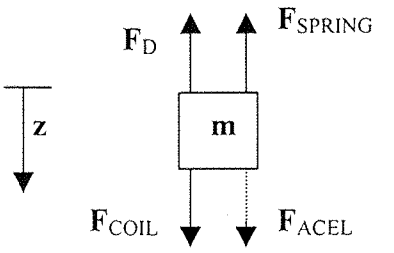

Figure 57: Free body diagram of generator mass relative to enclosure

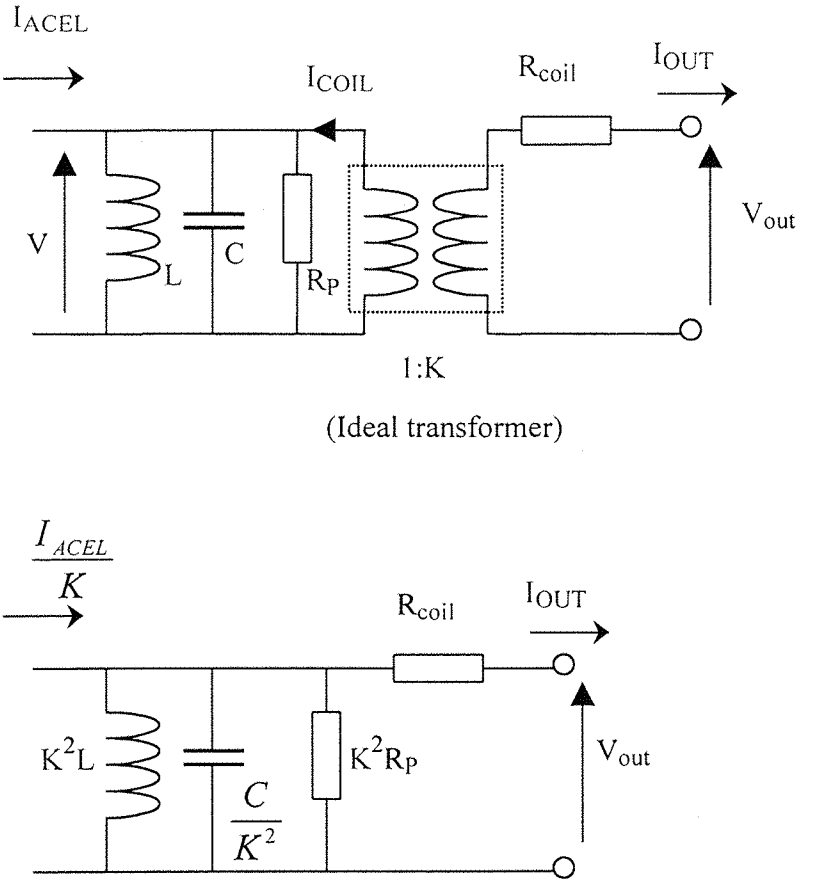

Figure 58: Generator equivalent circuits

Table 18: Equivalent circuit model mapping

Magnetic model equations	Equivalent Circuit model equations
$m \cdot \ddot{z} = -F_d - F_{SPRING} + F_{ACEL} + F_{COIL}$	$C\frac{dV}{dt} = -I_{RP} - I_L + I_{ACEL} + I_{COIL}$
$F_{SPRING} = k \cdot z$	$I_L = \frac{1}{L}\int V$
$F_d = c \cdot \dot{z}$	$I_{RP} = \frac{1}{R_P}V$
$V_{OUT} = K \cdot \dot{z} - R_{COIL} \cdot I_{OUT}$	$V_{OUT} = K \cdot V - R_{COIL} \cdot I_{OUT}$
$F_{COIL} = K \cdot I_{OUT}$	$I_{COIL} = K \cdot I_{OUT}$
Notes: I_L and I_{RP} refer to the current defined as positive when flowing into the components from the upper LH node of the circuit. K, the electromechanical coupling coefficient, is given by $K=BlN$.	

Table 19: Equivalent circuit parameters

Magnetic model parameter	Equivalent Circuit model parameter
z	$\int V dt$
$\dot{z}$	V
F	I
c	$\frac{1}{R_P}$
m	C
k	$\frac{1}{L}$

7.3 Prototype generators

Prototypes were constructed to demonstrate the concept of magnet-coil generators. The prototypes were also designed to enable verification of the models presented above, and to illuminate some of the potential problems arising from the manufacture of such a device. The initial prototype (prototype A) was subsequently improved to produce prototypes B.

7.3.1 Prototype: A

A diagram and photo of the generator is shown in figure 59. The device consists of a cantilever beam supported in a clamp. At the tip of this stainless steel beam, a C-shaped core is mounted, with two magnets inside each end of the core. Attached to the clamp block, a coil consisting of 27 turns of 0.2mm diameter enamelled copper wire was wound so that each turn passes around the beam, including passing through the magnetic field in the core gap. The core was attached to the beam using double sided adhesive tape. It is acknowledged that this would be inadequate for a practical generator, however, for the short tests described here it performed well.

To test the device the shaker and measurement apparatus described in section 4.5.1 was used. The following experiments were performed:

(a) The resonant frequency was determined using the technique described in section 4.5.2. The following experiments were all performed with excitation at the resonant frequency.
(b) The open circuit coil voltage was measured for a range of different amplitudes of base vibration (base amplitude measured using an accelerometer; see section 4.5.1).
(c) Various load resistors were applied across the coil terminals, and the resulting load voltage, and electrical power measured for a fixed base excitation.
(d) The load voltage across an optimum load resistance was measured for a range of different amplitudes of base vibration

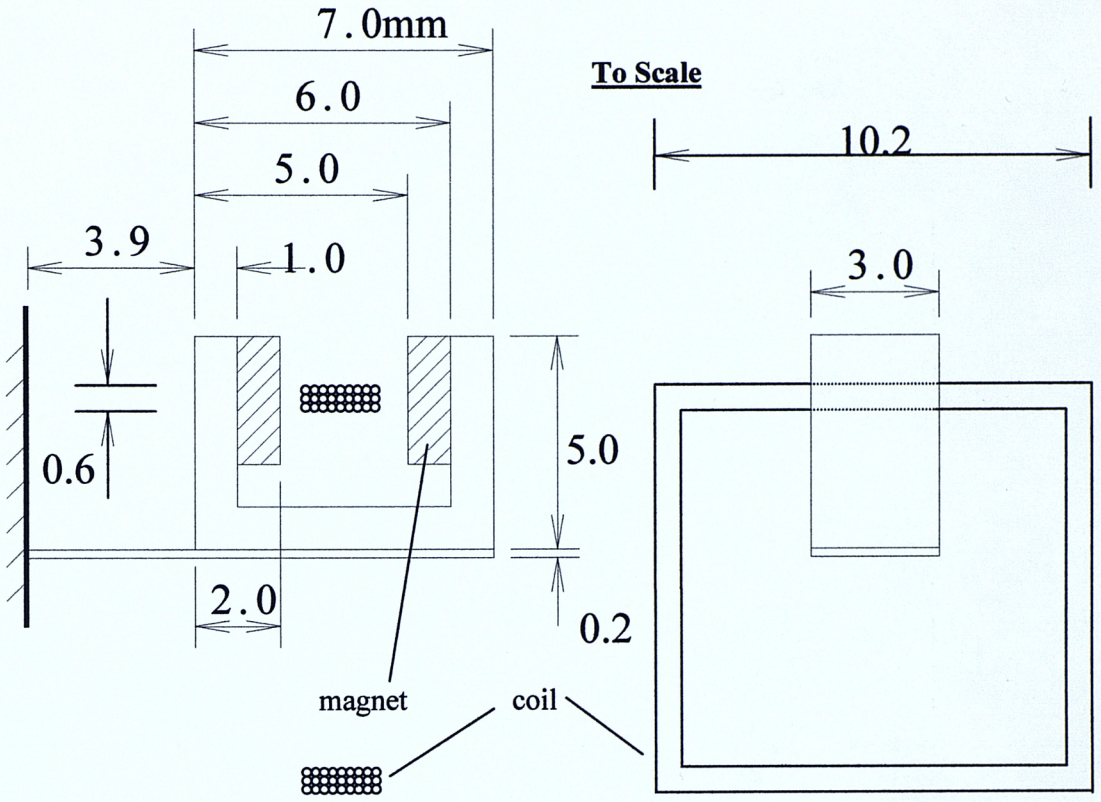

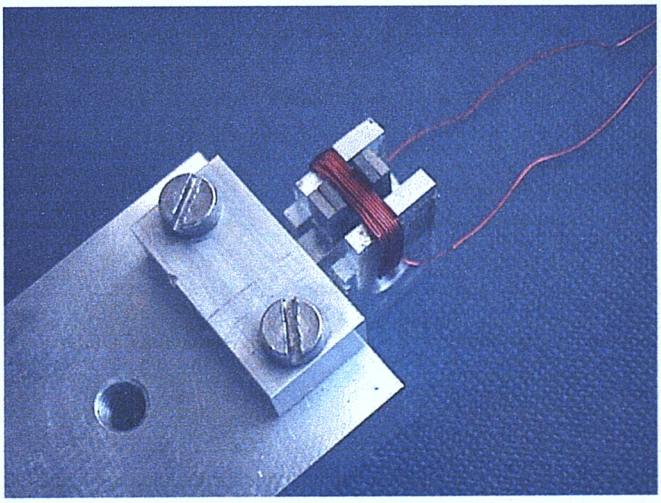

Figure 59: Prototype generator A

7.3.1.1 Results and Discussion

The device was found to have a resonant frequency of 322Hz (±1Hz). The results of experiments (b) to (d) are illustrated in the figures below.

The graphs show that the coil voltage is a linear function of amplitude, which indicates a uniform and constant magnetic field through the coil. The generator is shown to deliver most power to the load when an optimum load resistance of 0.6Ω is applied. A maximum power of 37μW was produced at a beam amplitude of 0.36mm. Beyond this amplitude, gradual shifts in the resonant frequency were observed, indicating that irreversible mechanical changes were occurring in the generator. This maximum amplitude could be increased by improving the mechanical stability of the generator (e.g. improving the bonding between the core and the beam). Tests showed that at a beam amplitude of 0.85mm up to 180μW could be produced.

This generator is reasonably small, and shows potentially useful amounts of power when it is shaken sufficiently hard. A major drawback with this design, however, is the very low output voltages developed across the coil. Section 7.5.1 discusses the issue of coil voltage, where it is proposed that such a voltage is essentially unusable by potential applications. This prototype is also difficult to manufacture, especially the requirement to have the coil pass around the beam. The second prototypes described below seek to address these problems.

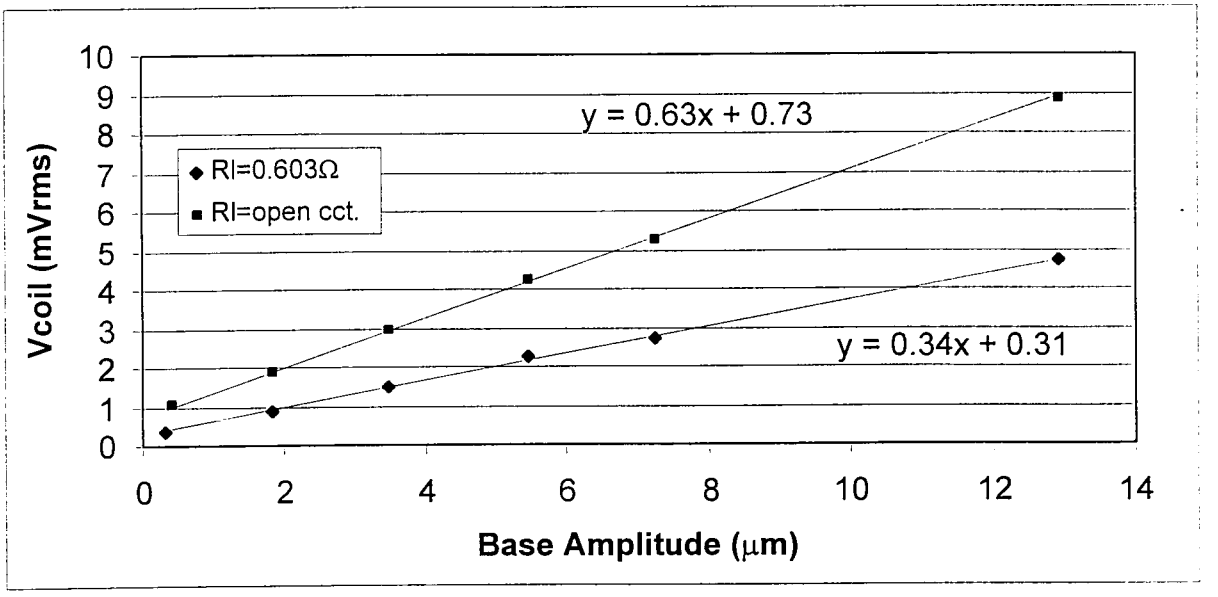

Figure 60: Coil voltage versus vibration amplitude, prototype A

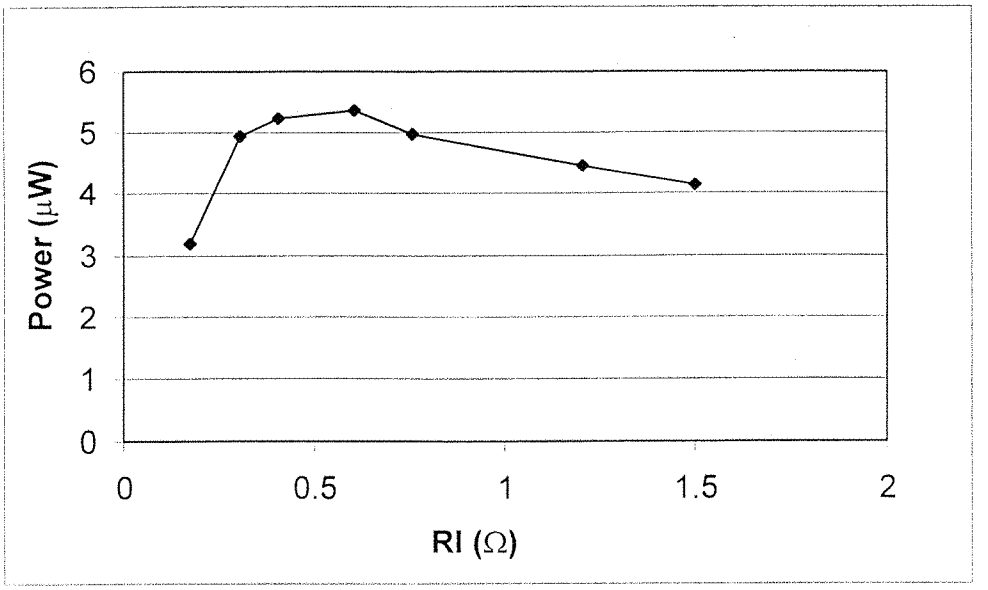

Figure 61: Power versus load voltage, Base amplitude=4.4μm, prototype A

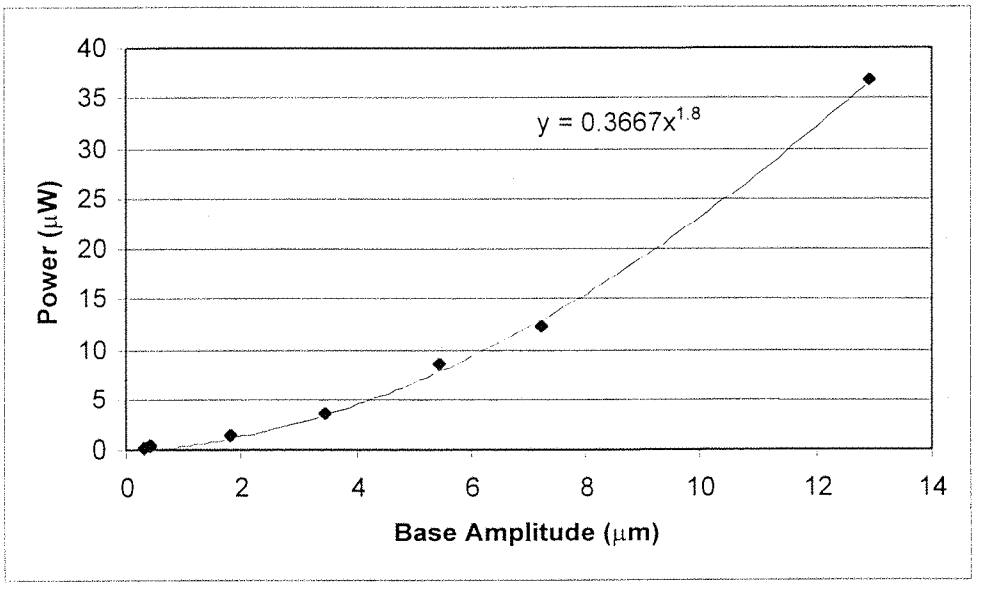

Figure 62: Power versus vibration amplitude with optimum load resistance, prototype A

7.3.2 Prototypes: B

This section describes three prototypes of different designs that are based on a similar construction method. Figure 63 shows the design of the prototypes, with the dimensions listed in table 20. There are three designs:

(1) B1 is a small cantilever beam generator.

(2) B2 is a larger cantilever beam generator.

(3) B3 is of a similar size to B2, but is a torsional resonator.

Figure 64 shows a photograph of a completed B2. The resonant frequency of the cantilever designs can be varied by adjusting the point at which they are clamped.

The common element in each design is the arrangement of the magnetic circuit (previously illustrated in figure 55c). On each generator, four magnets are mounted around a rectangular slot, and the flux guided around the outside by means of two steel keeper plates. Thus arranged, a magnetic circuit with two air-gaps is formed. The coil is passed through the slot so that when the beam rests in a central position, both the upper and lower portions of each turn pass through the magnetic field. The prototypes are designed so that during normal operation, the beam amplitude is never large enough to cause the coil to leave the magnetic gaps. The coils can thus be modelled as always remaining within a constant magnetic field. This arrangement is examined in more depth in section 7.4.3; the finite element model described in that section was used to iteratively pick core dimensions that provide both a gap wide enough for the coil, and a useful magnetic field strength in the gap. The predictions are compared to the measured values below.

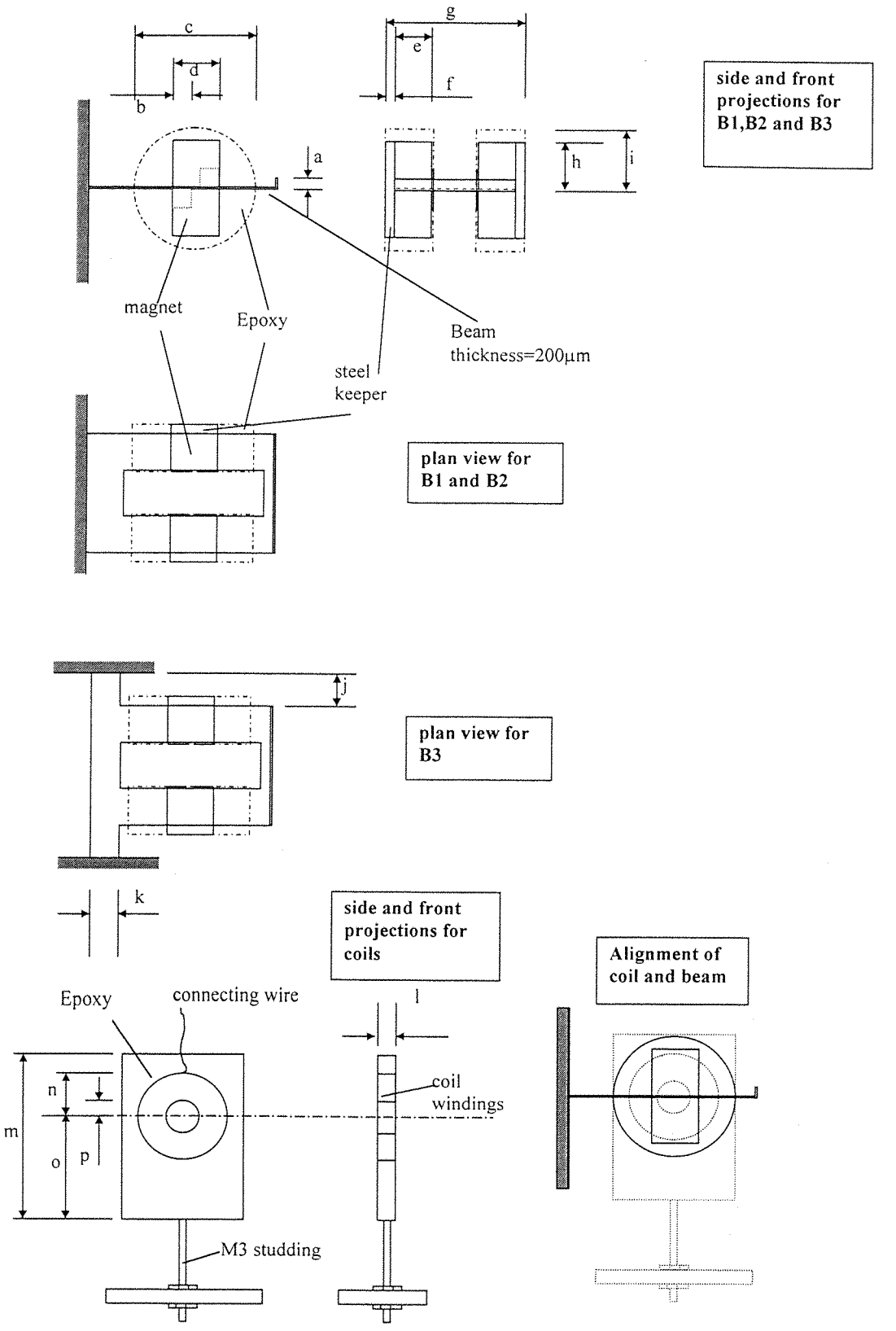

Figure 63: Designs for prototypes B1, B2 and B3

(see over for photographs)

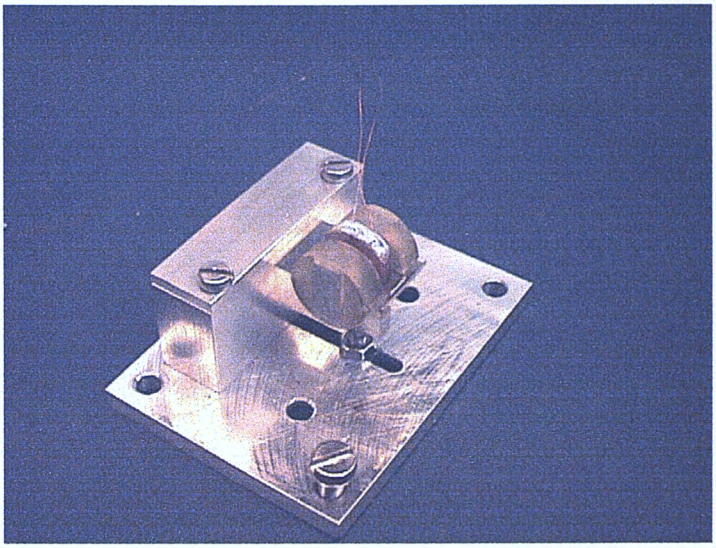

(a) Full generator

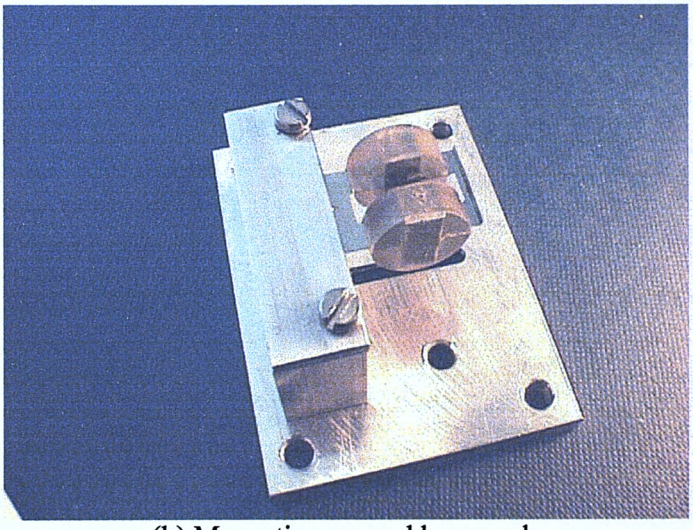

(b) Magnetic core and beam only

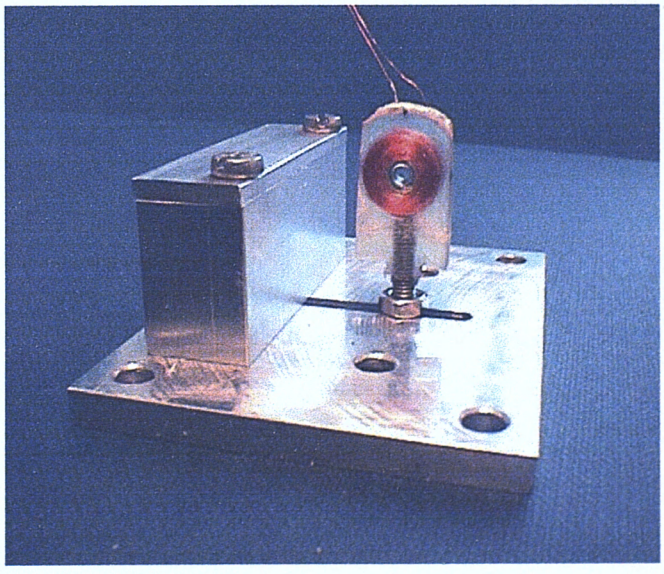

(c) Coil only

Figure 64: Photographs of generator B2

Table 20: prototypes B dimensions

Dimension from figure 63	Value (mm)		
	B1	B2	B3
a	1	1	1
b	2	2	2
c	8	13.5	13.5
d	3	5	5
e	2	4	4
f	1	1	1
g	10	15	15
h	3	5	5
i	3.5	6.5	6.5
j	-	-	3.5
k	-	-	3
l	2.5	3	3
m	16	20	20
n	2.5	5	5
o	12	11	11
p	1	2	2

7.3.2.1 Construction

Stainless steel sheets (302S25, hard) of 200μm thickness were photo-chemically etched to the designs shown in figure 65 (a commercial service supplied by Tecan Components Ltd). This etching includes partially etching along the base of the tabs marked with a dashed line in the diagram. Following the etching, these tabs were folded to an angle of 90 degrees. The tabs inside the slot are designed to hold the magnets in place, while the longer tab at the end of the beams serves to stiffen the structure to prevent distortion when the strong magnets are mounted close to each other. Two Neodymium Iron Boron magnets are put in place on one side of the slot, and the steel keeper plate placed across the outer poles of the magnets.

A mould, consisting of a disc shaped hole in a split aluminium block, is then prepared by covering it in a thin layer of a release agent, wax: the mould is heated to 75°C then candle wax (melting

temperature 60°C) is placed in the hole. The liquid wax is rolled around the mould, and as the mould cools an even layer is deposited. Capillary action draws away any excess wax leaving a film less than 0.05mm thick (measured using vernier callipers). The partially assembled beam is placed in the mould, and epoxy resin (Radio Spares potting epoxy, RS 561-628) is poured in using a syringe. The mould is then placed in a vacuum chamber to de-gas the epoxy. After the epoxy has hardened, the mould is heated to 70°C to release the beam. The epoxy is then filed down until it is flush with the inside of the slot. The process is repeated for the remaining pair of magnets.

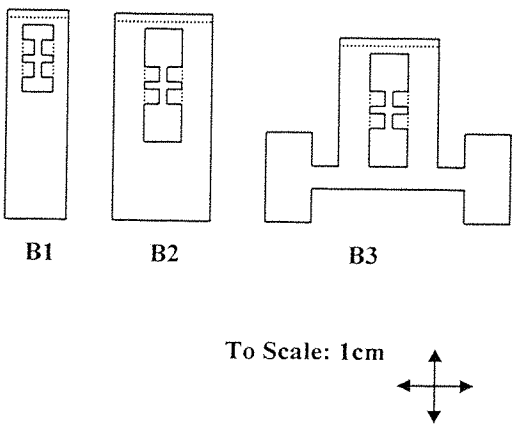

Figure 65: Photochemically etched steel beam designs

The coils are wound on a bobbin formed from a drilled out nut, and acetate sides. The bobbin is clamped in a hand drill, and 46swg enamelled copper wire is wound around the bobbin as the drill is turned. A gearing ratio between the handle of the hand drill and the chuck means that by counting the number of times the handle is turned, a larger number of coil turns can be wound on the bobbin. Once the wire has been wound on, blu-tak adhesive is pushed around the coil to form a mould. The mounting thread is placed next to the coil, and epoxy resin poured into the mould. After the resin is cured, the coil is filed down to leave the rectangular shape shown above in figure 63. To form the completed generator, the beam is clamped at its root, and the coil mounted in the correct position using the thread set in its epoxy. The clamp (seen in figure 64) is formed by an aluminium plate held in place on an aluminium block by a pair of threads in a similar manner to that used for piezoelectric generators (illustrated in figure 25).

7.3.2.2 Testing

The experiments performed on the prototype had the following goals:

(a) To generate data to verify the model presented in section 7.2

(b) To evaluate the amount of damping present in these devices, and establish whether a vacuum would significantly improve their Q-factor.

(c) To test whether the finite element analysis described above successfully predicts the magnetic field strength in the gap.

(d) To establish how much electrical power these particular devices can generate.

Many of the experiments described here require that the beam be excited at its resonant frequency. This resonant frequency is sensitive to beam amplitude, environmental temperature, and small variations in the clamping position. It is thus hard to achieve this resonant excitation with a fixed frequency signal generator - even small frequency errors can introduce significant errors when measuring quantities such as the Q-factor. A closed loop control circuit was developed to solve this problem. The circuit is described in appendix E, and consists of a phase-locked-loop (PLL) connected in positive feedback between the coil voltage and the shaker input.

Before the experiments were performed, calculations were performed (simple beam theory, see section 7.4.4) to determine the maximum beam amplitude that should be allowed to prevent damage through over straining the beam material. Table 21 lists the various configurations examined.

Table 21: Prototype parameters

Prototype	Beam length[1] (mm)	Measured Resonant frequency (Hz)	Maximum Deflection[2] (mm)
B1	17.1	106	2.44
	10.4	208	0.85
B2	11.75	99	1.15
B3	-	98.25	-[3]

(1) Distance from beam root to centre of mass.

(2) Deflection of mass required to generate a stress of 500MPa at beam root

(3) Not calculated since high amplitude testing not required (see below)

The following experiments were performed using the shaker and measurement apparatus described in section 4.5.1.

To investigate the Q-factor of the beams, the logarithmic decrement method was used. The transient response of the beam after it has been set moving by an impulse is examined. If the damping is purely viscous then the amplitude of successive cycles will decay logarithmically. The logarithmic decrement, δ, is defined as

$$\delta = \frac{1}{N}\ln\left(\frac{W_n}{W_{n+N}}\right) \qquad \textbf{Equation 7.1}$$

where N is a number of cycles, and W_n and W_{n+N} are the amplitudes of cycles separated by N cycles. If the damping factor, ζ, is small then it can be shown [51] that

$$\zeta \approx \frac{\delta}{2\pi} \qquad \textbf{Equation 7.2}$$

The circuit shown in figure 66 was used. Beams were excited at their resonant frequency using a sinusoidal waveform from the signal generator applied across the coil. The signal analyser was connected as an oscilloscope across the electrodes of the coil to monitor the voltage. A double-throw switch is used to simultaneously disconnect the signal generator, and generate a trigger signal to the oscilloscope. When the switch is thrown, the scope triggers, and the decaying waveform can be examined. In each case the decay was measured over a total of 12 cycles, with an initial coil voltage amplitude of 250mV. The clamp design includes a vacuum-sealed cover so that the air surrounding the beam could be evacuated with a vacuum pump.

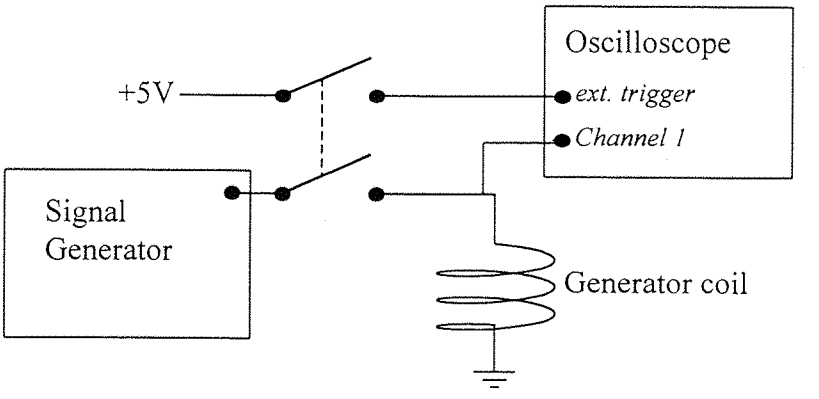

Figure 66: Q-factor test circuit

Table 22 shows the results. Each entry represents the average of four readings, an error of around 10% is associated with each entry. The Q-factors were also measured in a partial vacuum for the B1 beams, but this vacuum was found to have little measurable effect. It is thus deduced that support damping accounts for the majority of the damping observed (material damping is also

present, but will be less significant). The first two rows also show an increase in Q-factor as the frequency is increased from 106Hz to 208Hz. The torsional resonator, B3, can be compared to the beam, B2, which has the same size core mounted on the end of the beam. It can be seen that the torsional resonator shows a lower Q-factor than the planar spring case. For this reason, B3 is not tested further in this section, as B2 is seen to perform better.

Table 22: Prototype Q-factors

Beam	Frequency (Hz)	Q-factor in air	Error (%)
B1	210	120	10
B1	110	140	10
B2	99	86	10
B3	98	66	10

To measure the strength of the magnetic field in the gap of each generator, experiments were performed to measure the open circuit coil voltage as a function of beam amplitude. Figure 67 shows the results for beams B1 and B2. They show a good degree of linearity, which means that the magnetic field around the coil remains constant over the full range of even the larger amplitudes of vibration shown here. The zero intercept of the graphs is poor, due to the difficulty involved in zeroing the vernier screw-gauge. The magnetic field, B, is calculated using the formula:

$$B = \frac{V_{COIL}}{N \cdot l \cdot |\dot{x}|} = \frac{V_{COIL}}{N \cdot l \cdot A\omega}$$

where l is the length of coil in the field, and A is the amplitude of the displacement, x.

Table 23 lists the measured values, and the values predicted using the FEA model described below in section 7.4.1. The FEA model is within 12% of the measured value, the underestimation of the field strength by the model is probably due to the fact that the keeper pieces surrounding the outside the core are thin, and will thus have some flux leakage that is not described in the model.

Table 23: Magnetic field values

Beam	Magnetic Field, B (T)	
	Measured	Predicted
B1	0.192	0.214
B2	0.239	0.267

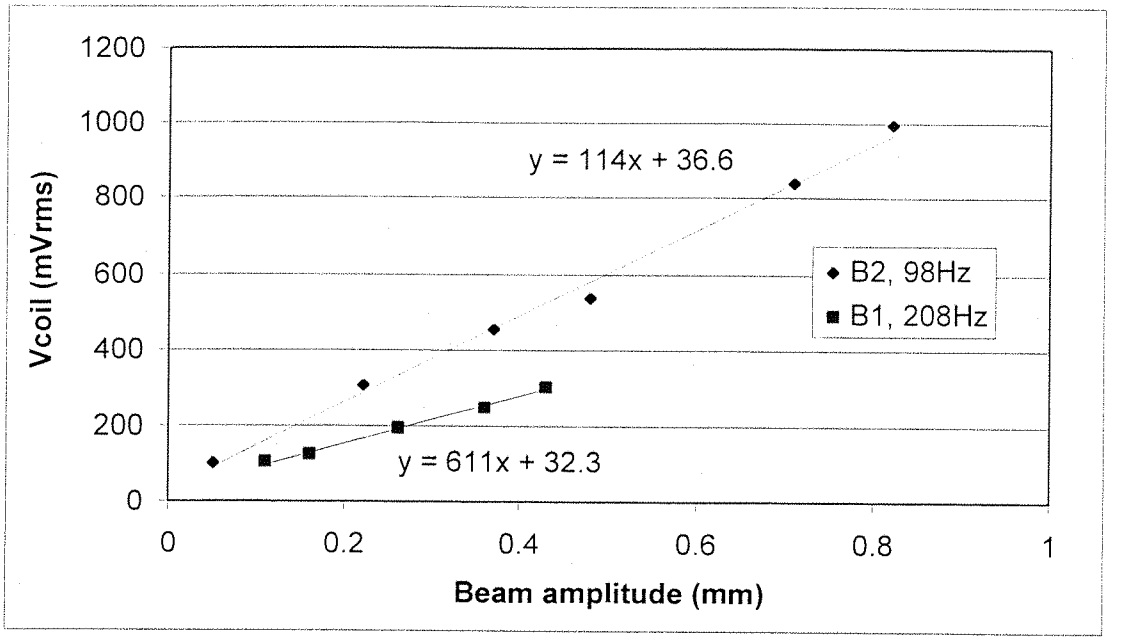

Figure 67: Coil voltage versus beam amplitude, prototype B

Figure 68 shows how the power delivered to the load varies with its resistance. The data was obtained for beam B1 at a frequency of 208Hz for a range of different base excitations. The figure includes the predictions made by the equivalent circuit model described above. The mass used in the model was calculated from the stiffness of the beam (derived from simple beam theory), and the measured resonant frequency. The reason for using this value rather than the actual measured mass of the beam is that the beam is short compared to the length of the mass, and significant rotational inertia will be present. By calculating the mass in this way, an equivalent mass is derived that takes this into account.

The graph shows that the model provides a reasonable prediction. The graph illustrates the existence of an optimum load resistance for extracting power from a generator. The value of this optimum load resistance is shown by the equivalent circuit model to be equal to the sum of the coil resistance and the equivalent resistance of the damping losses.

Table 24 lists the maximum power that can be generated from each of the prototypes discussed above. It is based on the generators being shaken at sufficient amplitude that the beam vibrates with the maximum permitted amplitude (see table 21 above). The prototypes can be seen to be capable of producing useful (see section 3.3) amounts of power. It is hard to compare the power densities meaningfully; it was hoped that the different designs would have more widely varying volumes, but since the thickness of the beam was held constant the beam length had to increase as the core size decreased to produce the required resonant frequencies. This means that the devices are of similar volume; with a thinner beam, the smaller prototype, B1, could be made smaller but still produce a similar power output.

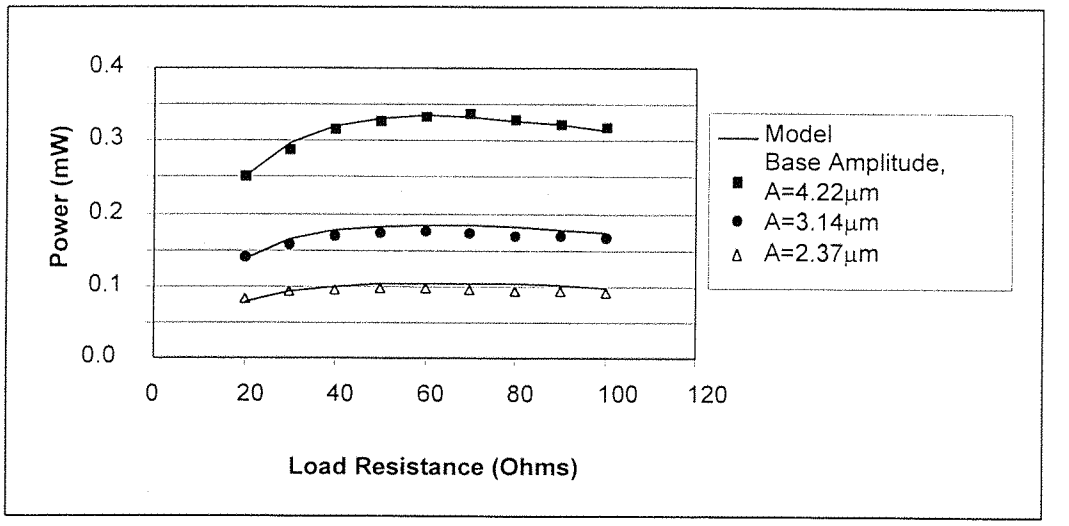

Figure 68: Power versus load resistance, beam B1

Table 24: Prototype power results

Beam	Frequency (Hz)	Maximum Deflection (mm)	Optimum Load (Ohms)	Base amplitude (m)	Power (mW)	Volume (cm^3)	Power density (W/m^3)
B1	106	2.44	100	2.94E-05	2.80	3.66	0.765
	208	0.85	70	1.13E-05	2.37	2.04	1.16
B2	99	1.15	240	1.77E-05	4.99	4.08	1.22

The following experiment was performed to demonstrate that the technology has the potential to be useful in a practical application. Generator B2 was mounted within a die-cast aluminium box for screening. The generator's coil was loaded with a 240Ω resistor. The voltage from the load

was rectified, and then smoothed with an R-C circuit with a time constant of 0.5s. The resulting average load voltage was monitored using a Gemini data logger (model: TINYTAG RE-ED Volt), which took a reading once a second. The generator was mounted on the top of the engine block of a Volkswagen Polo (5 years old). Experimentation showed that the power produced by the generator was largely determined by the engine speed with a resonant peak at around 3000 revs/s, perhaps relating to a resonance in the engine mounting. Figure 69 shows data taken from a typical short drive in the Highfield area of Southampton. During the three minute run, 1.24km was covered at an average speed of 25kmph. The run includes stops at three traffic lights. The major peaks seen on the graph occur as the engine reaches the 3000 revs/s resonance described above. Over the period, an average power of 157μW was produced, with a peak value of 3.9mW. This demonstrates that an application in this environment could feasibly generate enough power to perform useful tasks. Further work would be required to examine this concept in detail.

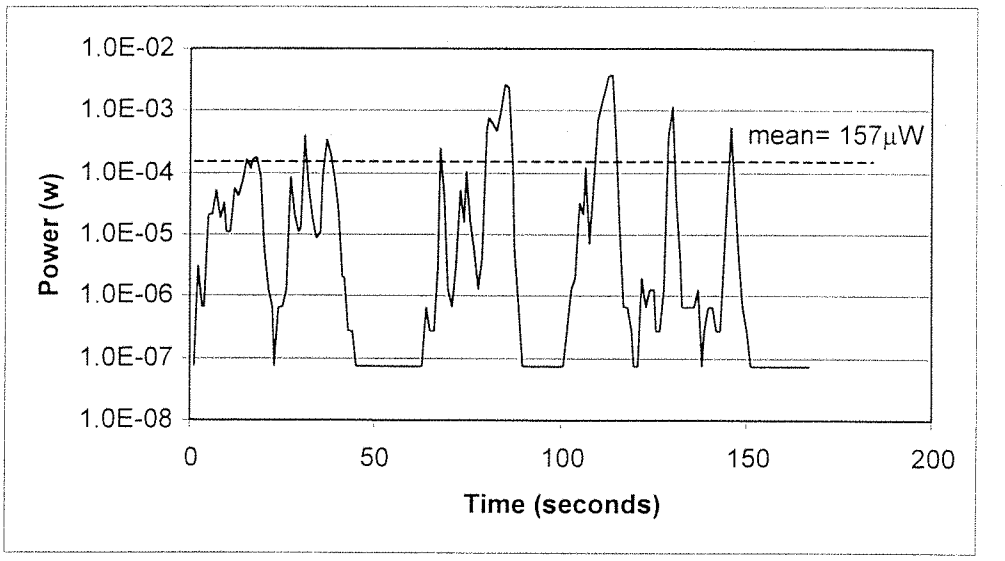

Figure 69: Demonstrator power during a driving trip

7.4 Theoretical Limits for electromagnetic generators

Two types of magnet-coil generator design will be explored here. The first, the vertical-coil configuration, is similar to the prototypes described above. To simplify the analysis some assumptions are made, which lead to expressions for the amount of power this configuration might ideally and practically be expected to produce for a range of different base excitations and generator sizes. Due to the assumptions, however, the model is not adequate for some types of excitation. A second configuration, the horizontal-coil configuration, is then considered. This

design is geometrically simpler, which means that the assumptions can be relaxed to provide a more widely applicable model. It is shown that the first design can produce more power, but the more complex nature of the model means that the simpler second design is used for comparing magnet-coil generators to piezoelectric ones. In the first configuration the coil is fixed relative to the enclosure, and in the second the magnet is fixed to the enclosure; this was chosen to simplify the modelling process. In practice, either configuration could be used with either a fixed or a moving coil. Both of the configurations have a common magnetic core design that will be analysed first.

7.4.1 Magnetic Core Analysis

The core analysed here is of a similar configuration to that used in prototype B described above. Figure 70 shows the design, which comprises of four block-shaped magnets, and a pair of keeper blocks made from a ferromagnetic material. The magnets in the core have length, l_m, and thickness, t_m. The ferromagnetic rods have length, l_c, and thickness, t_c. The gap between the two magnets is given by g. The depth of all parts is equal, and is given by T

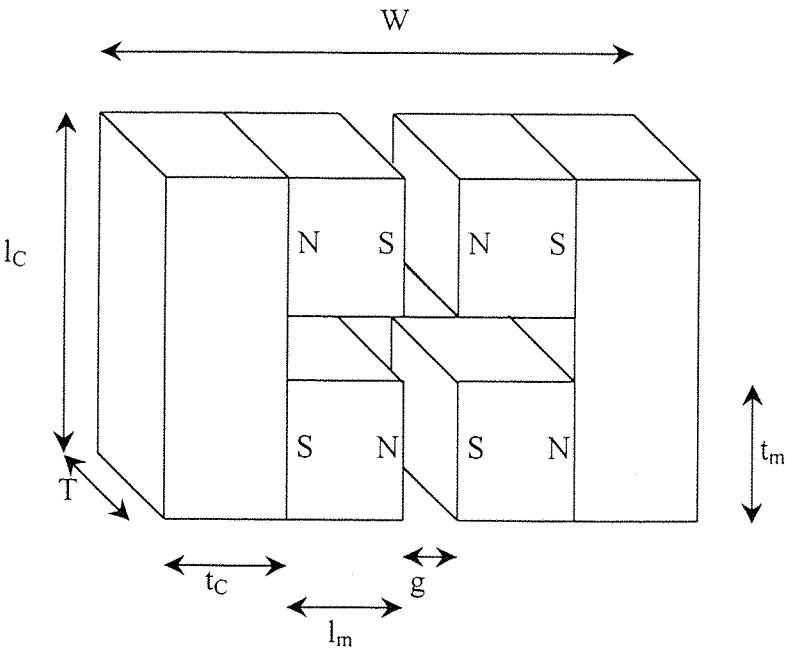

Figure 70: Magnetic core design

To explore the effect of core geometry on the magnetic field in the air gap, a finite element model was generated using the ANSYS computer package. The model (the listing is given in appendix F) exploits the symmetry of the design, and simulates only a quarter section. The model is a

planar one, and ignores any edge effects in the depth direction. The model for a typical set of dimensions is shown in figure 71, and is annotated to show boundary conditions.

The magnet regions of the model are given the material properties of Neodymium Iron Boron magnets. The ferromagnetic bars are modelled as having a linear B-H characteristic, with a relative permeability of 5000. The exact value of the permeability is not critical, as the reluctance of the large air gaps will tend to dominate the results. Saturation is ignored during the finite element analysis, but the design is checked after the modelling to ensure it does not occur.

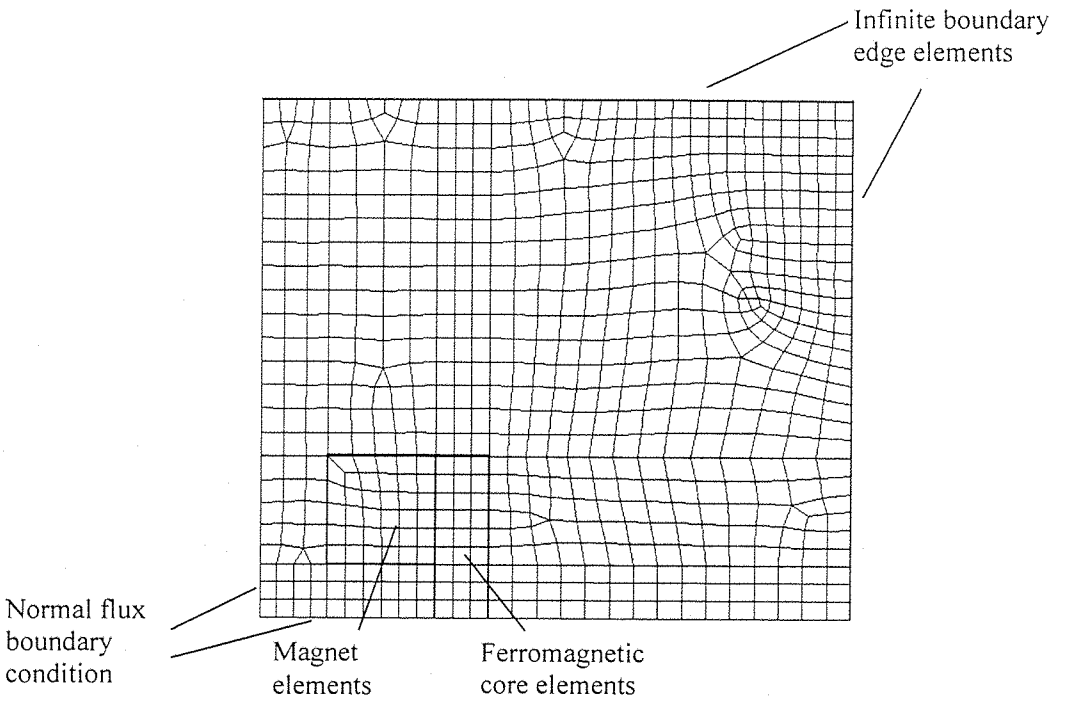

Figure 71: FEA model of magnetic core

Figure 72 shows typical magnetic flux patterns for different extremes of geometrical configuration. When the magnets are close together, (a), most of the flux lines flow straight across the gap, with little leakage. As the magnets are separated (b), some of the flux curls around between magnets on the same side of the core. This can be partially alleviated by increasing the length of the core (c).

A batch program (see appendix F) was written to automatically vary the geometrical parameters of the model, and calculate suitable output data. Output data included the B-field, and the value

of $\int_{airgap} B^2 dA$ for each configuration. The value of this integral is proportional to the magnetic energy stored by the magnetic field in the air gap. Since the model is a linear one, the B-field predicted by the model is scale invariant. Thus, the parameter t_m was fixed during the analysis, and the parameters g, l_m, and l_c varied as proportions of t_m. The core thickness, t_c, has little effect on the resulting field pattern (so long as it is sufficiently large) and was set to a value of $2t_m$. It was found that the effect on a typical configuration of doubling t_c is to increase the average magnetic field in the air gap by only 0.3%.

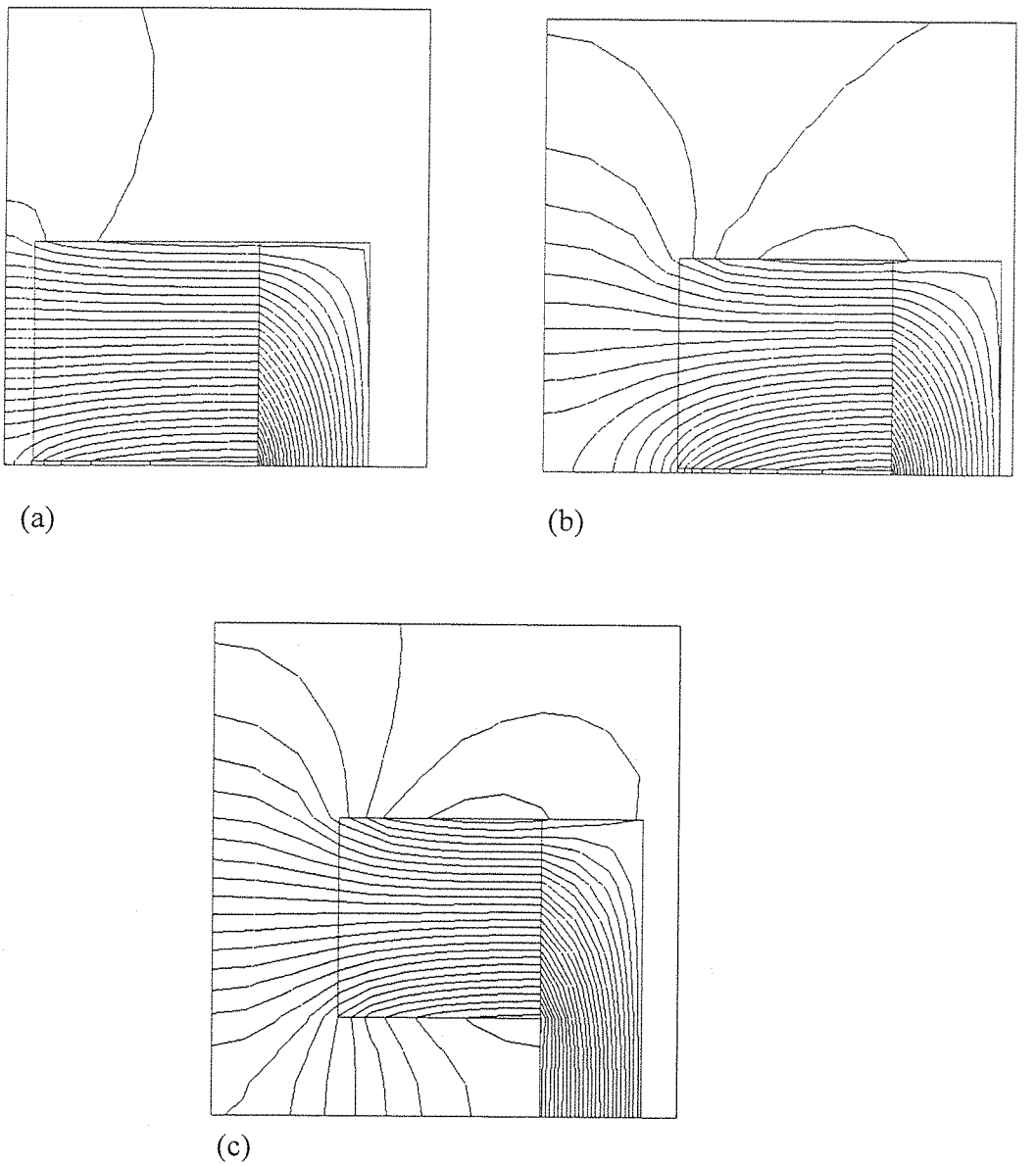

Figure 72: The effects of varying core parameters

After processing, the simulation yields a 3-dimensional data set showing the results for each combination of g, l_m and l_c. For each data point the minimum value of t_c that would avoid magnetic saturation in the core was determined (assuming a value of B_{sat} of 2 Tesla), which in turn permitted the total width of the core, W, to be found for each point.

A variable ψ which relates to the amount of magnetic energy stored per core volume, is defined as

Equation 7.3

$$\psi = \frac{\int_{airgap} B^2 dA}{\text{total area of core}}$$

The importance of this quantity for a core in a generator design is described below in sections 7.4.2 and 7.4.3. By examining the data-set from the batch program it is found that there exists a single maximum for ψ in the three-dimensional parameter space of l_m/l_c , g/l_c , t_m/l_c.

The optimum dimensions are listed in table 25, and illustrated in the scale drawing, figure 73. The error associated with each of the entries in the table estimates the potential error between the stated value, and the actual value of the parameter at the maximum. The error is a result of numerical noise in the output data, which is caused by non-ideal element shapes in thinner areas of the model. This noise blurs the position of the maximum. It should be noted that ψ tends to decrease more slowly as g and lc are increased from their optimum value than if these quantities are decreased. Thus to ensure a good value of ψ in a design, it is better to err on the side of large g and l_c.

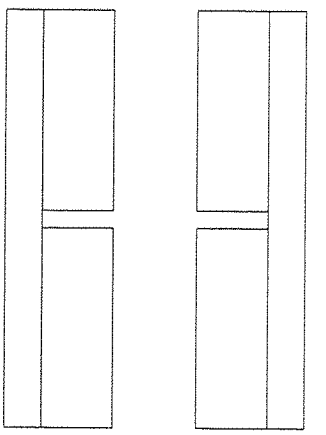

Figure 73: Optimum core design (dimensionless, to scale)

The resulting field pattern for the optimum design is shown in figure 74. The existence of this maximum and the associated optimum dimensions for a core will be utilised in the analyses that follow., , l_m/l_c , g/l_c, , t_m/l_c ,

Table 25: Optimum core dimensions

Parameter	Value	Error (%)
W/l_c	0.71	6
l_m/l_c	0.17	24
g/l_c	0.195	15
t_m/l_c	0.48	2
t_c/l_c	0.087	12
$\Psi=\psi_{max}$	0.0491	0.5
Average B-field	0.366	11

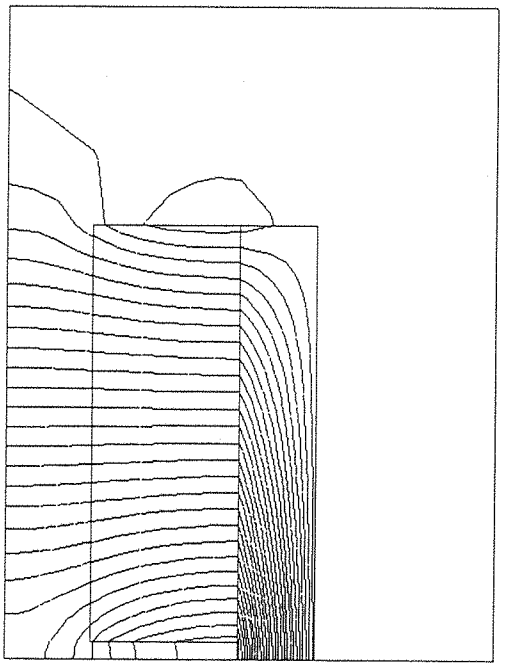

Figure 74: Field pattern for optimum core design

It should also be noted that if the dimensions determining the maximum size of the generator are not of the correct proportions to produce this optimum design, the optimum value can be

approached by splitting the available volume into several smaller volumes of a more ideal proportion.

7.4.2 Vertical-coil Configuration

The calculations in this section are based on the design of magnet-coil generator shown in figure 75. The generator fits within an enclosure (box) of length, L; height, H; and depth, T. It consists of a beam (spring) of length l_s attached to the magnetic core described above. In the space between magnets and also extending outside of this space is a coil of N turns, whose turns can each pass twice through the magnetic field. The coil is fixed relative to the enclosure. The coil is approximated by straight wires that run parallel to the depth for the full depth of the device; the part of the coil that connects these parts together at each end is approximated as being of negligible volume. A resistive load of R_l is connected across the coil, and the resistivity of the coil material is given by ρ. The total mass of the core attached to the beam is given by m, and the system has a natural circular frequency of ω_n. The flux density in the region between the magnets is approximated as uniform, and is given by B. Excitation is supplied to the base of the beam with a peak amplitude of α.

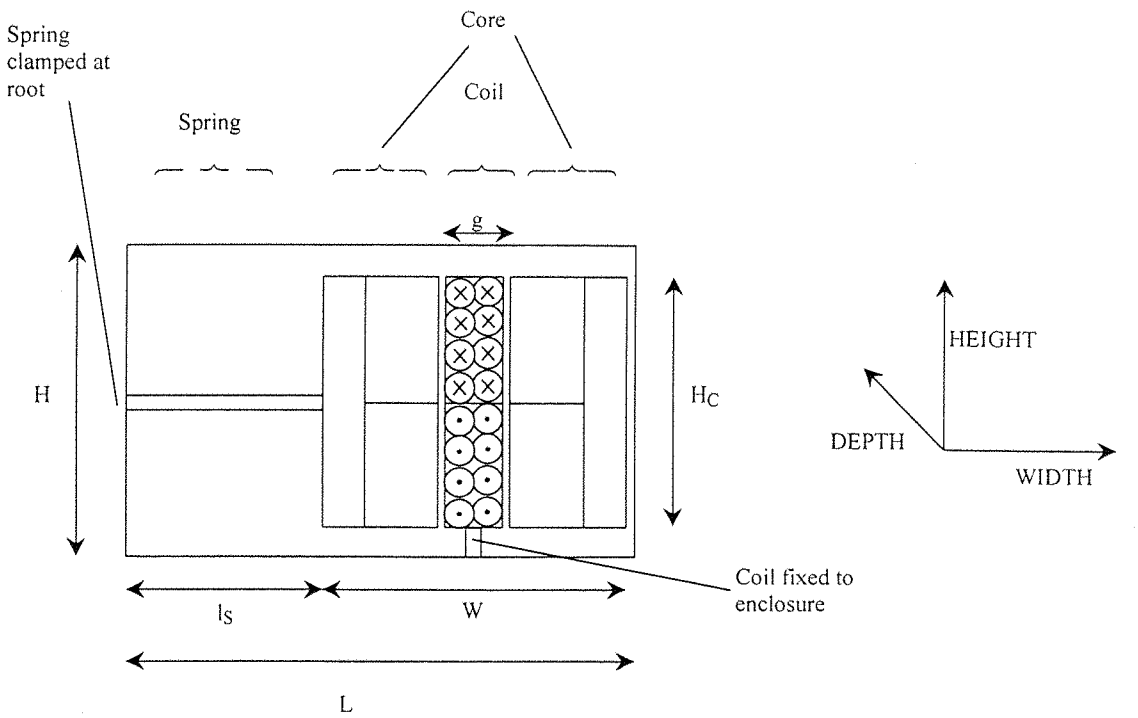

Figure 75: Vertical-coil generator configuration

For simplicity, the clearance required at the end of the box to prevent the corners of the core touching the end wall will be assumed to be small enough to be ignored in the following analyses. As a further approximation, it will also be assumed that the amplitude of the beam is small enough that rotation of the core can be ignored.

7.4.2.1 Analysis

First, assume that the amplitude of the beam is small compared to the size of the core. This means we can make the approximation that the coil is always in a constant, uniform magnetic field. This assumption is assessed below. It was shown above in section 7.2, that this arrangement can be represented by the equivalent circuit shown in figure 76(a). The device is operated at resonance, which means that the impedances of the capacitor and inductor cancel each other out. The circuit parameters take the following values:

$$I_{ACEL} = m \cdot \alpha \cdot \omega_n^{\,2}$$

$$R_p = \frac{Q_u}{m \cdot \omega_n}$$

where Q_u is the quality factor of the electrically-unloaded beam resulting from unwanted support and gas damping. K, the electromechanical coupling factor, is given by:

$$K = 2B \cdot T \cdot N$$

The factor of two is a result of the fact that each turn of the coil passes twice through the magnetic field. R_C, the coil resistance, is calculated by assuming that the insulation on the coil is negligibly thin, and that the coil occupies the full width of the gap in the core. In practice a small clearance gap would be required.

$$R_C = \frac{\rho \cdot \text{coil length}}{\text{X - sectional area of each turn}} = \frac{\rho \cdot (2 \cdot N \cdot T)}{\left(\frac{g \cdot \frac{H_C}{2}}{N} \right)} = \frac{4\rho \cdot N^2 \cdot T}{g \cdot H_C}$$

Equation 7.4

where ρ is the resistivity of the coil material.

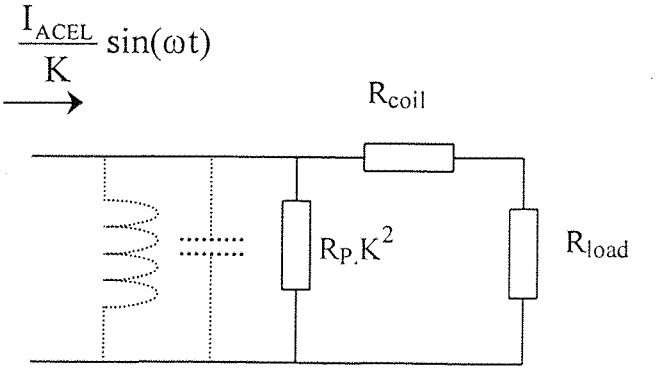

(a) Equivalent circuit

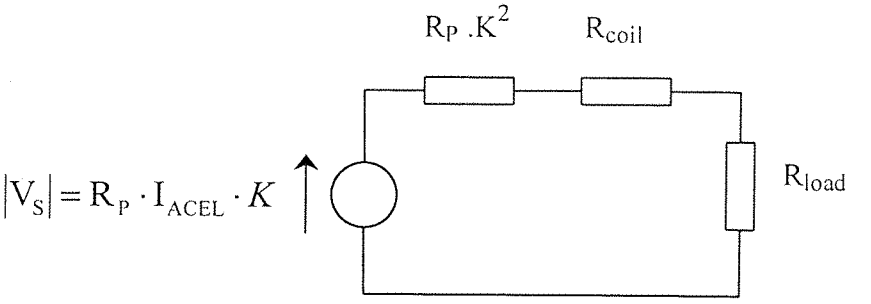

(b) Transformed circuit

Figure 76: Vertical-coil equivalent circuit

Transforming the current source, and the parallel resistance R_P using Thevenin's equivalent circuit, circuit (b) is obtained. Circuit theory shows that maximum power can be delivered to the load by matching the load impedance, R_L, to the source impedance:

$$R_L = \frac{K^2 Q_u}{m \cdot \omega_n} + R_c$$ **Equation 7.5**

The voltage across the load resistor is now given by

$$|V_L| = \frac{|V_S|}{2}$$

The power delivered to the load resistor, P_L, is given by

$$P_L = \frac{|V_L|^2}{2R_L} = \frac{|V_S|^2}{8R_L} = \frac{(K \cdot Q_u \cdot \alpha \cdot \omega_n)^2}{8\left(\frac{K^2 Q_u}{m \cdot \omega_n} + R_c\right)}$$

Equation 7.6

Substituting for R_C, and K and factoring out an expression for the core volume (TH_CW), we have

$$P_L = T \cdot H_C \cdot W \frac{(Q_u \cdot \alpha \cdot \omega_n)^2}{8\left(\frac{Q_u}{\left\{\frac{m}{T \cdot H_C \cdot W}\right\} \cdot \omega_n} + \frac{\rho}{\left[\frac{g \cdot B^2}{W}\right]}\right)}$$

Equation 7.7

An important feature of this equation is that the power that can be generated by the core of this generator is proportional to the volume of that core (the term in curly brackets is equal to the average density of the complete core, and is thus independent of volume). In addition, the amount of power that can be generated is independent of the number of coil turns (although the number of turns does affect the optimum load resistance). This means that N can be chosen independently of the other geometric parameters, and hence simplifies the problem of finding an optimum design for a given application. In practice N will be chosen to give a suitable output voltage across the coil (see section 7.5.1, below).

The term in square brackets $[...]$ can be seen to be approximately equal to the value of the variable ψ, that was discussed above in section 7.4.1. It was seen in that section that there exists a maximum value for ψ, Ψ, corresponding to a certain geometrical configuration. For the purposes of this analysis this value of ψ *is* used. Although the shape of the generator may not permit these exact proportions it will be assumed as an approximation that this value of ψ can be approached. This configuration will not be the optimum generator design, since there are **two** other terms that also depend on the geometrical configuration in the expression for P_L. The **first** is the amount of unwanted damping, represented by Q_u; this will be a complicated function of geometrical parameters, beam amplitude, and other factors such as details of the spring clamping at the beam root, that are not modelled in this analysis. It is acknowledged that variations in this parameter will have a significant effect on the power output, but by using the value of Q obtained experimentally, it is hoped that this analysis will provide a useful indication of how much power might typically be expected. The **second** is the term in curly brackets $\{...\}$ that represents the average density of the core, excluding the mass of the coil. There may be cases (especially at low

excitation) when more power could be generated by decreasing the gap, g, from the optimum value predicted in section 7.4.1. By doing this the electromagnetic coupling (and hence ψ) will be reduced, but the mass will be increased. In the limit, when the mass term dominates, this could increase the power by a maximum of 38% (the increase if the mass term dominates and the gap is reduced to zero, given the material parameters used below). The scale of this difference is noted, but it is felt that the simplicity of the analysis makes its predictions useful. Thus this analysis can not claim to show the most optimum design for a generator, but instead examines this particular case (which in the author's opinion will be close to the optimum design in most cases).

The mass attached to the end of the spring, m, is given by the product of the volume of the core and its average density, D.

$$m = WTH_C D\beta \qquad \textbf{Equation 7.8}$$

where β is the ratio of gap to core width, found above to have a value of 0.275 for an optimum field (for the materials examined there).

Thus, we can write

$$P_L = T \cdot H_C \cdot W \frac{(Q_u \cdot \alpha \cdot \omega_n)^2}{8\left(\frac{Q_u}{D\beta \cdot \omega_n} + \frac{\rho}{\Psi}\right)} \qquad \textbf{Equation 7.9}$$

For a given core size, base excitation, and level of unwanted damping, equation 7.9 enables us to determine how much power can be produced. To find the power that can be generated within a given volume, we must also allow for the space required for beam movement, and the space required for the spring. The space required for the beam amplitude can be calculated exactly, or if we assume that the damping induced by the coil resistance is small compared to the unwanted damping (which it is in the examples discusses below), then as a result of the impedance matching, the total Q-factor of the loaded beam can be approximated as $0.5*Q_u$, so that beam amplitude, A, can be written;

$$A = \frac{1}{2} Q_u \cdot \alpha \qquad \textbf{Equation 7.10}$$

The space required in the generator for a spring is considered in section 7.4.4. Example predictions for this configuration will be listed in table 27 after the next configuration has also been analysed.

7.4.3 Horizontal-coil Configuration

A horizontal-coil generator of the form shown in figure 77 will now be considered. The figure shows a magnetic core of the type described above, with a gap, g, that is fixed relative to an enclosure (box) of length, L; height, H; and depth, T. A beam (spring) of length l_s is clamped at one end, and attached at the other to a coil. The coil encircles the magnetic core, passing once through the field-gap. To simplify the model, the space required for the coil to pass around the sides of the core is ignored. The coil has a height, l_w, and consists of N turns. A resistive load of R_l is connected across the coil, and the resistivity of the coil material is given by ρ. The total mass of the coil attached to the beam is given by m, and the system has a natural circular frequency of ω_n. The flux density in the region between the magnets is assumed to be uniform, and is given by B.

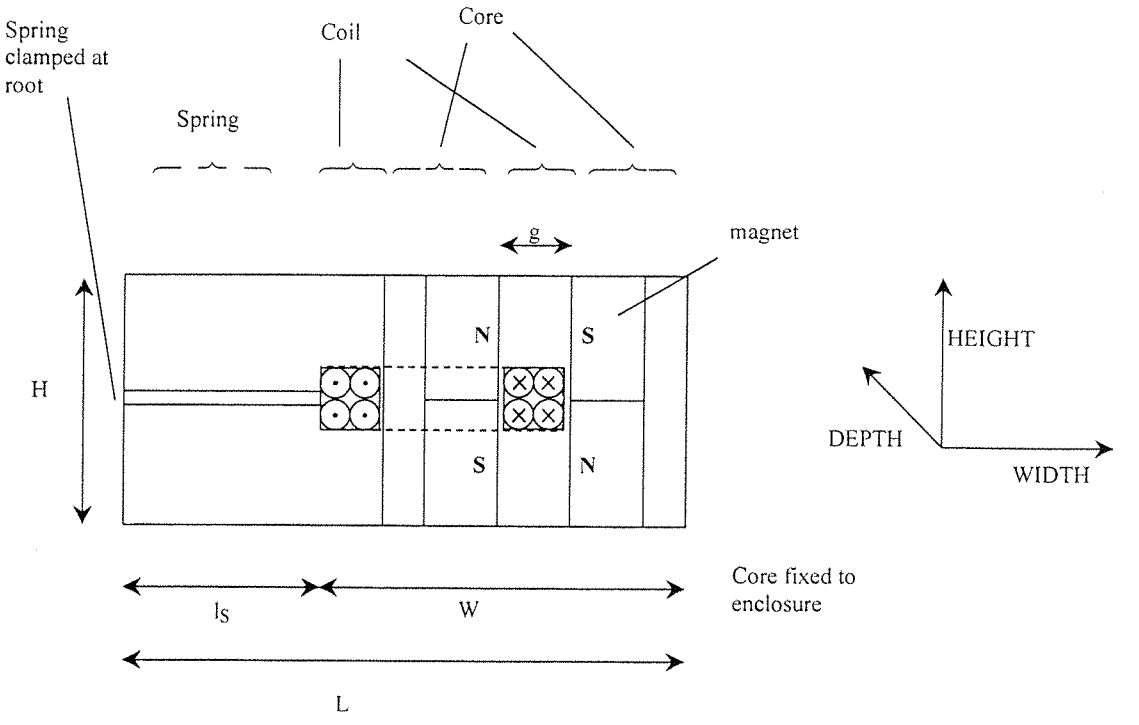

Figure 77: Horizontal-coil generator configuration

As before, the clearance required to prevent the coil touching the magnet will be assumed to be small enough to be ignored in the following analysis. As a further approximation, it will also be assumed that the amplitude of the beam is small enough that rotation of the coil can be ignored.

The resistance of the coil, R_{coil}, can be expressed as

$$R_{coil} = \frac{\rho l}{A} = \frac{2\rho n^2 l_w T}{g}$$ **Equation 7.11**

where n, the winding density, is given by

$$n = \frac{N}{l_w}$$

The mass of the horizontal coil is given by

$$m = 2l_w \cdot g \cdot T \cdot D$$ **Equation 7.12**

where D is the average density of the coil.

Harmonic motion is assumed, with time measured from the position of extreme negative displacement.

$$x = -A\cos(wt)$$ **Equation 7.13**

where x is the displacement of the coil, and A is the amplitude of motion. The energy delivered to the electrical circuit by the generator during one cycle of operation, W_d, can be calculated by integrating the force applied on the magnet by the coil over a full cycle.

$$W_d = 4\int_{-A}^{0} Force(x)dx = 4\int_{0}^{\frac{\pi}{2}} Force(\omega t)\frac{dx}{d(\omega t)}d(\omega t)$$ **Equation 7.14**

The total force on the magnet from the coil is given by

$$\begin{aligned} Force(\omega t) &= \left(\sum^{\text{all turns}} B\right) T I_{COIL} \\ &= \left(\sum^{\text{all turns}} B\right) T \cdot \frac{V_{COIL}}{R_{coil} + R_l} \\ &= \left(\sum^{\text{all turns}} B\right) T \cdot \frac{\left(\sum^{\text{all turns}} B\right) T \dot{x}}{R_{coil} + R_l} \\ &= \frac{T^2 \dot{x}}{R_l + R_{coil}} \left(\sum^{\text{all turns}} B\right)^2 \end{aligned}$$ **Equation 7.15**

Thus,

$$W_d = 4\int_0^{\frac{\pi}{2}} \frac{T^2 A^2}{(R_l + R_{coil})} \omega \sin^2(\omega t)\left(\sum^{\text{all turns}} B\right)^2 d(\omega t)$$

Equation 7.16

The summation ($\sum^{\text{all turns}} B$) depends of the displacement of the coil.

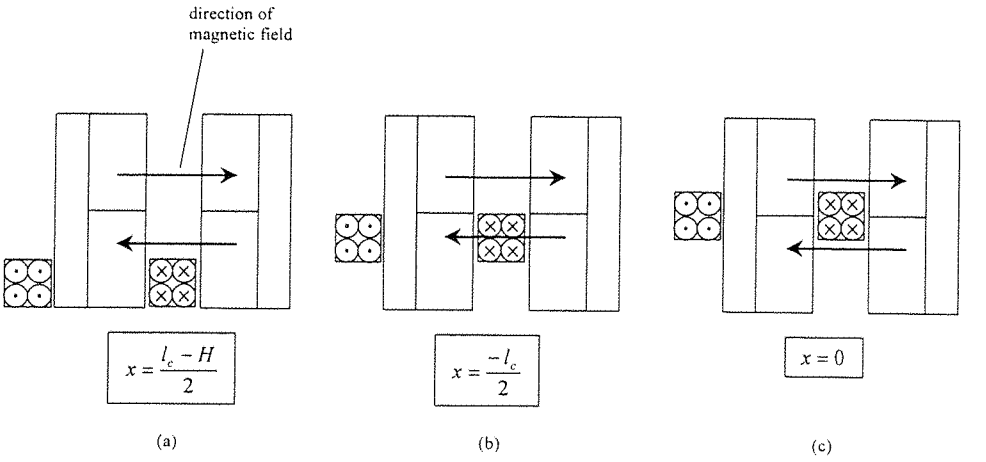

Figure 78: Coil positions relative to core

If the coil lies entirely in one half of the core, as depicted in any of the positions lying between the states shows in figure 78(a) and (b), then we have

$$\sum^{\text{all turns}} B = Bnl_w \quad -A < x < -\frac{l_w}{2}$$

Equation 7.17

If the coil crosses between the two halves of the core (positions lying between states shown in figure 78(b) and (c), then we have

$$\sum^{\text{all turns}} B = \int_{x-\frac{l_c}{2}}^{0} Bndh - \int_{0}^{x+\frac{l_c}{2}} Bndh \quad -\frac{l_w}{2} < x < 0$$

Equation 7.18

The two integrals evaluate the field in the portions of the coil in the two halves of the magnetic core. The sign change between the integrals reflects the field changing direction between the two halves. Evaluating the integrals we have,

$$\sum^{\text{all turns}} B = -2Bnx = 2BnA\cos(\omega t) \quad -\frac{l_w}{2} < x < 0$$ **Equation 7.19**

Substituting the above into equation 7.16 we have

$$W_d = \frac{4T^2A^4\omega}{(R_l + R_{coil})}B^2n^2\Lambda = \frac{2TA^4\omega}{\rho \cdot l_w(R'+1)}gB^2\Lambda$$ **Equation 7.20**

where R' is the ratio of load resistance to coil resistance, $\frac{R_l}{R_{coil}}$, and Λ is a non-dimensional function of $\frac{l_w}{A}$ that relates to the degree of electromagnetic coupling over a complete cycle, and is given by

$$\Lambda = \begin{cases} 4\int_0^{\frac{\pi}{2}} \sin^2(\omega t)\cos^2(\omega t)d(\omega t) & A < \frac{l_w}{2} \\ \left(\frac{l_w}{A}\right)^2 \cdot \int_0^{(\omega t)_1} \sin^2(\omega t)d(\omega t) + 4\int_{(\omega t)_1}^{\frac{\pi}{2}} \sin^2(\omega t)\cos^2(\omega t)d(\omega t) & A > \frac{l_w}{2} \end{cases}$$

where $(\omega t)_1 = \cos^{-1}\frac{l_w}{2A}$

It is important to note that, in a manner similar to the previous analysis, the amount of energy that can be extracted is independent of the number of coil turns (although the number of turns does affect the optimum load resistance). This means that N can be chosen independently of the other geometric parameters, and hence simplifies the problem of finding an optimum design for a given application. In practice N will be chosen to give a suitable output voltage across the coil (see section 7.5.1, below).

Λ has been evaluated numerically using the Maple and Matlab packages. The function is plotted in figure 79. The figure shows that as the coil length increases as a proportion of the beam amplitude, the value of Λ increases until it reaches $\frac{\pi}{4}$ at $\frac{l_w}{A} = 2$. The figure also shows a piecewise linear approximation for Λ of

$$\Lambda_{approx} = \begin{cases} \frac{\pi}{7}\frac{l_w}{A} & \frac{l_w}{A} < \frac{7}{4} \\ \frac{\pi}{4} & \frac{l_w}{A} > \frac{7}{4} \end{cases}$$

This approximation will be used to simplify the model below. This approximation shows large percentage errors when the beam amplitude is high, but so long as the beam amplitude is less than one and a quarter times the coil height (the case in all the real examples explored below) the approximation has an error of no more than 7%.

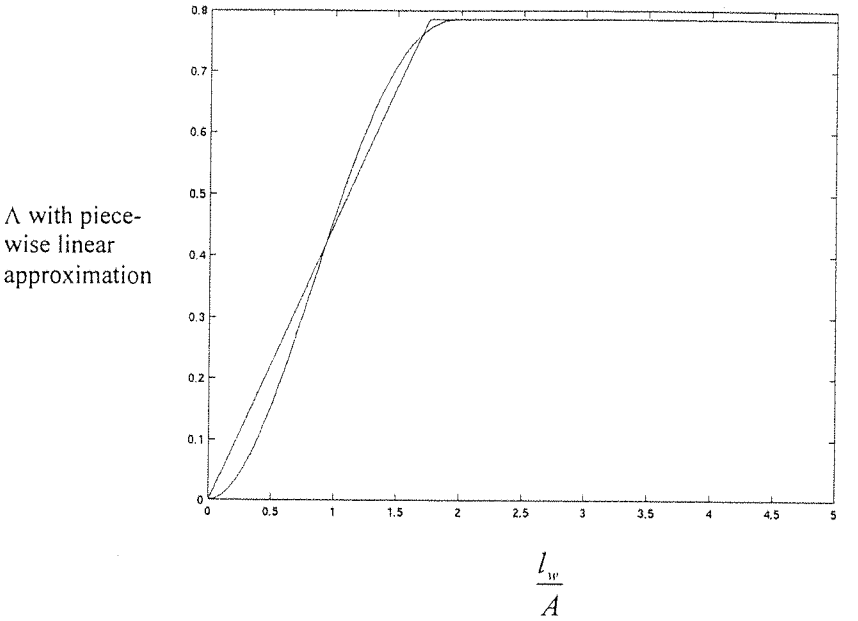

Figure 79: Graph of the function $\Lambda(l_w,A)$

The damping factor resulting from the electrical load, ζ_{el}, is approximately given by

$$\zeta_{el} = \frac{W_d}{4\pi U} = \frac{W_d}{4\pi \cdot \frac{1}{2} m|\dot{x}|^2} = \frac{W_d}{2\pi m \omega^2 A^2}$$ **Equation 7.21**

where U is the maximum strain energy stored in the resonator (also approximately equal to maximum kinetic energy for small ζ_{el}).

substituting equation 7.20 into the above we have

$$\frac{1}{\zeta_{el}} = \frac{2\pi D \omega l_w^{\,2} \rho}{B^2 A^2 \Lambda}(R'+1)$$ **Equation 7.22**

It is interesting to note that the damping factor depends on the amplitude of oscillation. To find the amplitude, A, for a particular excitation, we use the relation

$$A = QZ \text{ or } \frac{A}{Q} - Z = 0$$ **Equation 7.23**

where Z is the amplitude of base excitation applied to the generator, and Q is the Quality factor of the resonator, and is given by

$$Q = \frac{1}{2(\zeta_{el} + \zeta_{unwanted})}$$ **Equation 7.24**

where $\zeta_{unwanted}$ is the damping factor caused by air, support, and material damping. Using the piecewise linear approximation for A described above, we can write

$$A\left(A\frac{C_1}{7} + 2\zeta_{unwanted}\right) - Z = 0 \quad \frac{l_w}{A} < \frac{7}{4}$$
$$A\left(A^2\frac{C_1}{4l_w} + 2\zeta_{unwanted}\right) - Z = 0 \quad \frac{l_w}{A} > \frac{7}{4}$$ **Equation 7.25**

where $C_1 = \dfrac{B^2}{2D \cdot \omega \rho l_w (R' + 1)}$

We can also calculate the power delivered to the load resistor by writing

$$P = \frac{R_l}{R_l + R_{coil}} \frac{\omega}{2\pi} W_d$$

substituting equation 7.20 into this, we have

$$P = \frac{R'}{(R'+1)^2} \frac{\omega^2 A^4 B^2 g \Lambda T}{\pi \rho l_w}$$ **Equation 7.26**

To continue the derivation in a mathematically exact manner would require an expression for B in terms of the geometrical parameters for the core. Since this expression is complicated and non-linear even a reasonable approximation would yield an expression that is too complicated to easily optimise. The method adopted here (as in the previous section) is to choose the core shape that produces the highest magnetic energy in the air gap. This has been found above (section 7.4.1)

for a core unconstrained in its relative proportions. In this case, the relative proportions of the core are constrained by H, W, and T, but as an approximation it will be assumed that even in these cases, this maximum energy can still be approached. This maximises the B^2g term in equation 7.26, but the beam amplitude, A, also depends on B, so this will not be the optimum design. Thus this analysis can not claim to show the most optimum design for a generator, but instead examines this particular case (which in the author's opinion will be close to the optimum design in most cases). The average value of B^2 that relates to this arrangement is $0.179T^2$. The small separation between the magnets (l_m-$2t_c$) discussed in section 7.4.1 is ignored here.

7.4.3.1 Finding the optimum generator dimensions

To find the best geometrical parameters for a particular set of constraints, the Matlab package was used.

Figure 80 shows how the power produced by a generator core (i.e. not including the space required by the spring) of height, width and depth 5mm varies with the height of the coil, l_w, and the normalised load resistance, R'. The excitation supplied for to the generator represents a car floor (data, and source described in section 5.7). At each point, the beam amplitude, A, has been evaluated, and if the amplitude causes the beam to protrude beyond the constraining volume, defined by H, then extra unwanted damping has been applied to limit the beam to the constraining dimension. The figure shows that maximum power (0.24mW) is generated when lw=0.53mm and R'=2.0.

The equations given above do not readily yield an analytic solution for the dimensions that yield the maximum power, so Matlab has been used to find the maximum using the *fmins()* function, which performs a non-linear unconstrained search for the maximum. The Matlab code written for this purpose is listed in appendix G. The code optimises for power density, and it is found that in some cases that the optimum consists of a single beam using all of the available height, whilst in others (generally those with a low excitation amplitude or high frequency), an optimum is found that uses only a proportion of the available height. In these cases the total power is calculated as that which could be generated from several of these smaller height optimum cells stacked on top of each other (See section 5.7 for discussion of this concept with piezo-generators). The results of this optimisation are listed for a selection of real examples in table 27 after the next section.

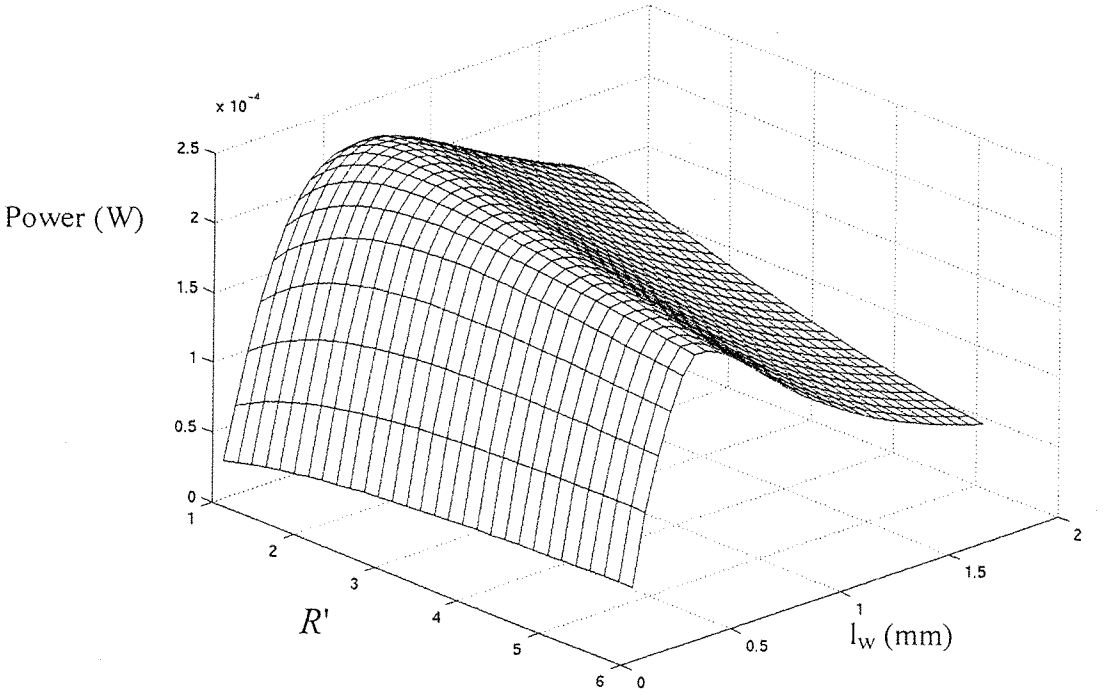

Figure 80: Visualisation of part of the optimisation space

7.4.4 Planar Springs

Two types of spring will be analysed; a simple planar beam, and a tapered / coiled spring. The simple beam will be seen to require at least a certain proportion of the generator volume, while it is found that the tapered spring can be made arbitrarily small, subject to manufacturing limitations.

First we take a simple planar beam of the type illustrated above in figure 75, with length ls, depth T, and thickness t. The stiffness, k, of the beam is given by simple beam theory as

$$k = \frac{3E \cdot T \cdot t^3}{12 \cdot l_s^3}$$ **Equation 7.27**

where E is the Young's modulus of the beam material. To achieve the required resonant circular frequency, ω_n, we must satisfy the equation

$$\omega_n = \sqrt{\frac{k}{m}} = \sqrt{\frac{E \cdot T \cdot t^3}{4 \cdot l_s^3 (L - l_s) H_C \cdot T \cdot D \cdot \beta}}$$

Equation 7.28

(the expression for the mass has been taken from the vertical-coil section, equation 7.8)

We must also ensure that the stress in the beam does not exceed a safe level. Simple beam theory shows that the stress at the beam root, T^r, is given by:

$$T^r = \frac{M \frac{t}{2}}{I} = \frac{3\Delta E t}{2 l_s^2}$$

Equation 7.29

where M is the bending moment caused by the beam deflection, Δ, at the beam root, and I is the second moment of area of the beam about the neutral axis. The most compact spring will make maximum use of the spring material, and operate at as high a stress as possible, T^r_{MAX} (this is not equal to the yield strength of the material, allowance must be made for tolerances, and safety margins.) Thus we set $T^r = T^r_{MAX}$.

Rearranging this last equation in terms of t, and substituting into the expression for ω_n, we derive an equation whose roots with respect to l_S give the length of the spring required to achieve the resonant frequency without exceeding the breaking strain of the beam material.

$$\omega_n^2 = \frac{2 T^r_{MAX}{}^3}{27 \Delta^3 E^2 H_C D \beta} \cdot \frac{l_s^3}{(L - l_s)}$$

Equation 7.30

This equation will be used below to show the effectiveness of a simple beam spring for a range of example applications.

It should be noted that this analysis ignores the mass of the beam, and any rotational inertia of the mass.

A tapered / folded spring will now be considered. Figure 81 shows an ideal model of a tapered spring with initial depth T_0, and length L_s. This represents a tapered spring folded into a generator in a manner similar to the example shown in figure 82.

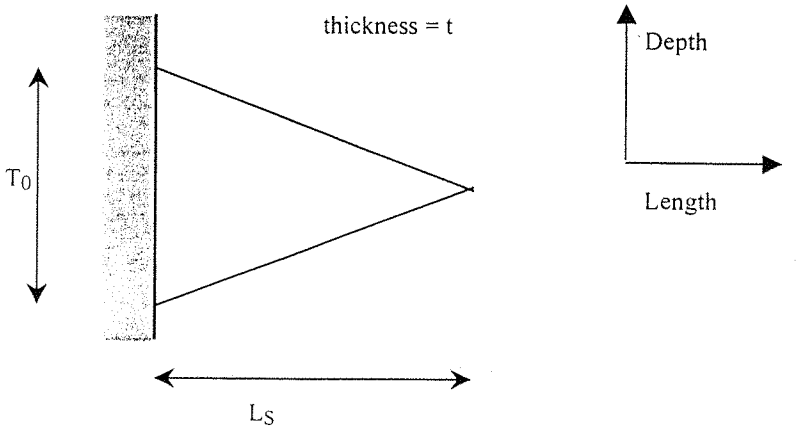

Figure 81: Tapered spring (model)

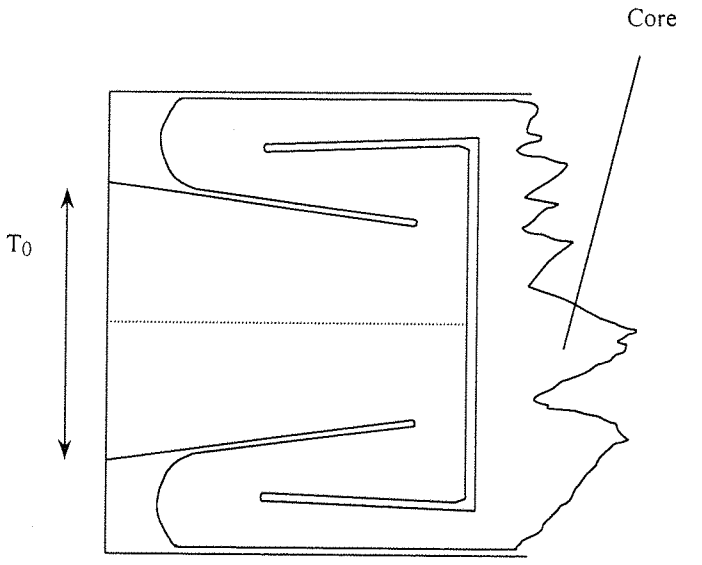

Figure 82: Tapered spring (example)

It can be shown using simple beam theory (edge effects cause departure from this theory, but it is sufficiently accurate here - see section 5.4) that the bending stiffness of this tapered spring is given by

$$k = \frac{2E \cdot I_0}{L_s^{\ 3}}$$ **Equation 7.31**

where I_0, the second moment of area of the beam about the neutral axis at the beam root, is given by

$$I_0 = \frac{1}{12} T_0 \cdot t^3$$ **Equation 7.32**

The area occupied by this tapered spring, A_S, is given by

$$A_S = \frac{1}{2} T_0 L_S$$ **Equation 7.33**

If the spring is constrained to fit within a rectangular area of depth T, and length l_S (the space reserved for a simple beam spring in figure 75 above), then by equating the areas, we derived the relationship

$$L_S = \frac{2T \cdot l_S}{T_0}$$ **Equation 7.34**

which expresses the uncoiled length of a tapered spring in terms of the bounding space, and the initial depth of the spring.

The stress in the outer fibres of the beam, T^r, is given by the equation

$$T^r = \frac{M \frac{t}{2}}{I} = \frac{k\Delta L_S \frac{t}{2}}{I_0} = \frac{Et\Delta}{L_S^{\ 3}}$$ **Equation 7.35**

where M is the bending moment caused by the beam deflection, Δ, at the beam root. A material will have a maximum rated stress, T^r_{MAX}, therefore we must ensure that

$$T^r_{\ MAX} > \frac{Et\Delta}{L_S^{\ 3}}$$ **Equation 7.36**

Substituting equation 7.31 and equation 7.34 into this to eliminate *Ls* and *t*, we have

$$\left(T^{r}{}_{MAX}\right)^{3} > \frac{12 \cdot k \cdot T_0{}^{3} \cdot E^{2} \cdot \Delta^{3}}{32T^{4} \cdot l_S{}^{5}} \qquad \textbf{Equation 7.37}$$

This equation can always be balanced by choosing a suitably small value for T_0.

This means that in the limit, subject to manufacturing difficulties, a tapered spring can fit into any space however small in a generator, and still provide sufficient stiffness, and amplitude. Thus when assessing the generator designs it is hard to form an estimate of how much space is required for a spring, since the limiting factor is the way the generator is produced.

7.4.5 Example Calculations

The models described above have been applied to a selection of real examples to produce the results shown in table 27. Table 26 list the material parameters and constraints used to produce the results. The Matlab code for the calculations is listed in appendix G. The vibration sources used for each example are the same as those used in table 9, section 5.7 where they are described more fully.

Table 26: Model parameters

Parameter	Value
Width, W, and depth, T	Twice the generator height
Unloaded resonator quality factor	100
Resistivity of copper	1.69e-8 Ωm^{-1}
Density of coil	8000 kgm^{-3}
Magnetic flux density in air gap	0.42 T

Comparing the figures produced by the two different models, it can be seen that the vertical-coil model produces estimates that are between 2.9 and 6.6 times bigger than the horizontal-coil model. It is not clear whether this difference is due to the effect of the modelling approximations or the effect of the different geometrical configuration. This difference is reasonable given the doubled electromechanical coupling and increased mass of the vertical-coil configuration.

The power produced from the different example sources shows wide variation. It should be noted that the approximations used in the modelling mean that these results are not to be taken as an

exact measure of how much power can be generated, but rather an indication of the order of magnitude that is possible. The sources represent a range of different extremes - from the low-frequency, low-amplitude car case, to the high-frequency, high amplitude caulking hammer. The power generated reflects this. For each sample vibration source, the power available is seen to grow rapidly with increasing generator height. Even at the smaller 2.5mm height, however, the more vigorous sources can be seen to be capable of producing useful power (see section 3.3 for a discussion of what might constitute useful power).

These figures are misleading if taken without consideration of the spring size. A column is presented in the table that shows the power that would be produced by the horizontal-coil configuration when a simple planar beam spring is used (as calculated from equation 7.30). As discussed above, a coiled spring could be constructed to occupy less space than this, but this column gives an idea of how challenging it would be to produce a smaller spring. In several of the low frequency and high vibration cases, over 90% of the space needs to be set aside for a beam spring.

It should be noted that the assumption of a small amplitude of vibration used in the vertical-coil analysis is violated in some cases (those left blank on the table). This assumption was used to approximate the field around the coils as always constant, thus this model cannot be used in these cases.

For each analysis, a column shows how many turns would be required on the coil to provide a 2volt peak-peak amplitude output signal. Calculations show that if polyester coated copper wire were used with a total diameter of 24μm (commercially available), then the required number of turns could be produced (at a cost) for all but the two largest of the table entries. The difficulty involved in extracting power from cases where only low output voltages are available is discussed below.

The horizontal-coil model will be used below to produce further predictions for direct comparison with piezoelectric generators.

Table 27: Applying magnet-coil models to sample applications

		Horizontal-coil analysis:				Vertical-coil Analysis:		
Application (see table 9 in section 5.7)	Total generator height (mm)	Power, no spring (mW, 2s.f.)	Proportion of length required for a steel planar spring (2s.f.)	Power including space required for spring (mW, 2s.f.)	Number of turns required for 1Volt output voltage (2s.f.)	Power, no spring (mW, 2s.f.)	Turns required for 1Volt peak output (2s.f.)	Ratio of powers between model results (no spring, 2s.f.)
car floor	2.5	0.0020	0.19	0.0022	23000	*See note below*		
	5	0.044	0.19	0.036	5800			
	10	0.73	0.28	0.53	1500			
truck floor	2.5	0.0042	0.20	0.0032	23000			
	5	0.080	0.20	0.064	5700			
	10	1.4	0.29	1.0	1500			
Caulking hammer	2.5	0.68	0.30	0.48	310	4.3	810	6.2
	5	5.5	0.30	3.8	72	35	410	6.5
	10	44	0.20	35	17	290	200	6.6
Motorbike handlebars	2.5	3.8	0.90	0.37	780			
	5	59	0.90	5.8	220			
	10	610	0.95	29	69	1800	40	2.9
loaded pinion	2.5	0.0014	0.033	0.0014	2200	0.0072	11000	5.8
	5	0.0091	0.033	0.0092	550	0.054	5500	5.8
	10	0.074	0.021	0.072	140	0.43	2800	5.9
Bearing cap in machinery	2.5	0.0032	0.20	0.0032	7500	0.012	4900	3.7
	5	0.021	0.20	0.017	2400	0.11	2400	5.1
	10	0.17	0.13	0.15	560	0.88	1200	5.3

Notes: Blank entries show cases where the small amplitude assumption used in the vertical-coil coil analysis is invalid
Figures are for a generator of width and depth that are twice the generator height

7.5 Producing practical generators

This section has focussed on modelling generators, and making theoretical predictions concerning how applicable the technology is to potential applications. Other issues must be considered before these generators can become a reality.

7.5.1 Extracting power

The requirement for extracting and storing the energy produced places strong constraints on the generator design. Further work is required in this area, however some initial thoughts are discussed below.

Before the power can be stored in an electrochemical cell, capacitor, or super-capacitor, it will need to be rectified. Rectifiers based on junction diodes are the most conventional solution, however, they require a forward voltage of a least a few hundred milli-volts to provide a reasonable forward current (the HP HSCH-3486 schottky diode would be a good low-voltage rectifier with a forward current of 0.1mA at V_F=100mV). Other possibilities include active (switched) rectification with either micro-relays (expensive) or semiconductor devices such as FETs (hard to produce low 'on' resistance without consuming too much power). Another possibility is to use a transformer to boost the voltage before rectification. For the low frequencies seen in many of the potential applications described above, producing an efficient wound transformer in the space available would be difficult. Also, since the voltage is already being derived from an electromagnetic interaction, perhaps it would be more efficient to focus on increasing the voltage at source by improving the number of coil turns. A piezoelectric transformer [89] has also been considered, however, these devices become inefficient at typical generator dimensions, and their working frequency is typically in the region of tens of kilohertz. It is thus suggested that in general a generator will need to produce a peak voltage of at least a few hundred milli-volts before the power can usefully be stored. The calculations above show that the number of turns can be increased without decreasing the potential power, thus the challenge is to produce a significant number of sufficiently thin windings. In some situations, however, the output voltage may be so low that no practical way of extracting the power can be found.

7.5.2 Micro-devices

Many potential applications would benefit from a small generator. As the dimensions are reduced we must consider how the power scales with volume, and how small devices might be manufactured.

The predictions made above in section 7.4.5 show that devices of total height 2.5mm could only provide useful power in certain high amplitude applications. The power scales as a function of approximately the third power of height, thus even smaller generators are unlikely to produce useful power. These high amplitude applications seem rare, and it is anticipated that a generator height of 5mm is the smallest that is likely to be required.

MEMS technologies are currently an area of intense research, and it is natural and fashionable to ask whether a micro-generator could be produced in this way. MEMS devices typically range in size between an order of micrometres to orders of millimetres. Thus, the device sizes described above are at the larger (and hence more expensive) end of the spectrum. There are three main parts to the generators described above:

(a) Spring: Silicon is a good material for producing springs. Both equation 7.30 and equation 7.37 show that springs can be made smaller and withstand a higher amplitude if the quantity $\frac{\left(T^{r}_{MAX}\right)^{3}}{E^{2}}$ is increased. Taking T^{r}_{MAX} as the yield strength, this takes a value of 9,500Pa for Silicon compared to 12,000Pa for some Be-Copper alloys, and 52,000Pa for precipitation hardened 17Cr-4Ni Cu Stainless steel. The photochemical processes that can be used in silicon micromachining mean that detailed tapered spring designs of the type described above in chapter 4 could be produced. An advantage with photochemical etching processes is that the dimensions of devices can be controlled to very high tolerances. A possible drawback with silicon springs would be the brittle nature of the material. Small defects, and sharp edges can cause stress concentrations that will cause fracture of the spring. Both Silicon and Copper springs have been used by Chan [87], he concludes that copper is a more suitable material in his context.

(b) Magnets: The modelling described above shows that strong magnetic fields are required to produce good generators. Techniques for depositing thick film magnets which are suited to MEMS processing techniques are not capable of producing either the field strength or the dimensions required. It would thus be necessary to apply pre-formed magnets to a structure using some more conventional approach.

(c) Coil: The modelling work shows that there is a requirement for a relatively thick coil structure with a high density of turns. As discussed above, it is possible to create this type of structure using thick-film printing (Chan uses this approach). For large numbers of turns, printed coils may be uneconomic compared to winding coils mechanically from wire. The coil will typically lie out of the plane of the spring; micromachining is best suited to semi-planar structures, and would probably require complex processing to produce a suitable configuration.

We thus see that it is possible to create a silicon micromachined generator. It is questionable, however, whether there is any advantage in pursuing this route. The traditional advantage of silicon micromachining is that it enables batch processing of devices in a manner similar to integrated circuit technologies. The requirement to individually place the magnets on each generator reduces this important factor, and could lead to high unit cost systems. Furthermore, steel and other materials can be photochemically etched in much the same manner as silicon, providing a similar degree of precision. Experience gained during the production of the prototype beams showed that generators can be produced using a sequence of etching, bending, casting, and filing. It is felt that the method used to produce the prototype beams would be straightforward to automate for a mass-produced device.

7.6 Comparison of piezoelectric and magnet-coil generators

The horizontal-coil model has been applied to a range of base excitations and frequencies (using the code in appendix G) to produce the graph shown in figure 83, which also includes data for piezoelectric generators from figure 47 in section 5.7. This graph thus enables direct comparison between the two technologies. The calculations are for generators occupying a total volume of 5mm x 10mm x 10mm (height x width x depth), quality-factor 100, and include the space required for a planar spring as described by equation 7.30. The appendix also contains graphs (figure 90) that show the internal dimensions that correspond to each magnet-coil point on this figure. Table 26, above, shows the material parameters and constraints applied to the model.

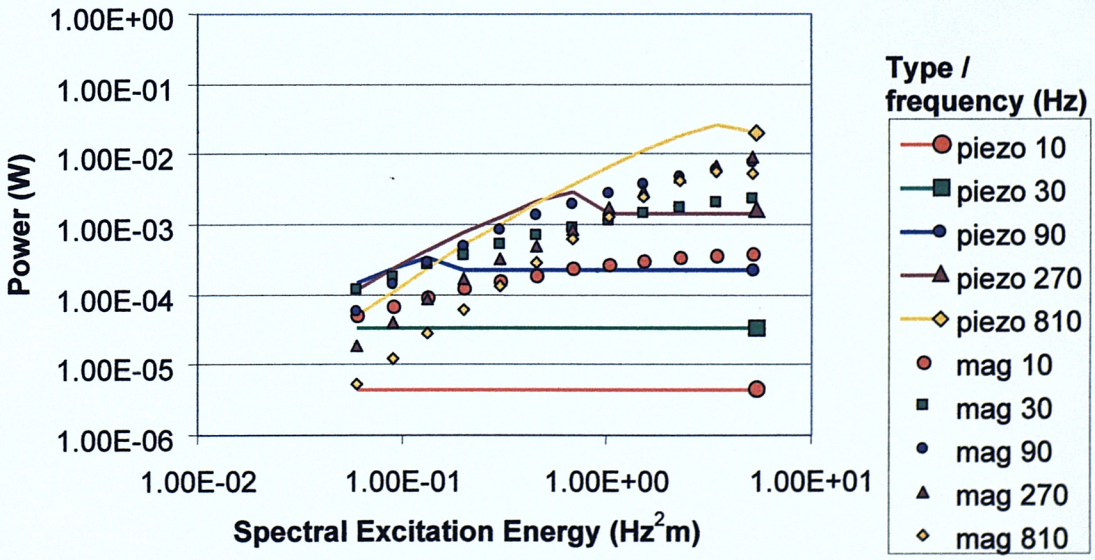

Figure 83: Comparison of magnet-coil and piezoelectric generators

As an example of how to use the graph, the vibration data from a bearing cap in heavy machinery listed in table 9 will be used to determine how much power could be generated, as estimated by the graph. The frequency of base excitation is 100Hz, at an amplitude of 3.58μm. Forming the product of frequency squared and amplitude we obtain the spectral excitation energy as $0.0358Hz^2m$. Since the frequency of 100Hz does not have a data series on the graph, the frequency will be approximated as 90Hz (to be more thorough, we could interpolate between 90 and 270Hz). Calculations for 90Hz are plotted on the graph as a blue line (piezoelectric) and blue circles (magnet-coil). Extending a line from the x-axis at $0.0358\ Hz^2m$ and intersecting with these two blue series, we find that powers of 1.1mW and 0.25mW are predicted from the magnet-coil and piezoelectric generators respectively. In this case it would thus seem that a magnet-coil generator would be the best design, and that enough power could be generated to perform useful work. To find the geometric proportions of the best generator in this case figure 90 should be examined (this will be a good starting point for generator design, but the final design will be different due to non-ideal parameters that are not modelled here).

The graphs above show the power that could be delivered to a resistive load of an optimum value. Further work is required to examine methods of extracting and storing the power generated by both technologies; it is not clear in which of the technologies this will be more efficient.

It can be seen that the technology that generates the most power depends on the excitation conditions. The piezoelectric generators produce more power at the highest frequency examined (810Hz) and for the lower excitation amplitudes of the 270 and 90Hz cases. For the cases examined, the magnet-coil generator never supplies less than a tenth of the power of the piezoelectric case. The most marked difference can be seen at lower amplitudes and lower frequencies, when the magnet-coil generator is seen to be up to 90 times more powerful. Under these conditions, the piezoelectric generators are unable to apply as much damping as the magnet-coil ones. Note that the horizontal-coil configuration (as modelled in the above figure) is shown above to be around one quarter as powerful as the vertical-coil configuration, thus, if the vertical-coil configuration were compared to piezoelectric generators, the piezoelectric generators would be more powerful in even fewer cases.

When choosing which technology is most suitable for a given application, other factors must be considered. Piezoelectric generators are not easy to manufacture. Thick-film generators discussed in chapter 4 are currently limited by the low activity of the PZT material used (although materials research may solve this problem in the future). Bulk devices are required to produce the power shown above, however producing (often multi-beam, multi-layer) devices of the size found to be optimum is difficult. The lifetime and reliability of the devices must also be examined; the

piezoelectric devices use a brittle ceramic material as a spring, compared to the metallic springs of the magnet-coil devices. Finding a suitable method to clamp the piezoelectric beams at their root without introducing extra potentially damaging stresses would be difficult. Thus, it is envisaged that piezoelectric generators will rarely be the best choice, except perhaps in particularly high frequency (several kilo-Hertz) applications.

7.7 Summary

Typical design configurations for inertial generators based on electromagnetic induction have been examined. An electrical equivalent circuit model has been described, and verified by producing a prototype generator. The prototypes produced a maximum power of 2.4 and 5.0mW in volumes of 2.0 and 4.1cm^3 respectively.

Generators have a specific optimum load resistance, which depends on both the amount of damping present, and the coil resistance. The unwanted damping present in the prototypes described here is dominated by support damping, and is thus hard to predict theoretically. The prototypes have revealed that output voltages can be very low. This is important as once power has been generated it must also be rectified and stored in a suitable medium such as a battery. Both batteries and rectifiers require voltages of at least a few hundred milli-volts. Thus, producing reasonable output voltages will often require a large number of fine turns on the coil.

The concept has been validated using a demonstrator mounted on a car engine block that has been shown to be capable of producing a useful amount of power.

An analysis of two possible generator structures has provided a method of calculating theoretical limits on the power that can be generated within a given volume for a particular excitation. The resulting equations can be used to predict (to an order of magnitude) power output for any application. The equations have been applied to a number of existing vibration sources to show typical output powers. These show that the power delivered is very application specific, with figures ranging from 1μW to 35mW.

The model has also been used to provide a graph of power output for a range of different excitations. This graph permits direct comparison between magnet-coil generators and piezoelectric ones. The comparison shows that both technologies have merits, and that the excitation conditions determine which will produce the most power. It is suggested that even in cases where a magnet-coil generator may be predicted to generate less power, it will often be the best choice due to the difficulties of manufacturing piezoelectric devices. Magnet-coil generators are also likely to be more reliable.

CHAPTER 8

Conclusions and Suggestions for Further Work

8.1 Conclusions

Vibration powered devices provide an alternative to batteries, and offer a solution to the power requirements of distributed sensor systems. In combination with suitable wireless communications techniques vibration power has the potential to permit fully wireless and autonomous sensors with operational lifetimes that are not constrained by built in power sources. Two main technologies have been identified as ways of harvesting vibration power: piezoelectric materials, and magnet-coil combinations using electromagnetic induction. While both ideas can be found in the existing literature, no existing studies have sought to provide a framework upon which these techniques can be evaluated and compared. Engineers have had no way to answer the questions 'For which applications is vibration power suitable?' and 'Which technology should I use?'. This thesis has addressed these issues, culminating in calculations typified by figure 84 below.

It has been shown that in some applications, vibration-powered generators can produce energy at a rate comparable to other self-powered technologies such as solar power. The decision to use vibration power will be a result of having considered what other sources of power are available and weighing up the issues of output power, cost, long-term stability, etc. Vibration power has an advantage over solar power in dark, vibrating environments such as car engines and other heavy machinery. Potential disadvantages of vibration-powered generators include their higher production costs, moving parts that are more likely to fail than solid-state devices, and the lack of existing development of devices of this type.

Initially, thick-film PZT was explored as a potential technology for a generator. A process to form a multi-layered thick-film device has been developed. The devices consist of two thick-film PZT layers, with electrodes, sandwiching a steel beam. By clamping the beams at their root, and attaching a mass to the tip of the structure, power is generated when the base is shaken. Producing the devices required overcoming some materials problems. It was found that PZT films react with the steel substrate during the firing processes, to prevent this interaction glassy

dielectric layers were incorporated into the structure. Also, thermal mismatch between the layers causes warping to occur during the firing process. The warping was reduced by producing symmetrical structures, however, variations in the screen printing process meant that some warping still occurs which places a lower limit on the thickness of the steel. The material properties of the device layers have been measured, since mechanical data is not commonly available for thick-film materials. Methods to measure the piezoelectric constants of the PZT have been developed. Measuring these constants is not trivial, and the methods presented here are more accurate that any reported in the literature to date for thick-film piezoelectric materials.

The thick-film devices were tested using an electromechanical shaker. Working in linear regions of operation, the results showed that small amounts of power could be generated (around 3μW). Modelling was undertaken to examine why such small amounts of power were generated, and also to predict the power output from piezoelectric generators of arbitrary dimensions. It was found that analytic models became too complex when such factors as edge effects and varying stresses through the piezoelectric material were incorporated. It was also found that commercially available finite element modelling packages, will not at this time simulate resistively shunted piezoelectric elements. The problem was made more tractable by decoupling the electrical and mechanical domains, representing the resistively shunted piezoelectric material as exhibiting a frequency dependant stiffness and loss factor. The existing model of a shunted piezoelectric element, however, did not include the effect of non-uniform strain through the piezoelectric layer that is a feature of generator designs. A new model of a resistively shunted piezoelectric element undergoing pure bending was therefore developed. The model shows that this effect can cause a reduction in available damping of up to 30%. This reduction can be reduced by using laminated piezoelectric / electrode structures. Comparing the model to experimental results, accurate predictions are seen at low beam amplitude, with slight under prediction at higher amplitudes due to non-linear effects.

The model reveals that the reason for the low power produced by the thick-film generator, is the low electromechanical coupling coefficient of thick-film PZT. If this technology is to be useful, devices must be constructed with either bulk PZT, or densified thick-film PZT. The model was also used in conjunction with numerical methods to find optimum generator dimensions for a range of excitations that might be found in practice. These figures show that bulk PZT generators could produce useful amounts of power in many applications.

Experiments have been devised to assess the long-term stability of thick film PZT materials. Prior research has shown that bulk piezoelectric ceramics suffer a long term ageing process after polarisation, however, no studies have been reported that measure this important process in thick-

film piezoceramics. A technique for measuring the ageing rate of the d_{31} coefficient of a PZT thick-film sample has been presented. The method has been found to be reliable, and be sufficiently accurate for observing the decaying response. The accuracy obtained is of an order of magnitude higher than that reported previously. The d_{31} coefficient is found to age at –4.4% per time decade (for PZT-5H). A method is presented for measuring the ageing of the dielectric constant, K_{33}, and found to show an ageing rate of –1.34% per time decade.

Turning to generators based on electromagnetic induction, typical design configurations have been examined. An electrical equivalent circuit model has been described, and verified by producing a prototype generator. The prototypes produced a maximum power of 2.4 and 5.0mW in volumes of 2.0 and 4.1cm^3 respectively. The prototypes have revealed that output voltages can be very low. This is important as once power has been generated it must also be rectified and stored in a suitable medium such as a battery. Both batteries and rectifiers require voltages of at least a few hundred milli-volts. Thus, producing reasonable output voltages will often require a large number of fine turns on the coil. The concept has been validated using a demonstrator mounted on a car engine block that has been shown to be capable of producing an average of 160μW.

An analysis of two possible magnet-coil generator structures has provided a method of calculating theoretical upper limits on the power that can be generated within a given volume for a particular excitation. The resulting equations can be used to predict (to an order of magnitude) power output for any application. The equations have been applied to a number of existing vibration sources to show typical output powers. These show that the power delivered is very application specific, with figures ranging from 1μW to 35mW.

The model has also been used to predict power output for a range of different excitations. This data has been combined with similar results for a piezoelectric generator, to permit direct comparison between the two technologies. Figure 84 shows the power that can be produced by both technologies from generators occupying a total volume of 5mm x 10mm x 10mm (height x width x depth). See section 7.6 for a description of how to use this graph. The comparison shows that both technologies have merits, and that the excitation conditions determine which will produce the most power. Piezoelectric generators, however, would not be easy to manufacture. The lifetime and reliability of the devices must also be examined; the piezoelectric devices use a brittle ceramic material as a spring, compared to the metallic springs of the magnet-coil devices. For these reasons it is envisaged that piezoelectric generators will rarely be the best choice, except perhaps in particularly high frequency (several kilo-Hertz) applications.

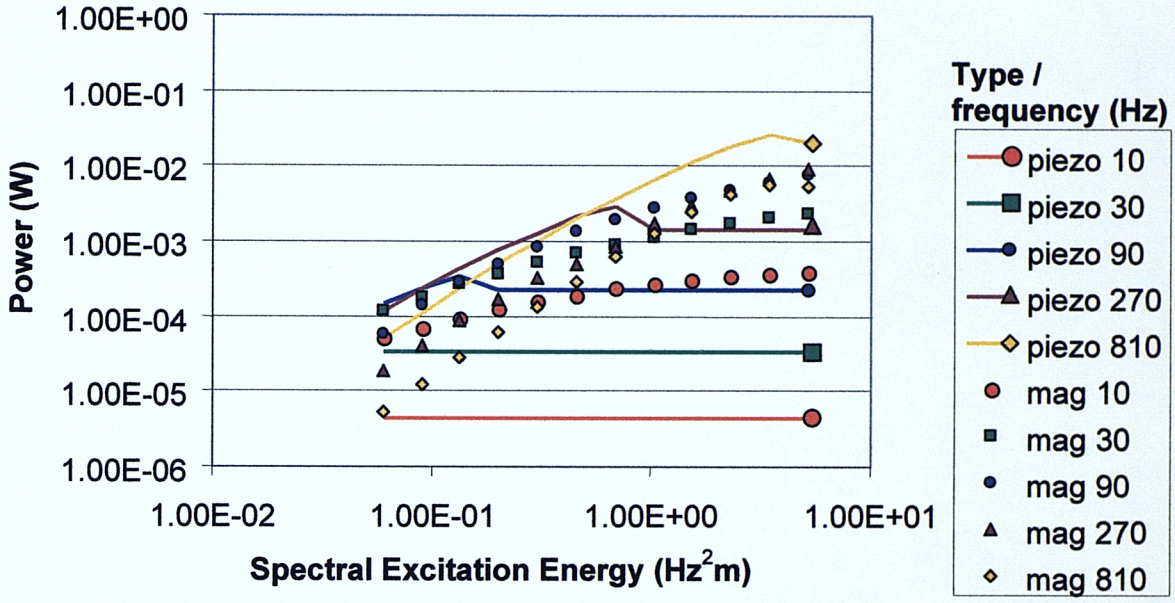

Figure 84: Comparison of magnet-coil and piezoelectric generators (repeated)

8.2 Key Contributions made by thesis

The following points have been identified as the key contributions to knowledge made by this thesis:

- A thick-film piezoelectric generator has been presented for the first time, and its performance assessed.
- A simple way of calculating the power that can be produced by a piezoelectric generator has been presented, including a new model of a resistively shunted piezoelectric element undergoing bending.
- An investigating to measure the previously unquantified long-term stability of thick-film PZT has been described.
- Idealised generator models have been used to make predictions of how much power can be generated from both piezoelectric and magnet-coil generators for a range of harmonic excitation frequencies and amplitudes. This data has been collected in a graph that permits future designers to simply calculate the most suitable technology for a given application, and to obtain an estimate of how much power can be produced.

8.3 Suggestions for Further Work

The future for self-powered systems seems bright, and interest in self-power is currently growing rapidly. Caution is also important though, as this is a subject where misplaced optimism can last for a long time. Consider, for example, the work on generating power from vibrations in road bridges; much work was done before it was realised that small devices could not generate useful power. In contrast self-winding wristwatches are a widespread success, with a power source that is well matched to its intended application. The message is that before continuing research into the areas mentioned below, it is important to choose a target application and tailor designs accordingly.

This thesis presents a background that should enable future designers to choose a suitable technology, and estimate how much power it will produce for a given application. Piezoelectric generators are unlikely to feature much in future research, unless a superb high frequency application is found for them. If they are used further, then significant effort will need to be expended in producing a design that can be economically manufactured. If current research into thick-film piezoelectric materials yields materials comparable in activity to bulk ones (possible) then producing generators would be much simpler. Magnet-coil generators have been explored in some depth here. The question of which configuration is best has been approached, but it is found that the results depend on many practical considerations that will vary from application to application. Thus, further fundamental research is unlikely to yield further useful insights in this area. It is the author's opinion that the double-gap core design will be found to be superior in most cases. Further work in this area is more likely to be concerned with producing generators for practical applications, and discovering how closely the theoretical predictions made here can be approached through careful and inspired engineering.

This thesis focuses on linear resonant generators. Another type of design [8] which may be particularly suitable for impulse type excitations could be explored; Power can be generated through impacts between an inertial mass, and a piezoelectric element. This type of generator is non-linear, and will require a different type of analysis to that presented here. Another unexplored possibility is that resonant generators can be modified to allow electrical tuning of their resonant frequency through the addition of reactive loads, which would allow higher power generation in environments where a narrow excitation frequency is not stable in time.

The question of how power is to be extracted and stored has not been addressed in detail in this thesis. It must be appreciated that the power generated (as the term has been used in this thesis, referring to the power that can be delivered to an optimum resistive load) is not the same as the

amount of power that will be ultimately delivered to a storage device such as a battery following rectification and voltage scaling. Impedance matching will be important here to ensure optimum power transfer. The cause of this disparity is the low output voltages that may be produced by small generators in weak vibration applications. Section 7.5.1 points out some possible ways of tackling this problem, but it is acknowledged that in some cases it may not be possible to 'get hold' of the power.

Power extraction is important, but the most interesting problems lie with systems issues: Producing a miniature system that can gather, process and transmit data using only the small amounts of power that will be present. The electronics is unlikely to be particularly novel, innovation must come in finding a solid application, and using the system in an adroit manner (for instance making use of the fact that data processing is power efficient to reduce the amount of power hungry data transmission that must be used). There is potential for arrays of self-powered systems working together, since communications power can be reduced when neighbour to neighbour communications are used. There is also scope for novel communications methods since communications is likely to consume the largest proportion of a power budget. An ultra-low power communications technique could open up many potential applications, even if it were only capable of very poor data rates. Systems will also require ultra-low power sensors, another area that has not been examined in this thesis.

Finally, vibration power is not the only solution! There is no single technological answer to self-power: To realise the vision of a world filled with tiny wireless and autonomous sensor systems, each potential application must be evaluated to determine where power might be derived. Applying such solutions will require devices to be carefully tailored to each specific application, with devices often needing to search for power at the edges of feasibility.

APPENDICES

Appendix A: Publications List

1. P. Glynne-Jones, S. P. Beeby, P. Dargie, T. Papakostas and N. M. White, "An Investigation Into The Effect Of Modified Firing Profiles On The Piezoelectric Properties Of Thick-Film PZT Layers On Silicon.", *IOP J. Measurement Science and Technology,* Vol. 11, pp. 526-531, 2000.

2. P. Glynne-Jones, S. P. Beeby, and N. M. White, "Towards a Piezoelectric Vibration-Powered Microgenerator", *IEE Proc. Science, Measurement and Technology, Vol 148, No 2, pp. 68-72, March 2001.*

3. P. Glynne-Jones, S. P. Beeby and N. M. White, "A Method to Determine the Ageing Rate of Thick-Film PZT Layers", Accepted: IOP *J. Measurement Science and Technology.*

4. P. Glynne-Jones and N. M. White, "Self-powered Systems: A Review of Energy Sources", *Sensor Review*, Vol 21, No 2, pp. 91-97, 2000.

5. M. El-hami, P. Glynne Jones, E. James, S. Beeby, N. M. White, A. D. Brown, and M. Hill, "Design and fabrication of a new vibration-based electromechanical power generator", Accepted for *Sensors and Actuators, Special Issue, Eurosensors XIV.*

6. E. P. James, P. Glynne-Jones, M. El-Hami, S. P. Beeby, J. N. Ross, and N. M. White, "Planar signal extraction techniques for a self-powered microsystem", *Measurement and Control* , Vol 34, No. 2, March 2001.

7. P. Glynne-Jones, S. P. Beeby and N. M. White, "A Novel Thick-Film Piezoelectric Micro-Generator", Accepted for *Smart Materials and Structures*

8. P. Glynne-Jones, S. P. Beeby, E. P. James, and N. M. White, "The Modelling of a Piezoelectric Vibration Powered Generator for Microsystems", *Proc. 11th Int. Conf. on Solid-State Sensors and Actuators, Transducers 2001 / Eurosensors X,* Munich 2001.

9. P. Glynne-Jones, M. El-hami, S. P. Beeby, E. P. James, A. D. Brown, M. Hill, and N. M. White, "A vibration-powered generator for wireless microsystems", *Proc. Int. Symp on Smart structures and Microsystems 2000,* Hong Kong, October 19th-21st 2000.

10. M. El-hami, P. Glynne Jones, S. Beeby, and N. M. White, "Design analysis of a self-powered micro-renewable power-supply", *Proc. Int. Conf. on Electrical Machines (ICEM 2000),* Helsinki, Finland, Vol. 3, pp. 1466-1470, 28th-30th August 2000.

11. M. El-hami, P. Glynne Jones, E. James, S. Beeby, N. M. White, A. D. Brown, and M. Hill, "A new approach towards the design of a vibration-based microelectromechanical generator", *Proc. of The 14th European Conf. on Solid State Transducers (Eurosensors 2000)* Denmark, pp. 483-486, 27th-31st August 2000.

12. E. P. James, P. Glynne-Jones, M. El-hami, S. P. Beeby, J. N. Ross and N. M. White, "Planar signal extraction techniques for a self-powered microsystem", *Accepted - Proc. Int Conf. on Sensors and Transducers (MTEC 2000),* Sensors Measurement Instrumentation and Control Exhibition, NEC, Birmingham, 15th February 2001.

Appendix B: Finite element programs for thick-film generator analysis

Program to generate a finite element model of a generator using the ANSYS® package (See section **4.3** for details of the devices that this program models, and section **5.5** for how the results from this program are used).

```
!FILE B12A3.TXT

!

!Model of a piezo generator beam of type made in Batch 12
!Includes layered elements to represent the ip222 dielectric layer
!Model exploits symmetry across width: HALF MODEL ONLY


finish              !Leave any existing modules
/clear,start        !reset
/FILNAM,TRIPLAN3    !File name for run
/TITLE,Plane comp beam
/UNITS,SI           !Use SI units

/PREP7
! Dimensional parameters

IPTHK=22E-6     !IP THICKNESS

PZTTHK=70E-6     !PZT THICKNESS
PZTWID1=(20E-3)/2    !HALF PZT WIDTH at root
PZTWID2=(10E-3)/2    !HALF PZT WIDTH at end of pzt
PZTLEN=10E-3    !PZT LENGTH

SITHK=104E-6      !SI  THICKNESS (Steel not silicon, but its easier to
leave the names)
SIWID1=(22.5e-3)/2  !HALF SI  WIDTH at root
SIWID2=(3.5e-3)/2  !HALF SI  WIDTH at end of taper
SILEN=18.5E-3  !SI  LENGTH
SIBORDER=0.1e-3 !Substrate length before pzt starts
```

```
RODWID=SIWID2  !HALF ROD WIDTH in stiff rod area
RODTHK=SITHK  !ROD Thickness
RODLEN=3.5e-3   !ROD LENGTH

MASSLEN=0.1e-3
MASS=0.5e-3  !Mass in kg of tip mass

MSHSIZE=1e-3  !MESH SPACING IN LENGTH DIRECTION

! Material properties

ET,1,SOLID46,,,,,2,4          ! LAYERED SOLID ELEMENT:
R,1,3                         ! 3 LAYERS (IP222 then substrate then IP222)
RMORE
RMORE,1,0,IPTHK,2,0,SITHK
RMORE,3,0,IPTHK            ! RELATIVE LAYER THICKNESSES

exip=74E9  !Modulous of Elasticity of ip222
densip=2640  !density OF ip222

exsi=162E9  !Modulous of Elasticity of Substrate (Steel)
denssi=7690  !density OF Substrate

MP,EX,1,exip                ! MATERIAL 1, 1st ip222 layer PROPERTIES
MP,NUXY,1,0.3
MP,DENS,1,densip

MP,EX,2,exsi                ! MATERIAL 2, Steel PROPERTIES
MP,NUXY,2,0.3
MP,DENS,2,denssi

MP,EX,3,exip                ! MATERIAL 3, 2nd ip222 layer PROPERTIES
MP,NUXY,3,0.3
MP,DENS,3,densip

ET,4,45  !piezo layer
MP,EX,4,15E9 !Modulous of Elasticity of PZT
mp,nuxy,4,0.3
mp,dens,4,5440
```

```
ET,5,45  !stiff rod material
MP,EX,5,1000E9 !Modulus of Elasticity of stiff area
mp,nuxy,5,0.3
mp,dens,5,1   !almost weightless

ET,6,45  !stiff mass material
MP,EX,6,1000E9 !Modulus of Elasticity of stiff area
mp,nuxy,6,0.3
mp,dens,6,MASS/((SITHK+2*IPTHK)*MASSLEN*(SIWID2*2))   !density fixed to
give right mass



! Build model
!X-Length Y-Width Z-Thickness

sitop=(SITHK/2+IPTHK)

!Defining key points around the model
K,1,0,SIWID1,-SITOP
K,5,0,PZTWID1,-SITOP

K,2,0,-SIWID1,-SITOP
K,6,0,-PZTWID1,-SITOP

K,3,SILEN,SIWID2,-SITOP
K,7,PZTLEN,PZTWID2,-SITOP

K,4,SILEN,-SIWID2,-SITOP
K,8,PZTLEN,-PZTWID2,-SITOP

K,9,SILEN+RODLEN,SIWID2,-SITOP
K,10,SILEN+RODLEN,-SIWID2,-SITOP
K,11,SILEN+RODLEN+MASSLEN,SIWID2,-SITOP
K,12,SILEN+RODLEN+MASSLEN,-SIWID2,-SITOP

K,13,-SIBORDER,SIWID1,-SITOP  !the border at the root
K,14,-SIBORDER,PZTWID1,-SITOP
K,15,-SIBORDER,-PZTWID1,-SITOP
K,16,-SIBORDER,-SIWID1,-SITOP
```

```
K,17,PZTLEN,SIWID2+(SILEN-PZTLEN)*((SIWID1-SIWID2)/SILEN),-SITOP     !mid
side node levevel with node 7
K,18,PZTLEN,-(SIWID2+(SILEN-PZTLEN)*((SIWID1-SIWID2)/SILEN)),-SITOP  !mid
side node levevel with

K,24,-SIBORDER,0,-SITOP
K,19,0,0,-SITOP
K,20,PZTLEN,0,-SITOP
K,21,SILEN,0,-SITOP
K,22,SILEN+RODLEN,0,-SITOP
K,23,SILEN+RODLEN+MASSLEN,0,-SITOP

a,1,5,7,17   !uncovered si area on bottom of block normal direction is z
+ve
*get,AR1,area,,num,max

a,17,7,20,21,3  !uncovered si area on bottom of block normal direction
is z +ve
*get,AR10,area,,num,max


A,5,19,20,7 !covered si area on bottom of block
*get,AR2,area,,num,max

A,3,21,22,9 !rod bottom area
*get,AR4,area,,num,max

A,9,22,23,11 !mass bottom area
*get,AR5,area,,num,max

A,13,14,5,1 !SI border a
*get,AR6,area,,num,max
A,14,24,19,5 !SI border a
*get,AR7,area,,num,max

asel,all

Aoffst,AR2,SITOP*2  !area to be extruded to make top pzt block
*get,AR3,area,,num,max

vext,AR1,,,,,SITOP*2,1,1,1  !extrude AR1 to make uncovered si volume B
```

```
*get,VJ,volume,,num,max
vext,AR10,,,,,SITOP*2,1,1,1  !extrude AR10 to make uncovered si volume B
*get,VB,volume,,num,max

vext,AR2,,,,,SITOP*2,1,1,1  !extrude AR2 to make covered si volume A
*get,VA,volume,,num,max
vext,AR6,,,,,SITOP*2,1,1,1  !extrude AR6 to make border vol G
*get,VG,volume,,num,max
vext,AR7,,,,,SITOP*2,1,1,1  !extrude AR7 to make border vol H
*get,VH,volume,,num,max


VATT,,,1                !ATTATCH VOLUMES TO ELEMENT TYPE 1, material type
done automatically
vsel,none

vext,AR2,,,,,-PZTTHK,1,1,1  !extrude AR2 to make bottom pzt volume D
*get,VD,volume,,num,max
vext,AR3,,,,,PZTTHK,1,1,1  !extrude AR3 to make top pzt volume D
*get,VC,volume,,num,max

VATT,4,,4               !ATTACH VOLUMEs TO ELEMENT TYPE 4,MATERIAL 4
vsel,none

vext,AR4,,,,,SITOP*2,1,1,1  !extrude AR4 to make rod volume E
*get,VE,volume,,num,max
VATT,5,,5               !ATTACH VOLUMEs TO ELEMENT TYPE 5,MATERIAL 5
vsel,none


vext,AR5,,,,,SITOP*2,1,1,1  !extrude AR5 to make mass volume F
*get,VF,volume,,num,max
VATT,6,,6               !ATTACH VOLUMEs TO ELEMENT TYPE 4,MATERIAL 4

allsel


LSEL,S,LOC,Z,0    !SELECT ALL RISERS IN SI BLOCK/ ROD/MASS
LESIZE,ALL,(SITHK+2*IPTHK)/1          !SPACING ON MESH IN Z-DIRECTION
(one element)
```

```
LSEL,S,LOC,Z,SITOP+PZTTHK/2 !SELECT some RISERS IN pztBLOCK
LSEL,a,LOC,Z,-(SITHK/2+IPTHK+PZTTHK/2)  !SELECT rest of RISERS IN
pztBLOCK
LESIZE,ALL,PZTTHK/1              !SPACING ON MESH IN Z-DIRECTION (one
element)

ALLSEL
NUMMRG,KP,1e-8       !MERGE DUPLICATE THINGS closer than 1e-8

ASEL,S,LOC,X,PZTLEN
ASEL,R,LOC,Z,0    !GET AREAS IN SI AND COMBINE TO MAKE ONE FACE FOR
MESHING
ACCAT,ALL

LSEL,S,LOC,X,PZTLEN
LSEL,R,LOC,Z,SITOP
LCCAT,ALL

LSEL,S,LOC,X,PZTLEN
LSEL,R,LOC,Z,-SITOP
LCCAT,ALL

VSEL,ALL
ESIZE,MSHSIZE           !DEFAULT SPACING ON REST OF STRUCTURE

VMESH,ALL               !MESH REMAINING volumes
/VIEW,1,1,1,1

ASEL,S,LOC,X,-SIBORDER      !SELECT END FACEs
NSLA,S,1                !GET ITS NODES
D,ALL,ALL   !CONSTRAIN THEM IN ALL DIRECTIONS
ALLSEL

asel,s,loc,y,0  !GET THE AREAS ALONG THE JOIN WITH THE NON-EXISTENT HALF
NSLA,S,1                !GET ITS NODES
d,all,uy          !CONSTRAIN THEM TO MOVE ONLY IN X,Z DIRECTIONS
ALLSEL

save
FINISH
```

```
!Modal analysis commands


/solu

ANTYPE,MODAL      !Modal analysis
MODOPT,REDUC,3  !extract only 3 modes
MXPAND,3,,,YES  !expand them all, and generate element results
TOTAL,30,1        !automatic generation of structural DOF (exclude volt
DOFs)
SAVE
SOLVE
*GET,myfreq,MODE,1,FREQ  !get freq of 1st mode
FINISH

!/post1
!set,1,1    !choose first mode
!pldisp           !display mode shape


!To find the harmonic response of beam from file B12A3 to base excitaion


*ask,AMPLIT,Amplitude of Aceleration to apply:, 0.1
!*ask,myfreq,Frequency to evaluate:, 78
*ask,mydamp,Beta Damping in PZT layer:,0.1

!setup damping in the piezolayer
finish
/prep7
mp,damp,4,mydamp
finish


/SOLU
ANTYPE,HARMIC
HROPT,full

HROUT,ON        !Real/imag output
outres,all,all  !save all to file.rst
```

```
HARFRQ,myfreq   !look at response between these frequencies
NSUBST,1        !number of steps in this range

KBC,1           !stepped load - load is constant over all freq steps
ACEL,,,AMPLIT   !applies a harmonic excitation to beam of given amplitude
in z direction

SAVE
SOLVE
FINISH

/post1
nsel,s,loc,x,SILEN+RODLEN+MASSLEN/2 !get a node at beam tip
prnsol,UZ                       !print amplitude of beam tip


!to find energy stored at a given displacement for beam modeled in file
B12A3

/prep7
nsel,s,loc,x,SILEN+RODLEN+MASSLEN/2
*get,tip,node,,num,max  !get a node at beam tip, call it "tip"

NSEL,S,NODE,,tip
d,all,uz,0.80e-3  !apply a fixed displacement to node
!f,all,fz,1e-4    !(or apply a fixed force to node)
ALLSEL

FINISH

/solu
ANTYPE,static     !do static analysis
OUTPR,VENG,ALL  !calculate output energies
SAVE
SOLVE
FINISH

/post1
!*****Do not forget that this is a half model, energies must be doubled
to get
```

```
!values for full structure

ESEL,s,mat,,4
etable,enpzt,sene !Print energy stored in PZT layers
ssum
esel,s,mat,,1
esel,a,mat,,2
esel,a,mat,,3
esel,a,mat,,5
esel,a,mat,,6

etable,enrest,sene      !Print sum of energy in other layers
ssum
```

Appendix C: The Proportion of Energy Stored in the Piezoelectric Layers of a Composite Beam

Symbols

ρ	Radius of curvature
Δl	incremental length
Δy	incremental distance
E	Energy
W	Width
Y	Young's modulus
y	Distance from centre beam
y_b	Distance from centre of beam to bottom of PZT layer
y_t	Distance from centre of beam to top of PZT layer

This appendix calculates the proportion of elastic strain energy stored in the piezoelectric layers of a composite beam of the type shown in figure 85.

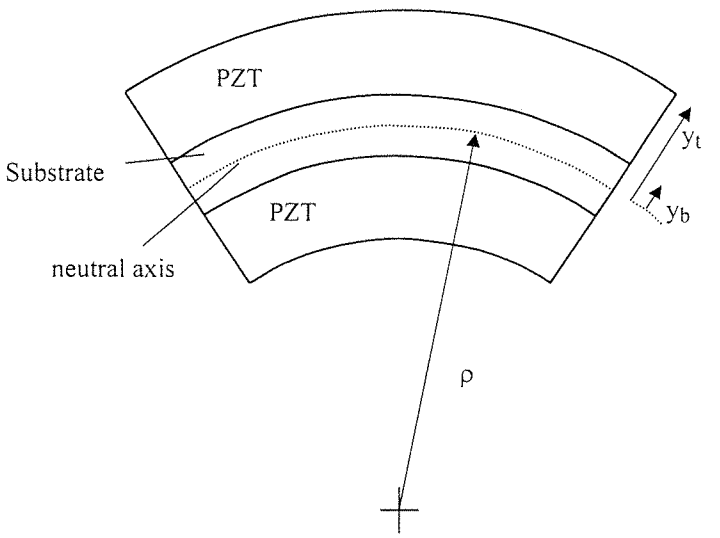

Figure 85: A composite PZT beam.

The figure shows a short section of a beam undergoing pure bending. The strain, S, at any point in the beam is given by the Bernoulli-Euler approximation as

$$S = \frac{y}{\rho}$$

where y is the distance from the neutral axis of the beam, and ρ is the radius of curvature of the neutral axis.

The elastic strain energy stored in a small thickness of beam, Δy, is given by

$$E = \frac{1}{2} YW\Delta l \Delta y \left(\frac{y}{\rho}\right)^2$$

where Y is the Young's modulus of the material, W the width of the beam, and Δl the length of the segment.

The total energy stored in both the PZT layers is found by integrating this over the thickness of the layer (and doubling to include the second layer):

$$E_{PZT} = 2\int_{y_b}^{y_t} E dy = \frac{Y_{PZT} W\Delta l}{3\rho^2}\left(y_t^{\,3} - y_b^{\,3}\right)$$

Similarly, the energy stored in the substrate layer is given by

$$E_S = \int_{-y_b}^{y_b} E dy = \frac{Y_S W\Delta l}{3\rho^2} y_b^{\,3}$$

Thus the ratio of strain energy in the PZT to total strain energy is given by:

$$\frac{E_{PZT}}{E_{PZT} + E_S} = \frac{Y_{PZT}\left(y_t^{\,3} - y_b^{\,3}\right)}{Y_{PZT}\left(y_t^{\,3} - y_b^{\,3}\right) + Y_S y_b^{\,3}}$$

If $Y_{PZT} \approx Y_S$ then

$$\frac{E_{PZT}}{E_{PZT} + E_S} \approx 1 - \left(\frac{y_b}{y_t}\right)^3$$

Appendix D: Optimisation program for piezoelectric generators

This appendix shows the code used to produce figure 47. For details of the derivation of the equations used here, see section 5.7. This appendix comprises two files: the main program, and the genpow() function that is used by this program.

```
% This file uses the fmins() function to minimise the genpow()
% function (which returns the amount of power predicted for
% a generator of a given size), thus finding the optimum
% generator size.  It does this for a range of different base
% excitations and generator sizes, as determined by the
% constr [] matrix

clear constr
%format is f then Z then H in each row

constr=[ ...
%this set of input excitations used for the trend
%search.  Each frequency step goes through a linearly
%increasing value for f^2*Z
10 0.0006 5.00E-03
10 0.0009 5.00E-03
10 0.00135 5.00E-03
10 0.002025 5.00E-03
10 0.0030375 5.00E-03
10 0.00455625 5.00E-03
10 0.006834375 5.00E-03
10 0.010251563 5.00E-03
10 0.015377344 5.00E-03
10 0.023066016 5.00E-03
10 0.034599023 5.00E-03
10 0.051898535 5.00E-03

90 7.40741E-06 5.00E-03
90 1.11111E-05 5.00E-03
90 1.66667E-05 5.00E-03
90 0.000025 5.00E-03
```

```
90 0.0000375 5.00E-03
90 0.00005625 5.00E-03
90 0.000084375 5.00E-03
90 0.000126563 5.00E-03
90 0.000189844 5.00E-03
90 0.000284766 5.00E-03
90 0.000427148 5.00E-03
90 0.000640723 5.00E-03

270 8.23045E-07 5.00E-03
270 1.23457E-06 5.00E-03
270 1.85185E-06 5.00E-03
270 2.77778E-06 5.00E-03
270 4.16667E-06 5.00E-03
270 0.00000625 5.00E-03
270 0.000009375 5.00E-03
270 1.40625E-05 5.00E-03
270 2.10938E-05 5.00E-03
270 3.16406E-05 5.00E-03
270 4.74609E-05 5.00E-03
270 7.11914E-05 5.00E-03

810 9.14495E-08 5.00E-03
810 1.37174E-07 5.00E-03
810 2.05761E-07 5.00E-03
810 3.08642E-07 5.00E-03
810 4.62963E-07 5.00E-03
810 6.94444E-07 5.00E-03
810 1.04167E-06 5.00E-03
810 1.5625E-06 5.00E-03
810 2.34375E-06 5.00E-03
810 3.51563E-06 5.00E-03
810 5.27344E-06 5.00E-03
810 7.91016E-06 5.00E-03

]


%This set of inputs used to generate the example
%applications as an alternative to the previous set
```

```
%constr=[ ...
%10 4.01e-4 5e-3
%10 8.17e-4 5e-3
%1000 2.15e-6 5e-3
%300 3.58e-5 5e-3
%250 6.31e-7 5e-3
%100 3.58e-6 5e-3

%10 4.01e-4 10e-3
%10 8.17e-4 10e-3
%1000 2.15e-6 10e-3
%300 3.58e-5 10e-3
%250 6.31e-7 10e-3
%100 3.58e-6 10e-3

%10 4.01e-4 2.5e-3
%10 8.17e-4 2.5e-3
%1000 2.15e-6 2.5e-3
%300 3.58e-5 2.5e-3
%250 6.31e-7 2.5e-3
%100 3.58e-6 2.5e-3
%]
temp=size(constr);numc=temp(1);

global spring_flag  %determines whether the simulation is to include the
space required for a spring (1-> spring 0->no spring)
global Qunglobal ne_max    %the maximum electrical damping that can be
applied
global density  %mass density
%depth and width are set to 2*H in the equations
global alpha   %the base excitation
global w %circular frequency
global Hmaxval  %generator height
global unwant_tot    %total unwanted damping after extra has been added
to limit beam amplitude
global dampun
global amplitude
global Youngs %youngs modulus of beam material
global Tmax  %max stress allowed in piezo beam
global Lval  %length of enclosing box
global Wval  %width of enclosing box
```

```
global stress %output: stress in beam
global aflag  %stress too big flag.
global afactor  %how much correction has been applied to the amplitude
for stress reasons

%determines whether the simulation is to include the space required for
a spring (1-> spring 0->no spring)
spring_flag=1;
%spring_flag=0;  %this option used to get the maximum power for any type
of generator


Youngs=75e9;
Tmax=40e6;
Qun=100;
density=8000;  %steel density

%three possibilities: (only uncomment one of them)
%ne_max=10000  %this is unlimited to find max for any
                  %transducer use with spring_flag=0
ne_max=0.049 %bulk pzt8
%ne_max=4e-4  %thick-film pzt

% max iteration steps in search, minimisation, tolerance [x f(x)]
op(14)=20000;op(1:3)=[0,1e-5,1e-5];

clear powden hratio damp h hratio flagnum d_un amp lenb power lenratio

disp('Total table entries=');
disp(numc)

for ind=1:numc
   %set  the  parameters  corresponding  to  this  step  f  z  h  q
   w=constr(ind,1)*2*pi;
   Hmaxval=constr(ind,3);
   Lval=Hmaxval*2;
   Wval=Hmaxval*2;
   alpha=constr(ind,2);

   disp('first try:');
   disp(genpow([Hmaxval*0.99,ne_max/200,Lval*0.99]));
```

```
   for trial=1:5  %mess with different start conditions to get a good
optimum search
      if                        (spring_flag=1)                    then
      [x,options]=fmins('genpow',[Hmaxval*0.99,ne_max/trial,Lval*0.99],o
      p);
      else
      [x,options]=fmins('genpow',[Hmaxval*0.99,ne_max/trial],op);
       %search for min starting at [...] with options op
      for min starting at [...] with options op
      temp(trial)=-genpow(x);
   end
   [tempb besttrial]=max(temp);
   [x,options]=fmins('genpow2',[Hmaxval*0.99,ne_max/besttrial,Lval*0.99
],op);
   h(ind)=x(1);
   damp(ind)=x(2);
   lenb(ind)=x(3);
   lenratio(ind)=lenb(ind)/Lval;
   powden(ind)=-genpow2(x);
   power(ind)=powden(ind)*Lval*Hmaxval*Wval;%disp(dampun);
   d_un(ind)=dampun;
   space_filled(ind)=(2*amplitude+h(ind))/Hmaxval;
   flagnum(ind)=options(10);          %the   number   of   optimisation
   stepssflag(ind)=aflag;
   afacts(ind)=afactor;
   hratio(ind)=h(ind)/Hmaxval;
   stress_ratio(ind)=stress/Tmax;
   options(10)
end
save  out  numc  constr  power  damp  h  hratio  lenratio  flagnum  d_un
space_filled  -ascii
```

Function: genpow()

```
%The following code is a function used by the above program.
%It returns the amount of power predicted for a generator
%of a given size

function val=genpow(vect)
```

```
global spring_flag;
global Qun
global ne_max   %the maximum electrical damping that can be applied
global density  %mass density
%depth and width are set to 2*H in the equations
global alpha   %the base excitation
global w %circular frequency
global Hmaxval  %generator height
global dampun    %total unwanted damping after extra has been added to
limit beam amplitude
global amplitude
global Youngs %youngs modulus of beam material
global Tmax  %max stress allowed in piezo beam
global Lval  %length of enclosing box
global Wval  %width of enclosing box
global stress %output: stress in beam
global aflag  %stress too big flag.
global afactor  %how much correction has been applied to the amplitude
for stress reasons

h=vect(1);  %beam height
damp=vect(2);     %applied electrical damping ratio

length=Lval/2;  %dummy default value
if (spring_flag==1) then length=vect(3); end %the length of the beam

stress=0;
aflag=0;

correctiona=1.0;   %this permits a smoothing of non-valid functional
bits, to promote a good minimisation
correctionb=1.0;
correctionc=1.0;
correctiond=1.0;
afactor=1;

dampun=1/Qun;
%check that limits have not been reached
thickness=(4*w^2*density*h*length^3*(Lval-length)/Youngs)^(1/3);
  %beam thickness for required natural frequency
```

```
 %slope off the function in invalid areas (see below)
if(damp>ne_max) correctiona=(ne_max/damp)^6; damp=ne_max; end
if(h>Hmaxval) correctionb=Hmaxval/h; h=Hmaxval; end
if(length>Lval) correctionc=(Lval/length); length=Lval; end


if(h+2*alpha/(damp+dampun)>Hmaxval)    dampun=(2*alpha)/(Hmaxval-h)-damp;
end
%that set total damping to limit beam to box if amplitude too big
 amplitude=alpha/(damp+dampun);
%disp(dampun);

stress=3*Youngs*thickness*amplitude/(2*length^2);
if     (spring_flag==1     &     Tmax<stress)     a=amplitude;     aflag=1;
amplitude=Tmax*a/stress; afactor=amplitude/a; correctiond=afactor^2; end
%catch the case where too much stress is in beam.  If it is too much,
% reduce beam amplitude to an ok value.  add correctiond to persuade
% away from this area.  afactor indicates how far past we went

powden=(1/(Lval*(h+2*amplitude)*Wval))*w*damp*0.5*w^2*Wval*(Lval-
length)*density*h*(amplitude)^2;

powden=powden*correctiona*correctionb*correctionc*correctiond;
%the correction factors are activated when a limiting constraint is
%broken.  By using this technique, a gradient is set up that guides
%the optimisation back into valid regions.  After the solution, all
%output must be checked to ensure that the optimisation finished
%outside of the invalid regions

if(vect(1)<0  |  vect(2)<0  |  length<0)  powden=0;  end     %catch negative
input arguments

val=-powden;     %the minus gives the minimisation function the correct
polarity to do an effective maximisation.
```

Appendix E: Phase Locked Loop (PLL) test circuit

This appendix describes the design of the Phase Locked Loop (PLL) circuit used to drive the electromechanical shaker at the resonant frequency of the generator beam for the experiments described in section 7.3.2.2.

Figure 86 shows a block diagram of the arrangement, with each block expanded in the following figures. The circuit comprises a PLL connected in positive feedback to the generator structure. The positive feedback is designed to operate in a manner similar to the situation found when a microphone and speaker arrangement produces a feedback whistle. The difference here is that the PLL produces an output of fixed amplitude, so the 'feedback whistle' is of a controlled amplitude. To produce positive feedback in the circuit, the PLL is required to lock-on in phase with the input signal derived from the generator core. To fulfil this requirement, the PLL was built from discrete components with a phase-detector of the author's own design.

The comparators IC1 and IC2 take the sine wave inputs from the coil and VCO, and form them into a TTL 5V square wave. Resistors R2, 3, 5 and 6 introduce a small amount of hysteresis. The high-pass filters formed by R1/4 and C1/2 remove any DC component in the inputs. IC4 is set-up so that it produces a pulse approximately 0.75 of the period of the input waveform. The logic formed by IC4 and IC5 is arranged so that if the output from IC1 is in advance of that from IC2 then IC5a will produce short pulses, and if the reverse condition is true then IC5b will produce short pulses. The output from IC5b is inverted, then summed with that from IC5a and a DC offset. The resulting signal from IC7 indicates the relative phase of the two input signals with short positive or negative pulses about a DC level. The DC level is used to introduce a permanent phase offset in the circuit which can be adjusted to compensate for any phase leads or lags in the remainder of the positive feedback loop. After the signal is smoothed by the loop-filter, it passes into the VCO block. The output from the loop-filter is summed in IC9 with a DC offset that determines the center frequency of the oscillator. IC10 is a VCO chip that produces the sine wave required to close the PLL loop.

To set-up the circuit it may be necessary to experiment with the polarity of the generator coil so that its output is in-phase with the signal supplied to the shaker. To achieve correct closed loop performance from the PLL care must be taken with which of the phase detector inputs is connected to the VCO. Operating with a generator with a resonant frequency of 105Hz, the circuit was found to achieve a resonant lock over a centre frequency range of ±25Hz. Lock time (time for the outer positive feedback loop to produce 90% of final beam amplitude) was around

0.7 seconds. Experiments showed that the circuit also operated well at the higher beam frequency of 300Hz.

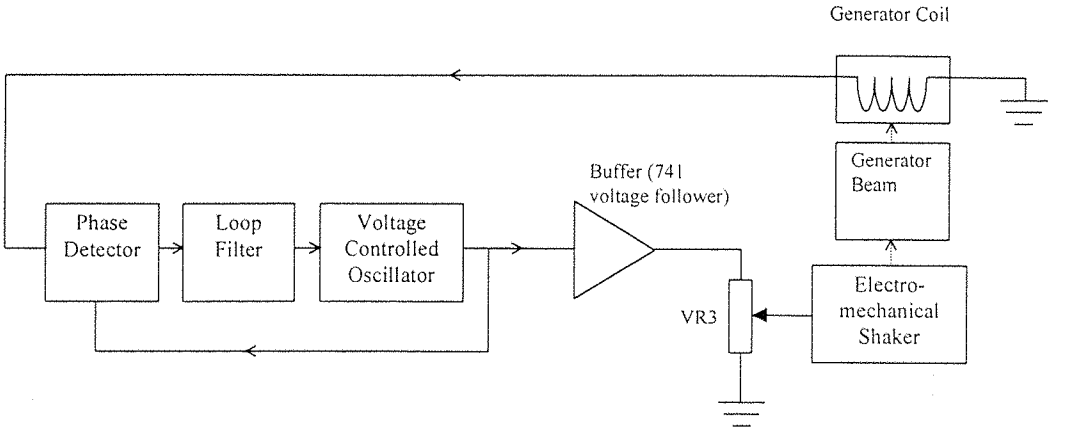

Figure 86: PLL block diagram

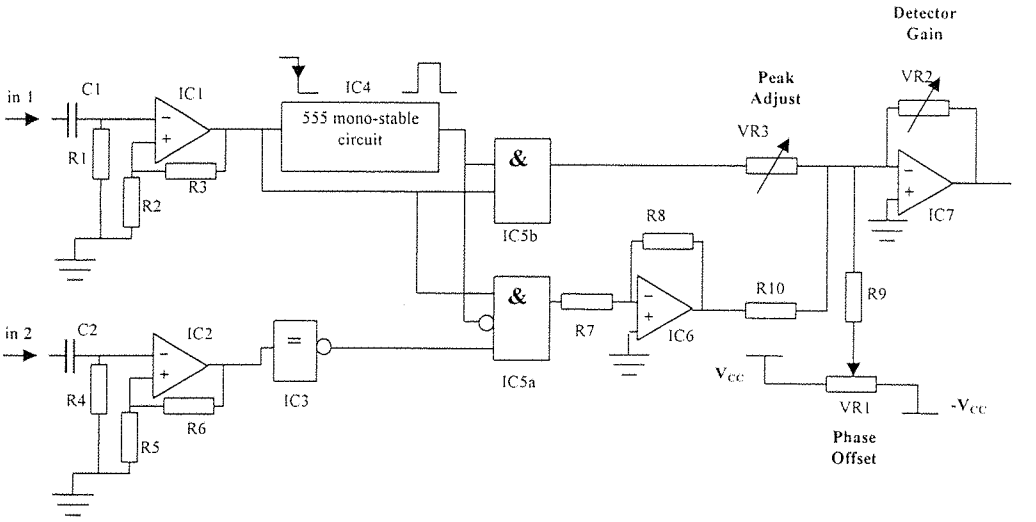

Figure 87: Phase detector circuit

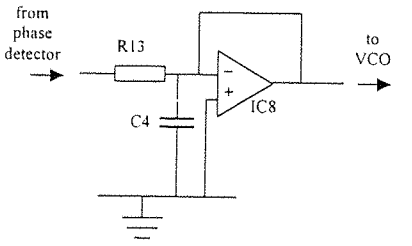

Figure 88: Loop filter circuit

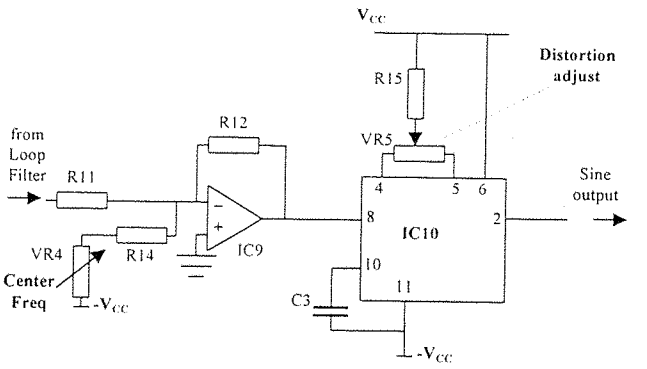

Figure 89: VCO circuit

Table 28: Component values

R1	50K	VR1	10K	IC1	LM311
R2	100R	VR2	10K	IC2	LM311
R3	510K	VR3	10K	IC3	HCT04
R4	50K	VR4	47K	IC4	NE555
R5	100R	VR5	10K	IC5	HCT08
R6	510K	C1	2µ	IC6	741
R7	1K	C2	2µ	IC7	741
R8	1K	C3	0.1µ	IC8	741
R9	220K	C4	0.47µ	IC9	741
R10	5K			IC10	XR3038ACP
R11	15K				
R12	47K				
R13	100K				
R14	47K				
R15	4K7				

Appendix F: Magnetic circuit model

This code that examines the magnetic field in a magnetic core over a range of input parameters. The design and configuration of the core is described in section 7.4.1. The appendix comprises two ANSYS programs. The first controls the parameters, and invokes the second '*corex.txt*' which performs a finite element analysis to determine the resulting field pattern. Results are saved in an output file.

```
!loop control program: (calls corex.txt)

finish
/clear,start
*dim,forfile,ARRAY,1,6

!syntax:
!do,par,ival,fval,inc
!parsav,lab,name,ext
!parres,lab,name,ext


*do,parma,0.1e-3,7.1e-3,0.5e-3      !loop this variable
*do,parmb,20.1e-3,22.2e-3,0.3e-3    !loop this variable
*do,parmc,0.1e-3,7.1e-3,0.5e-3      !loop this variable


parsav,ALL,psave,dat  !save the  variables
/clear,start             !clear database
parres,NEW,psave,dat  !retrieve variables

/inp,corex,txt
finish      !ensure exit of post1 or prep7

forfile(1,1)=parma  !variables
forfile(1,2)=parmb
forfile(1,3)=parmc
forfile(1,4)=Bavg !the average B-field in the gap
forfile(1,5)=ab2tot     !the integral of b-field squared over air gap
```

```
forfile(1,6)=ab2tot2    !the integral of b-field squared over all air
regions


/com,done
/out,magres3,dat,,APPEND

!write the contents of the forfile results array to file  the (...) line
is a format string
!formaT  (prepointFspace.afterpoint)  (4F10.5) works!
*vwrite,forfile(1,1)
(4E10.5)
*vwrite,forfile(1,2)
(4E10.5)
*vwrite,forfile(1,3)
(4E10.5)
*vwrite,forfile(1,4)
(4E10.5)
*vwrite,forfile(1,5)
(4E10.5)
*vwrite,forfile(1,6)
(4E10.5)



/com delimiter..
/out

*enddo
*enddo
*enddo
```

Batch File: corex.txt

```
!receives model parameters parma,parmb,parmc and returns magnetic field

!this file takes parameters parma,parmb,parmc and feeds then into
! g (gap), lc( length of core) and lm (length of magnet)
! tm is fixed at 10e-3.  The core is kept thick, to avoid any saturation
```

```
!  is is assumed that the reluctance of the core is much
! less important than the rel.  of the air gap, and is
!thus kept at a constant low value.

finish
/FILNAM,magcore
/TITLE,magnetic core
/UNITS,SI

/PREP7
Hc=600e3   !magnet coecive force
Br=0.85  !magnet remenance
muzero=4e-7*3.14159
ironperm=5000   !relative permeability of metal core

g=parma  !air gap
lm=parmc  !maglength
tm=10e-3  !mag thickness
lc=parmb  !core length
tc=20e-3  ! core thick
b=4e-2      !distance to boundaries of model


!now define coordinates for keypoints
x0=g/2+lm+tc+b
x1=g/2+lm+tc
x2=g/2+lm
x3=g/2
x4=0

y0=0
y1=lc/2-tm
y2=lc/2-tm+tm
y3=lc/2-tm+tm+b


et,1,PLANE13
et,2,infin9
emunit,MKS  !use mks units
```

```
!air:
MP,murx,1,1.0

!iron
mp,murx,2,ironperm

!magnet
mp,mgxx,3,Hc
mp,murx,3,Br/(muzero*Hc)

!key points at coordinates xy:

K,100,x0,y0,0
!this is keypoint 00, but it doesn't like the number zero

K,10,x1,y0,0
K,20,x2,y0,0
K,30,x3,y0,0
K,40,x4,y0,0

K,01,x0,y1,0
K,11,x1,y1,0
K,21,x2,y1,0
K,31,x3,y1,0
K,41,x4,y1,0

K,02,x0,y2,0
K,12,x1,y2,0
K,22,x2,y2,0
K,32,x3,y2,0
K,42,x4,y2,0

K,03,x0,y3,0
K,13,x1,y3,0
K,23,x2,y3,0
K,33,x3,y3,0
K,43,x4,y3,0

!infinite boundary edges
```

```
L,100,01
L,01,02
L,02,03

L,03,13
L,13,23
L,23,33
L,33,43
Latt,,,2    !infin boundary
lsel,none

!now define areas

!first the magnet
Asel,none
a,21,22,32,31
aatt,3,,1    !magnet mat,,type

asel,none
a,10,11,21,20
a,11,12,22,21
aatt,2,,1  !iron    mat,,type

lsel,all
asel,none
a,100,01,11,10
a,01,02,12,11
a,02,03,13,12
a,12,13,23,22
a,22,23,33,32
a,32,33,43,42
a,31,32,42,41
a,30,31,41,40
a,20,21,31,30
aatt,1,,1  !air    mat,,type

!The undefined boundaries automatically carry a flux normal condition.
specify AZ=0 using
!D command for parallel flux condition

allsel
```

```
lsel,s,type,,2
LESIZE,all,2e-3
lmesh,all
lsel,all

asel,all

!ESIZE,all,0.25e-3

amesh,all
allsel
save
fini

/solu
antype,static,new
solve

fini

/post1
!plf2d
!prnsol,b,sum

!plvect,b

!gets b-field in gap

asel,s,loc,x,x4+(x3/2)
asel,r,loc,y,y1+((y2-y1)/2)
esla,s
etable,bfield,bx  !get the bfield for each gap element
etable,vol,volu         !get the area of each element
smult,b2,bfield,bfield  !get the square of the B-field
smult,ab2,b2,vol        !get area b squared product for each element
ssum              !sum  for  Ab2  gives  B-field  squared  integrated  over
area

*get,thesum,ssum,0,ITEM,bfield
*get,howmany,ELEM,0,COUNT     !how many elements
Bavg=thesum/howmany     !the average B-field in gap
```

```
*get,ab2tot,ssum,0,ITEM,ab2    !get the integrated b-field over area

!Now get the integrated B squared value over all regions, including air
gap
esel,s,mat,,1                  !get all the air (material1) elements
etable,bfield2,bx !get the bfield for each element
etable,vol2,volu          !get the area of each element
smult,b22,bfield2,bfield2  !get the square of the B-field
smult,ab22,b22,vol2          !get area b squared product for each element
ssum                !sum for Ab2 gives B-field squared integrated over
area
*get,ab2tot2,ssum,0,ITEM,ab22    !get the integrated b-field over area
```

Appendix G: Optimisation program for magnet-coil generators

This appendix shows the code used to produce the magnet-coil data for figure 83. It implements the equations derived in section 7.4.3 to optimise the horizontal-coil model described there. This appendix comprises three files: the main program, the coilpow() function that is used by the main program, and finally a program to calculate the space required in each generator for a planar spring. At the end of the appendix a set of graphs shows the internal dimensions that correspond to the magnet-coil data.

```
% This file uses the fmins() function to minimise the coilopt()
% function (which returns the amount of power predicted for
% a generator of a given size), thus finding the optimum
% generator size.  It does this for a range of different base
% excitations and generator sizes, as determined by the
% constr [] matrix

clear constr

%format f Z H Qunwnat
%this matrix is the set of input excitations that are examined
%see Appendix D for the excitations used in the trend search.
constr=[ ...
10 4.01e-4 5e-3 100
10 8.17e-4 5e-3 100
1000 2.15e-6 5e-3 100
300 3.58e-5 5e-3 100
250 6.31e-7 5e-3 100
100 3.58e-6 5e-3 100

10 4.01e-4 10e-3 100
10 8.17e-4 10e-3 100
1000 2.15e-6 10e-3 100
300 3.58e-5 10e-3 100
250 6.31e-7 10e-3 100
100 3.58e-6 10e-3 100

10 4.01e-4 2.5e-3 100
```

```
10 8.17e-4 2.5e-3 100
1000 2.15e-6 2.5e-3 100
300 3.58e-5 2.5e-3 100
250 6.31e-7 2.5e-3 100
100 3.58e-6 2.5e-3 100

]

temp=size(constr);
numc=temp(1);


clear Abest

global invQun
global g_ratio dens B2 rho
global pow_sub flags Abest
global Z f Hmaxval
global K1 K5 K2 pi4

global Abest lam
pi4=pi/4;

g_ratio=0.195/(0.195+0.71);  %magnetic gap as proportion of total width
dens=8000; %density of coil
B2=0.0491*0.71/0.195;  %is psi * Wopt/gopt  %value of B^2 in gap
rho=1.69e-8;   %resistivity of copper
B_=sqrt(B2);


% max iteration steps in search, minimisation, tolerance [x f(x)]
op(14)=1000;
op(1:3)=[0,1e-4,0.00001];

clear powres flagnum lenc Resload flagop Amp lambda Voltload powcube
Qfact

disp('Total table entries=');
disp(numc)

for ind=1:numc
```

```
        ind
        %set the parameters corresponding to this step f z h q
        w=constr(ind,1)*2*pi;


        Hmaxval=constr(ind,3);
        Z=constr(ind,2);
        invQun=1/constr(ind,4);



        %partial calculations
        K1=pi*g_ratio*dens*w/(2*B2);
        K5=w^2/(2*pi);
        K2=Z*K1*7/pi;

        ltrial=Hmaxval;     %find a value oflenc that lies in the non-
zero solution set
        ptrial=0;
        while (ptrial==0 & ltrial>1e-10)
           ltrial=ltrial/2;
           ptrial=coilpow2([ltrial 1]);
        end

        [x,options]=fmins('coilpow',[0.9*Hmaxval,3],op);    %search  for
min starting at [...] with options op

        lenc(ind)=x(1);
        Resload(ind)=x(2);
        powres(ind)=-coilpow2(x);
        flagnum(ind)=options(10);   %the number of optimisation steps
        flagop(ind)=flags;   %records  which  type  of  root  was  found  in
coilpow1
        Amp(ind)=Abest;
        lambda(ind)=lam;
        options(10)
end
```

```
for i=1:numc
        powcube(i)=powres(i)*constr(i,3)^2;   %calculate the power that
would be generated from a cube of side H
        Voltload(i)=Resload(i)/(1+Resload(i))*B_*(constr(i,3)-
2*Amp(i))*2*pi*constr(i,1)*Amp(i);

%Voltload(i,j,k)=Resload(i,j,k)/(1+Resload(i,j,k))*B_*wrange(i)*Amp(i,j,
k);
        Qfact(i)=Amp(i)/constr(i,2);
end

save out numc constr powres flagnum lenc Resload Amp lambda Voltload
powcube Qfact -ascii
```

Function: coilpow()

```
%The following code is a function used by the above program.
%It returns the amount of power predicted for a generator
%of a given size

function val=coilpow1(vect)

if (size(vect)~=2) error('minim: wrong number of parameters: need
(l,h)'); end

lc=vect(1);
r=vect(2);

global r1 r2 val1 val2
global invQun           %this is 1/Qunwanted
global g_ratio dens B2 rho
global pow_sub flags Abest
global Z w Hmaxval

global K1 K5 K2 pi4

global Abest lam
```

```
K3=2*rho*lc/g_ratio;
Aregion=4*lc/7;
%K4=K2*Aregion;
pi7lc=pi*lc/7;

R1=(2*rho*lc/(g_ratio))*r;

K8=pi/(K1*(K3+R1));

p1=[K8/7 invQun -Z];  %the polynomial for lc/A<(7/4)
p2=[K8/(4*lc) 0 invQun -Z];  % the > region

r1=roots(p1);  %r1 has two roots
r2=roots(p2);          %r2 has 3 roots

val1=r1>Aregion;  %these tell us wheteher the roots (assuming they are
real) are in valid ranges
val2=r2<Aregion;

%the following will find the root with the largest amplitude
%ie it returns root for p1 first if they are real and valid
%Justification: the optimum design is expected to lie on the larger of
any two possibilities - trying to return more than
%one root would confuse the optimisation routine.

Abest=0;
lam=0;
if (isreal(r1))
   if (val1(1) & val1(2)) Abest=max(r1); flags=1; end
   if (val1(1) & ~val1(2)) Abest=r1(1); flags=2; end
   if (~val1(1) & val1(2)) Abest=r1(2); flags=3; end

   if (Abest>0) lam=pi7lc/Abest; end
end

if (Abest==0)     %if no good roots yet....
   if (val2(1) & isreal(r2(1))) Abest=r2(1); flags=4; end
   if (val2(2) & isreal(r2(2)) & r2(2)>Abest) flags=5; Abest=r2(2); end
   if (val2(3) & isreal(r2(3)) & r2(3)>Abest) flags=6; Abest=r2(3); end
   lam=pi4;
end
```

```
if (Abest==0)      %if no good roots yet....
   flags=7;
end


if (2*Abest+lc>Hmaxval) Abest=(Hmaxval-lc)/2;   end %does the amplitude
exceed allowed space?
power=R1/((R1+K3)^2)*K5*4*B2*Abest^4*lam;  %calculates Power/(T*W)

% if (2*Abest+lc>Hmaxval) power=0;    %does the amplitude exceed allowed
space?
%    else    power=R1/((R1+K3)^2)*K5*4*B2*Abest^4*lam;        %calculates
Power/(T*W)
% end

 if(vect(1)<0  |  vect(2)<0)  power=0;  end      %catch  negative  input
arguments



val=-power;     %the minus gives the minimisation function the correct
polarity
```

Program: beamsize.m

```
% This file has output data from the previous program built
%into its input data.  It calculates the proportion of the
%enclosure length that is required to form a planar spring

%finds minimum straight beam length for Sm constraints .  See log5 pp.
111

%constants
%Q=100
E=2.1E11
Sm=4.2E8
Density=8000
beta=0.5
```

```
%inputdata

HG=[5.00E-03  5.00E-03  5.00E-03  5.00E-03  5.00E-03  5.00E-03  1.00E-02
1.00E-02 1.00E-02 1.00E-02 1.00E-02 1.00E-02 2.50E-03 2.50E-03 2.50E-03
2.50E-03 2.50E-03 2.50E-03];  %generator enclosure height
L=2*HG;  %generator enclosure length

fn=[1.00E+01  1.00E+01  1.00E+03  3.00E+02  2.50E+02  1.00E+02  1.00E+01
1.00E+01 1.00E+03 3.00E+02 2.50E+02 1.00E+02 1.00E+01 1.00E+01 1.00E+03
3.00E+02 2.50E+02 1.00E+02];
wn=2*pi*fn;
%the frequencies of each data set

Ampl=[1.48E-03  1.62E-03  1.79E-04  1.46E-03  5.26E-05  2.98E-04  2.72E-03
2.96E-03 1.79E-04 2.26E-03 5.26E-05 2.98E-04 8.06E-04 8.88E-04 1.79E-04
8.76E-04 5.26E-05 2.77E-04];
%the beam amplitude

HC=[2.05E-03  1.77E-03  5.31E-04  2.09E-03  3.11E-04  2.79E-03  4.55E-03
4.08E-03 5.31E-04 5.48E-03 3.11E-04 2.79E-03 8.88E-04 7.24E-04 5.31E-04
7.48E-04 3.11E-04 1.95E-03];
%the core height lc


numdataitems=18

for i=1:numdataitems
 A(i)=27*(Ampl(i))^3*E^2*HC(i)*Density*beta*(wn(i))^2/(2*Sm^3);
 poly(i,:)=[1 0 A(i) -A(i)*L(i)];
 solns(:,i)=roots(poly(i,:));
end

%solves the equation for spring length ls from equation given in
%main text

propn=solns(3,:)./L

save out.txt propn -ascii
```

Results graphs

These graphs show the internal dimensions that correspond to figure 83. See that section for more details.

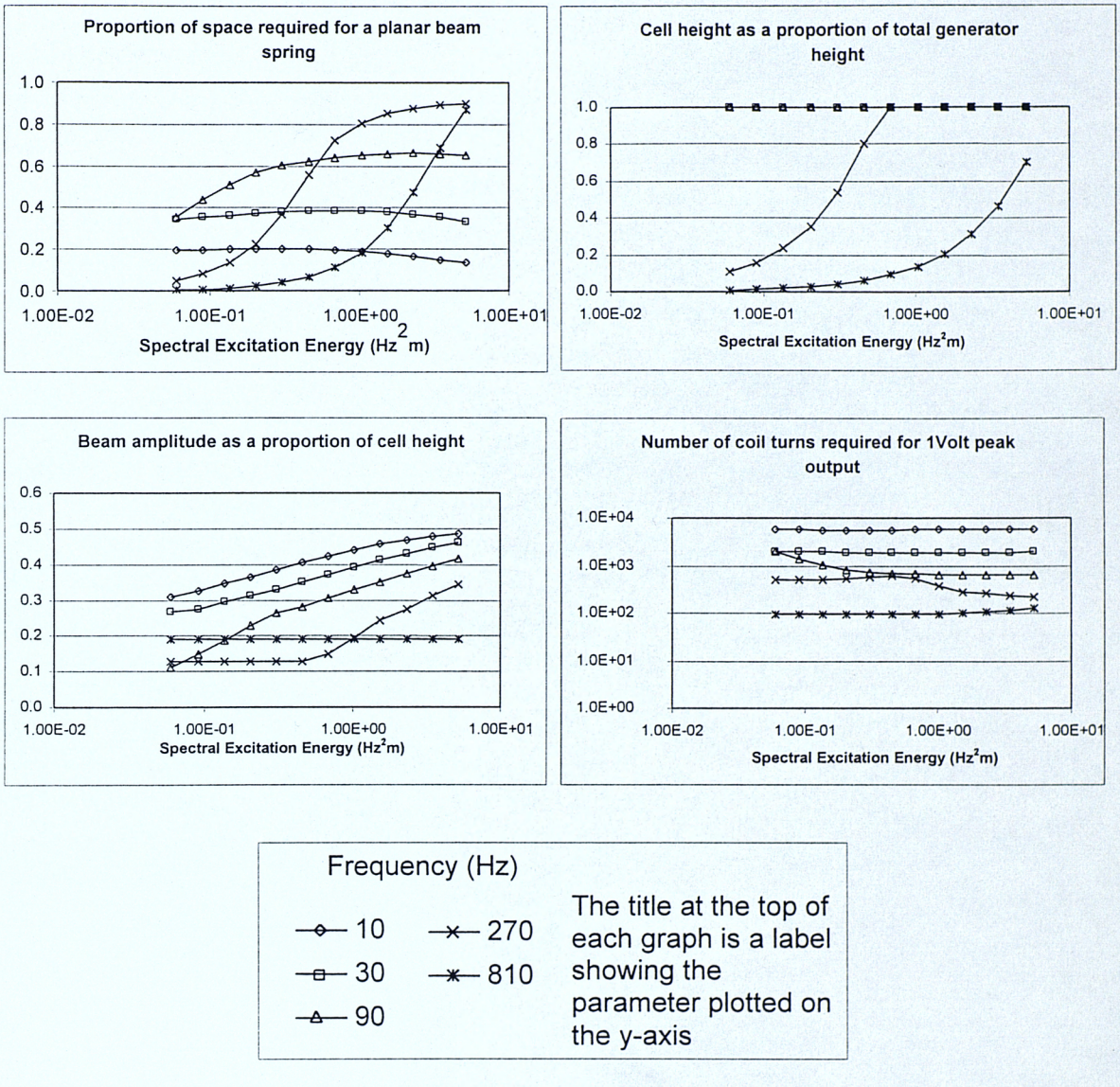

Figure 90: Internal dimensions of optimum horizontal-coil generators

References

[1] A home page for the company Perrelet 1777:
http://www.perrelet.com.au/

[2] *Transducers '01 / Eurosensors XV* and the *Int. Symp on Smart structures and Microsystems 2000* both had sessions devoted to self-powered devices.

[3] C. B. Williams and R. B. Yates, "Analysis of a micro-electric generator for microsystems", *Sensors and Actuators A-Physica.*, **52**, No.1-3, pp.8-11, 1996.

[4] C. B. Williams, A. Pavic, R. S. Crouch, and R. C. Wood, "Feasibility study of vibration-electric generator for bridge vibration sensors", *IMAC-PROCS 16TH Int. Modal Analysis Conf.*, Vol 3243, pp1111-1117, 1998.

[5] C. Shearwood and R. B. Yates, "Development of a Resonant Electromagnetic Micro-Generator", *Electronic letters*, Vol.33, No.22, pp.1883-1884, 1997.

[6] W. J. Li, Z. Wen, P. K. Wong, G. M. H. Chan, and P. H. W. Leong, "A micromachined vibration-induced power generator for low power sensors of robotic systems", *World Automation Congress: 8th International Symposium on Robotics with Applications*, June 16-21, Hawaii, USA, 2000.

[7] R. Amirtharajah and A. P. Chandrakasan, "Self-powered signal processing using vibration-based power generation", *IEEE Journal of Solid-State Circuits*, Vol 33, No 5pp 687-695, 1998.

[8] M. Umeda, K. Nakamura, and S. Ueha, "Energy storage characteristics of a piezo-generator using impact induced vibration", *Jpn. J. Appl. Phys.*, Vol 36, pp. 3146-3151, 1997.

[9] Personal communications with Manabu Aoyagi, May 2000.

[10] M. Hayakawa, *Electronic wristwatch with generator*, United States Patent, number 5001685, March 19th, 1991.

[11] P. B. Koeneman, H. J. Busch-Vishniac, K. L. Wood, "Feasibility of Micro Power Supplies for MEMS", *Journal of Microelectromechanical Systems*, Vol 6, No 4, pp 355-362, 1997.

[12] M. J. Konak, I. G. Powlesland, S. P. van der Velden, and S. C. Galea, "A Self-Powered Discrete Time Piezoelectric Vibration Damper", Smart Materials Structures & Integrated Systems, Vol 3241, pp 270-279, 1997.

[13] T. Starner, "Human Powered Wearable Computing", *IBM System J.*, Vol 35 [3&4, pp 618-29], 1996.

[14] Shi-Hiu Chen, *Dynamoelectric shoes*, United States Patent, number 5495682, March 5th, 1996.

[15] N. Lakie, *Inflatable boot liner with electrical generator and heater*, United States Patent, number 4845338, July 4th, 1989.

[16] J. Kymissis, C. Kendall, J. Paradiso, and N. Gershenfeld, "Parasitic Power Harvesting in Shoes", *2nd Int. Symp. Wearable Computers, Digest of Papers*, Ch. 28 pp.132-139, 1998.

[17] E. Hausler and L. Stein, "Implantable Physiological Power Supply with PVDF Film", *Ferroelectrics*, Vol. 60, pp.277-282, 1984.

[18] A page dedicated to Trevor Baylis supported by the company "Innovative Technologies" : http://windupradio.com/baylis.htm

[19] D. Segal, I. Bransky, "Testing of a piezoelectric generator for in-flight electrical powering of projectile guidance systems", *Ferroelectrics*, Vol 202, pp.81-85, 1997.

[20] J. B. Lee, Z. Chen, M. G. Allen, A. Rohatgi, and R. Arya, "A Miniturized High-Voltage Solar Cell Array as an Electrostatic MEMS Power Supply", *Journal of Microelectromechanical Systems*, Vol. 4 No. 3, pp102-108, 1995.

[21] A. C. van der Woerd, M. A. Bais, L. P. de Jong, and A. van Roermund, "A highly efficient micro-power converter between a solar cell and a rechargeable lithium-ion battery", *SPIE Conference on Smart Electronics and MEMS*, Vol 3328, pp. 315-325, 1998.

[22] J.N. Ross, "Optical power for sensor interfaces", *Meas. Sci. Technol.* Vol 3, pp 651-655, 1992.

[23] W. Kuntz and R. Mores, "Electrically Insulated Smart Sensors: Principles for Operation and Supply", *Sensors and Actuators A*, 25-27, pp 497-505, 1991.

[24] W. Gross, "Optical Power Supply for Fibre-optic Hybrid Sensors", *Sensors and Actuators A*, Vol 25-27, pp. 475-480, 1991.

[25] M. R. Al-Mohanadi, J. N. Ross, and J. E. Brignell, "Optical power and intelligent sensors", *Sensors and Actuators A,* 60, pp 142-146, 1997.

[26] T. Renner, G. Rittmayer, D. Falkenberg, and G. Grubmuller, "An Isotropic Thermoelectric Battery for Cardiac Pacemakers", *Proc. of the 2nd International Symposium on Power from Radioisotopes*, Madrid, pp.207-216, 1972.

[27] Personal communications with Wolfgang K. Scheibelhofer (cardiologist in Vienna, Austria), 03 February 1999.

[28] M. Stordeur and I. Stark, "Low Power Thermoelectric Generator - self sufficient energy supply for micro systems", *Proc. ICT'97 16th Int. Conf. Thermoelectrics*, pp 575-577, 1997.

[29] Texas Instruments TIRIS homepage: http://www.ti.com/mc/docs/tiris/docs/index.htm

[30] U. Kaiser, W. Steinhagen, "A Low Power Transponder IC for High-Performance Identification Systems", *IEEE J. of Solid-State Circuits*, Vol. 30 No. 3, 1995.

[31] D. Friedman, H. Heinrich, and D-W. Duan, "A Low-Power CMOS Integrated Circuit for Field-Powered Radio Frequency Identification Tags", *IEEE International Solid-State Circuits Conference*, pp. 294-295, 1997.

[32] Department of cybernetics, Reading university:
http://www.cyber.rdg.ac.uk/K.Warwick/WWW/fpage.htm

[33] J. Bouvier, Y. Thorigne, S. Abou Hassan, M.J. Revillet, and P. Senn, "A Smart Card CMOS Circuit with Magnetic Power and Communications Interface", *IEEE International Solid-State Circuits Conference*, pp. 296-297, 1997.

[34] H. Matsuki, M Yamaguchi, T. Watanabe, K. Murakami, K. Nadehara, and T. Yamamoto, "Implantable transformer for an artificial heart utilizing amorphous magnetic fibres", *J. Appl. Phys.*, Vol 64 (10), pp. 5859-5861, 1988.

[35] Ultralife Batteries Inc., product data sheet:
http://www.ultralifebatteries.com/

[36] J.B. Bates, G.R. Gruzalski, and C.F. Luck, "Rechargeable Solid State Lithium Microbatteries", *Proc. IEEE Micro Electro Mechanical Syst. Workshop*, pp. 82-86, 1993.

[37] N. M. White and J. E. Brignell, *Intelligent Sensor Systems,* Institute of Physics Publishing, *1996.*

[38] K. S. J. Pister, J. M. Kahn, and B. E. Boser, "Smart Dust: Wireless Networks of Millimeter-Scale Sensor Nodes", *Highlight Article in 1999 Electronics Research Laboratory Research Summary*, 1999.

[39] P. B. Chu, N. R. Lo, E. C. Berg, and K. S. J. Pister, "Optical Communication Using Micro Corner Cube Reflectors", *Proc. of IEEE MEMS Worksho*p, Nagoya, Japan, pp. 350-355, 1997.

[40] G. Asada, M. Dong, T. S. Lin, F. Newberg, G. Pottie, W. J. Kaiser, and H. O. Marcy, "Wireless Integrated Network Sensors: Low Power Systems on a Chip.", *Proceedings of the 1998 European Solid State Circuits Conference*, 1998.

[41] K. Bult, A. Burstein, D. Chang, M. Dong, M. Fielding, E. Kruglick, J. Ho, F. Lin, T.-H. Lin, W. J. Kaiser, H. Marcy, R. Mukai, P. Nelson, F. Newberg, K. S. J. Pister, G. Pottie, H. Sanchez, O. M. Stafsudd, K. B. Tan, C. M. Ward, S. Xue, J. Yao, "A Distributed Wireless MEMS Technology for Condition Based Maintenance.", *Proceedings of the 1996 Integrated Monitoring, Diagnostics and Failure Prevention Conference, Society of Machine Failure Protection Technology (MPFT)*. Mobile, Alabama, USA, pp. 373-380, 24 April 1996.

[42] See MIT's "Ultra Low Power Wireless Sensor Project": http://www-mtl.mit.edu/ research/sodini/ ultra_low_power_wireless_sensor.html

[43] B. Jaffe, W. R. Cook, and H. Jaffe, *Piezoelectric Ceramics*. Academic Press, 1971.

[44] *Piezoelectric Ceramics Data Book for Designers*, Morgan Electroceramics, 1999.

[45] N. W. Hagood and A. von Flotow, "Damping of Structural Vibrations with Piezoelectric Materials and Passive Electrical Networks", *Journal of Sound and Vibration*, **146**(2), pp. 243-268, 1991.

[46] *IEEE Standard on Piezoelectricity*. ANSI/IEEE Standard 176-1987, 1988.

[47] J. F. Shackleford, *Introduction to Material Science for Engineers*, New York: McMillan Publishing Co., pp516-518, 1988.

[48] H.R. Gallantree, "Review of transducer applications of polyvinylidene fluoride", *IEE Proc.*. **130**, 219-224, 1983.

[49] W.G. Cady, *Piezoelectricity*, New York: Dover Publications, vol. 1, 1964.

[50] R. Kornbluh, R. Pelrine, J. Eckerle, and J. Joseph, "Electrostrictive Polymer Artificial Muscle Actuators", *Proc. of the IEE*, pp. 2147-2154, 1998.

[51] W.T. Thomson, *Theory of Vibration with Applications, 3rd Edition*, London: Allen & Unwin, 1988.

[52] A. D. Nashif, D. I. G. Jones, and J. P. Henderson, *Vibration Damping*. New York: John Wiley & Sons, 1985.

[53] T. Priede, "Road vehicle noise", *Noise and Vibration,* ed R.. G. White, and J. G. Walker, New York: John Wiley & Sons, pp. 389-437, 1986.

[54] E. A. Vittoz, "Low-Power Design : Ways to Approach the Limits", *IEEE Int. Solid-State Circuits Conf.*, pp. 14-18, 1994.

[55] K. Aoki, Y. Fukuda, and A. Nishimura, *Jpn. J. Appl. Phys* **32** 4147-4149, 1993.

[56] V. Tvarozek, I. Novotny, I. Cerv-en, J. Kovac, and T. Lacko, *Sensors and Actuators A* **30** 123-127, 1992.

[57] W. C. Hendricks, S. B. Desu, J. Si, and C. H. Peng, *Mat. Res. Soc. Symp. Proc.* **310** 241-247, 1993.

[58] N. M. White and JD Turner, "Thick-film sensors: Past, present and future", *Measurement Science and Technology,* 8, pp.1-20, 1997.

[59] D. Peckner and I. M. Bernstein, *Handbook of stainless steels,* New-York: McGraw-Hill, 1977.

[60] S. P. Beeby, A. Blackburn, and N. M. White, "Processing of PZT piezoelectric thick-films on silicon for microelectromechanical system", *Journal of Micromechanics and Microengineering,* **9** pp. 218-29, 1999.

[61] Heraeus Silica and Metals Ltd, *Preliminary Data Sheet: IP222L Dielectric Paste for Chromium-Steel.* Undated.

[62] Heraeus Silica and Metals Ltd, *Data Sheet: Steel Preparation.* Undated.

[63] Electro-Science Laboratories Inc., *Data Sheet: 9635-C, Cermet Silver/Palladium Conductor.* 1998.

[64] Electro-Science Laboratories Inc., *Data Sheet: 9633-B, Cermet Silver/Palladium Conductor.* 1998.

[65] P. G. Dargie, *A Study of the Effect of Process Parameter Variation Upon the Characteristics of Screen Printed Piezoelectric Materials,* MPhil thesis, University of Southampton, 1998.

[66] L. L. Hench and J. K. West, *Principles of Electronic Ceramics,* New York: John Wiley & Sons, pp22-27, 1990.

[67] W. P. Mason and H. Jaffe, "Methods for measuring piezoelectric, elastic, and dielectric coefficients of crystals and ceramics", *Proceedings of the IRE*, 1954.

[68] B. Jaffe "Measurement of piezoelectric ceramics", *IRE Standards on piezoelectric crystals*, 1961.

[69] Personal communications with P. Dargie, 17th September, 1999.

[70] D. Berlincourt and H. A. F. Krueger, *J. Applied Physics* **30** (11) 1804-1810, 1959.

[71] Y. Nemirovsky, A. Nemirovsky, P. Muralt, and N. Setter, *Sensors and Actuators A* **56** 239-249, 1996.

[72] *Vibration Generator type V50 Mk1, Service Instruction Manual,* Goodmans Industries Limited Vibrator Division, Publication No. V50 Mk.1, 1964.

[73] J. Soderkvist, "Dynamic behaviour of a piezoelectric beam", *J. Acoust. Soc. Am.*. **90** (2), Pt. 1, pp.686-691, August 1991.

[74] J. Soderkvist, "Using FEA To Treat Piezoelectric Low-frequency Resonators", *IEEE trans. on Ultrasonics, Ferroelectrics, and Frequency Control.* **45** (3), May 1998.

[75] P. Lorrain, D. R. Corson, and F. Lorrain, *Electromagnetic Fields and Waves*, New York: W.H. Freeman and Company, 1988.

[76] A. C. Ugural and S. K. Fenester, *Advanced Strength, and Applied Elasticity*, London: Elsevier, 1987.

[77] N. W. Hagood, W. H. Chung, and A. von Flowtow, "Modelling of Piezoelectric Actuator Dynamics for Active Structural Control", *Proc. of the 31st Struct. Dynamics, & Mat'ls Conf.*, Long Beach, CA, May 1990.

[78] *ANSYS GUI Help Manual.* ANSYS Inc, 1998.

[79] M. J. Griffin, *Handbook of human vibration*, London: Academic Press, 1990.

[80] M. H. Chen, *Combining the active control of gear vibration with condition monitoring.* Southampton University PhD Thesis, 1999.

[81] C. Jackson, *The Practical vibration primer,* Houston: Gulf Pub. Co., 1979.

[82] P. Glynne-Jones, S. P. Beeby, P. Dargie, T. Papakostas, and N M White, "An Investigation Into The Effect Of Modified Firing Profiles On The Piezoelectric Properties Of Thick-Film PZT Layers On Silicon", *IOP J. Measurement Science and Technology,* Vol. **11**, pp. 526-531, 2000.

[83] M.Kosec, J. Holc, B. Malic, M. Hrovat, "Processing and Characterisation of High Quality (Pb,La,)(Ti,Zr)O3 Thick Films", *12th European Microelectronics and Packaging Conf.*, pp. 175-181, 1999.

[84] W. Mason, "Aging of the properties of Barium Titanate and Related Ferroelectric Cermaics", *The Journal of the Acoustical Society of America* **27** (1) 73-84, 1955.

[85] Q. M. Zhang and J. Zhao, "Electromechanical Properties of Lead Zirconate Titanate Piezoceramics Under the Influence of Mechanical Stresses", *IEEE Trans. Ultrasonics, Ferroelectrics and Frequency Control* **46** (6) 1518-1526, 1999.

[86] J. F. Shepard, Chu Fan, and S. Trolier-McKinstry, "Characterisation and aging response of the d31 piezoelectric coefficient of lead zirconate titanate thin films", *Journal of Applied Physics* **85** (9) 6711-6716, 1999.

[87] Chan Ming-Ho Gordon, *Design and Modeling of a Micro Vibration-Based Power Generator*, PhD thesis, Chinese University of Hong Kong, June 2000.

[88] Eclipse rare earth magnetics Limited:
http://www.eclipse-magnetics.co.uk/rare_earth.html

[89] H. W. Katz, *Solid State Magnetic and Dielectric Devices*, pp.171, 1959.

The following published papers were included in the bound thesis. These have not been digitised due to copyright restrictions, but the links are provided.

P.Glynne-Jones, et al. (2000) “An investigation into the effect of modified firing profiles on the piezoelectric properties of thick-film PZT layers on silicon.” Measurement Science and Technology, Vol. 12, pp. 663-670

https://doi.org/10.1088/0957-0233/12/6/302